NUMERICAL INVESTIGATIONS OF FLOW AND FILM COOLING WITH ENDWALL CONTOURING AND BLADE TIP EJECTION UNDER ROTATING TURBINE CONDITIONS

A Dissertation

by

KUN LU

Submitted to the Office of Graduate and Professional Studies of
Texas A&M University
in partial fulfillment of the requirements for the degree of

DOCTOR OF PHILOSOPHY

Chair of Committee,	Meinhard Taher Schobeiri
Co-Chair of Committee,	Je-Chin Han
Committee Members,	Hamn-Ching Chen
	Robert Handler
Head of Department,	Andreas A. Polycarpou

December 2014

Major Subject: Mechanical Engineering

ABSTRACT

An effort is made to numerically study the impact of rotating turbine conditions on the aerodynamic performance, film cooling effectiveness and heat transfer with the application of the endwall contouring and blade tip ejection. For this purpose, the three-stage HP turbine research facility at the Turbomachinery Performance and Flow Research Laboratory (TPFL), Texas A&M University, was newly designed and equipped. Using the geometry of this three-stage research turbine rig, comprehensive numerical simulations are performed to systematically study the impact of the rotation from the perspectives of both aerodynamics and heat transfer.

Introducing endwall contouring has become a promising means to reduce the secondary flow losses. Thus TPFL developed a physics-based method which enables researchers and engineers to design endwall contours for any arbitrary blade types regardless of the blade loading, degree of reaction, stage load and flow coefficients. Using this approach, TPFL designed the new endwall contouring which was implemented on the platform of both the first-stage and second-stage rotors. The rotation impacts on the aerodynamics performance due to the endwall contouring were numerically studied using four different rotational speeds namely, 2000 rpm, 2400 rpm, 2600 rpm and 3000 rpm. Meanwhile, the influence on film cooling effectiveness and heat transfer caused by the endwall contouring was investigated for the first-stage rotor. Different purge-to-mainstream mass flow ratios of MFR = 0.5%, 1.0% and 1.5% were

taken into account at the design rotational speed of 3000rpm. The effect of rotational speed (2400rpm, 2550rpm and 3000rpm) was investigated at typical MFR=1.0%.

To investigate the flow characteristics and film cooling at high pressure turbine blade tips, four different rotor-blade tip configurations are designed and studied at TPFL: the plane and squealer tips with tip hole cooling and the plane and squealer tips with pressure-side-edge compound angle hole cooling. Seven perpendicular holes that are evenly distributed along the camber line are used for the tip hole cooling, whilst eight compound-angle holes for the pressure-side-edge cooling. The coolant was ejected through the cooling holes with low, medium and high global blowing ratios at 3000 rpm to study the impact of the blowing ratio on both the cooling effectiveness and heat transfer. Effects of rotation on the cooling effectiveness and heat transfer were calculated at the rotational speeds of 2000rpm, 2550 rpm, and 3000 rpm.

DEDICATION

To my family and friends.

ACKNOWLEDGEMENTS

I would like to express my greatest gratitude to my committee chair, Dr. Schobeiri and my co-chair, Dr. Han for their inappreciable advice, guidance and education throughout the course of this research. I also would like to appreciate my committee members, Dr. Chen and Dr. Handler, for agreeing to serve on my advisory committee.

Thanks also go to my friends and colleagues and the department faculty and staff for making my time at Texas A&M University a great experience. I also want to extend my gratitude to the Supercomputing Center, which provides a platform that allows me to conduct all of the numerical simulations.

Finally, thanks to my father and mother for their constant support and encouragement that help me overcome the hard times.

NOMENCLATURE

C_{ax}	axial chord length of the blade
C_{Ptr}	relative total pressure coefficient, $C_{Ptr} = \frac{P_{tr,out} - \overline{P_{tr,in}}}{\overline{P_{tr,in}}}$
C_{SKE}	coefficient of secondary kinetic energy, $C_{SKE} = \frac{w_{sec}^2 + w_{rad}^2}{w_{ref}^2}$
d	diameter of film cooling holes
H	mass-averaged total enthalpy
ΔH_{stage}	total enthalpy change within a stage
h	height of the diffuser section
h_f	heat transfer coefficient with film cooling, $h_f = \frac{q''_{w,f}}{T_w - T_{aw,f}}$
HP, IP, LP	high, intermediate, low pressure
k	thermal conductivity of the air
L	length of the diffuser section
$\dot{m}$	mass flow rate
M	global blowing ratio, $M = \frac{\rho_c V_c}{\rho_m V_m}$
MFR	purge-to-mainstream mass flow rate

n	rotational speed
Nu	Nuesselt number with film cooling, $\mathrm{Nu} = \frac{h_f C_{ax}}{k}$
P	pressure
ΔP	pressure difference
$q''_{w,f}$	wall heat flux with film cooling
$\frac{q''_{w,f}}{q''_{w,f_0}}$	heat flux ratio with film cooling, $\frac{q''_{w,f}}{q''_{w,f_0}} = \frac{h_f}{h_{f_0}}\left(1 - \eta_{aw}\frac{T_{aw,f_0} - T_{t,c}}{T_{aw,f_0} - T_w}\right)$
R	radius
R1, R2, R3	first, second and third rotors
RANS	Reynolds Averaged Navier-Stokes
S1, S2, S3	first, second and third stators
SST	Shear Stress Transport turbulence model
T	temperature
u/c_o	dimensionless performance parameter, $u/c_0 = \frac{\pi n R_{mid}}{30\sqrt{\Delta H_{stage}}}$
U_P, U_S	diffuser inlet and exit velocity outside the boundary layer
URANS	unsteady Reynolds Averaged Navier-Stokes
V	velocity
w	relative velocity

W	width of the diffuser section
w_{sec}	secondary velocity in relative frame, $w_{sec} = -w_{ax} \sin \Psi_{mid} + w_{circ} \cos \Psi_{mid}$
X	axial location

Greeks

δ	boundary layer thickness
η	globle film cooling effectiveness, $\eta = \frac{T_{t,\infty} - T_{aw,f}}{T_{t,\infty} - T_{t,c}}$
$\eta_{t\text{-}s}$	total-to-static efficiency, $\eta_{t-s} = \frac{1 - \frac{T_{t,out}}{T_{t,in}}}{1 - \left(\frac{P_{out}}{P_{t,in}}\right)^{\frac{\kappa-1}{\kappa}}}$
η_{aw}	adiabatic film cooling effectiveness, $\eta_{aw} = \frac{T_{aw,f_0} - T_{aw,f}}{T_{aw,f_0} - T_{t,c}}$
κ	heat capacity ratio
λ	diffuser recovery factor, $\lambda = \frac{\Delta P_{target}}{\frac{1}{2}\rho U_p^2} = 1 - \frac{(\Delta h_i)_P^2}{(\Delta h_i)_S^2}$
ρ	density
Ψ_{mid}	mid-span turning angle, $\Psi_{mid} = \tan^{-1}\left(w_{circ,mid}/w_{ax,mid}\right)$
ζ_{Ptr}	relative total pressure loss coefficient,

$$\zeta_{Ptr} = \frac{P_{tr,in} - P_{tr,out}}{\frac{1}{2}\rho w_{ref}^2}$$

Subscripts

0	reference film cooling
aw	adiabatic wall
ax	axial
c	coolant
circ	circumferential
f	film coolant that is cooler than mainstream
f_0	film coolant that is as hot as mainstream
i	i^{th}
in	inlet
lim	limit
m	mean value between rotor inlet and exit
mid	mid-span
out	outlet
P	pressure side
r	relative
rad	radial
ref	reference
s	isentropic
S	suction side
sec	secondary

SKE	secondary kinetic energy
t	total or stagnation value
t-s	total-to-static
w	wall
∞	mainstream

Superscript

$\bar{}$	pitchwise-averaged value
$\bar{\bar{}}$	area-averaged value

TABLE OF CONTENTS

Page

LIST OF FIGURES

Page

LIST OF TABLES

Page

1. INTRODUCTION

Motivated by the energy crisis, disposal of highly radioactive waste material from reactor operations and severe reactor accidents, more than three decades ago, the power generation industry started looking into an alternative old concept of gaseous fuel extraction from coal, the coal-based integrated coal gasification combined cycle (IGCC). Due to the continuous release of CO2 from burning fossil fuel leading to alarming global warming and therefore frequent occurrence of extreme weather, clean coal technology that can significantly reduce the CO2 emissions has become a promising solution to the climate change. The abundance of coal as the primary energy source and the availability of necessary technology to extract clean hydrogen and syngas with carbon capture have re-attracted the interest of industry and government in re-introducing the IGCC concept, which offers superior environmental performance as pointed out by Dennis and Harp [1]. The gas turbine, as one of the most important components in IGCC, also plays a large role in our modern world, generating power for communities, supplying thrust for aircrafts, driving propellers for ships, etc. Engineers and researchers are always attempting to maximize its efficiency and output energy however there are several challenge technical issues to be resolved.

1.1 Turbine Aerodynamic Performance

Even though the gas turbine has been developed for a century old and the maximum thermodynamic efficiency of some advanced gas turbines has been pushed to around 40%, the increasing demand in power and running out of fossil fuel has become a

driving force for engineers and researchers all over the world to implement new designs for higher turbine performance approaching the ideal Braydon cycle.

Ewen et al. [2] reported the results of an experimental investigation on small axial turbine performance characteristics. They studied the effects of several design variables on small turbine aerodynamic performance: (a) blade height, (b) vane endwall contouring, (c) blade reaction, (d) blade tip clearance, (e) stage work, and (f) vane and blade airfoil row solidity. The impacts of vane, blade and disk cooling air injection on turbine efficiency were also presented. The tested efficiency data included both design and off-design conditions. Their results indicated that relatively high efficiency could be achieved in small, low aspect ratio axial turbines with optimized design. Malzacher et al. [3] developed and tested the new MTU LPT concept for a high speed turbine in a turbine rig. The concept involved a two-stage turbine for extremely high speed and high stage pressure ratio. Their experiments measured the efficiency level, the turbine characteristic and profile pressure distributions. Meanwhile 3D CFD was also performed for comparisons. To investigate the effect of the blade geometry on total pressure loss coefficient and turbine performance, a comparative study by Schobeiri et al. [4] was presented which focused on the aerodynamic performance of a three-stage HP research turbine facility utilizing two different blade geometries. Two different rotors with same inner and outer diameters were experimentally tested. The first rotor used 3D convexly bowed blades whereas the second one utilized 2D cylindrical blades. The results showed that the 3D bowed blades were able to effectively reduce the extent of the secondary flow region when compared to the cylindrical blades. Atkins et al. [5] presented the

development of aerodynamic performance measurement in the Oxford Rotor Facility, which was conducted at engine representative specific speed, pressure ratio, temperature ratio, Mach number and Reynolds number. A relative resolution in the region of ±0.3% was achieved. Atkins et al. [6] also performed the accurate measurement of the shaft power in the same test facility. Visualization of surface flows in a large-scale, low speed, axial turbine rig was conducted by Rao and Camci [7]. A visualization mixture of oil and pigment was used in the tests. The visualized local separation and reattachment could be helpful explaining heat transfer results on the rotor surface and validating the viscous flow solvers. An experimental study of unsteady flow physics and performance of a $1^1/_2$-stage unshrouded high work turbine was performed by Behr et al. [8]. The paper showed the design of the new $1^1/_2$-stage unshrouded turbine within the Turbomachinery Laboratory of ETH Zurich. A detailed analysis of the unsteady stator-rotor interactions with special attention on the blade tip flows was presented. A combination of experimental and numerical investigations on a three-stage HP research turbine at various operating conditions were carried out by Abdelfattah and Schobeiri [9]. The aerodynamics measurements were performed in a rotational speed range of 1800 to 2800 rpm. They concluded that the numerical simulations were able to provide fairly accurate predictions for the overall efficiency and massflow, however failed in some extent to accurately predict the near-wall flow fields that primarily leaded to the major performance losses in turbomachines. Abdelfattah et al. [10] also conducted numerical simulations on the aerodynamic performance of a two-stage HP research turbine at both design and off-design conditions. The discrepancy in overall turbine efficiency between

the experiment and CFD prediction existed and larger difference was obtained at off-design points. However the CFD results were able to provide the global efficiency trend and capture the location of the highest efficiency point.

1.1.1 Endwall secondary flows and losses

Apparently the direct and most effective way to enhance the turbine performance is to reduce the various kinds of losses in gas turbines. Schobeiri [11] dedicated a full chapter of his book to the physics of loss generation and its calculation. Comprehensive discussion of loss mechanisms including mixing processes, blade boundary layer loss, trailing edge loss, tip leakage loss and endwall loss, etc. in turbomachines has been made by Denton [12]. It is reported that the endwall loss or so-called secondary loss is a major source of lost efficiency of turbines, which typically accounts for 1/3 of the total loss. Approximate 2/3 of it can be attributed to the entropy generation in the annulus wall boundary layers. A second component is resulted from mixing loss of the inlet boundary layer, which is amplified by the secondary flow. Secondary kinetic energy is the third component which contributes to about 1/4 of the total endwall loss. Other contributions may result from local flow separations, pressure gradient and thickening of the boundary layer. Thus, reducing the secondary loss is a key means of improving turbine performance.

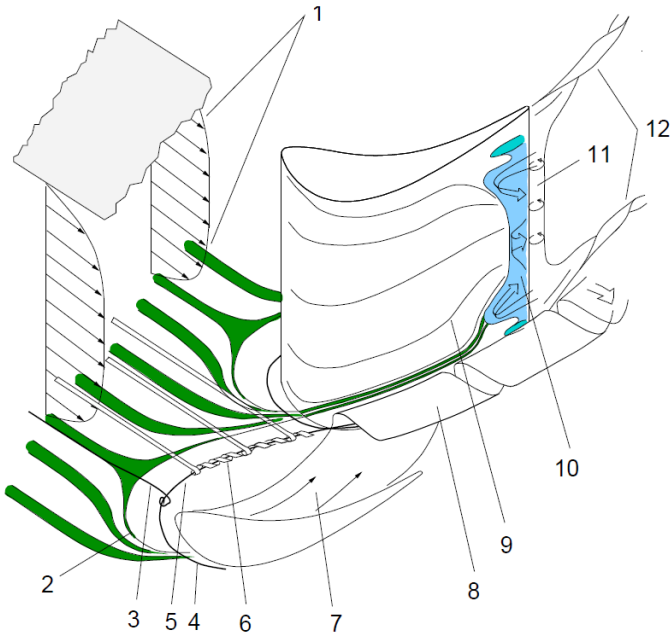

1: inlet boundary layer
2: separation line of the inlet boundary layer
3: horseshoe vortex core, inlet flow
4: suction side leg of horseshoe vortex
5: pressure side leg of horseshoe vortex
6: rolling up the inlet boundary layer
7: cross flow in the passage
8: passage vortex
9: motion of the suction side boundary layer
10: separation with backflow
11: eddying in the wake
12: trailing edge vortices

Figure 1: Schematic structures of flow field within a turbine cascade from Eymann et al. [13] who reproduced it from Vogt and Zippel [14].

First of all, it is necessary to briefly review the flow field within the turbine passage to understand the structure and the mechanism of the secondary flow. Generally speaking, secondary flows are relatively minor flow superimposed on the primary flows such like the passage vortex, the trailing edge vortex, the corner vortex and horseshoe vortex etc. Figure 1 depicts the schematic structures of the three-dimensional flow field in a turbine cascade. The upstream inlet boundary layer is forced downward due to the pressure difference at the intersection of leading edge and endwall. Then it rolls up and generates the horseshoe vortex, which is afterwards split to pressure-side leg and suction-side leg of horseshoe vortex by leading edge. The pressure-side leg of the horseshoe vortex keeps entraining the low-momentum boundary layer near the endwall to form so-called passage vortex. The strong crossflow due to the pressure gradient

pointing from the pressure side to suction side enhances the rotation of the passage vortex and it is gradually lifted away from the endwall as it travels to further downstream. Meanwhile, its size is growing since it keeps entraining the main flow and endwall boundary layer. However, the suction-side leg of horseshoe vortex is convected around the leading edge to the suction surface and remains close to the suction surface-endwall intersection until it is pulled off the endwall by the pressure-side leg. When the stronger pressure-side leg and the weaker suction-side leg of the horseshoe vortex approach each other, they generate a counter-rotating vortex pair. At further downstream, the intense rotation of the passage vortex pulls the suction-side leg away from the suction surface but the suction-side leg remains distinct till the cascade exit. The passages of both legs of the horseshoe vortex and the crossflow with low momentum are dramatically impacted by the strong pressure gradient across the turbine passage. Similar flow behavior in the turbine passage has been reported in [15, 16, 17 and 18].

1.1.2 Endwall contouring

As interpreted in [19], the HP-turbine, in contrast to LP-turbine, has a relatively small aspect ratio which causes major secondary flow regions close to the hub and tip. As a result, the secondary flow caused by a system of hub and tip vortices that induce drag forces resulting in an increase of secondary flow losses. The secondary flow loss is almost inversely proportional to the aspect ratio. Thus, in HP-turbines with small aspect ratios, the secondary flow loss of almost 40-50% is the major loss contributor. It can be reduced by introducing the following measures:

(1) Three-Dimensional compound lean design.

(2) Special design for turbines that are subjected to extreme off-design incidence change.

(3) Modification of the blade leading edge using fillets.

(4) Endwall contouring.

(5) Hub cooling mass flow injection to interact with the hub secondary flow.

(6) Blade tip cooling ejection to reduce the tip secondary flow losses.

One of the promising measures to improve the turbine efficiency is the endwall contouring. Both axisymmetric and non-axisymmetric endwall contouring have been studied by several researchers. Particularly, the non-axisymmetric contouring attracts more attention since it specially considers the effect of non-axisymmetric properties of the flow field and the mechanism of the secondary flow formation. As recommended by Hazelbach et al. [20], non-axisymmetric endwall contouring has been considered as a most effective way of reducing the high losses associated with the secondary flows in turbine passages. There are basically three types of non-axisymmetric contouring presented in the literature: large leading edge fillets, endwall "fences," and "full-passage" contouring [21]. Studies for fillet are primarily focusing on suppressing the horseshoe vortex resulting from the rolling up of the inlet boundary layer around the leading edge region, whereas the endwall fences are designed to guide the direction of cross-passage flows as well as the passage vortex. Full-passage contouring, which has attracted a lot of researchers' attention, is primarily concentrating on decreasing the

pressure gradient across the passage, secondary kinetic energy (SKE), and other factors that have positive impact on the generation of secondary losses.

1.1.2.1 Endwall contouring in cascades

In fact, a large amount of researches focusing on the endwall modifications applied in cascades have been well documented in the public literatures. Zess and Thole documented the computational design and experimental validation of a fillet placed at the leading edge of a guide vane to eliminate the horseshoe vortex in [22]. The results verified the effectiveness of the leading edge fillet at accelerating the inlet boundary layer therefore mitigating the horseshoe vortex. And the turbulent kinetic energy levels were significantly reduced because of the absence of the horseshoe vortex. Shih and Lin [23] simulated three fillet configurations: no fillet, a fillet whose thickness decays on the blade and a fillet whose thickness decays on the endwall. Their results showed that both leading edge fillets can reduce aerodynamic loss and surface heat transfer. Becz et al. [24, 25] experimentally tested a baseline configuration, two leading edge bulbs and a leading edge fillet in a large-scale, high turning linear cascade. The results obtained 7%~8% of reduction of total loss for the small bulb and fillet geometries. Both computations and experiments were performed by Saha et al. [26] for the endwall region of a linear blade cascade with contoured leading edge fillets. Several improvements were achieved including the reduction of cross-passage pressure gradient, decrease of the wall shear stress and less turning of the streamlines etc. Nagel et al. [27] applied the non-axisymmetric endwall contouring to the optimization procedure for a turbine vane. Their high-speed cascade wind tunnel experiments confirmed the computational results. Torre

et al. [28] designed the endwall contouring for a linear cascade and the experimental data showed that the contoured endwall achieved a reduction of 72% of SKEH and 20% of the mixed-out endwall losses. Saha and Acharya [29] and Gustafson et al. [30] designed a 3D non-aixsymmetric endwall with a shape function and a decay function, as shown in Figure 2. Both numerical simulations and experimental measurements presented reduction of the mass averaged pressure losses and heat transfer. Their results showed smaller pitchwise pressure gradient, weaker cross flow, less turning of the endwal region flow, smaller passage vortex and reduction of pressure losses. Knezevici et al. [31, 32] designed a 3D non-aixsymmetric endwall contouring with several distributed control points for high-lift turbine airfoils. And a Sequential Quadratic Programming gradient-based algorithm was used to find the best geometry. Both CFD simulations and measurements indicated that the application of endwall contouring resulted in lower secondary losses. Similar researches that have been done in cascades can be found in [33, 34].

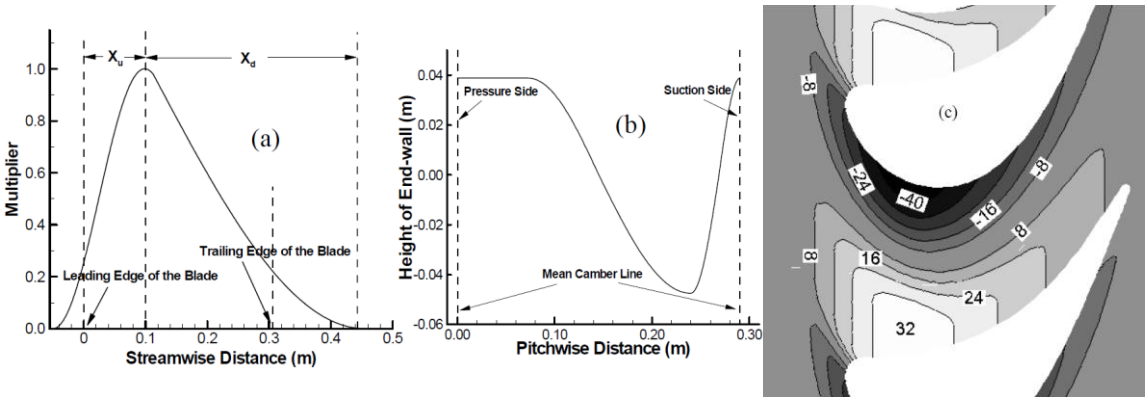

Figure 2: Contour endwall generation curves (a) streamwise, (b) pitchwise, and (c) contour endwall height in millimeters [29, 30].

1.1.2.2 Endwall contouring in rotating rigs

Due to the difficulties in measurements, there are very limited public literatures that investigate the effects of the endwall contouring under rotating conditions. Brennan et al. [35] redesigned the HP turbine of the Rolls-Royce Trent 500 engine with the application of non-axisymmetric end walls. The profiled end-wall shape was determined by six control stations which were fixed at specified axial distances along the mean camber line of the airfoil. The addition of profiling to the end-walls of the HP Turbine is predicted to reduce secondary loss by 0.24% of the NGV and by 0.16% for the Rotor. The total improvement in stage efficiency for the HP Turbine is therefore +0.4%. At the meanwhile, related experiments were performed by Rose et al. [36] and greater improvement in stage efficiency which was 0.59% ± 0.25% was tested. Harvey et al. [37] applied non-axisymmetric endwalls to the vane and blade passages in the IP turbine model of the Rolls-Royce Trent 500 engine. The results met expectations with an improvement in stage efficiency of 0.9% ± 0.4% at the design point. Germain et al. [38] studied the improvement of efficiency of a one-and-half stage high work axial flow turbine by non-axisymmetric endwall contouring. The endwalls have been designed using automatic numerical optimization by means of a Sequential Quadratic Programming (SQP) algorithm. Both hub and tip endwalls of the first stator as well as the hub endwall of the rotor were modified. The experimental results confirm the improvement of turbine efficiency, showing a total-total stage efficiency benefit of 1%±0.4%, while the improvement is underestimated by CFD. They reported that the transition modeling on the airfoil strongly affected the secondary loss predictions. The

correlated analysis of time-resolved flow physics was presented in [39]. Snedden et al. [40, 41] utilized 5-hole probe measurements in a 1.5 stage low speed, model turbine in conjunction with computational fluid dynamics to gain a more detailed understanding of the influence of a generic endwall design. Results indicated a 0.4% improvement in total-total rotor and stage efficiency as a result of the application of the generic non-axisymmetric endwall contouring. However, at higher loading the rotor efficiency was reduced by 0.5%.

1.2 Endwall Film Cooling and Heat Transfer

Over the past six decades, the thermal efficiency of gas turbine engines has been continuously growing as a result of an increased turbine inlet temperature. In order to obtain higher thermal efficiency, modern advanced gas turbines are operating at an inlet temperature approximately 1600 ℃. Right downstream the combustion chamber exit, the inlet stages of turbines are constantly exposed to incoming gases with high temperature that is close to the melting point of the blade metal. Continuous operation under high turbine inlet temperatures leads to the risk of thermal failure of the turbine components due to the excessive thermal stresses. To protect the blades from excessive thermal loads, internal and external cooling techniques, as well as the combination of both, are applied in the general practice. For the thermal protection of first stage blades, external cooling is utilized, where cooling mass flow is charged into the blades' internal cooling passages and ejected from the film cooling holes at all the blade surfaces. Also, the advanced well-designed combustors can generate uniform exit temperature profile which exposes the turbine platform to excessively high temperature. Therefore, advanced

cooling technologies are also required to protect the turbine endwalls from thermal failure.

1.2.1 Cascade: non-contoured versus contoured

1.2.1.1 Non-contoured cascade

To better understand the effect of different parameters on heat transfer and film cooling at turbine endwalls, numerous experimental and numerical investigations have been conducted in turbine cascades. Blair [42] conducted experiments to determine the film cooling effectiveness and convective heat transfer coefficient on the endwall of a large-scale turbine vane passage. The author found that the heat transfer at the van passage endwall was profoundly impacted by the presence of the large vrtex located in the corner between the endwall and suction surface. Graziani et al. [43] experimentally measured the local heat transfer rates on the endwall, pressure, and suction surfaces of a large scale turbine blade cascade for two inlet boundary layer thickness and for a typical Reynolds number. The results showed that the heat transfer on the endwall was strongly influenced by the passage secondary flows as well as the inlet boundary layer thickness. Gaugler et al. [44] utilized various flow visualization to define the endwall secondary flows in a large scale turbine vane cascade. The visualized flow patterns were compared to the measured Stanton number distributions for cases where the inlet Reynolds number and exit Mach number were matched. They reported that the correlation between the horseshoe vortex and the endwall heat transfer was observed near the vane leading edge, where a local peak in heat transfer occurs and the horseshoe vortex rolling up initiated. Harvey et al. [45] compared the predicted surface heat transfer rates with measurements

at three conditions on a modoel of the van tested in annular cascade. In the areas of highest heat transfer, they obtained accuracy of predictions within 20% of measurement at all conditions.

Measurements of heat transfer and adiabatic film cooling effectiveness in a transonic flow field at the endwall of a turbine nozzle guide vane were carried out by Nicklas [46]. It was reported that the stronger horseshoe vortex due to the coolant ejection from the slot leaded to a great increase of the heat transfer at the leading edge. Moreover the heat transfer downstream of the cascade was primarily affected by the passage vortex. High film cooling effectiveness was obtained in the front part of the passage due to the coolant ejection from the slot, but rapidly decreased towards the pressure side corner. Knost and Thole [47] presented their work of a computational study of two endwall film-coooling hole configurations combined with cooling from a flush slot. The results indicated acceptable agreement between predictions and measurements of the endwall cooling with the flush slot alone. However the CFD overpredicted the cooling effectiveness along the endwall for the combination of endwall film-cooling and slot cooling. Lynch and Thole [48] experimentally obtained the adiabatic cooling effectiveness and heat transfer coefficients on the endwall of a nozzle guide vane with slot cooling. Two slot flow rates and two slot widths were tested. When fixing the slot width, increasing the slot mass flow resulted in slightly increased heat transfer but higher adiabatic cooling effectiveness. Decreasing the slot width at a constant slot mass flow resulted in larger coolant coverage and increased local effectiveness but lower heat transfer augmentations. Liu et al. [49] experimentally investigated the impact of coolant density

on the turbine endwall film cooling effectiveness with the presence of stator-rotor purge flow and compound-angle cooling holes in a five-blade linear cascade. The results showed that the platform film cooling effectiveness grew with increasing density ratio but declined with decreased turbulence intensity. The results also showed that shaped holes were able to deliver higher film cooling effectiveness and wider coverage than the cylindrical holes.

1.2.1.2 Contoured cascade

As the improvement of aerodynamic efficiency is achieved due to the reduction in secondary losses by utilizing the endwall contouring which has been reported in many public papers, researchers also exhibit strong interests in the performance of endwall heat transfer and film cooling with the presence of endwall contouring. Piggush and Simon [50] studied the leakage flow and misalignment effects on the endwall heat transfer coefficients within a first-stage stator cascade that had one axially contoured and one flat endwall. The impact of endwall film cooling on the aerodynamic performance of a linear blade cascade incorporating a non-axisymmetric endwall contouring was experimentally investigated by Gustafson et al. [51]. They reported that compared to the uncooled endwall the suction side-leg vortex near the leading edge was weakened when the film cooling was employed. Utilizing the same linear cascade, Mahmood and Acharya [52] measured the endwall flow and heat transfer with endwall contouring and leading edge fillets. Results with those modifications were compared with each other and as well as with the flat endwall baseline. Since weaker and smaller passage vortex was obtained for the contour endwall and fillets, the endwall heat transfer and the Nusselt

number was reduced along the endwall particularly upstream of the mid-chord portion. And the leading edge fillets further decreased the endwall Nusselt numbers. Barigozzi et al. [53] reported the experimental investigations of the influences of endwall film cooling on the aerodynamic performance in a nozzle vane cascade with endwall contouring. The results showed that the overall losses of contoured geometry are always lower than the planar vane. The minimum loss injection condition was found when the injected mass flow rate was around 1%.

A computational study on the endwall film cooling in an annular nozzle cascade with an asymmetric contoured passage was presented by Okita and Nakamata [54]. The results indicated that since the secondary flow was effectively suppressed and thus less coolant jets were deflected by the secondary vortices with the presence of asymmetric endwall contouring, more uniform film coverage was achieved especially in the rear portion of the endwall, where the laterally averaged cooling effectiveness was also improved. Saha and Acharya [55] conducted the 3D numerical simulations of the flow and heat transfer through a nonaxisymmetric blade passage. It was reported that the mass-averaged pressure loss values were reduced by about 3.2% by endwall contouring. Moreover, the endwall contouring reduced the overall Nu by 8% and more significant reduction in the heat transfer near the leading edge and the passage region was obtained. The subsequent study by Mahmood et al. [56] reported the measured flow and film cooling effectiveness on the non-axisymmetric contoured endwall in the linear cascade passage. The flow temperature field and Nusselt number distributions at the contoured endwall without film cooling were used to determine the locations of the film cooling

holes. The results showed that the coolant jets covered more distance in both the axial and pitchwise directions at higher blowing ratios. Further, the local and averaged film cooling effectiveness enhanced with the blowing ratio. Thrift et al. [57] presented the measurements of heat transfer at the endwalls of a flat and contoured passage with and without upstream slot leakage flow in a nozzle guide vane. Results indicated that the heat transfer was reduced on both endwalls of the contoured passage compared to the flat passage. Larger leakage mass flow rate resulted in higher heat transfer near the suction side near the vane leading edge. Thrift et al. [58] also experimentally investigated the effect of axisymmetric ednwall contouring on the endwall film cooling performance. The measurements showed that the coolant ejected from the leakage slot covered a larger area of the contoured endwall than the flat passage. In addition, for all cases, increasing leakage and film cooling mass flow rate led to an augmentation of cooling effectiveness and coolant coverage.

1.2.2 Rotating rig: non-contoured versus contoured

1.2.2.1 Non-contoured rotating rig

Blair [59] conducted an experimental study of the heat transfer distribution in a large-scale rotating turbine rotor passage. Heat transfer was measured for both the blade pressure and suction surfaces and for the endwall platform. Results showed that the horseshoe vortex system enhanced heat transfer on the endwall near the leading edge with local Stanton numbers 90% larger than that at the leading edge midgap. Additionally, it also led to a local area of high heat transfer on the suction side close to the leading edge/endwall corner with local Stanton numbers 50% higher than that at

midspan. Paniagua et al. [60] experimentally and numerically analyzed the interaction between the stator-rotor cavity flow and the mainstream in a high-pressure transonic turbine stage. Different cooling flow ratios were tested and both time-averaged and time-resolved data were illustrated. Results indicated that the stator-rotor cavity flow significantly influenced the mainstream flow when the large amount of gas was ejected. Moreover, the CFD predictions showed how the ejected cooling flow was entrained by the rotor endwall vortex. Ong et al. [61] conducted a study of the effects of two types of hub coolant injection on the rotor endwall flow in a high pressure turbine stage. The first injected the leakage flow from the hub cavity into the mainstream and the second injected coolant from a row of angled holes at the edge of the stator hub. Results showed that the endwall leakage flow was entrained into the hub secondary flow and the negative incidence of the leakage strengthened the secondary flow which increased the penetration depth. However, increasing the injected coolant swirl angle decreased the penetration and improved the cooling coverage on the rotor endwall.

Yang et al. [62] performed numerical simulations to investigate the film cooling effectiveness and heat transfer coefficient distributions on a rotating endwall with stator-rotor gap purge flow and downstream film cooling in a $1\text{-}^{1}/_{2}$ turbine stage using a Reynolds stress turbulence model with a non-equilibrium wall function. The sliding mesh was utilized under three rotational speeds to investigate the rotation effects while the purge coolant-to-mainstream mass flow ratio was maintained at 1% and the blowing ratio at unity for the downstream film cooling. They reported that high unsteadiness due to the stator-rotor interaction was obtained for the purge flow cooling and heat transfer,

whereas the downstream discrete holes film cooling was slightly impacted. The heat transfer coefficient decreased rapidly with increasing rotational speed and the highest film cooling effectiveness in the upstream section of the rotor passage was achieved at the design condition of 2550 rpm. Suryanarayanan et al. [63] experimentally examined the film cooling effectiveness on a rotating blade platform in a three-stage HP research turbine employing the purge coolant from the first stator-rotor gap. In total three different rotational speeds and four coolant-to-mainstream mass flow ratios (MFR) were tested. It was reported that the film cooling effectiveness increases with an increase in the MFR at all rotating speeds. Higher rotational speed delivered more local cooling film spread on the endwall. In the subsequent paper Suryanarayanan et al. [64] equipped nine discrete cooling holes located in the rear portion of the rotor platform to supply the film cooling on the endwall. Different parameters were experimentally investigated by varying the rotational speed, blowing ratio as well as the purge flow MFR. It was found that the film cooling effectiveness and coolant coverage on the rotor endwall due to the cooling film ejected from the downstream cooling holes was highest at the reference condition. In addition, complete film cooling protection on the rotor endwall could be achieved with the combination of purge flows and cooling-hole ejections.

1.2.2.2 Contoured rotating rig

Marini and Girgis [65] carried out a CFD study of the impact on the blade leading edge platform shape on the flow interaction between the upstream cavity flow and the mainstream in a transonic high-pressure one-stage turbine that contained the blade upstream disk cavity. A recessed and a raised leading edge platform shapes were

computationally analyzed. It was reported that the raised leading edge platform shape provided an improvement in stage efficiency at the nominal condition and also a reduced sensitivity of the stage efficiency to the cavity flow amount. Schuepbach et al. [66] performed time-resolved experimental and computational results for a one-and-1/2-stage axial turbine to sudy the influence of purge flow on the performance of two different non-axisymmetric endwalls and the non-contoured baseline. All three turbines obtained deterioration in efficiency as purge flow was added. The baseline turbine showed the least reduction at -0.6% η per % injection. The first endwall contouring had a stronger sensitivity at -1.2% η per % injection while the second was slightly worse than the baseline with -0.7% η per % injection. Jenny et al. [67] reported a combined experimental and computational study of non-axisymmetric rotor endwall profiling on both hub and shroud in a low pressure turbine employing purge flow ejection. The measured efficiency showed a strong sensitivity in the efficiency to the purge flow. An 18% reduction of sensitivity to purge flow was obtained due to the endwall profiling.

1.3 Blade Tip Film Cooling and Heat Transfer

One of the major parameter for improving the thermal efficiency of gas turbines is to increase the turbine inlet temperature. Nevertheless, this has inevitably resulted in a larger thermal load on turbine components. Blade tip is one of the portions susceptible to excessive thermal stresses associated with cooling difficulties. For the unshrouded blade, failure of the blade tip is caused mainly by hot tip leakage flow entrained in the tip clearance. Due to the pressure difference between the pressure side and suction side, hot freestream gas is driven to penetrate through the tip gap, resulting a thin boundary layer

and high heat transfer. Hence, state-of-art cooling techniques must be developed and utilized on the blade tip to avoid the blade failure due to heavy thermal loads.

1.3.1 Blade tip film cooling and heat transfer in cascades

Understanding the complex mechanism of heat transfer on turbine blade tip is the prerequisite for appropriately designing the blade tip cooling systems. Metzger et al. [68] used a narrow slot-type channel with one of the bounding walls contains a transverse rectangular cavity to model the grooved turbine blade tips. A general reduction of overall heat transfer on the cavity floor was observed as the cavity depth is increase. Bunker [69] provided a comprehensive review and summary of the blade tip heat transfer based on the early public fundamental studies. Azad and Han [70, 71] experimentally investigated the heat transfer coefficient as well as static pressure distributions on gas turbine blades with plane tip and squealer tip installed in a five-bladed linear cascade. All of the measurements were performed with three different tip gap clearances of 1%, 1.5% and 2.5% of the blade span. Their results showed that a larger tip gap leads to a stronger heat transfer process. The results also showed an increase in heat transfer on the rim and cavity surface with an increase in tip clearance. Bunker and Ameri et al. [72, 73] performed comprehensive experimental and numerical studies to investigate the heat transfer on the first-stage blade tip for a large power generation turbine. The detailed distribution of heat transfer coefficient was reported for different tip geometries at various inlet turbulence intensity levels.

Recently, more researchers showed interests in the film cooling on turbine blade tip. Kim and Metzger [74] developed an experimental approach to model and measure the

heat transfer on turbine blade tips with film cooling. Kim [75] continued the experimental work presented in [74] to study the effects of film cooling on the turbine blade tip heat transfer. The results indicated that the blade tip geometry and injection locations significantly affect the film cooling performance. Kwak and Han [76] measured the heat transfer coefficients and film effectiveness on a gas turbine blade plane tip with film cooling holes along the camber line and near the tip region of the pressure-side. The results indicated that both heat transfer coefficient and film effectiveness increased as the tip clearance increased. However, increasing the blowing ratio would increase the film cooling effectiveness whereas decrease the heat transfer coefficient. Kwak and Han [77] also performed similar measurements on the squealer tip with a 4.22% recess of a gas turbine blade. The experimental results indicated that the overall heat transfer coefficients increased as the tip clearance increased but decreased as the blowing ratio increased. Nevertheless, the overall film cooling effectiveness increased with increasing blowing ratio. Compared to the plane tip, the squealer tip would obtain higher overall film cooling effectiveness but lower heat transfer coefficients. Acharya et al. [78] presented the numerical simulations of flow and heat transfer for a GE-E^3 turbine blade with a film-cooled tip under three different tip clearances. For the flat tip, high film cooling effectiveness and low heat transfer coefficients are obtained along the cooling film, while the squealer tip alters the trajectory of the cooling jets and therefor reduces the effectiveness. Adiabatic effectiveness for a turbine blade with cooling holes placed along the pressure side tip as well as dirt purge holes placed on the tip was measured by Christophel et al. [79]. Yang

et al. [80] presented the numerical prediction of film cooling and heat transfer on the plane and squealer turbine blade tip with different cooling-hole arrangements. The predicted heat transfer coefficients had good agreement with the experiments made by Kwak and Han [76, 77]. It is noticeable that the predicted film cooling effectiveness of the camber arrangement for both the plane and squealer tips will not increase more with increasing blowing ratio after which reaches unity. Gao et al. [81] experimentally studied the effect of inlet flow angle on film cooling effectiveness for a cutback squealer blade tip under average blowing ratios of 0.5, 1.0, 1.5 and 2.0. According to their observation, the coolant jet direction and hence the cooling effectiveness was altered when the incidence angle was changed. However, their results showed that the flow angles have an effect on the area-averaged film cooling effectiveness. Acharya et al. [82] conducted a numerical study of heat transfer and film cooling effectiveness on a squealer tip with pressure-side and tip coolant holes. In this paper, larger regions of film cooling effectiveness with higher values between the camber line and suction side was reported with higher blowing ratio. However, the leading edge has highest heat transfer coefficients. Naik et al. [83] experimentally and numerically investigated the flow, heat transfer and film cooling effectiveness of the high pressure turbine blades with a full rim squealer tip and a partial squealer tip. They found that the suction-side rim within the mid-chord region exhibits the highest heat transfer coefficients.

1.3.2 Blade tip film cooling and heat transfer in rotating rigs

However, only few papers that consider rotating blades can be found in public studies, due to the difficulty of measurements. Metzger et al. [84] numerically studied

the heat transfer in a transverse rectangular cavity with a moving as well as stationary shroud using a finite-difference method. Later Metzger et al. [85] developed a simple model of the leakage flow to estimate both tip and shroud heat transfer. Dunn and Haldeman [86] reported their heat-flux measurements studying the influence of blade tip recess on the tip-region heat transfer for a full-stage rotating transonic turbine. Srinivasan and Goldstein [87] used a moving endwall belt mounted on the top of a five-blade linear cascade to simulate the effect of relative motion between the rotor tip and shroud. Their results indicated a reduction of around 9% in mass/heat transfer levels for 0.6% chord clearance. The pressure gradients on the blade tip were decreased as well. Zhou et al. [88] numerically investigated the effects of the endwall motion on the aero-thermal performance of a winglet tip without and with film cooling. With the endwall motion, the overall tip leakage loss was reduced by 15%. The cooling effectiveness was increased by 9% and the associated heat flux on the winglet tip was decreased by 31%. Acharya and Moreaux [89] performed a numerical study to investigate the blade tip heat transfer and flows with both pressure side and tip coolant in the presence of relative motion between the blade and casing. It was confirmed that the relative motion between the tip and shroud had significant effects and thus the statement of pressure-driven leakage flows was not appropriate. Yang et al. [90] numerically simulated the effect of the blade rotation on the flow and heat transfer for turbine blades with plane and squealer tips. The prediction indicated that the rotation effect on the flow behaviors and heat transfer primarily came from the relative motion of the shroud, especially for the squealer tip. Three different turbine blade tip configurations with film cooling under

different rotation speeds were numerically investigated by Zhang et al. [91]. The numerical prediction indicated that the overall heat transfer coefficient increased and overall film cooling effectiveness decreased as the blade rotation speed was increased. This trend was reversed when the blowing ratio was increased.

2. RESEARCH OBJECTIVES

Due to the complexity and difficulty of measurements on rotating rigs, very limited documents are available for rotating flow behaviors, heat transfer and film cooling and most of the investigations of aerodynamics and heat transfer are carried out in stationary cascades. However, the cascade studies are not able to reproduce the inherent rotational effects such as boundary layer centrifugation, centrifugal force, Coriolis force etc. in gas turbines. Therefore the rotating turbine conditions must be implemented when taking into account these effects. The application of computational fluid dynamics (CFD) has become an important tool in the design and analysis of turbomachinery, which obsesses the advantages to provide all the details of the entire flow field that are impossibly measured. This study utilizes CFD to complete the process of design, validation and analysis for the new endwall contouring based on an innovative technique “continuous diffusion method”. The impacts of new endwall contouring on the aerodynamic performance, film cooling effectiveness and heat transfer within the HP turbine are numerically investigated. In addition, simulations are also performed to do the parameter studies on the film cooling effectiveness and heat transfer with the presence of blade tip ejection under rotating conditions. In this study, the capability of CFD on turbomachinery application will be comprehensively discussed and its advantages and weaknesses will be also revealed. The research program intended during this project covers the following steps:

2.1 Endwall Contouring for Turbine Aerodynamic Performance

a. Following the physics-based approach using continuous diffusion, complete the design of the new endwall contouring that will be implemented on the platform of second-stage rotor.

b. Validate the reduction of secondary loss and thus the improvement of turbine aerodynamic performance due to the presence of new endwall contouring. Thoroughly study the flow behaviors and mechanism of the secondary loss reduction.

c. Numerically investigate the rotation effect with the presence of the new endwall contouring on the turbine performance at operating rotation speeds of 2000 rpm, 2400 rpm, 2600 rpm and 3000 rpm.

d. Generate the CFD-predicted performance curves for the contoured turbine that is compared to the performance of non-contoured turbine.

2.2 Endwall Contouring for Film Cooling on Rotor Platform

a. Using the continuous diffusion method, modify the design of the endwall contouring that is equipped on the platform of first-stage rotor, with the particular consideration of the geometric limitation due to the presence of the stator-rotor purge flow gap.

b. Compare the sensitivity of film cooling effectiveness, Nusselt number and heat flux ratio to the variation of the purge-to-mainstream mass flow ratio (MFR) for the contoured and non-contoured platform of first rotor. Three different MFRs of 0.5%, 1.0% and 1.5% are compared at the design rotational speed of 3000rpm.

c. Investigate the rotation effect on the platform film cooling effectiveness, Nusselt number and heat flux ratio at the turbine rotational speeds of 2400rpm, 2550rpm and 3000rpm with 1.0% of the purge coolant.

2.3 Rotor Blade Tip Ejection

a. Compare the flow characteristics, film cooling effectiveness and heat transfer on the rotor blade with plane tip and squealer tip as well as the tip hole cooling and the pressure-side-edge compound angle hole cooling.

b. Investigate the effects of the global blowing ratio on the film cooling effectiveness, Nusselt number and heat flux ratio on the rotor blade tips. Respectively low, medium and high blowing ratios are numerically studied at the rotational speed of 3000 rpm.

c. Study the rotation effects on the film cooling effectiveness, Nusselt number and heat flux ratio for each blade tip cooling configuration at the turbine operating speeds of 2000rpm, 2550rpm and 3000rpm with the medium blowing ratio.

3. TPFL THREE-STAGE RESEARCH TURBINE FACILITY

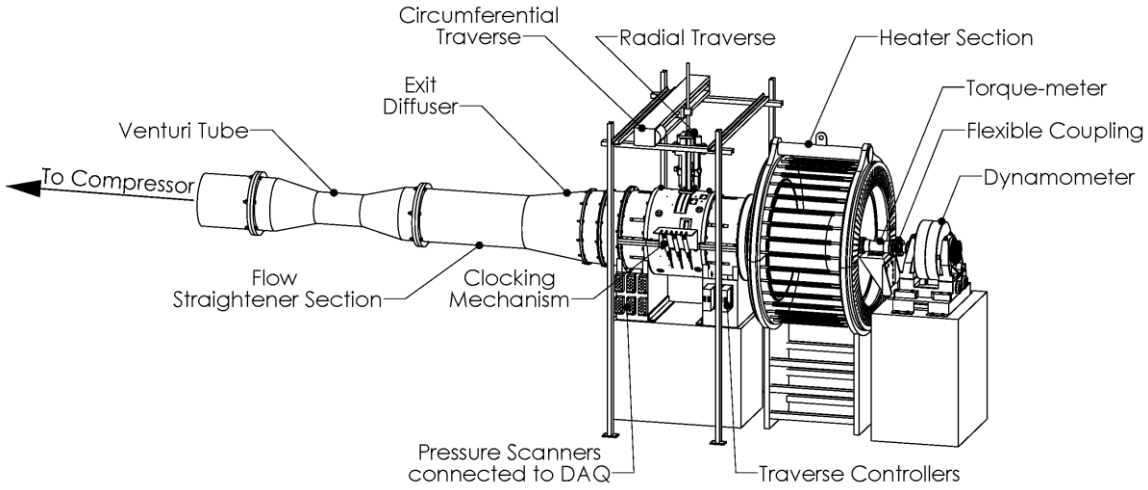

Figure 3: The overall layout of TPFL research turbine facility.

The research turbine facility used for the experimental measurements was designed by Schobeiri [92] to address the aerodynamic performance and heat transfer issues. Detailed aerodynamic, efficiency, loss and performance measurements were carried out to verify and document the efficiency and performance of several high efficiency turbine blades designed for major original turbine manufacturers.

The overall layout of the test facility is shown in Figure 3. It consists of a 300HP electric motor connected to a frequency controller which drives a three-stage centrifugal compressor capable of supplying air with a maximum pressure difference of 55kPa and a volumetric flow rate of $4m^3/s$. The compressor operates in the suction mode and its pressure and volume flow rate can be varied by the frequency controller operating between 0 to 66Hz. A pipe with a smooth transition piece connects the compressor to a

Venturi mass flow meter that is used to measure the mass flow through the entire turbine component. The three-stage turbine has an automated data acquisition system for detailed flow measurements at each blade row location in the radial and circumferential directions. The turbine inlet has an integrated heater that prevents condensation of water from humid air expanding through the turbine. The turbine shaft is connected, through a flexible coupling, to one end of a high precision torque meter that has a maximum rotational speed of 8500 rpm and a maximum torque rating of 677.9 N•m. The other end of the torque meter is coupled via a second flexible coupling to an eddy current low inertia dynamometer with a maximum power capacity of 150kW and a maximum torque of 500 N•m. Turbine dimensions and operating conditions are listed in Table 1.

Table 1: Turbine dimensions and operating conditions.

Stage No., N	3	Mass flow	3.58 kg/s
Tip diameter	685.8mm	Hub diameter	558.8mm
C_{ax}	41.6 mm	Reference speed	3000 rpm
Tested speed range	1800 to 3000 rpm	Pressure ratio	1.41
Re	220,000	Mach number	0.27

3.1 Turbine Performance Measurement Instrument

For the turbine performance measurements, combined total pressure, total temperature rakes are used upstream of the first stator row and downstream of the last rotor row. At the inlet, the rakes are mounted radially at 45 º, 135 º, 225 º, and 315 ºin the

circumferential direction. Each rake consists of 4 total pressure and 3 total temperature probes that are equidistantly distributed in the radial direction. The total pressure probes are of the Pitot tube types, and the total temperature probes are calibrated J-type thermocouples. The calibration curves for the thermocouples are implemented into the performance data reduction program. The exit rakes are located radially with the same spacing as the inlet rakes, but offset to them in order to prevent the interference with the inlet rake wakes. Wall static pressure taps are arranged at the top and bottom half of the main casing and on the T-rings, as well as on the stator rings. For the mass flow measurement, a calibrated Venturi flow meter is used.

The total to static efficiency from experiments was obtained using the net turbine power measured by the torque meter and taking into account the bearing and windage losses. The turbine casing is well sealed and insulated to prevent possible leakage and heat loss. Before taking data, the entire facility is fully preheated to thermal equilibrium by running the turbine for 1 ~ 2 hours. Keeping the engine mass flow and the turbine inlet temperature constant, the engine rotational speed is varied from 1800 rpm to 3000 rpm (reference rotational speed). For each testing point, 10 ~ 15 minutes of waiting time are guaranteed to ensure the turbine at the equilibrium state when data acquisition system is working. To show the performance behavior of the turbine engine, performance curves are generated with respect to the dimensionless performance parameter. The uncertainty for turbine efficiency measurements is 0.004 and more uncertainty values of different parameters can be found in [93].

3.2 Turbine Cooling Systems and PSP Measurement Setup

The three-stage turbine cooling system is shown in Figure 4 and Figure 5. As seen in Figure 4, two independently controlled concentric coolant loops provide the necessary mass flow for all the platform film cooling experiments. The inner loop (green) supplies coolant mass for film cooling experiments on the hub platform through an upstream stator-rotor circumferential gap positioned between the 1st stage stator and rotor. A concentric jet exits this circumferential gap at an angle of 25 º into the mainstream (Figure 6). The outer loop (blue) provides coolant mass for the discrete film cooling holes on both plane and squealer tips of the first rotor blades. Since the measurements for the rotor platform cooling and blade tip film cooling are performed separately, the two cooling loops are operating independently.

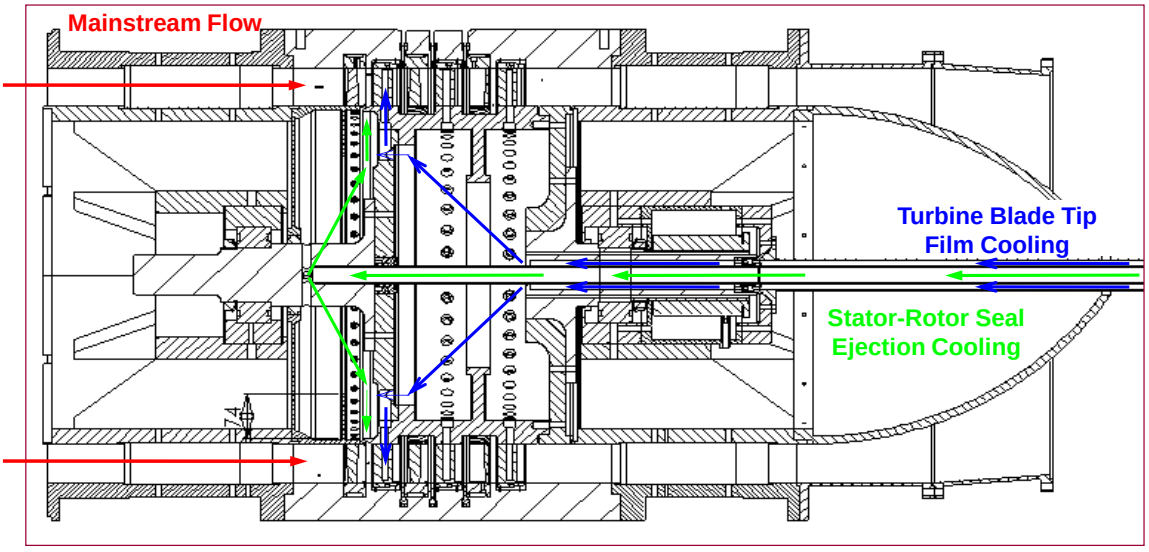

Figure 4: Turbine components with two independent cooling loops.

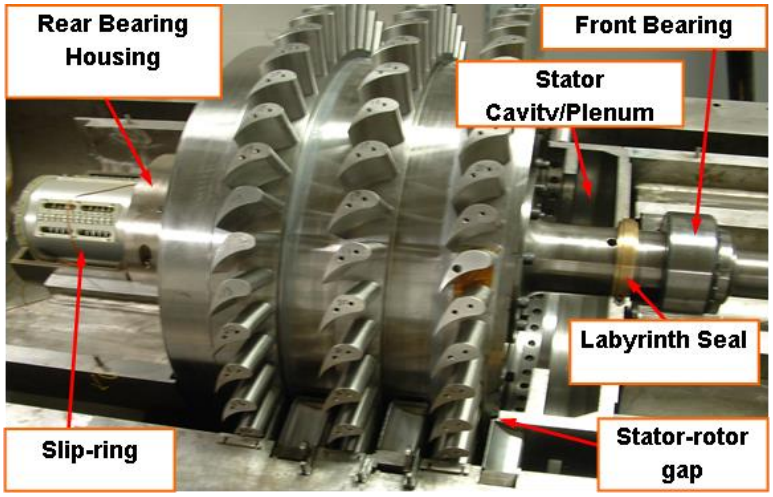

Figure 5: Turbine components with showing stator cavity and first stator-rotor gap.

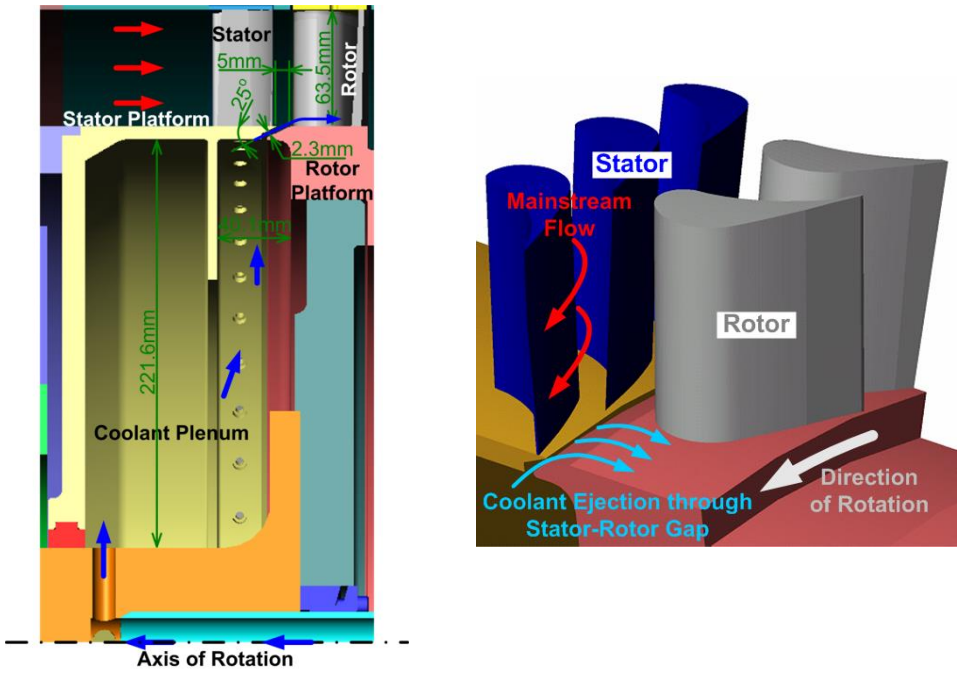

Figure 6: Detailed views of stator-rotor gap and schematic of purge flows.

The pressure sensitive paint (PSP) is used to obtain the distributions of film cooling effectiveness on the first-rotor platform. A schematic of the optical setup used in the PSP

measurements for film cooling effectiveness is shown in Figure 7. The camera, the strobe light and the data acquisition system are triggered simultaneously using an optical sensor triggered off the rotor shaft. By detecting the same angular position, the camera is able to view the same region of interest at every rotation, making it possible to average the image intensities without blurring the information. A minimum exposure time of 17 μs is used for image capture from the camera. Estimated rotor movement during image capture at 2550 rpm, for a 17 μs exposure time was approximately 1.1 mm. A total of 200 images are captured for each experiment with air and nitrogen injection and the pixel intensity for all images is averaged. A computer program is used to convert these pixel intensities into pressure using the calibration curve and then into film cooling effectiveness. The coolant flow rate is set using a rotameter based on prior calculation for the desired blowing and mass flow ratio. The coolant is heated to the same temperature as mainstream air before injection through the gap to eliminate the temperature effects of PSP. Uncertainties for the average blowing ratio calculations are estimated to be approximately 3.5 % using Kline-McClintock analysis and discussed in detail by Holman [94]. More details of PSP working principle and uncertainty analysis can be found in [95].

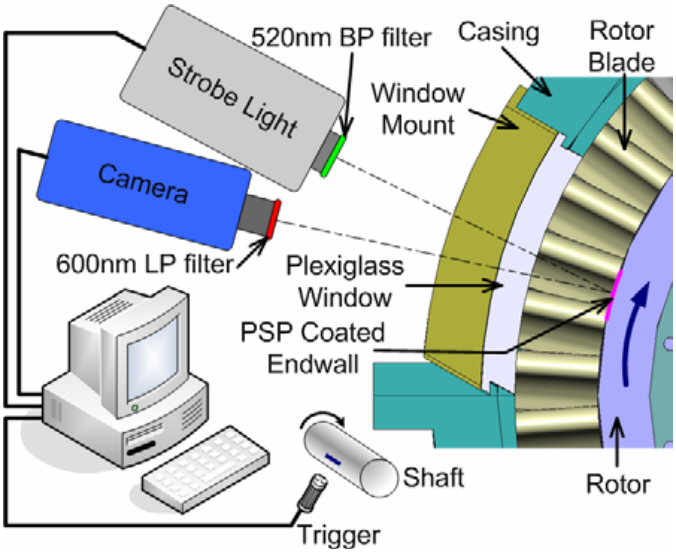

Figure 7: Optical set-up for PSP data acquisition.

4. COMPUTATIONAL DETAILS

4.1 Endwall Contouring for Turbine Performance and Film Cooling

Three-dimensional calculations using steady RANS equations were carried out for the TPFL three-stage high pressure research turbine. Figure 8 depicts the computational model and corresponding boundary conditions for CFD simulations. In order to represent the experimental turbine as realistically as possible, all the geometric information is taken exactly from the machine. As seen, the model consists of three stages aligned along the rotating axis. Each stage includes the upstream stator row and downstream rotor row. Both the stator and rotor are two-dimensional cylindrical blades. A tip clearance of 0.2mm is specified for each unshrouded rotor blade, whereas the stator sealing is not considered as it is not the research object in current study. All the interfaces between the components (stator-to-rotor or rotor-to-stator) are using mixing plane method. For the contoured turbine, the endwall contouring is applied to both first and second rotors, whereas the non-contoured case has annular platform for all the stages. The new contouring is applied for the second rotor which compares to the flat platform on the emphasis of the turbine aerodynamic performance. The modified new endwall contouring due to the limited space is utilized on the first rotor to investigate the impact of the endwall contouring on the film cooling effectiveness, Nusselt number and heat flux ratio. In order to numerically investigate the impact of the purge flow on the endwall film cooling, a large plenum with a narrow slot is attached to the first rotor domain which is a sector of the rotor cavity and stator-rotor gap. The axial width of the

slot is 7 mm with 25 °inclined angle to the rotor platform. As seen in Figure 8, the blue piece represents the stationary disk of S1and the green piece marks the rotating rotor disk. The coolant is supplied at three different MFRs (0.5%, 1.0% and 1.5%) through the lower part of the plenum for film cooling simulations only. Otherwise, a stationary wall is assumed for this portion if no purge flow is ejected to ensure the mass conservation through the entire machine.

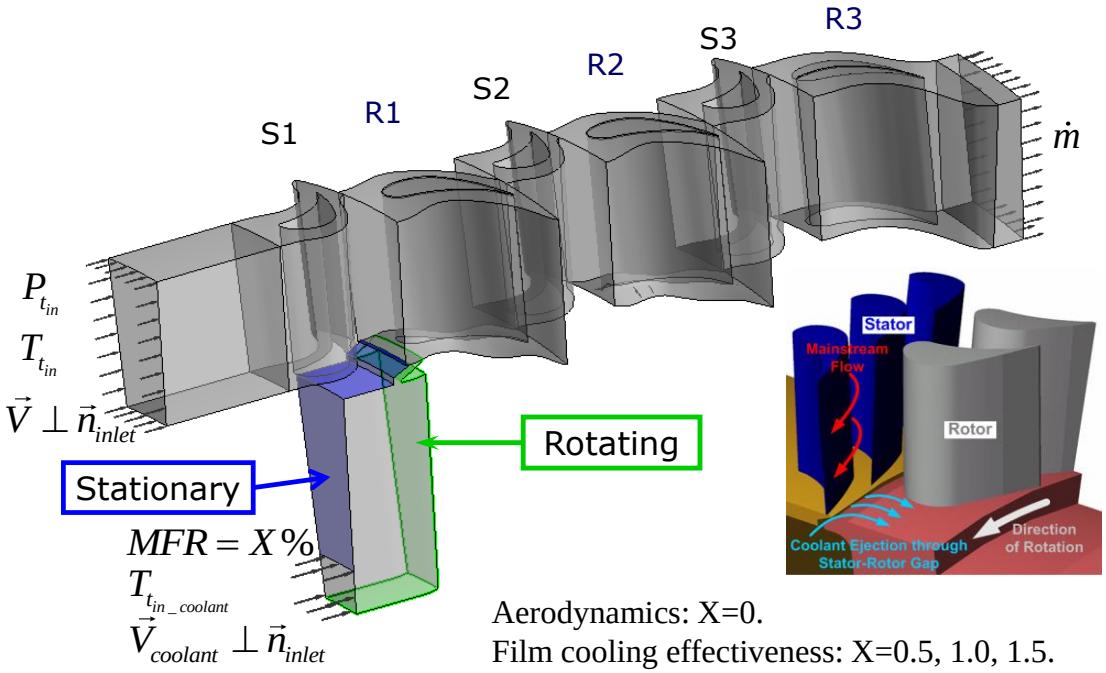

Figure 8: Computational domains and boundary conditions for the three-stage HP turbine.

The boundary conditions are taken from the corresponding experimental data. At the turbine inlet, the total pressure and total temperature are given and the air with typical turbulence intensity (5%) enters the machine in axial direction. Meanwhile, the mass

flow rate is fixed at the turbine exit. For performance calculations, the MFR is set to zero since there is no purge flow on. Systematic simulations are performed to obtain the turbine performance curves by varying the dimensionless performance parameter u/c_0 according to the measurements. To be specific, the variation of u/c_0 is achieved by either changing the turbine rotational speed or altering the mass flow rate. Starting from the lowest rotational speed of 1800 rpm, the turbine is operating with gradually increased rotational speed that is corresponding to increased u/c_0. After the turbine reaches to the design point of 3000 rpm, the mass flow rate is progressively reduced which would continuously enhance u/c_0. The boundary conditions are varied in such a way to complete an entire turbine performance curve that shows the machine efficiency at both design and off-design conditions.

Note that the performance of the HP turbine is evaluated by total-to-static efficiency, which is given by:

$$\eta_{t-s} = \frac{H_{in} - H_{out}}{H_{in} - H_{s,out}} \quad \textbf{(1)}$$

where H is the mass-averaged total enthalpy at turbine inlet or exit. Since the ideal gas model with constant specific heat coefficient is assumed in all the CFD calculations, equation (1) is further written by inserting isentropic relation $\left(\frac{P}{P_t}\right)_s = \left(\frac{T}{T_t}\right)_s^{\frac{\kappa}{\kappa-1}}$:

$$\eta_{t-s} = \frac{1 - \frac{T_{t,out}}{T_{t,in}}}{1 - \left(\frac{P_{out}}{P_{t,in}}\right)^{\frac{\kappa-1}{\kappa}}} \quad \textbf{(2)}$$

To investigate the impact of the MFR on endwall film cooling for the first rotor, different amount of coolant (MFR = 0.5%, 1.0% and 1.5% respectively) is ejected through the first stator-rotor gap at the design rotational speed of 3000 rpm. The total temperature and the mass flow rate are specified as boundary conditions for the coolant. The flow velocity at the coolant inlet is assumed normal to the boundary surface. However, the study of rotation effect on the film cooling for first rotor was conducted by setting the rotational speeds of 2400, 2550 and 3000 rpm while the MFR was fixed at 1%. In addition, non-slip conditions are assumed on the walls.

The adiabatic film cooling effectiveness is defined by:

$$\eta_{aw} = \frac{T_{aw,f_0} - T_{aw,f}}{T_{aw,f_0} - T_{t,c}} \quad \textbf{(3)}$$

where T_{aw,f_0} is the adiabatic wall temperature obtained with the coolant that is as hot as mainstream is, $T_{aw,f}$ is the adiabatic wall temperature obtained with the coolant that is cooler than mainstream and $T_{t,c}$ is the coolant total temperature that is lower than mainstream. Such definition completely eliminates the impact associate with different flow structures as well as the aerodynamic heating effects. In order to obtain the film cooling effectiveness on the R1 platform with a fixed MFR at a constant rotational speed, two cases that supply same amount of coolant with different total temperatures must be calculated respectively. Eventually 318K is used to obtain T_{aw,f_0} according to the experimental running conditions and 300K is arbitrarily chosen for calculating $T_{aw,f}$. In addition, the adiabatic assumption is added to all the non-slip wall surfaces.

Similarly, the heat transfer coefficient is calculated by:

$$h_f = \frac{q''_{w,f}}{T_w - T_{aw,f}} \tag{4}$$

where the T_w is the fixed wall temperature on the first rotor hub and thus certain heat flux q''_w occurs on the platform. In order to obtain the heat flux at the R1 hub, the adiabatic wall condition at R1 platform must switch to the constant-wall-temperature boundary condition. Again an arbitrary number of 300 K is implemented on the R1 hub so that it is able to maintain the consistency with cooling effectiveness.

Based on equation (4), dimensionless Nusselt number is given by:

$$Nu = \frac{h_f C_{ax}}{k} \tag{5}$$

In order to evaluate the realistic heat load at the wall surface, the heat load ratio is introduced as:

$$\frac{q''_{w,f}}{q''_{w,f_0}} = \frac{h_f}{h_{f_0}} \left(1 - \eta_{aw} \frac{T_{aw,f_0} - T_{t,c}}{T_{aw,f_0} - T_w} \right) \tag{6}$$

If any benefit is obtained from the film cooling, the heat flux ratio would be below 1. It is rather straightforward that high cooling effectiveness along with low heat transfer coefficient lead to small heat flux ratio or equivalently light heat loads.

The grid independence study was performed with consideration of both the performance and the film cooling purposes. The grid was refined until a constant efficiency was achieved for the entire turbine rig. This is imperative, whenever the efficiency verification is the most important outcome as is in this study. The efficiency convergence required for the rotor a mesh with over 2 million elements, 22 nodes at the wall region and around 9.3 million elements for the entire model, as seen in Figure 9 (a).

Particular attention was paid to accurately obtaining the temperature distribution on the first rotor hub, which was the critical parameter for predicting the endwall film cooling effectiveness and heat transfer. The cases with and without purge flow were both tested to obtain the convergence of the adiabatic temperature on R1 hub, as seen in Figure 9 (b). A part of the converged grid is shown in Figure 10.

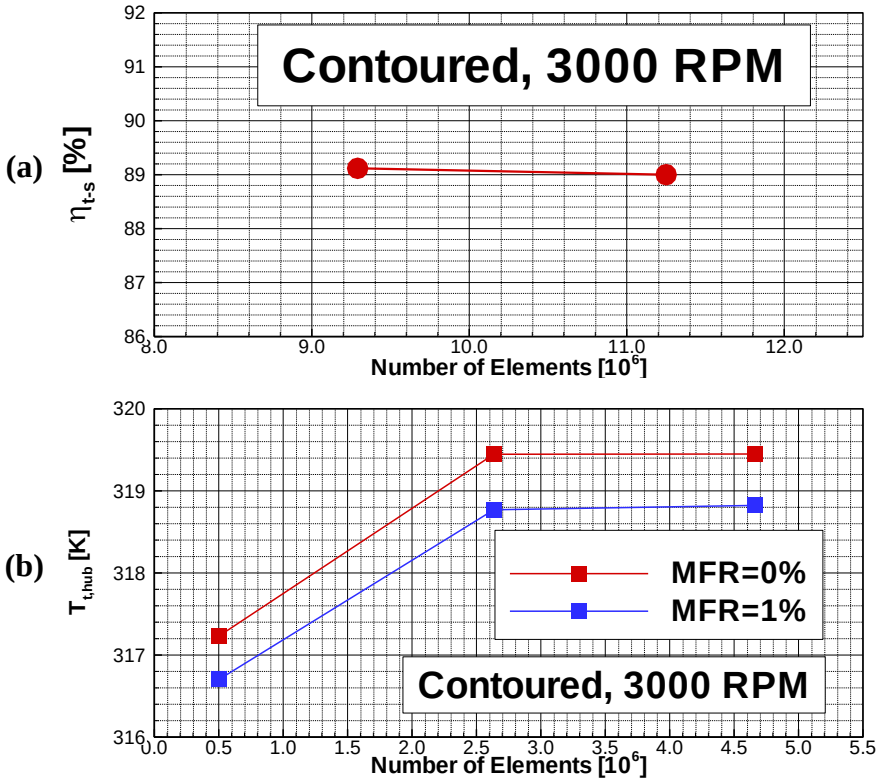

Figure 9: Grid sensitivity study: (a) Total-to-static efficiency of the three-stage HP turbine, (b) Area-averaged temperature on the first rotor hub with and without purge flow.

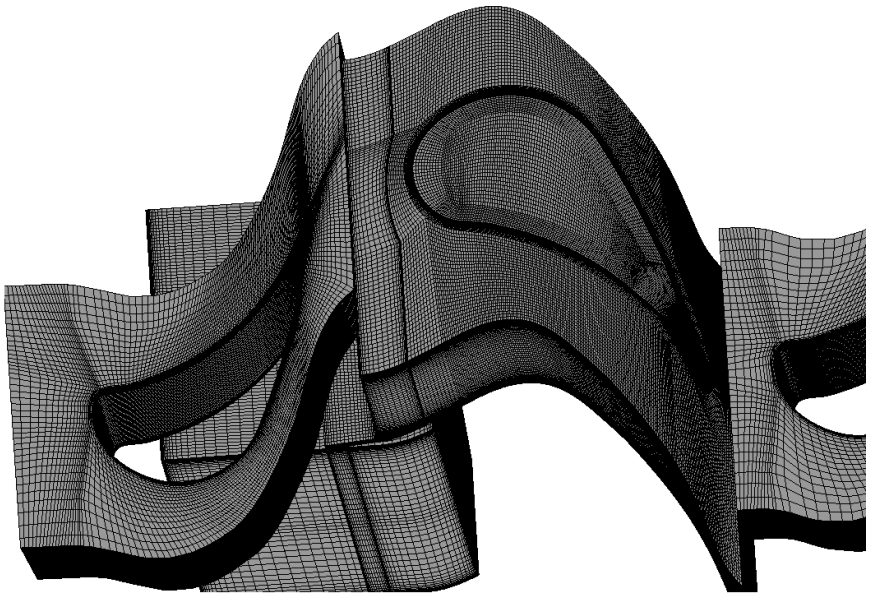

Figure 10: The details for the CFD mesh for the three-stage HP turbine (part).

All the simulations were performed using the CFD commercial software ANSYS CFX. The steady solutions were obtained by solving Reynolds-Averaged-Navier-Stokes (RANS) equations with a finite volume method. Menter's [96, 97] SST-turbulence model was chosen according to extensive turbulence model studies performed on several TPFL turbines and the numerical calculations showed the suitability of the SST-model for calculating the flow quantities [98]. Each simulation was calculated until the global root mean square residuals for the RANS equations reached values below 10^{-4}. Moreover, various parameters were monitored as the solver was running. Examples include the average pressure at the exit, the mass conservation for the entire machine and the isentropic efficiency of the machine, etc. Convergence was achieved when the residuals' magnitude was lower than 10^{-4}, and the stability was observed in the monitored variables. Typically, 1,500 iterations are necessary to achieve convergence.

As a result, each single case computed in the parallel mode on Texas A&M super computers consumed approximately 200 CPU hours on average.

4.2 Rotor Blade Tip Film Cooling

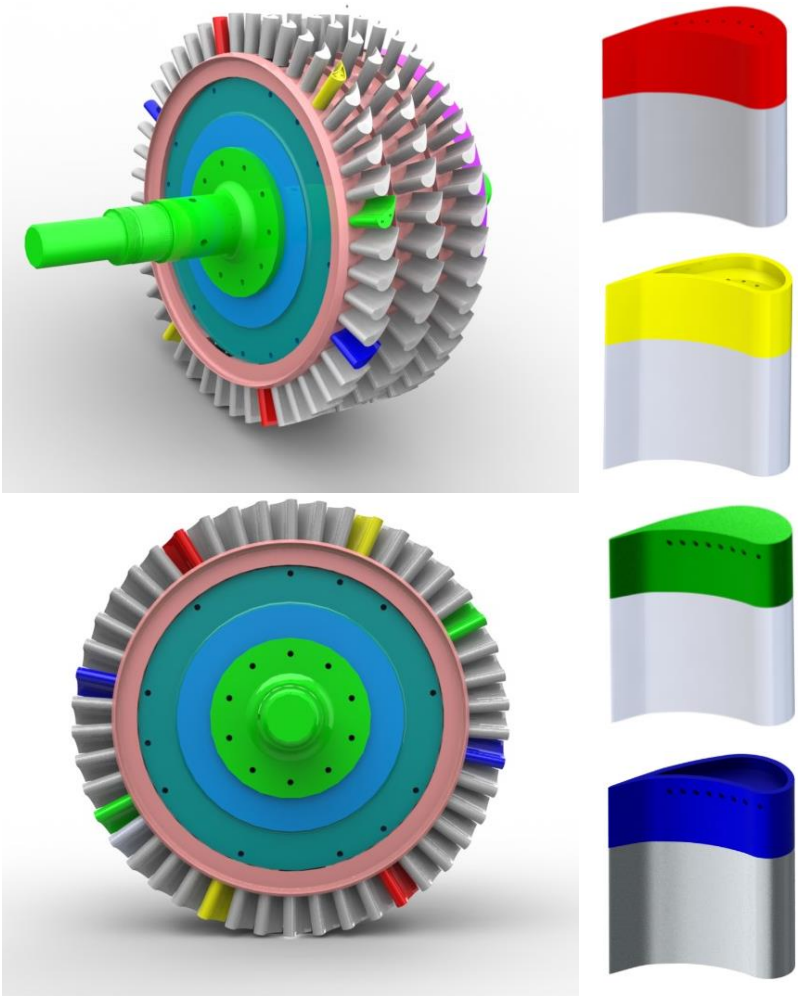

Figure 11: Four different rotor blade tip configurations: plane tip with tip hole cooling (red), plane tip with pressure-side compound angle hole cooling (green), squealer tip with tip hole cooling (yellow) and squealer tip with pressure-side compound angle hole cooling (blue).

To measure the film cooling effectiveness on rotating blade tips within the three-stage HP turbine, TPFL designed and manufactured four pairs of rotor blades with four different film cooling arrangements as showed in Figure 11: the plane tip with tip hole cooling (red), the squealer tip with tip hole cooling (yellow), the plane tip with pressure-side compound angle hole cooling (green), and the squealer tip with pressure-side compound angle hole cooling (blue). Note that the blade consists of top and bottom pieces due to the manufacturing requirements. In order to prevent any imbalance, the four pairs of rotor blades with film cooling holes were axis-symmetrically attached at the first rotor row (Figure 11 top left and bottom left). The detailed geometry for each blade tip with cooling configuration is shown in Figure 12. The blade height, axial chord length, and diameter (d) of film cooling holes are 62.865 mm, 40.7 mm, and 1.27mm, respectively. Seven perpendicular cylindrical holes evenly distributed along the camber line are used for the tip hole cooling, whereas eight compound angle holes for pressure-side-edge cooling are located 4.564mm below the blade tip edge. For the tips with tip hole cooling, the length of each cooling hole has a typical value of 4d that is 5.08mm however varies for the pressure-side hole cooling due to its inclined and compound angles. The inclined and compound angles of cooling holes for the pressure-side hole cooling are all 45^{o} except the one at the furthest upstream due to the local geometric restrictions as shown in Figure 12 (c). Moreover, the squealer tip has a rim width of 2mm and a recess of 4mm. Due to the squealer cavity, the blade with squealer tip has a bit smaller plenum inside the body than that of the blade with plane tip. However, both plena have adequate space to establish highly uniform pressure inside resulted from the

sudden expansion and fully mixing of coolant flow ejecting from the tiny holes on the bolt. As shown earlier in the figure located on page 31, the outer loop (marked by blue arrows) delivers coolant mass for film cooling experiments for the discrete film cooling holes on both plane and squealer tips of the first-stage rotor blades. The coolant flow is discharged through a long hollow pipe and fills the rotor internal cavity. A rotary seal is adapted to prevent any leakage. The coolant inside the rotor cavity is delivered to the blades and injected through the discrete film cooling holes on the blade tips.

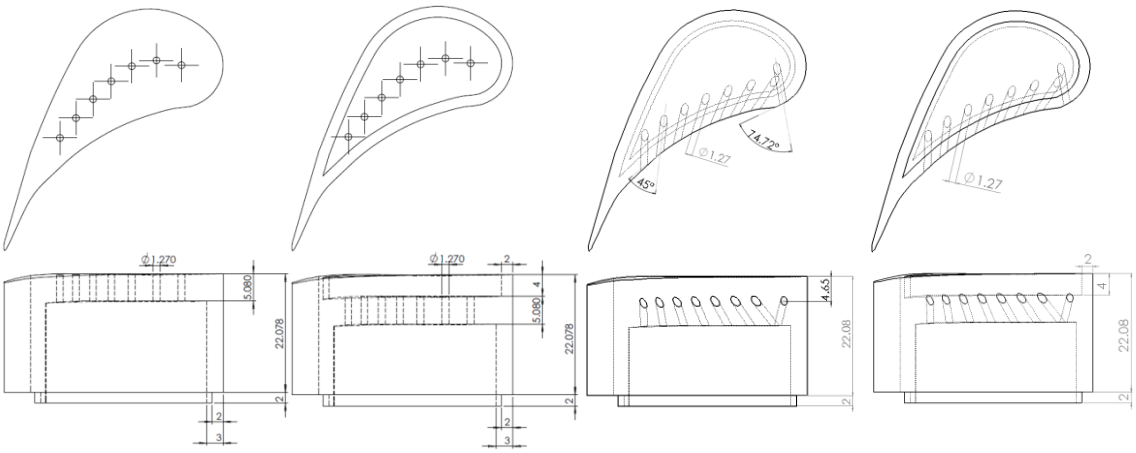

(a) **(b)** **(c)** **(d)**

Figure 12: Dimensions of blade tips: (a) Plane tip with tip hole cooling; (b) Squealer tip with tip hole cooling; (c) Plane tip with pressure-side-edge compound angle hole cooling; (d) Squealer tip with pressure-side-edge compound angle hole cooling.

Figure 13 shows the coolant path inside the blade. As seen, after passing through a cylindrical hole drilled at the center of the bolt that fastens the rotor blade, the coolant mass is ejected into a plenum through eighteen radially distributed tiny holes near the bolt tip, as shown in Figure 13. The presence of plenum aims to ensure a uniform coolant-discharge pressure distribution within it for each film cooling holes. Eventually

the coolant flow is injected to the mainstream from discrete film cooling holes located either on the blade tip or at the pressure-side edge near tip region. Since the rotor blade tip film cooling measurements are independent with the platform cooling tests, only the outer loop is turned on. Based on these cooling configurations, TPFL HP turbine is capable to measure the film cooling effectiveness on the blade tips with four different cooling configurations under rotating conditions.

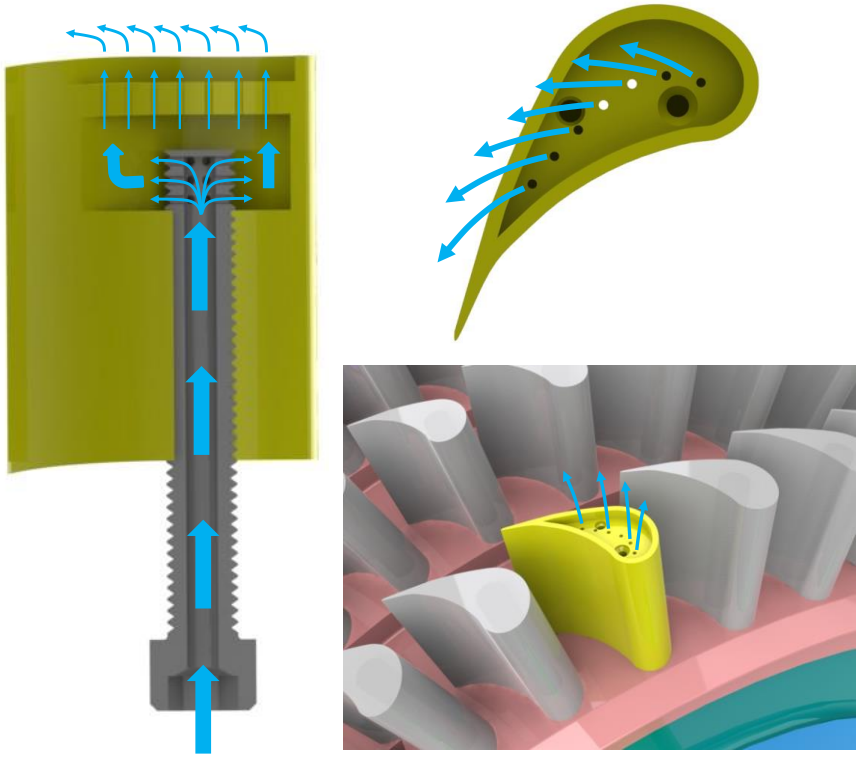

Figure 13: Schematic of the blade tip film cooling system.

Since the study of tip ejections is emphasizing the film cooling effectiveness and heat transfer that occurs in the first rotor row, three-dimensional calculations are carried out for the first 1.5 turbine stages, which consists of the first-stage stator (S1), the first-

stage rotor (R1) and the second-stage stator (S2), as shown in Figure 14 (top). In order to represent the experimental turbine as realistically as possible, all the geometric information was extracted exactly from the machine. Especially for R1, the endwall contouring and purge flow system [99] are involved according to the turbine structure. To reduce the complexity of the less important parts and decrease the difficulty of mesh generation for correlated geometry, the bolt with eighteen circumferentially distributed discrete holes (Figure 13 left) is simplified as a cylinder (Figure 14 bottom). The cylinder incorporates a bolt with inner holes from which the coolant is ejected.

With regard to boundary conditions (Figure 14), the total pressure and total temperature are given at the turbine inlet and mass flow rate is fixed at the S2 exit. The total temperature and mass flow rate are specified as boundary conditions for the coolant. The flow velocity at all inlets is assumed normal to the boundaries and typical turbulence intensity (5%) is specified. Additionally, non-slip conditions are used for the walls. For each blade tip configuration, the numerical simulations are conducted using low, medium and high global blowing ratios respectively. Note that the global blowing ratio is based on the average of the velocity between rotor inlet and exit. To study the rotation effect on the film cooling on blade tips which cannot be observed in cascades, calculations are performed for three different rotational speeds of 2000, 2550, and 3000 rpm, where 3000 rpm is the best performance point corresponding to the highest turbine efficiency for the test rig. The medium blowing ratio is specified for rotation effect studies. In addition, the calculation of adiabatic film cooling effectiveness, Nusselt number and heat flux ratio for each blade tip cooling configuration follows equations

(3), (4), (5) and (6). Similarly, in order to obtain the film cooling effectiveness on the R1 blade tips with a fixed blowing ratio at a constant rotational speed, two cases that supply same amount of coolant with different total temperatures must be calculated respectively. Still 318K is used to obtain T_{aw,f_0} according to the experimental running conditions and 300K is arbitrarily chosen for calculating $T_{aw,f}$. In addition, the adiabatic assumption is added to all the non-slip wall surfaces. In contrast, to obtain the heat flux at the R1 tips, the constant-wall-temperature boundary condition needs to be applied at R1 tip surfaces. Again an arbitrary temperature of 300 K is implemented on the R1 tips. Note that the squealer tip is comprised of the squealer cavity floor, the squealer cavity inner wall, and the rim, whereas the plane tip refers to the flat tip surface without any modifications.

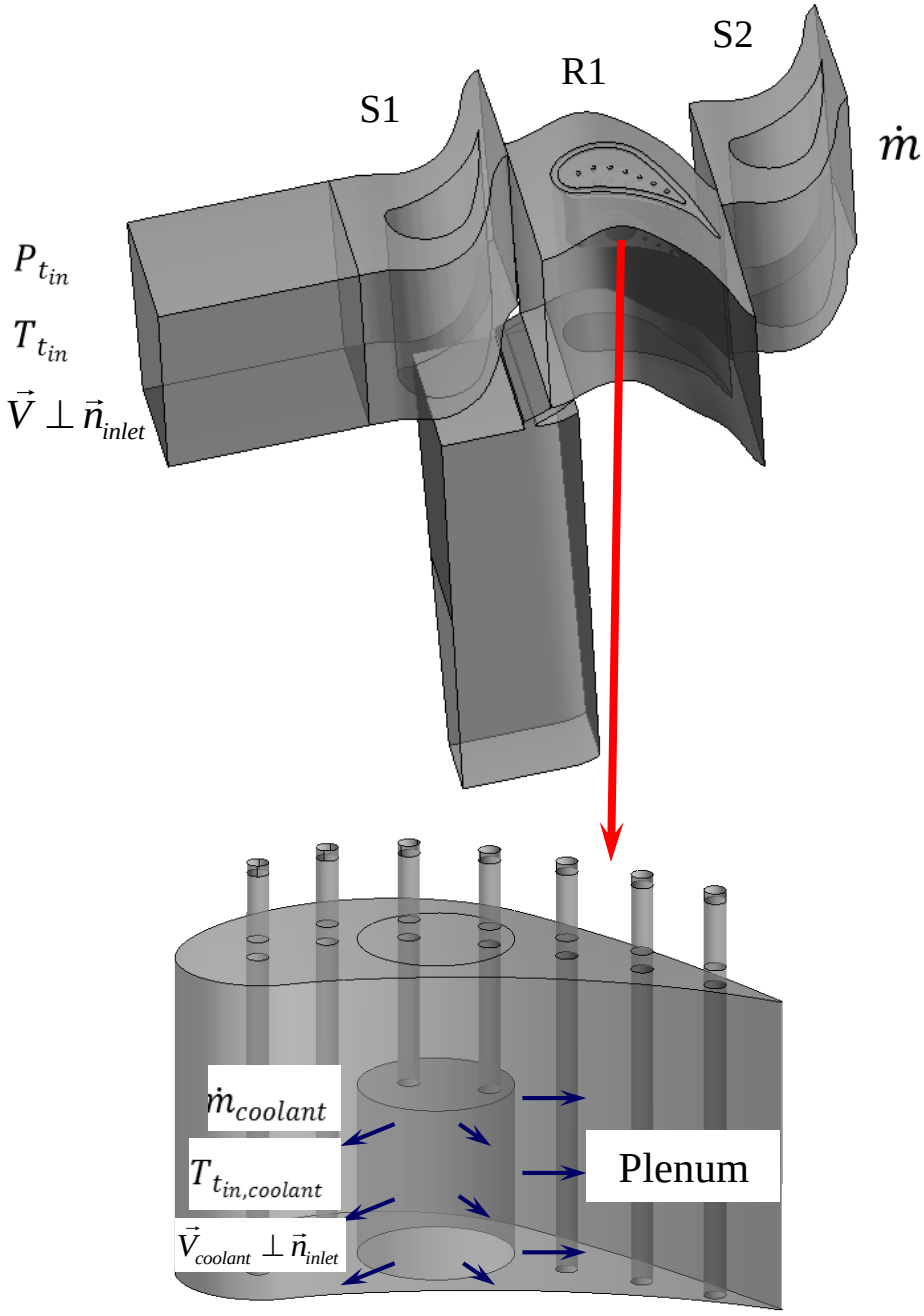

Figure 14: Computational domains and boundary conditions for mainstream (top); Geometries of plenum and boundary conditions for coolant (bottom).

Since R1 is the portion with tip film cooling, the finest mesh is used within this domain, especially at the blade tip region. The ANSYS product ICEM CFD is used to generate the hexahedral grids for R1. The grid independence study was performed for the plane tips with tip hole cooling as well as pressure-side-edge compound hole cooling. The typical condition with medium blowing ratio at 3000 rpm was utilized. Regarding the plane tip with tip hole cooling, three different grids with 2,447,434, 5,202,620 and 9,653,609 elements were numerically tested respectively. By examining the differences among the three solutions in Figure 15 (a) and (b), the second mesh was chosen considering the accuracy, time, and resources. For the squealer tip, mesh with the similar density was generated within the squealer cavity, while the rest of the parts obtain the same node clustering as the plane tip. The grid independent study was also conducted for the plane tip with pressure-side-edge compound hole cooling due to the significant difference in geometries. Similarly, three meshes that contain 2,448,757, 5,261,498 and 10,305,078 elements in R1 were generated and verified respectively. Figure 15 (c) and (d) suggest the results are independent of the Mesh #2.

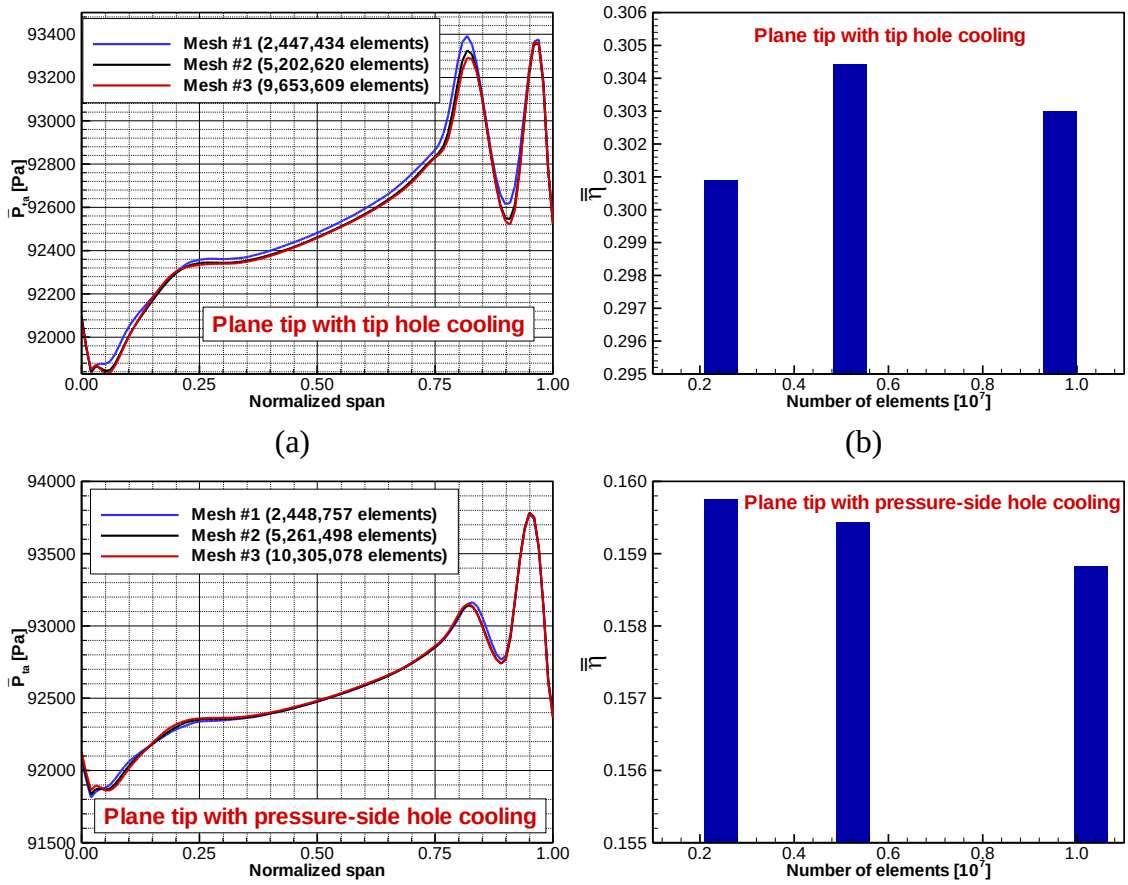

Figure 15: Grid sensitivity study for the first rotor with tip ejection: (a) Pitchwise-averaged exit absolute total pressure versus span for plane tip with tip hole cooling, (b) Overall global film cooling effectiveness for plane tip with tip hole cooling, (c) Pitchwise-averaged exit absolute total pressure versus span for plane tip with tip hole cooling, (d) Overall global film cooling effectiveness for plane tip with pressure-side hole cooling.

According to the grid independence study, in total 5,202,620 and 5,261,498 hexahedral elements were generated for the plane tips with tip hole cooling and pressure-side-edge compound hole cooling respectively. The numbers were increased to 6,333,988 and 5,864,330 for the squealer tips due to the presence of squealer cavity configuration. In both cases, the grids are clustered in the tip gap region as shown in

Figure 16 (a), (b), (d) and (e). To accurately predict and highly resolve the behaviors of cooling jets, sophisticated O-grid meshing technology that delivers high quality and good orthogonality is utilized to all the cooling holes as well as their vicinity, as shown in Figure 16 (c) and (f). To resolve the boundary layer, at least 22 grids with growth rate of 1.25 are distributed close to the wall and the first node is as small as possible to keep y^+ in the order of unity.

In the same manner, all the simulations were performed using the CFD software ANSYS CFX. The steady solutions are obtained by solving Reynolds-Averaged-Navier-Stokes (RANS) equations with a finite volume method. The SST-turbulence model was chosen to simulate the turbulence flow through the turbine. Each simulation was calculated until the global root mean square residuals for the RANS equations reached values below 10^{-4}. Moreover, various parameters were monitored as the solver was running. Examples include the average pressure at the exit, the mass conservation for the entire machine and each cooling hole, the area-averaged temperature and heat flux at blade tips, etc. Convergence was achieved when the residuals' target value was reached, and the stability was observed in the monitored variables. Typically, 2,500 iterations are necessary to achieve convergence. As a result, each single case computed in the parallel mode on Texas A&M super computers consumed several hundred hours of computation time.

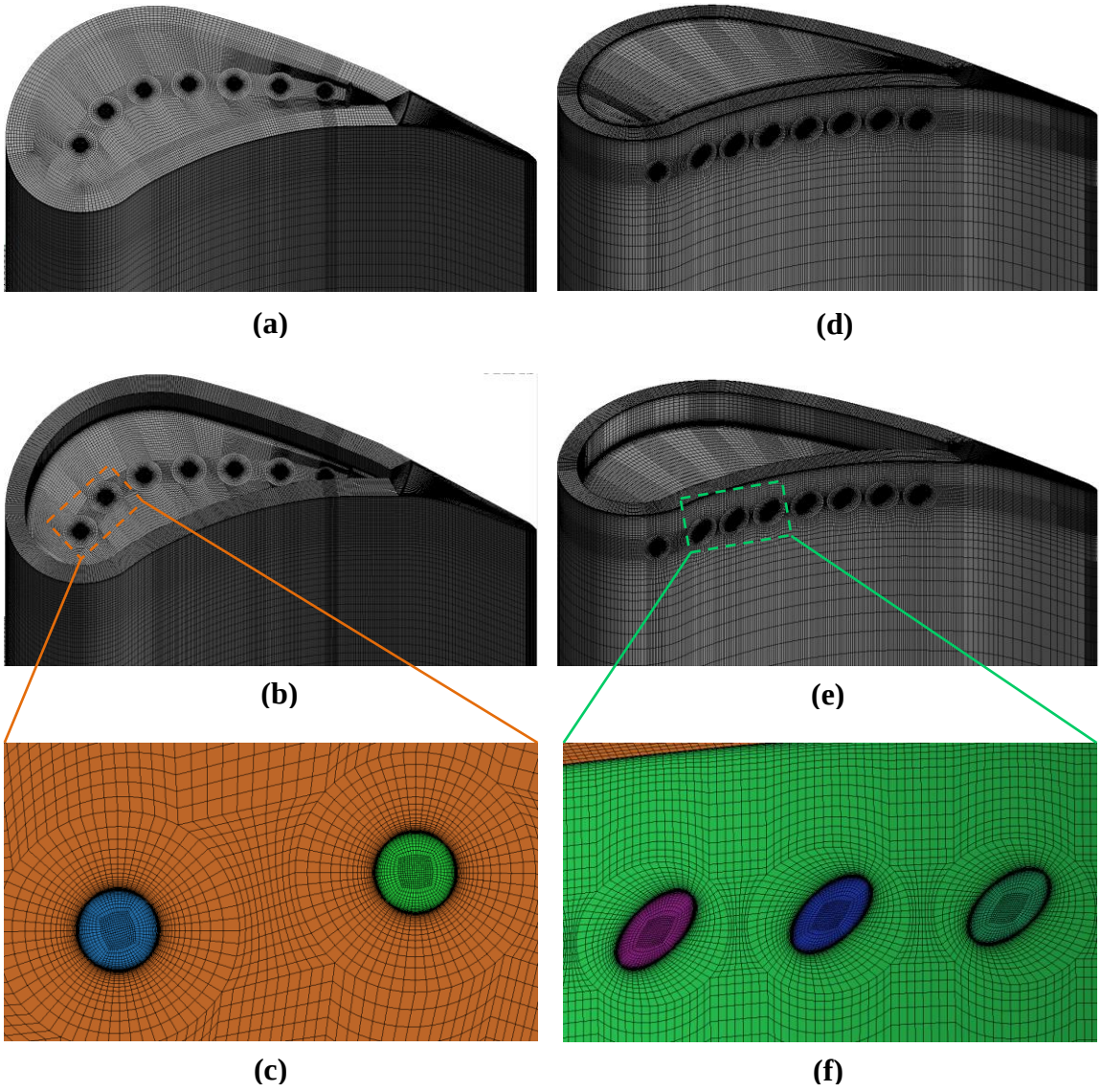

Figure 16: Detailed grid distributions: (a) the plane tip with tip hole cooling, (b) the squealer tip with tip hole cooling, (c) the O-grid for tip hole cooling, (d) the plane tip with pressure-side hole cooling, (e) the squealer tip with pressure-side hole cooling, (f) the O-grid for pressure-side hole cooling.

5. CONTINUOUS DIFFUSION FOR ENDWALL CONTOURING DESIGN*

5.1 Traditional Design Methods for Endwall Contouring

As extensively discussed in [100], the deficiencies in turbulence and transition models that cause major differences in efficiency calculations compared with the experiments, suggest that caution should be exercised, when interpreting numerical results. Therefore, the numerical results generated under these circumstances are of qualitative nature only. In performing parameter variations, however, the numerical simulation predicts the trends satisfactorily. For our turbine rig application shown in the figure located on page 28, extensive verifications and possible rectifications of the existing methods are fundamental before producing hardware to be tested. This requires extensive numerical studies to determine the impact of the above methods on the turbine rig flow field including pressure, velocity, vorticity, total pressure loss distributions and the turbine efficiency. We numerically simulated several cases. For each individual case several grids were generated to ensure the results were grid insensitive, Figure 17. The computational details have been extensively exhibited in Section 4.1.

* Reprinted with permission from "Endwall Contouring Using Continuous Diffusion: A New Method and its Application to a Three-Stage High Pressure Turbine" by M. T. Schobeiri and K. Lu, 2014. Journal of Turbomachinery, Volume 136, pp. 011006-1-10, Copyright © 2014 by ASME.

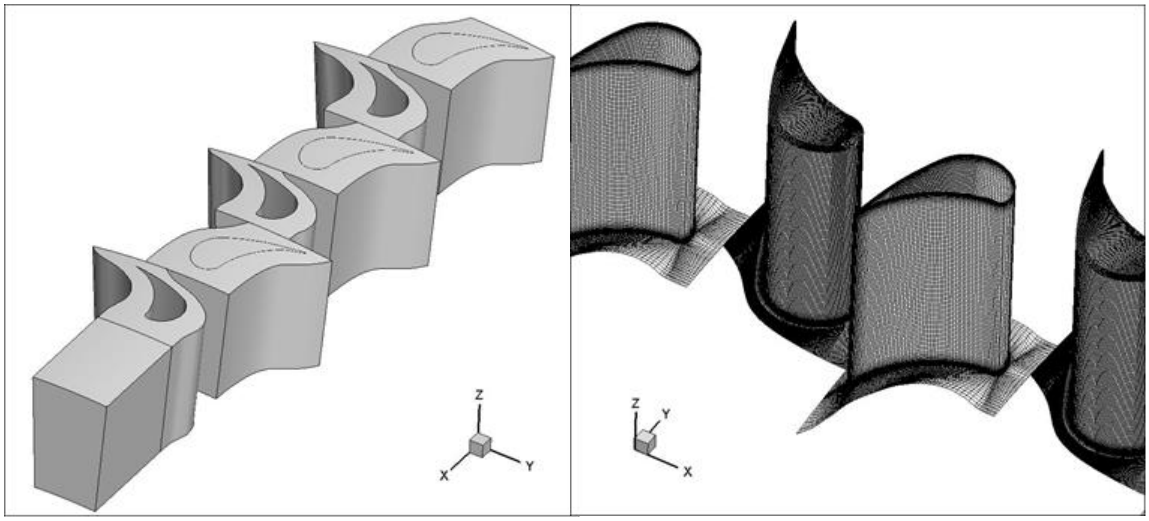

Figure 17: The computational model for TPFL three-stage HP turbine (left); CFD mesh (right).

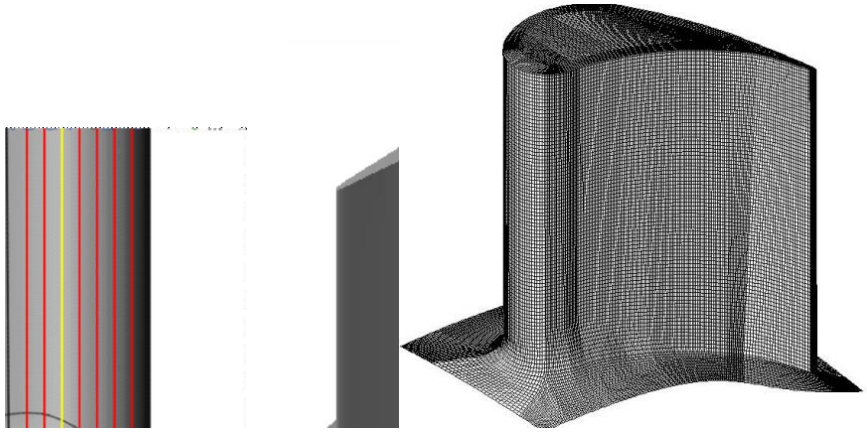

Figure 18: One of the contouring designs using the conventional method.

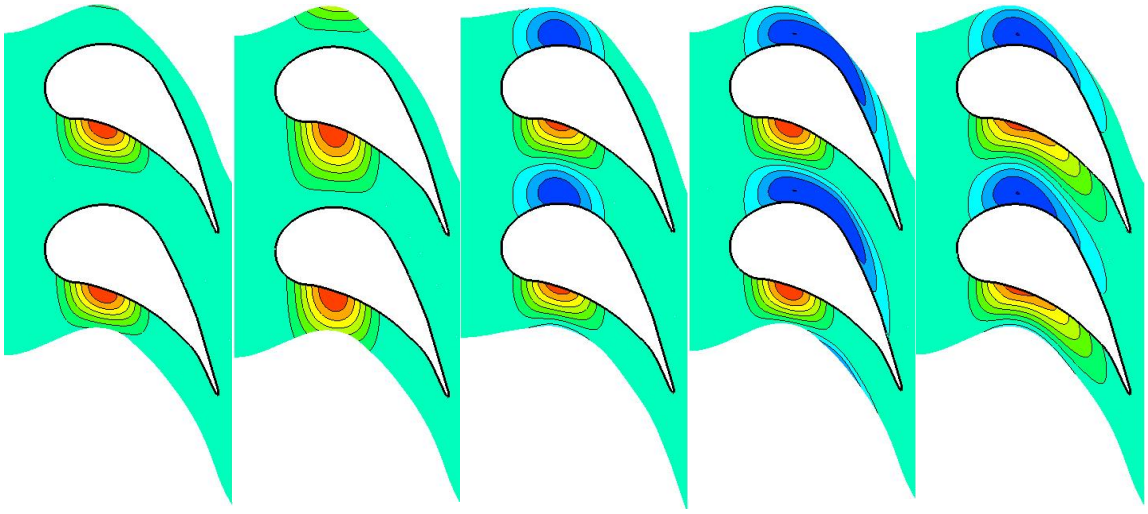

Figure 19: Contour variation: (a) partial positive contouring; (b) extended partial positive contouring, (c) partial positive, negative contouring; (d) extended partial positive, negative contouring; (e) full passage contouring. The maximum positive height for all cases is 6 mm, the minimum negative height is -3mm.

Following the conventional approach that is applied to the three-stage TPFL-HP-turbine blades, an example is given in Figure 18, where positive contouring (hill) is placed on the pressure side of the turbine while varying its height and the axial position. Several shape functions and decay functions were applied to define the variation of contour height and axial position in the streamwise direction, as shown in Figure 19. It shows configurations with (a) a contouring that is raised above the hub and occupies only a portion of the hub surface, called positive contouring, (b) a contouring that is raised above the hub surface but is circumferentially extended towards the suction surface, called extended partial positive, (c) a contouring with a portion that is raised above the hub followed by a portion that is lowered into the hub surface, called partial positive, negative contouring, (d) as (c) but with negative part extended along the suction

side and finally (e) a contouring with extended positive and negative portions that occupy the entire passage, called full passage contouring. Efficiency calculation results of the second rotor for different contouring used in this study are shown in Figure 20.

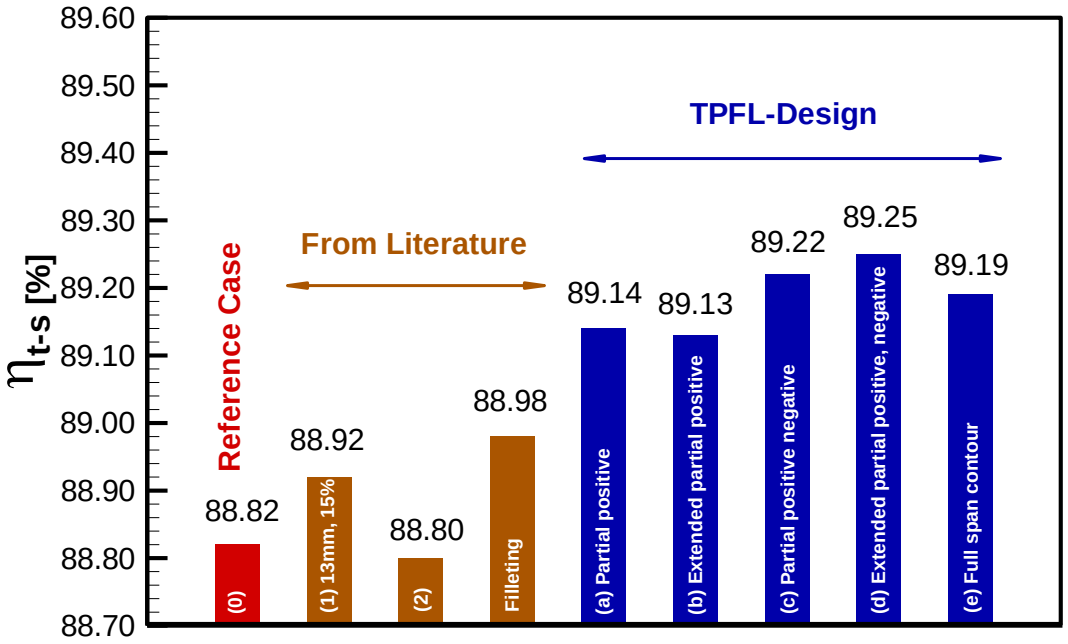

Figure 20: Efficiency chart of numerically investigated cases with endwall contouring designed by conventional approach.

Using the conventional approach, several cases were numerically simulated, where the peak height and its axial location were systematically varied. After variation of the height, the peak height was kept constant at 13mm, while its axial location was varied from 15% to 30% of the axial length. As representative examples, Figure 20 shows the efficiency calculation results labeled with (1) and (2). In addition, the filleting was also implemented into the catalog of simulations. Assuming an optimal position of the height within the range of 10%-15%, new contour shapes were introduced to perform an

optimization process with the efficiency as the objective function. For each case a new grid was generated, numerical simulations performed and the efficiency results presented in Figure 20 labeled with (a) through (e). As the results in Figure 20 show, using the trial and error approach associated with optimization process that was implemented into the numerical process has not delivered a trend toward an optimum solution. Furthermore, it was shown that the efficiencies were inconsistent throughout and the results were inconclusive to be transferred to different turbine blade types. Most importantly, the method used in the publically available literature is not suitable to provide a generalized design guideline for the research and design community. This circumstance motivated us to introduce a new and physics-based method to effectively design endwall contouring for any type of blading regardless its application to HP-, IP- or LP- turbine.

5.2 TPFL Innovative Continuous Diffusion Method

Turbine blades designed for applications in power generation and aircraft gas turbines as well as in steam turbines have in general different specific stage load coefficients, flow coefficients and degree of reaction. Furthermore, they are twisted from hub to tip to account for a prescribed radial equilibrium. The stator and rotor row for each turbine type have different solidity, aspect ratio and Zweifel number. In addition, the blades with the same inlet and exit flow angles might have different pressure distributions on pressure and suction surfaces. In the following paragraph a step-by-step physics-based method is introduced for endwall contouring design that can be recommended to the turbine design community as a general guideline.

The Continuous Diffusion Method for endwall contouring initiated and developed by TPFL utilizes a continuous prescribed deceleration of the secondary flow velocity from pressure to suction surface by a diffuser type of flow path that is consist of a number of imaginary narrow diffusers with the width ΔW_i, a given inlet height and variable exit heights that produce a desired target pressure distribution at the suction side. The diffuser raises the pressure on the endwall suction side thus reducing the secondary flow velocity, the strength of the secondary vortices, the associated induced drag forces and the total pressure loss due to the latter. The method can be applied to HP-, IP-, and LP-turbines and compressors regardless the load coefficient, flow coefficient and degree of reaction. It is strongly physics based, very straight forward and easy to use.

The following step-by-step instruction presents a tool for appropriately designing non-axisymmetric contours:

1) For the reference non-contoured blade place a cylindrical control surface at a radius $R_{hub}+\delta$ with δ as the boundary layer thickness developed by the secondary flow from the pressure to the suction side, Figure 21 (A). The boundary layer thickness can easily be estimated, [100].

2) For the reference blade obtain the pressure distribution on hub, Figure 21 (B).

3) For the reference (non-contoured) blade find the actual distribution of the pressure difference ΔP_i between the pressure and the suction surface and define a target pressure difference $\Delta P_{target} > \Delta P_{lim}$ with ΔP_{lim} as the minimum pressure difference, below which, the decelerating flow will separate. Ideally the target pressure should be close to zero. This, however, will lead to a large area ratio for the local diffuser and thus a flow

separation. The attached diffuser performance, Figure 21 (D) allows designing an appropriate diffusion path with an optimal performance.

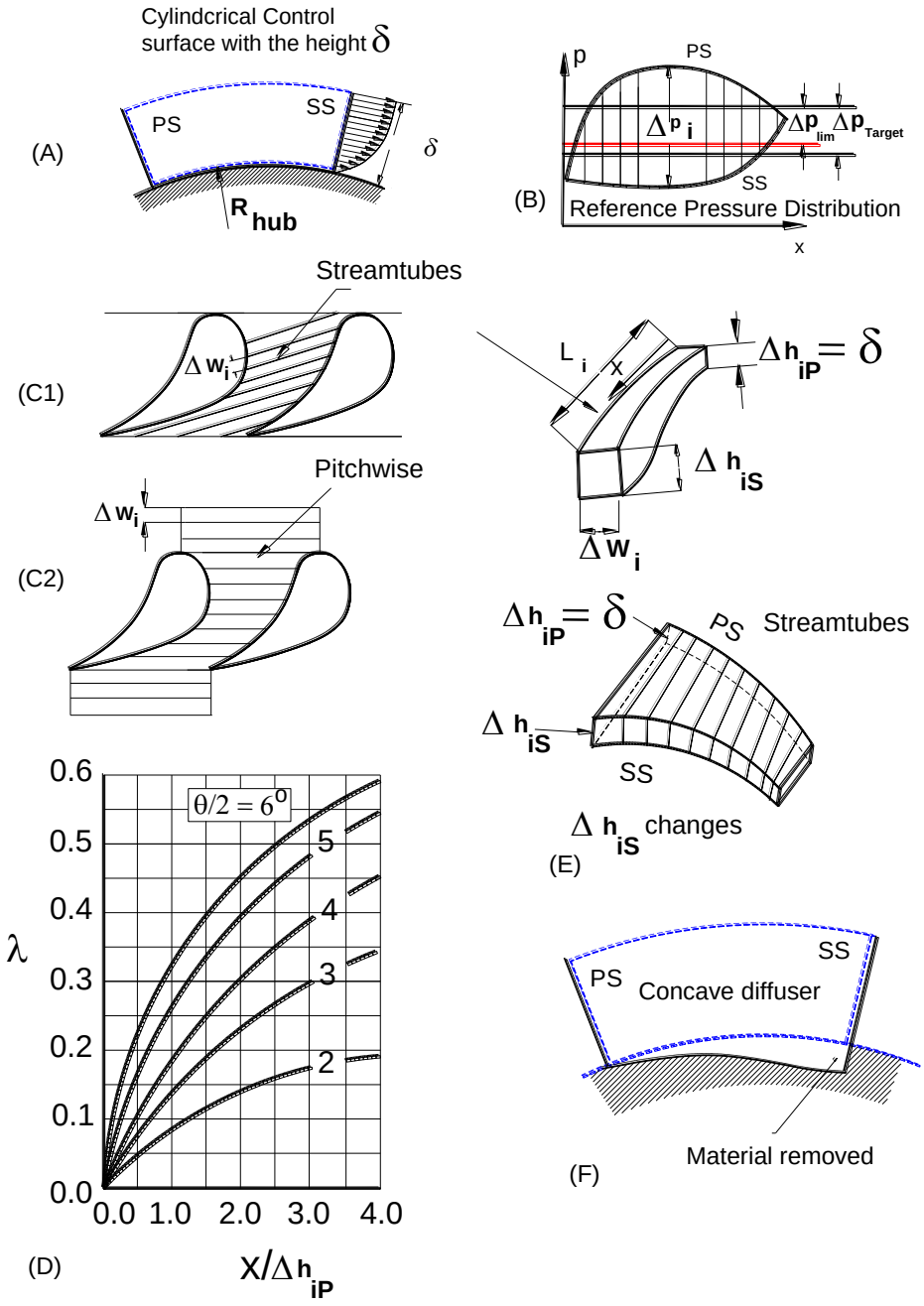

Figure 21: Explaining the continuous diffusion approach for designing physics-based endwall contouring.

4) Obtain the topology of streamlines at the same radial position, sketched in Figure 21 (C1) based on Figure 22. This step determines the local velocity vector pertaining to each streamline. This combined with step 5 provides the input to construct the diffuser channels that follow the streamlines. Another alternative is decomposing the velocity vector into axial V_{ax} and circumferential V_{circ} (pitchwise) components. This allows using V_{circ} for constructing diffuser channels that follow the pitchwise velocity component, Figure 21 (C2). Both alternatives are equally applicable, however the latter has the advantage of extending the diffuser channels slightly upstream of the leading edge and downstream of the trailing edge.

5) Starting with a constant ΔW_i for example $\Delta W_i = 0.05\ C_{ax}$, calculate the distribution of pressure recovery factor λ on the suction surface, by which the flow is still attached. This λ is taken from [101], where a series of diffuser performance maps for different diffuser-length/inlet-height ratios corresponding to $X/\Delta h_{iP}$ are presented. Figure 21 (D) schematically represents one of those diagrams. With the λ distribution, then calculate the contour height Δh_{iS} on the suction surface that establishes a pressure difference ΔP defined in nomenclature that should be approaching to ΔP_{target}. Up to this point, the diffuser can be constructed, Figure 21 (E), with the constant $\Delta h_{iP} = \delta$ at the pressure side and variable $\Delta h_{iS} > \delta$ at the suction side from leading edge to trailing edge, Figure 21 (D).

6) Design the 3-D contour by removing the hub material, Figure 21 (F). A decay function at the inlet and the exit ensures a smooth transition of the contour.

7) Make sure that the throat integrity is not affected, this can be checked by using the mass flow balance.

8) Generate a high density grid for the above design and run CFD with SST turbulence model.

9) Re-evaluate the results and make changes if necessary. An "aggressive" endwall design may require a complete re-design of the entire stage.

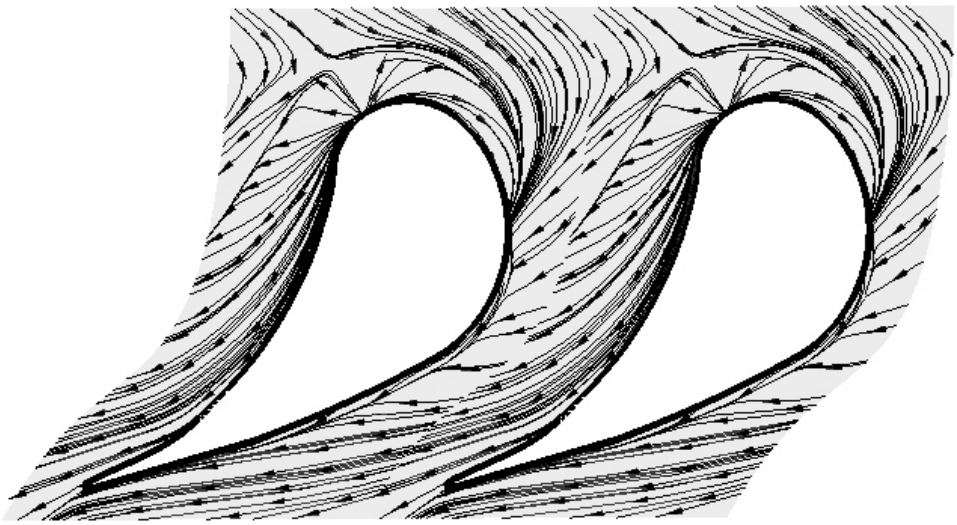

Figure 22: Streamlines from pressure to suction surface used for construction the diffusion channel.

5.3 The Endwall Contouring for Second Rotor

5.3.1 Geometric profiles

The new method is applied to the second rotor of the TPFL-HP-turbine, where steps 1 through 7 are executed. As shown in Figure 23, a target pressure (green lines) was constructed based on the reference ΔP for non-contoured rotor (black curves) by letting λ

< 0.7, and the corresponding height distribution Δh_{is} was calculated using the diffuser performance map. This allows a pressure recovery close to the separation point but still in the safe range. The critical range which was captured by the streamlines shown in Figure 22 extends from 0.17 to 0.55 C_{ax}. With the Δh_{is}-distribution implemented into the hub of the second rotor, fully three-dimensional non-axisymmetric endwall contouring was shaped after smoothing the surface. Figure 24 shows the construction of the new endwall contours for the second rotor compared to the reference case. The subsequent numerical simulations delivered the stage flow quantities, among other things, the new pressure distribution on the hub. The reduction of the total pressure loss by 27.9% and accordingly enhance of the second rotor efficiency by 0.68% was obtained based on the CFD predictions.

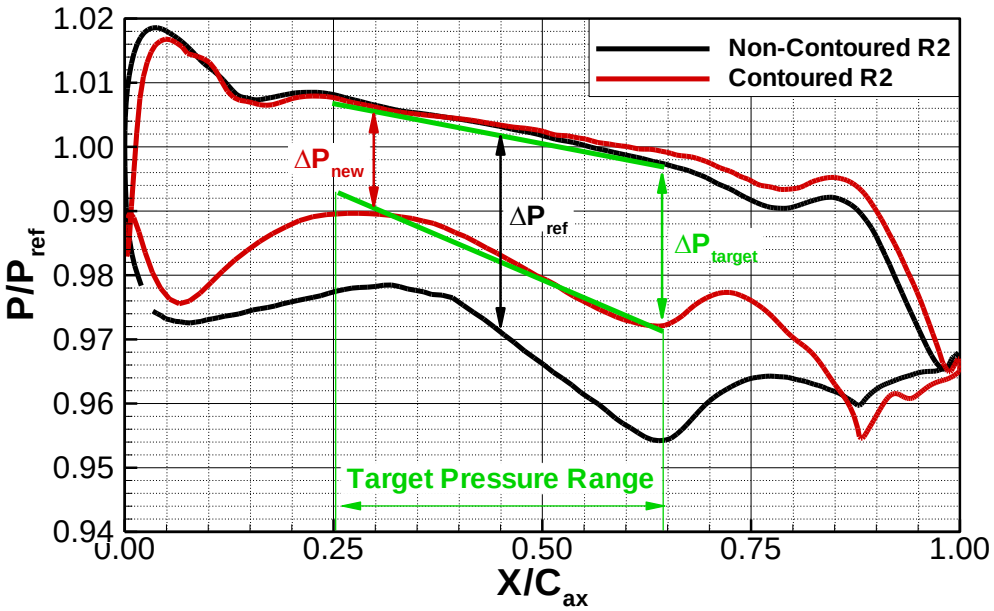

Figure 23: Pressure distribution directly on the hub of second rotor, a target pressure is set to construct the diffusion channel that leads to endwall contouring. Black line: the reference case; Red line: the new pressure distribution.

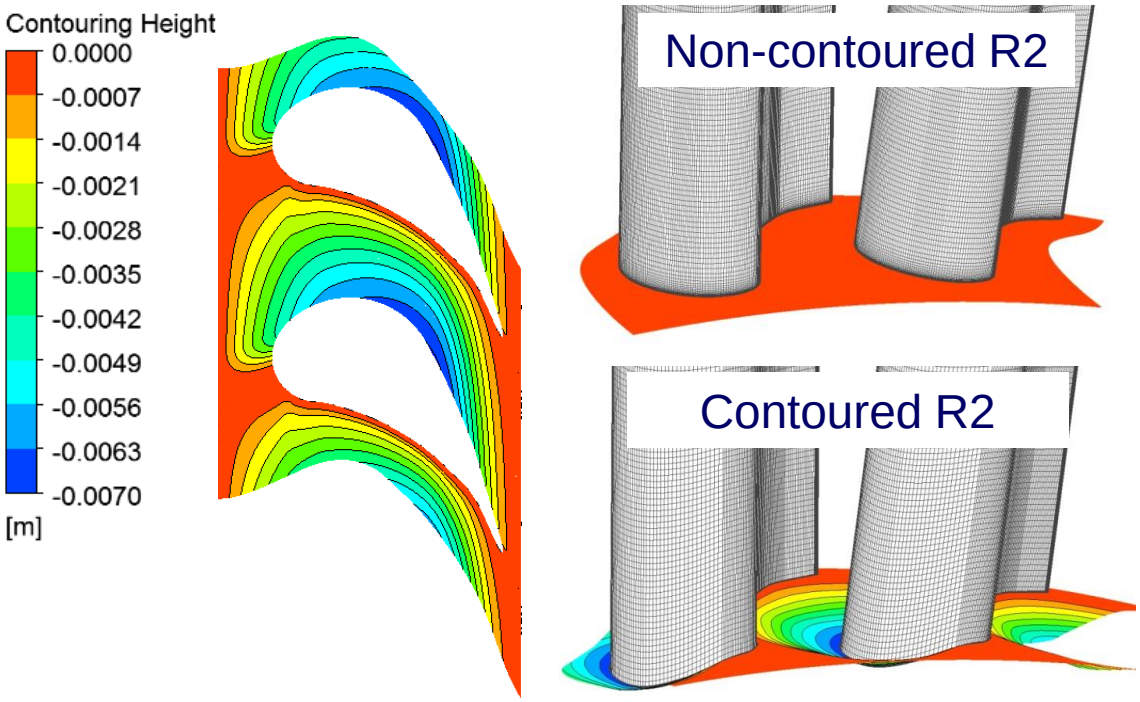

Figure 24: Profiles of new endwall contouring for the second rotor.

5.3.2 Pressure distributions

Figure 23 compares the pressure distributions directly on the R2 hub with and without endwall contouring. A major shift of the suction surface pressure toward the pressure surface with a maximum value of 1600 Pa and a minimum of 800 Pa is obtained in Figure 23. As shown, in the target pressure range, the suction surface pressure covers exactly the prescribed target pressure. From about 0.06 C_{ax} to 0.17 C_{ax} and from 0.55 C_{ax} to about 0.75 C_{ax} there are still substantial gains in pressure reduction on the suction surface reducing the suction effect. However upstream of 0.06 C_{ax} and downstream of 0.73 C_{ax}, no significant pressure increase is observed since the local endwall contouring profiles have diminished a lot due to the continuous decay towards upstream and downstream.

Figure 25 compares three different cases: (1) the reference case, (2) the conventional case using extended partial positive (+6 mm) and extended partial negative (-3mm) shown in the figure located on page 55 and the new case. The conventional case is effective only in a very narrow range close to the leading edge where the contouring's highest hill (the positive portion) and lowest trough (the negative portion) are located. Its effectiveness diminishes, when moving from this region away toward the leading and the trailing edge. Its effectiveness disappears completely when moving just a few millimeters from the hub surface as shown in Figure 26. In contrast, substantial reduction of ΔP is achieved with the presence of the new endwall contouring. It should be pointed out that the secondary vortices in this and the reference case extend above 2% span.

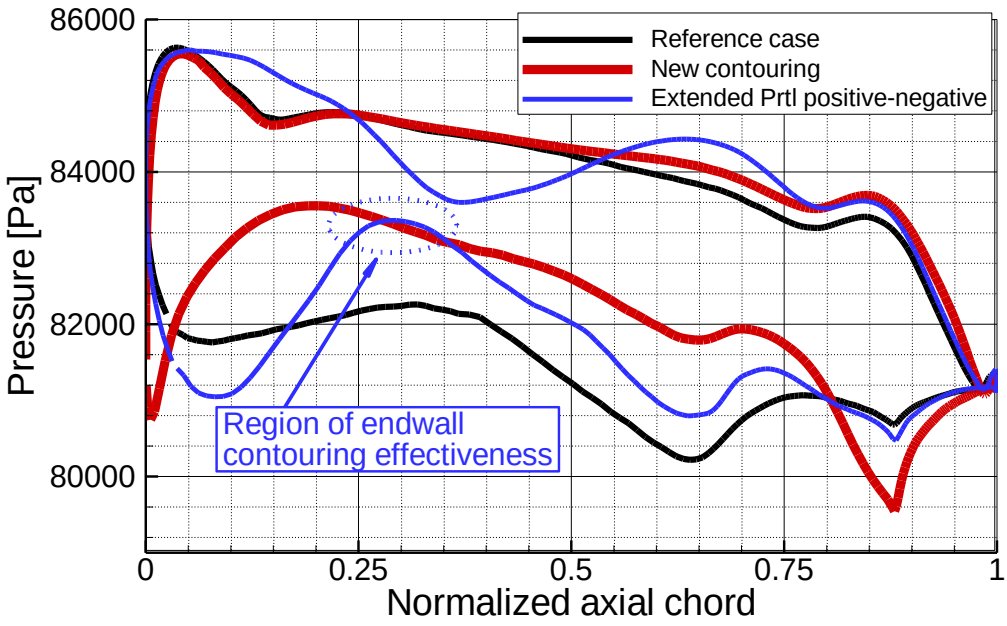

Figure 25: Pressure distributions at the R2 hub for reference case, new contouring and extended partial positive-negative contouring.

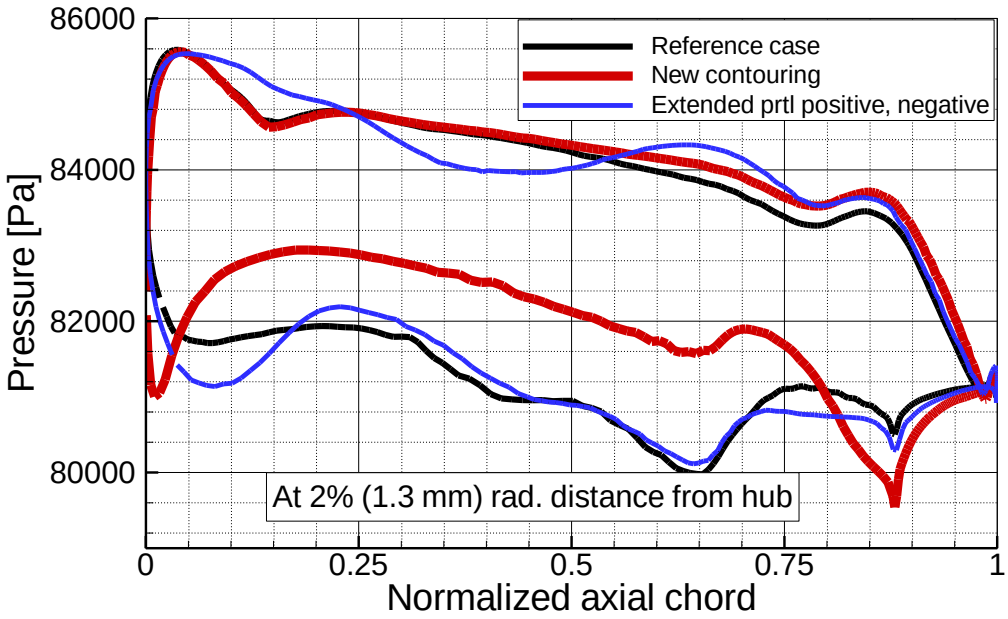

Figure 26: Pressure distributions above the R2 hub for reference case, new contouring and extended partial positive-negative contouring.

A clear picture of the impact of the endwall contouring on the pressure distribution is seen in Figure 27. In the reference case close to the axial location of about 0.28 C_{ax}, where the maximum positive height is located, with the exception of a wake-like pattern that is caused by the incoming horseshoe vortices, the isobars have more or less an orderly stable pattern. In pitchwise direction, however, a strong pressure gradient fieled dominates the flow picture from the leading to the trailing edge. Keep in mind that the purpose of the endwall contouring has been to weaken this pressure gradient field. The extended partial positive-negative case seems to only perturb the pressure field locally. This is quite consistent with the pressure distribution shown in Figure 25. A more orderly pattern of isobars associated with a much weaker pressure gradient is seen for the new contouring in Figure 27.

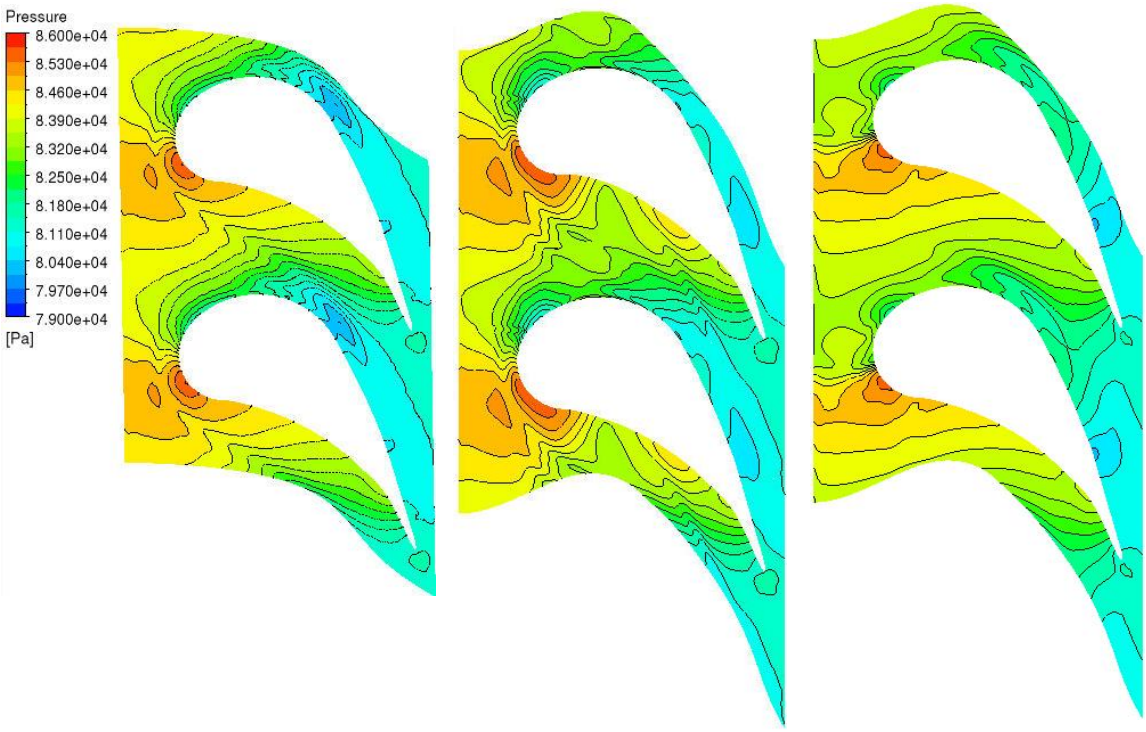

Figure 27: Contour plots of pressure distributions at the R2 hub for reference case (left), extended partial positive-negative contouring (middle) and new contouring.

5.3.3 Rotor efficiency and secondary losses

The results of efficiency calculations for the second rotor with the new endwall contour are presented in Figure 28. As seen, the new method has brought an increase of $\Delta\eta_{t\text{-}s}$ = 89.50 - 88.82 = 0.68%. This increase is quite remarkable given the fact that we defined our target pressure such that it covers the critical range of 38% of the axial length. Moreover, it has exceeded all the other values delivered by the conventional trial and error method discussed earlier. Further efficiency improvement would be expected by extending the target pressure upstream of 0.06 C_{ax} and downstream of 0.73 C_{ax}.

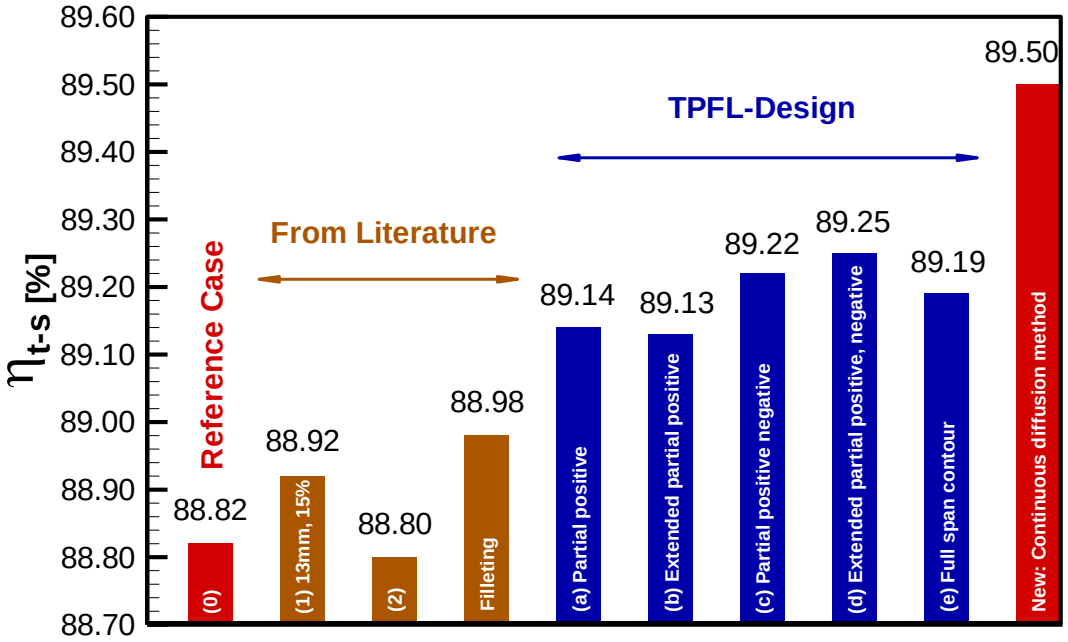

Figure 28: Efficiency chart of all investigated endwall contours for the second rotor.

Figure 29 displays the total pressure loss coefficient for the reference case, the case with extended partial positive, negative and the new endwall contour. For the new contour, the integration of the loss coefficients resulted in a reduction of secondary flow loss relative to the reference case of $\Delta\overline{\zeta_{Ptr}}$ = 27.9%. In contrast, in case of the extended partial positive-negative has caused an increase in relative secondary flow loss of $\Delta\overline{\zeta_{Ptr}}$ = 6.3%. Considering the calculated second rotor efficiency of 89.50% which is higher than the reference efficiency of 88.82% in Figure 28, one may conclude that the increase of the secondary flow loss coefficient and the increase of the efficiency are contradicting each other. However, this is not the case for two reasons: (1) A relative loss coefficient increase of 6.3% has only a marginal impact on the absolute value of the rotor efficiency, (2) when calculating the rotor efficiency the entire aero-thermodynamic

quantities are involved that includes total temperature, total pressure and the static pressure.

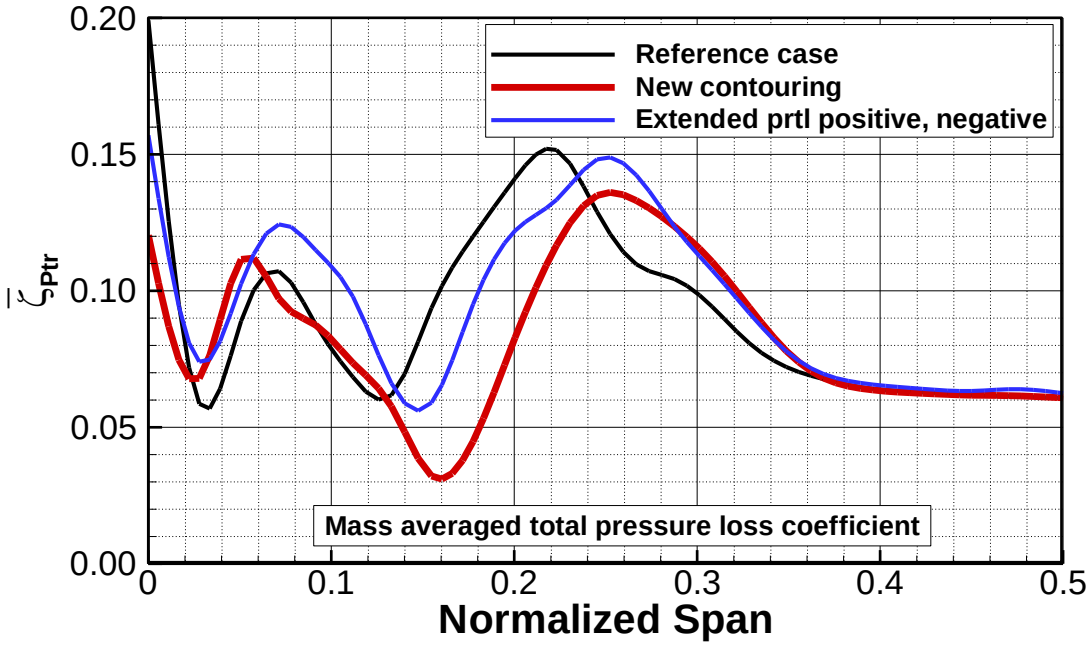

Figure 29: Pitchwise-averaged relative total pressure loss coefficients of the second rotor for reference case, new contouring and extended partial positive, negative.

5.3.4 Flow structures

Figure 30 depicts the streamlines near the endwall region for both the reference and new endwall contouring cases. In addition to reducing the secondary losses, Figure 30 also shows a substantial weakening of the upstream horseshoe vortices. As seen, the pressure-side and suction-side legs of horseshoe vortex have been reduced in both the size and strength.

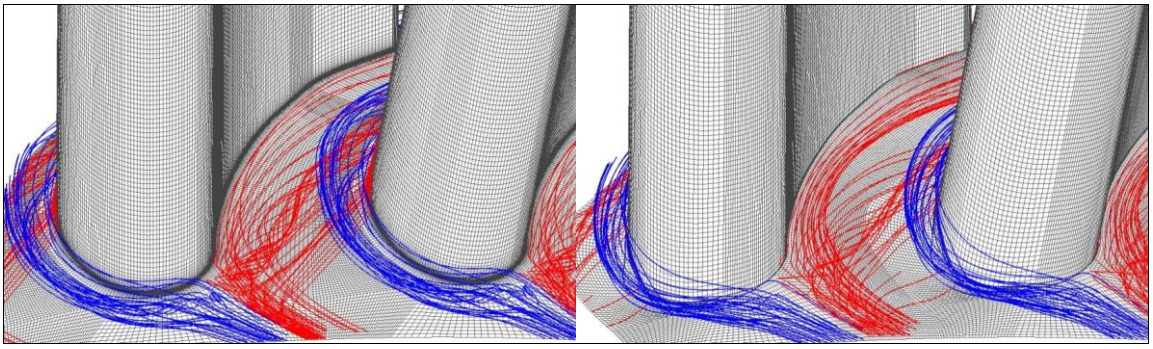

Figure 30: Streamlines close to the R2 endwall region for reference case (left) and new contouring (right).

Additionally, very close to the hub, the dominance of the pressure gradient from the pressure to suction surface causes the fluid particles to move pitchwise and produce a system of vortices. Figure 31 shows the vorticity distributions at three axial positions. The left column with three figures pertains to the reference (non-contoured) case. For the 0.3 C_{ax} case, the onset of the vortex seems to locate in between the suction and the pressure surface. It extends to the suction surface, where its strength becomes a maximum. Moving in axial direction its onset moves further toward the suction surface. Close to 0.55 C_{ax} the onset gains more strength with a maximum that extends radially from the suction surface hub edge to the blade mid-section and beyond. The right column shows the vorticity distribution for the new endwall case. As seen, the vorticity distributions generated by the new method has lower strength than the reference case. This is true for all three axial positions shown in Figure 31.

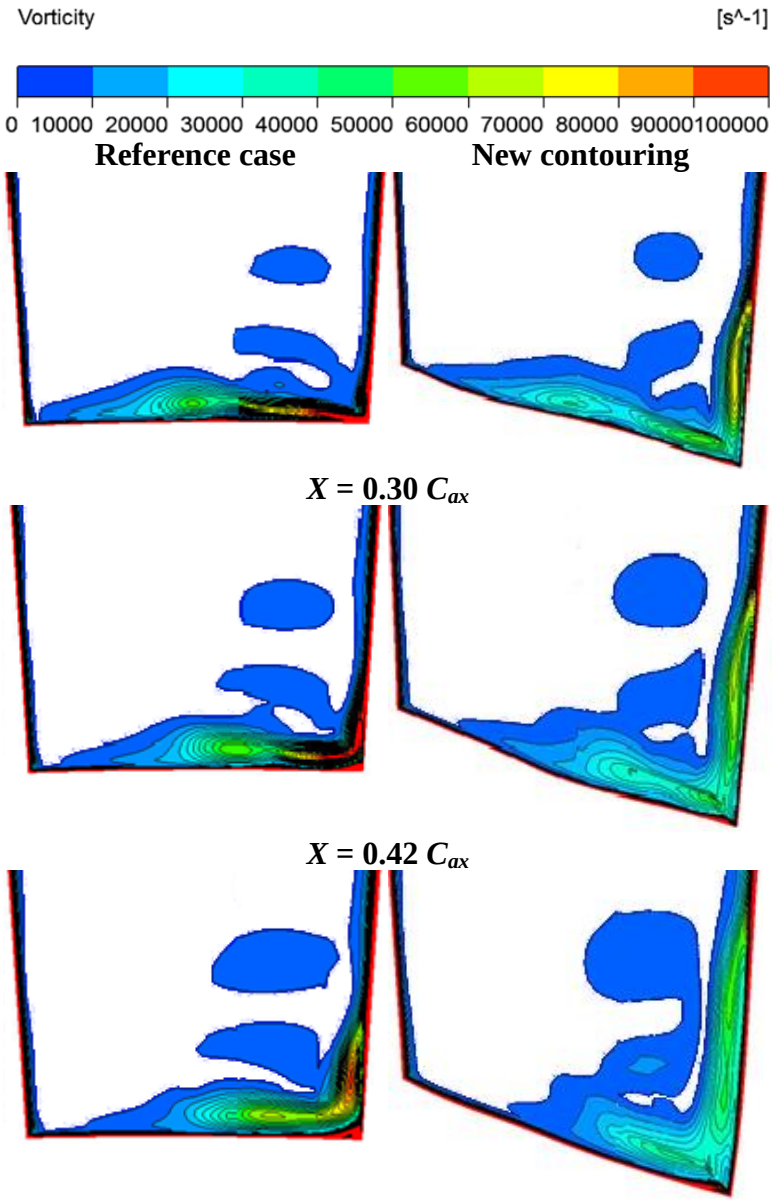

Figure 31: Vorticity distributions in the passage of second rotor: Reference case (left) and New contouring (right).

5.4 The Endwall Contouring for First Rotor

5.4.1 Geometric details

Besides the enhancement of efficiency due to the implementation of endwall contouring for the second rotor, it is also interesting to explore the impact of endwall contouring on the film cooling effectiveness and heat transfer at the first-rotor platform. For this purpose, the continuous diffusion method was also utilized for the design of endwall contouring for the first rotor. While in the case of the second rotor, (Figure 32 right) the endwall contouring extended upstream has brought substantial reduction in secondary flow losses and thus an efficiency increase, the first rotor is directly exposed to the purge flow with no space to extend the contouring upstream of the first rotor blade leading edge, as shown in Figure 32 left. This circumstance caused a shortening of the target pressure range to design an optimum endwall contouring for the first rotor.

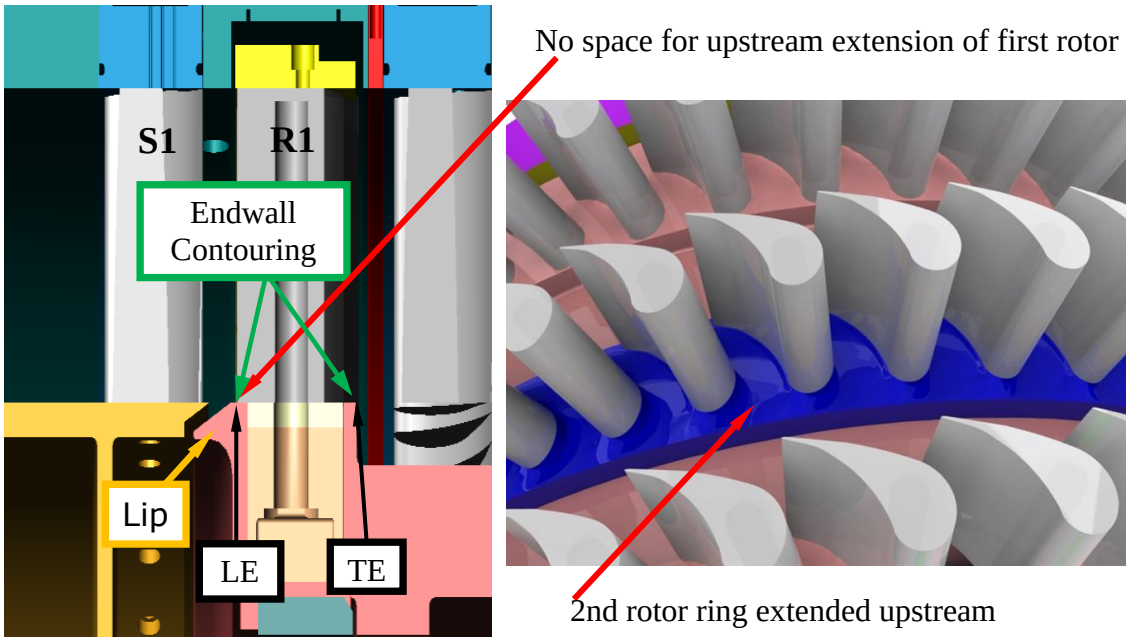

Figure 32: Position of the circumferential first-stator-rotor gap for ejection of purge flow (left), extension of the contouring upstream of second rotor endwall contouring.

Prior to directly adding the interaction of the purge flow with the endwall contouring, extensive numerical simulations were performed using commercial solver CFX with SST as the turbulence model and high density grid described in Section 4.1. To investigate the effect of the gap presence on the efficiency of the reference case considering the spatial restrictions mentioned above, we started with the reference case without contouring and prescribed a target pressure that caused a sharp deceleration rate (Figure 33 green curve). This resulted in an efficiency that was just slightly above the reference case without contouring. Apparently the corresponding diffuser contour experienced some flow separation at the upstream portion. Varying the target pressure by increasing ΔP_{target} (Figure 34) and thus leading to gradually decreasing the upstream

deceleration, a moderate deceleration rate was achieved that resulted in a fully attached flow inside the contouring (Figure 33 red curve).

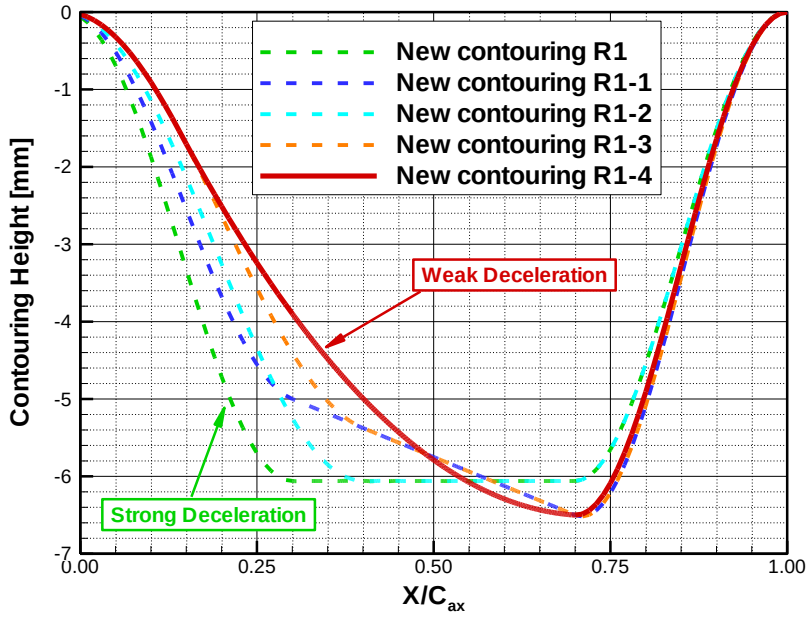

Figure 33: Variation of contouring height with different deceleration rate defined by the diffusion length to obtain the best efficiency for the first rotor.

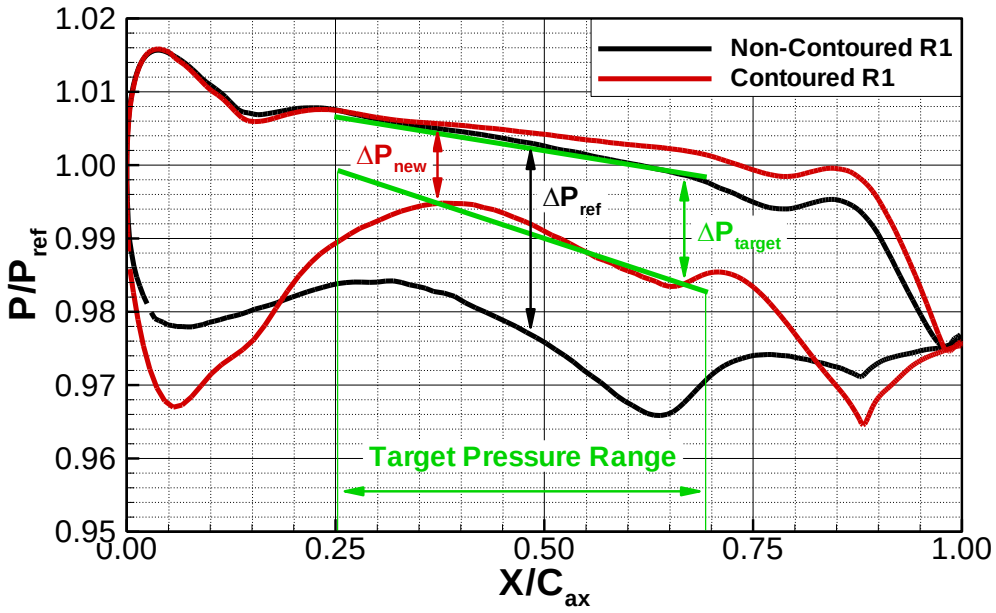

Figure 34: Pressure distributions directly at the first-rotor hub for reference case (black: non-contoured) and contoured case (red) with target pressure to design the contouring using the continuous diffusion method.

The profiles of the ultimate design of endwall contouring for the first rotor are shown in Figure 35. Apparently a shortage in the endwall contouring is seen due to the geometric restrictions when compared to that for the second rotor in the figure located on page 63.

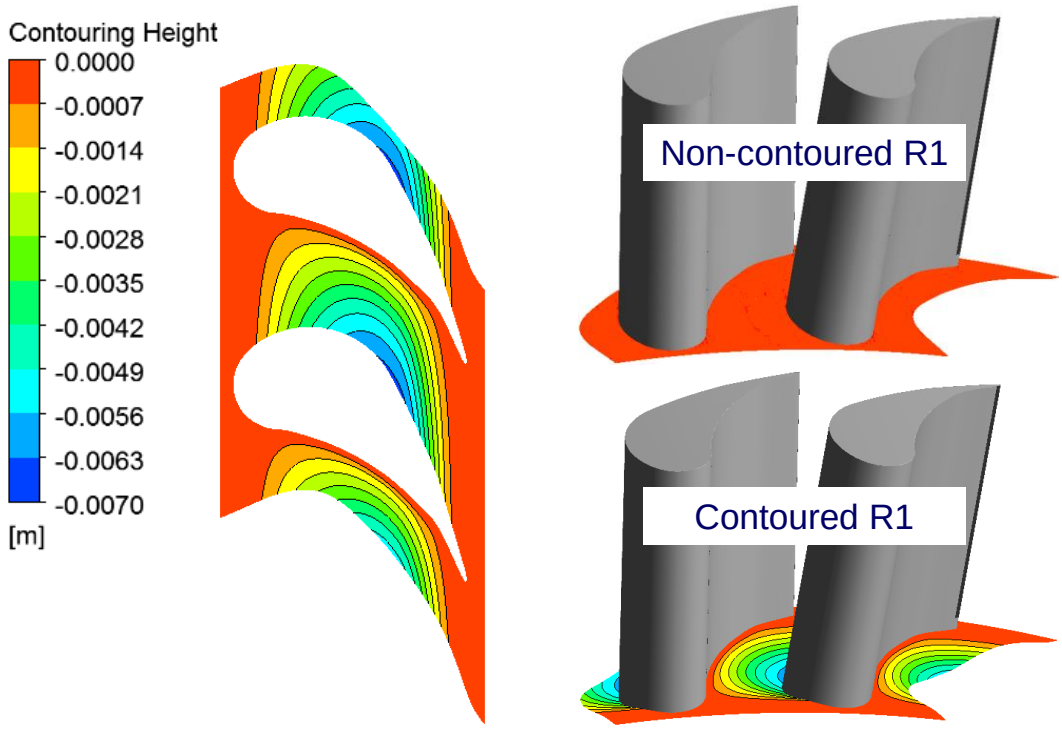

Figure 35: Profiles of new endwall contouring for the first rotor.

5.4.2 Pressure distributions

According to the working principle of the continuous diffusion method, the reduction of pressure gradient between the pressure and suction surfaces is one of the most important factors that are able to weaken the strength of secondary flows. Figure 36 depicts the pressure distributions at the first-rotor platform for the non-contoured and five contoured cases. As shown, from about 0.3 C_{ax} to trailing edge, the pressure gradient between the pressure- and suction-side is substantially reduced for all contoured cases, which is known by less pressure contour lines on the hub compared to the non-contoured R1. However, a low-pressure area (circled in Figure 36) is observed by the suction side close to the leading edge for every contoured rotor. It is believed to be

associated with the relative large deceleration rate compared to the circumstance for second rotor that allows contouring to extend upstream. Due to the inevitable geometric limitations of the first rotor, this region cannot be completely eliminated which to some extend undermines the effectiveness of endwall contouring on the first-rotor efficiency improvement.

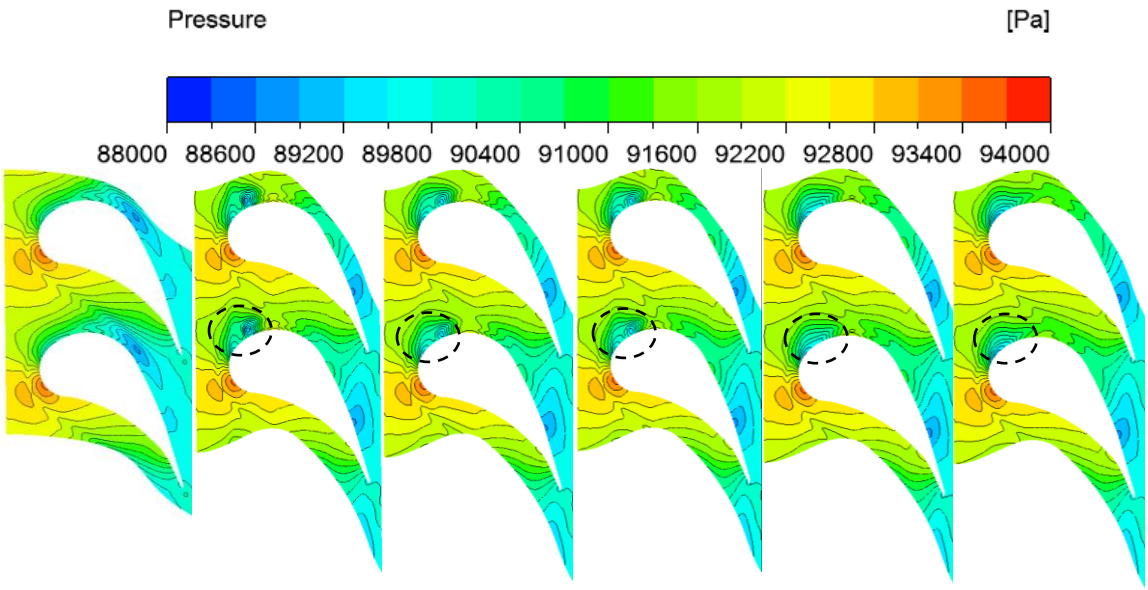

(a) (b) (c) (d) (e) (f)

Figure 36: Pressure distributions at R1 hub: (a) Non-contoured, (b) New contouring R1, (c) New contouring R1-1, (d) New contouring R1-2, (e) New contouring R1-3, and (f) New contouring R1-4.

The blade loading at R1 hub for both non-contoured and contoured cases is plotted in Figure 37. It is seen that the blade loading is consistent with the pressure distributions in Figure 36. As shown, the static pressure along the suction side is significantly enhanced between 0.3 C_{ax} and 0.75 C_{ax}, where the primary portion of the endwall contouring is formed in the figure on the page 73. Therefore the contouring designed with continuous

diffusion is working effectively for the first rotor as well. However, the relatively low pressure at the suction side is obtained between the leading edge and almost 0.2 C_{ax} for all the contoured cases. By carefully looking at the area, it coincides with the location where large deceleration rate exists in the figure on page 73. The deceleration rate gradually drops down beyound 0.2 C_{ax}. Another low-pressure area is seen close to the trailing edge, which might be also associated with the rapid change of the contouring height at suction side. It is noted that both low-pressure valleys can be improved or even removed by extending the contouring upstream and downstream with smaller deceleration and acceleration rate respectively as what has been done to the second rotor. However, the current contouring design for the first rotor is a compromise due to the geometric restrictions.

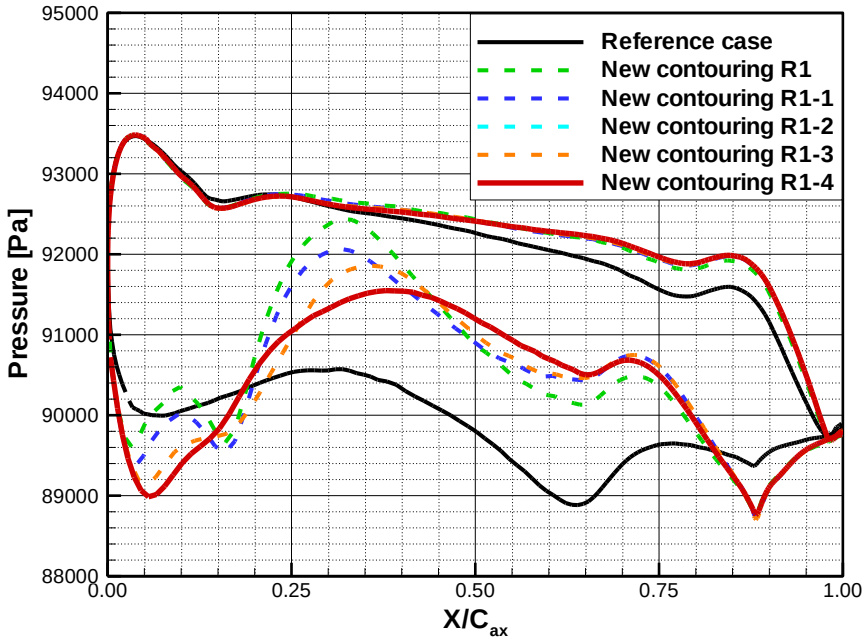

Figure 37: Pressure distributions on the R1 hub for reference case and five endwall contouring cases.

5.4.3 Rotor efficiency and secondary losses

The efficiency comparison between the non-contoured and five contoured cases for the first rotor is shown in Figure 38. As seen the total-to-static efficiency of first rotor increases as the deceleration rate declines. The new contouring labeled R1-4 has the highest efficiency of 90.81% compared to 90.47% of the reference case, which contributes an improvement of $\Delta\eta_{t\text{-}s} = 0.34\%$. This efficiency enhancement is half of the one that is obtained for the second rotor in Section 5.3.3. The drop in the efficiency augmentation is attributed to the shortening of the endwall contouring in the streamwise as well as the possible erosion of improvement due to the high deceleration and acceleration rate for upstream and downstream portions respectively.

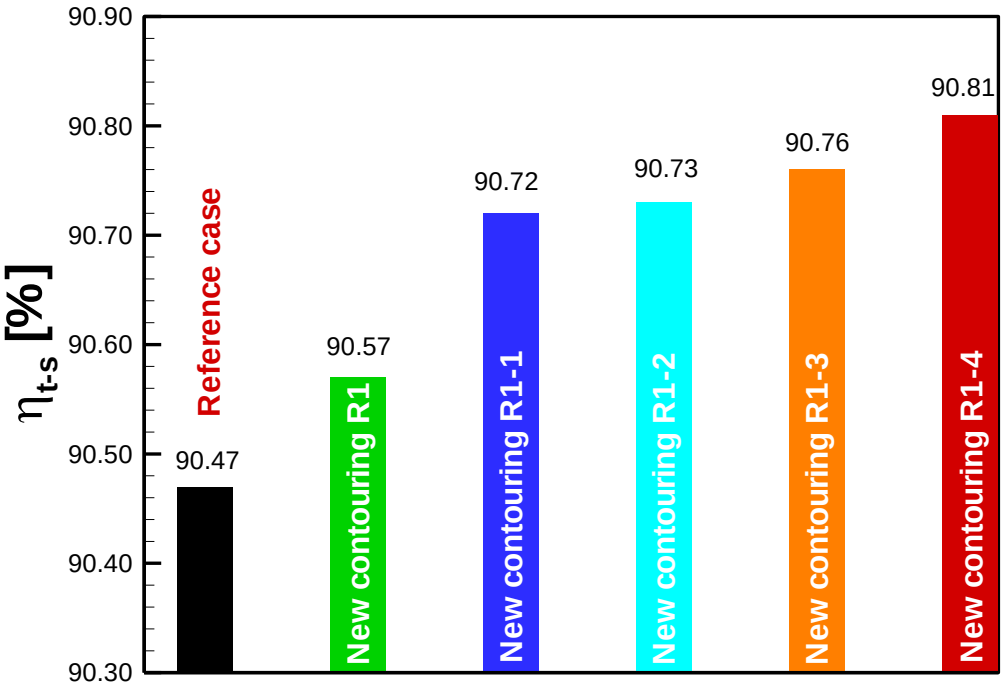

Figure 38: Efficiency chart of all investigated endwall contours for the first rotor.

Figure 39 depicts the comparison of total pressure loss coefficient for non-contoured and contoured first rotors. From the rotor hub to mid-span, there are two primary loss cores as marked in Figure 39. The first one (i) occupies the range from the hub to almost 10% of the span height. It is associated with the corner vortex and the movement of close-to-wall boundary layer with low momentum. The corner vortex is initiated at the blade-hub intersection which generates secondary losses in the region very close to the endwall. Meanwhile, the endwall boundary layer contributes to the loss balance by shifting up the peak of the loss. It is seen that the contoured R1 gets higher such type of loss that might be the results of fully 3D non-axisymmetric contouring surface and thus larger area than the flat platform. Another core (ii) is able to impact the area from 15% to 40% blade span. The loss core ii is the largest one that contributes to the primary portion of the endwall secondary losses. Its formation is the result of the passage vortex system. As shown, a higher peak as well as a larger loss core is obtained for non-contoured R1 but it decays a bit faster than that for contoured rotor. This core for the contoured R1 also shifts up about 5% span height. The integration of the loss coefficient resulted in a reduction of secondary flow loss relative to the non-contoured case of $\Delta\overline{\zeta_{Ptr}}$ = 0.5%. Apparently no substantial reduction of secondary losses due to the R1 endwall contouring is obtained. However there is still 0.34% of efficiency improvement for the contoured R1 which implies that the secondary losses due to the passage vortex has great impact on the rotor efficiency.

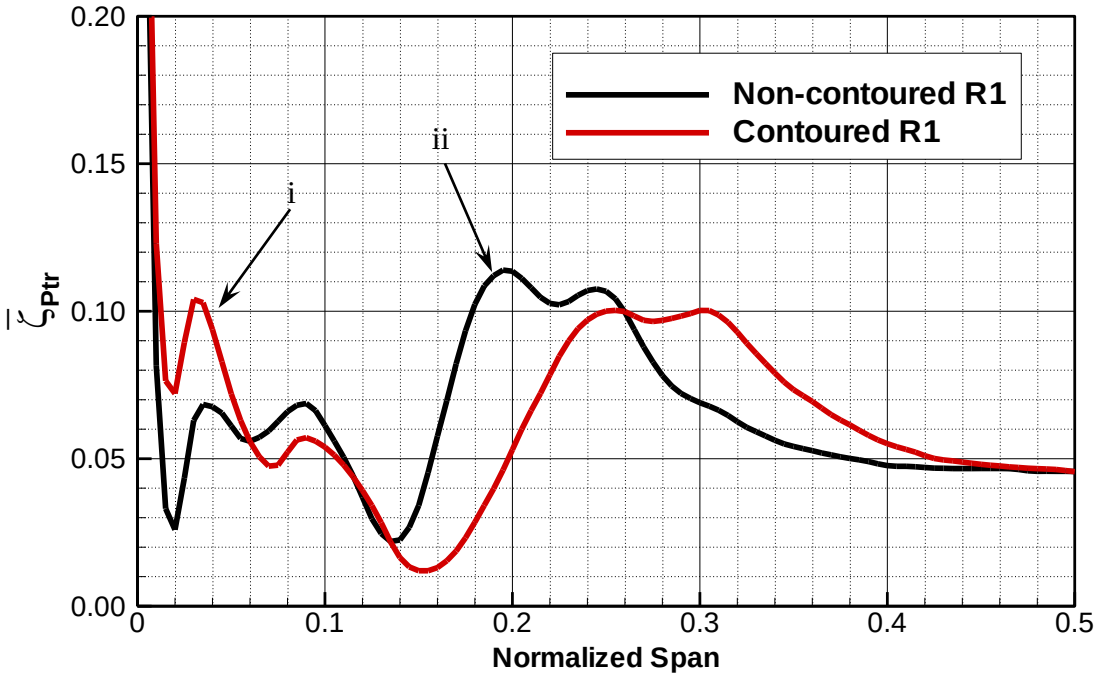

Figure 39: Pitchwise-averaged relative total pressure loss coefficients for non-contoured and contoured first rotors.

5.4.4 Flow structures

Figure 40 depicts the 3D streamlines close to the first-rotor endwall region for both non-contoured and contoured cases. The R1-4 is selected to illustrate the impact of endwall contouring on the flow field near the R1 hub due to its highest efficiency improvement. Unlike the endwall contouring for the second rotor, the contouring for the first rotor is not able to suppress the formation of horseshoe vortices which are generated in the upstream of the contouring starting point. However, at approximately 0.5 C_{ax} and the downstream, the turning of the flow is dramatically reduced, as marked in Figure 40. This is attributed to the decline of pressure gradient between pressure- and suction-side

due to the presence of endwall contouring. The driving force is weakened therefore the strength of cross flow is lessened.

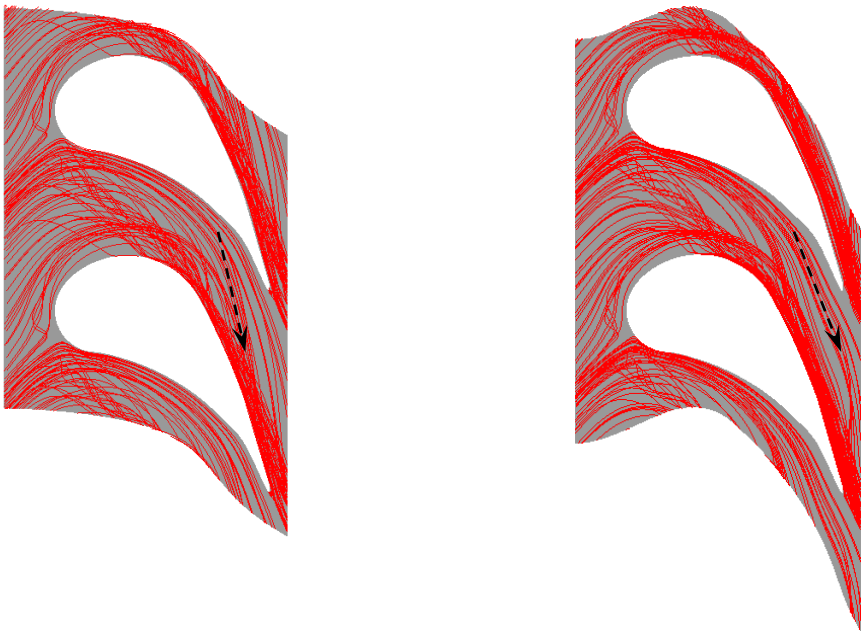

(a) **(b)**

Figure 40: Streamlines close to the R1 endwall region for (a) non-contoured case and (b) new contouring R1-4.

The vorticity distributions at three axial locations for both non-contoured and contoured R1 are plotted in Figure 41. The left column is for non-contoured R1 and the right for contoured one. As seen, the vorticity strength continuously decays however the size keeps growing along the streamwise direction in the R1 flow passage. It is to some extent a consequence of Helmholtz's theorems however the frictional losses occur when the flow particles travel downstream. Moreover, the high-vorticity area shifts and climbs up along the suction surface in the downstream. This phenomenon is associated with the formation of passage vortex systems. As shown, the vorticity strength for the contoured

R1 is lower at all three locations when compared to the non-contoured case. It reflects that the presence of endwall contouring is capable to weaken the endwall secondary flows.

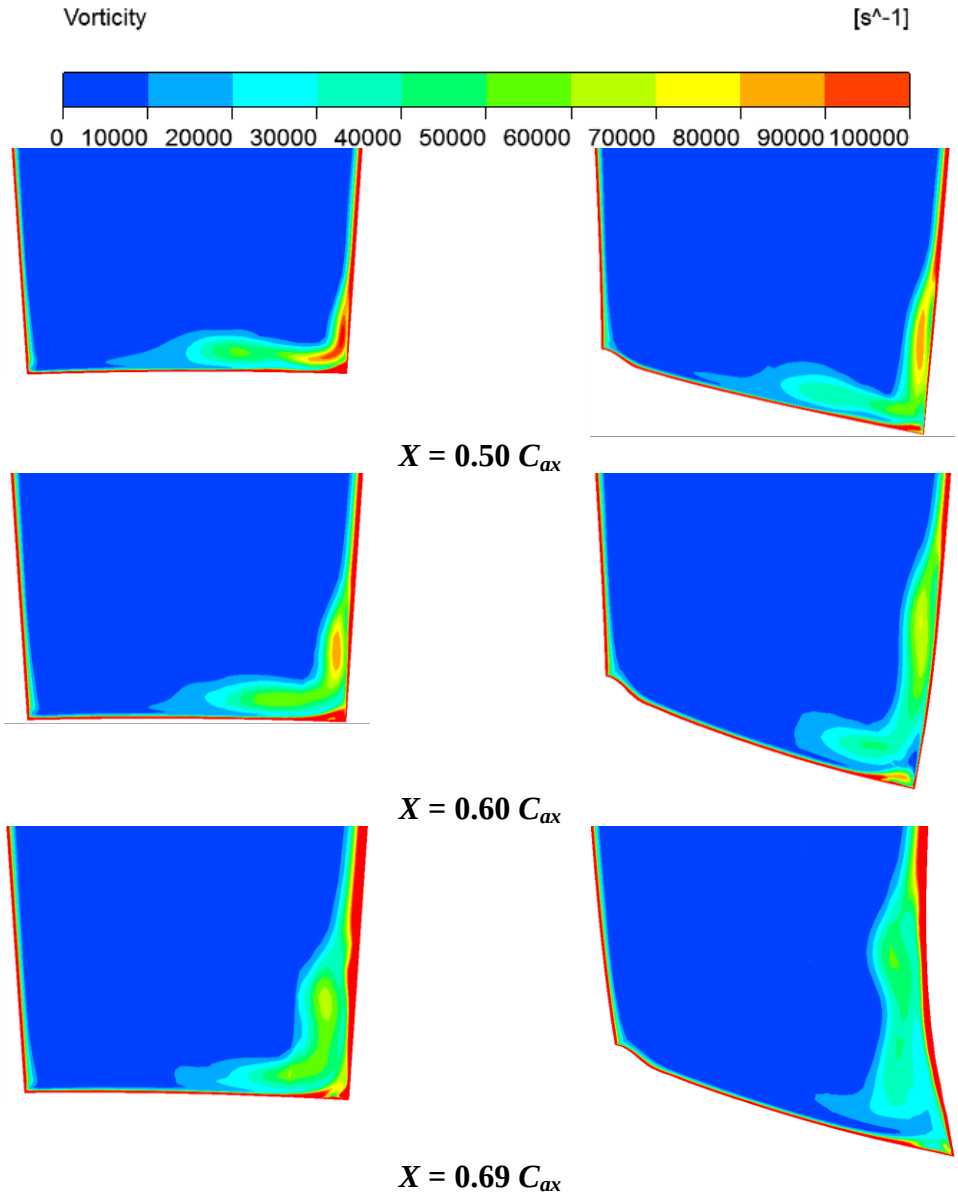

Figure 41: Vorticity distributions in the passage of first rotor: Non-contoured case (left) and new contouring R1-4 (right).

6. THE IMPACT OF ENDWALL CONTOURING ON TURBINE AERODYNAMIC PERFORMANCE

The HP-turbine, compared to the LP-turbine, has a relatively small aspect ratio which causes major secondary flow regions close to the hub and tip. As a result, the secondary flows formed by a system of hub and tip vortices that induce drag forces resulting in an increase of secondary flow losses, as extensively discussed in [11]. Focusing on the endwall secondary flow loss mechanisms, the fluid particles within the endwall boundary layers are exposed to a pitchwise pressure gradient in the blade channel. The particles move from the pressure side to the suction side and generate a system of vortices. These vortices induce drag forces that are the source of the secondary flow losses. In addition, their interaction with the main flow causes angle deviation inside and outside the blade channel, resulting in additional losses due to angle deviation.

One of the efficient methods of reducing the secondary flow zone is utilizing the compound lean blade design that reduces the secondary losses by varying the lean angle [11]. The effectiveness of the 3-D leaned design in suppressing the secondary flow is demonstrated in efficiency and performance studies by Schobeiri et al. [102, 103]. Another equally effective method for reducing the secondary flow losses is the endwall contouring based on a new method that uses continuous diffusion between the pressure side and suction side as detailed in [19]. The method reduces the pressure difference ΔP between the suction and pressure surface. As a result, the secondary flows are

significantly weakened. Following the method in [19], the effectiveness of the endwall contouring is also verified in terms of ΔP-reduction for different rotational speeds.

6.1 Pressure Distributions at Rotor Hub

Figure 42 depict the pressure distributions directly at the hub of the second rotor with four different rotational speeds. As seen in Figure 42, a comparison between the contoured and non-contoured cases shows a significant reduction of the pressure difference for the contoured case at all rotational speeds from 2000 rpm to 3000 rpm. For off-design speeds (2000 to 2600 rpm) the pressure differences for contoured and non-contoured are in general much higher than for the design speed of 3000 rpm. This is attributed to the variation of the incidence angle due to the change of the blade rotational speed. With an increase in the rotational speed, the circumferential component of the velocity increases. As a result, the stagnation point tends to move towards the suction side (Figure 42) and thus raises the local pressure on the suction surface, which provides smaller ΔP between the pressure side and suction side at leading edge. It is seen in Figure 42 that the presence of the endwall contouring is effective from the blade leading edge to approximately 0.88 C_{ax} for relatively low rotational speeds of 2000, 2400 and 2600 rpm. For the case of 3000 rpm, the profit is obtained from 0.10 C_{ax} to 0.88 C_{ax} due to smaller loading at the leading edge. The evidence of the effectiveness is the significant reduction of ΔP in the pitchwise direction. Particularly over 30% of reduction in loading at the hub is obtained from 0.25 C_{ax} to 0.75 C_{ax}. Additionally, the reduction slightly increases as the blade loading on the hub grows larger. The striking aspect of the results presented in Figure 42 is that the endwall contouring not only reduced the

secondary flow at turbine design point (3000 rpm) but it also has substantially reduced the intensity of the endwall secondary flow at off-design speeds.

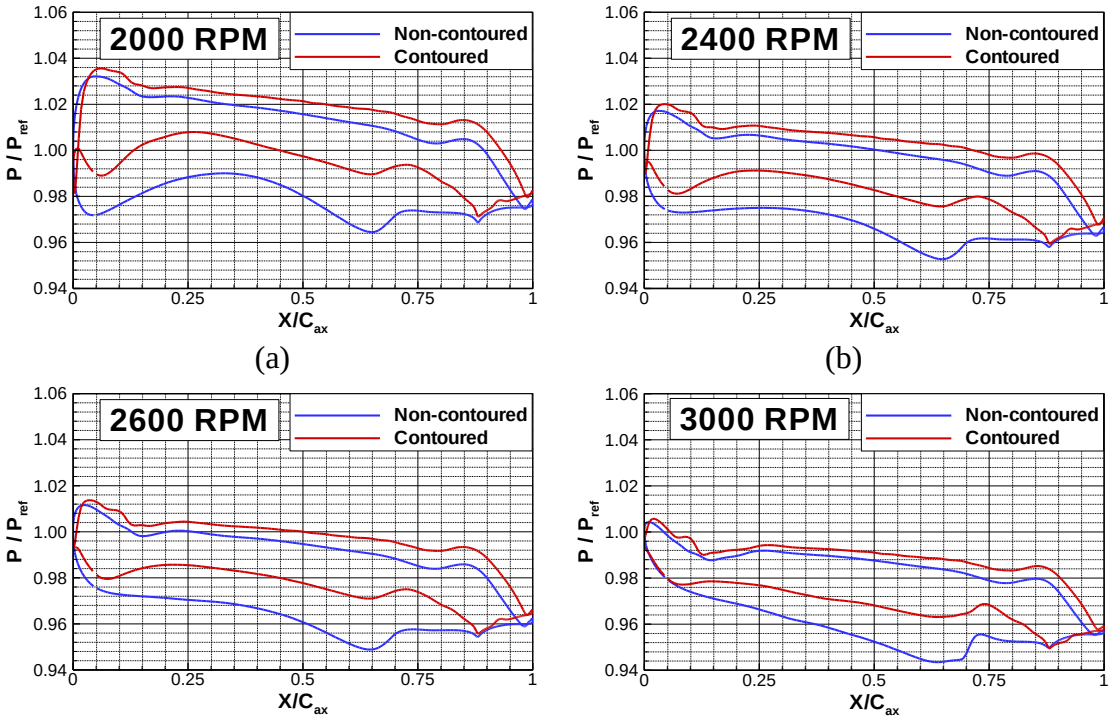

Figure 42: Pressure distributions directly at the hub of second rotor with different rotational speeds: (a) 2000 rpm, (b) 2400 rpm, (c) 2600 rpm and (d) 3000 rpm.

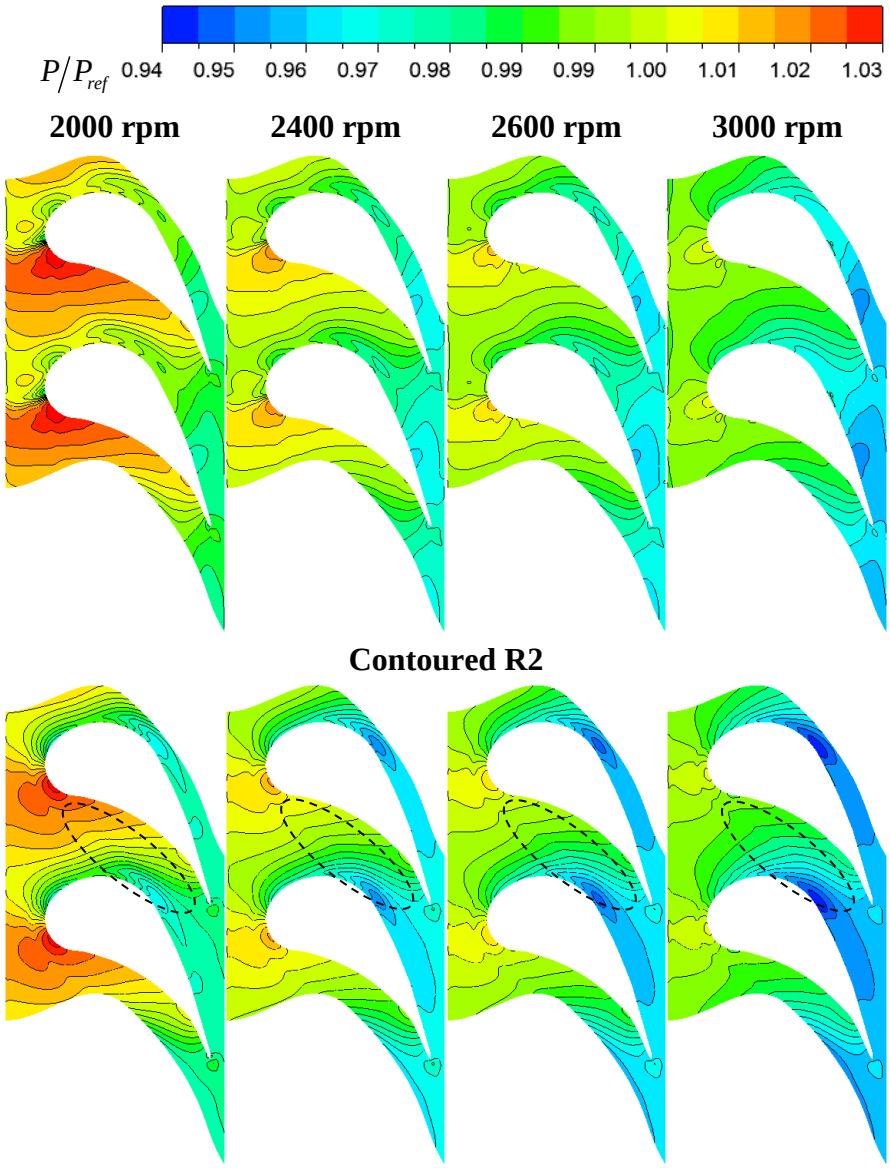

Figure 43: Pressure contours on the hub of second rotor with different rotational speeds.

Figure 43 shows the pressure contour plots on the hub of the second rotor with varying rotational speeds. For the non-contoured case, the minimum pressure is located on the suction surface at around 0.6 C_{ax}. It acts like a sink intensifying the strength of

secondary vortices. However, this point disappears due to the rise of the pressure on the blade suction side with the presence of endwall contouring. In fact, fewer contour lines on the contoured endwall indicate that the pressure gradient has been significantly reduced. This is consistent with the distribution of blade loadings on the hub in Figure 42. Additionally, each contour line has a small bump in the marked areas for non-contoured platform. The distortion of the pressure contour lines reflects the trace of the pressure leg of the horseshoe vortex. However, it is not found on the contoured endwall since the endwall contouring can to some extent suppress the formation of horseshoe vortex, which has been shown in [19]. By looking at the pressure distributions on the hub in Figure 42 and Figure 43, the substantial reduction in pressure gradient regardless of the varied rotational speeds indicates the robustness and effectiveness of the endwall contouring for both design and off-design turbine operation conditions.

The pressure distributions directly at the first rotor hub for four different rotational speeds are plotted in Figure 44. As seen from Figure 44, the endwall contouring for the first rotor is able to significantly reduce the pressure difference between the pressure and suction sides from around 0.25 C_{ax} to 0.8 C_{ax} where in fact the target pressure was put for the contouring design. As introduced in last section, the endwall contouring for the first rotor starts directly from the leading edge to the trailing edge that is not able to extend either upstream or downstream due to the geometric limitations. Therefore the contouring effective range shrinks when compared to the second rotor, especially for the upstream portion. Furthermore, the suction-side pressure is even lower than the non-contoured rotor between the leading edge and nearly 0.2 C_{ax}. This is corresponding to a

low-pressure spot at the suction side close to the blade leading edge as shown in Figure 45. It could be attributed to some slight separation when the incoming mainstream meets with the high deceleration rate at the suction side. Similar to the situation for second rotor, fewer pressure contour lines at the first rotor hub can be seen between the pressure and suction sides, which reflect the reduction in pressure gradient. In addition, based on the originally designed target pressure, it can be concluded that the endwall contouring for the first rotor is effective at both design and off-design rotational speeds.

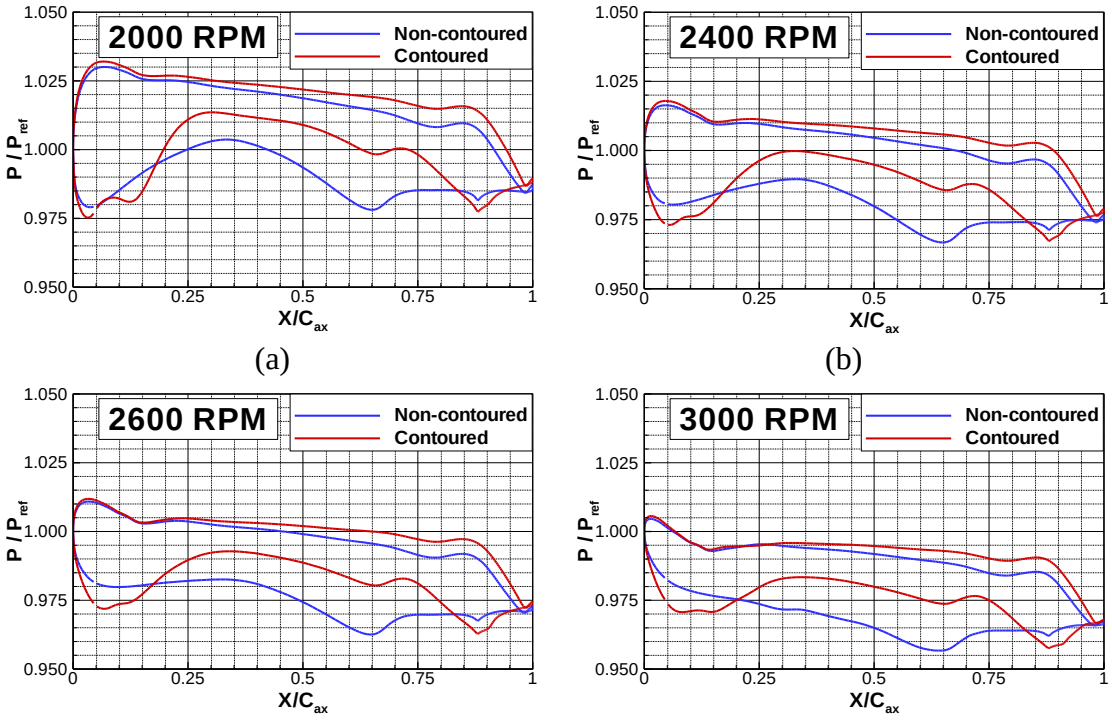

Figure 44: Pressure distributions directly at the hub of first rotor with different rotational speeds: (a) 2000 rpm, (b) 2400 rpm, (c) 2600 rpm and (d) 3000 rpm.

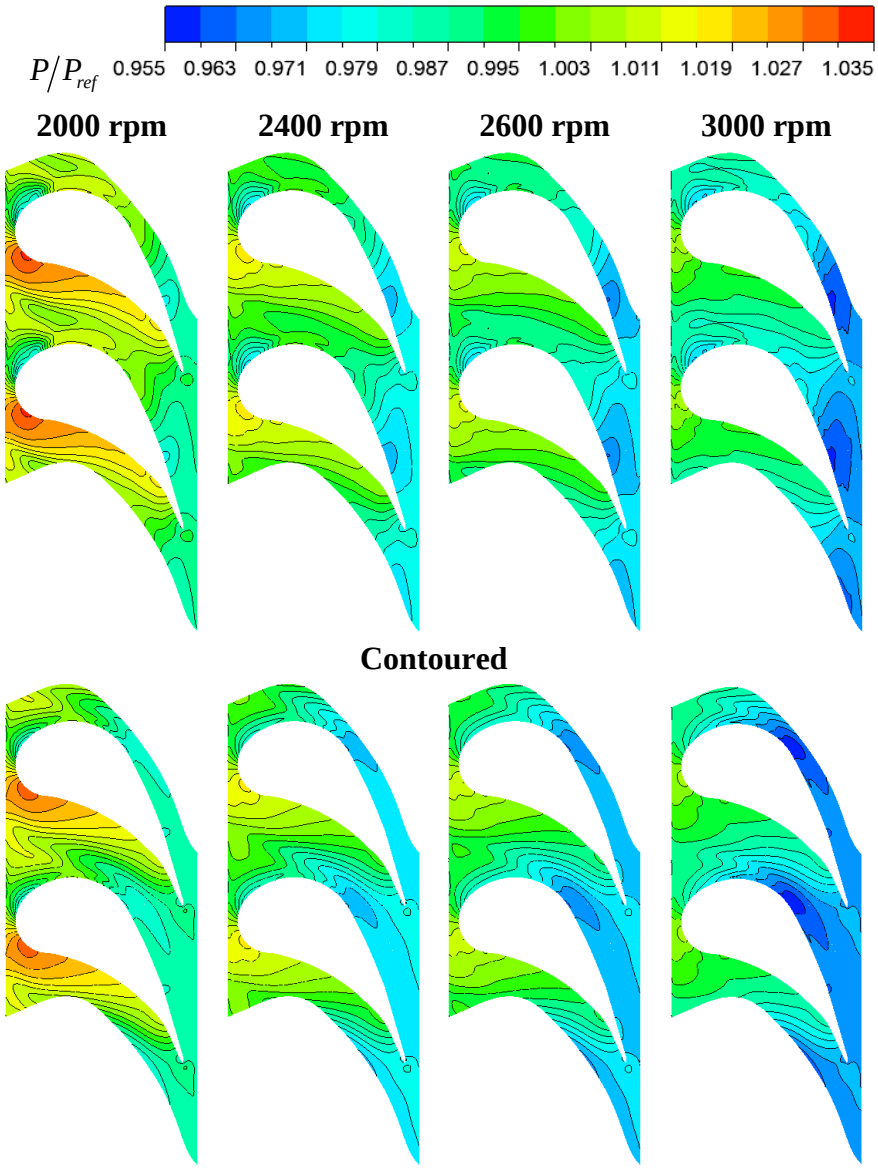

Figure 45: Pressure contours on the hub of first rotor with different rotational speeds.

6.2 Reduction of Secondary Losses

Figure 46 depicts the vorticity distributions at three different axial locations of 0.42, 0.55 and 0.69 C_{ax} for second rotor with the rotational speed of 2400 rpm. For both

contoured and non-contoured cases, the vorticity has similar distributions at each cross-section of the flow passage. High vorticity is seen at the region very close to the endwall near the suction side (I). It also appears in the area closed to the lower portion of the suction surface (II). Very close to the hub, the dominance of the pressure gradient from the pressure to suction surface pushes the fluid particles to the suction surface and produce the highly vortical crossflow. Region I is a result of the movement of the crossflow. The formation of region II is mainly attributed to the mixing of the pressure and suction legs of horseshoe vortex and rolling up of the formed complex vortex systems. As shown in Figure 46, from upstream to downstream, the region I is gradually shrinking whereas the region II is growing fast. Taking a look at the pressure distributions in Figure 43, it is seen that the pressure gradient is pointing from the leading edge to the minimum pressure point, rather than the pitchwise direction. The resulted crossflow follows the direction of the pressure gradient, traveling from the leading edge towards the downstream suction surface. Eventually the fluid particles of crossflow hit the suction surface and are swallowed by the horseshoe vortex systems. Meanwhile, by entraining the low momentum boundary layer and mainstream flow particles, the size of horseshoe vortex system keeps growing when traveling to the downstream. Therefore, a larger area of region II is obtained whereas the magnitude is decreased as approaching downstream. The conservation of the vorticity explains the decline in magnitude but increase in size. At all three axial locations, the level of vorticity is lower for the contoured case compared to the non-contoured one. A smaller

region I is also obtained with the presence of the endwall contouring. Both phenomena reflect the reduction of the secondary flow due to the contoured hub.

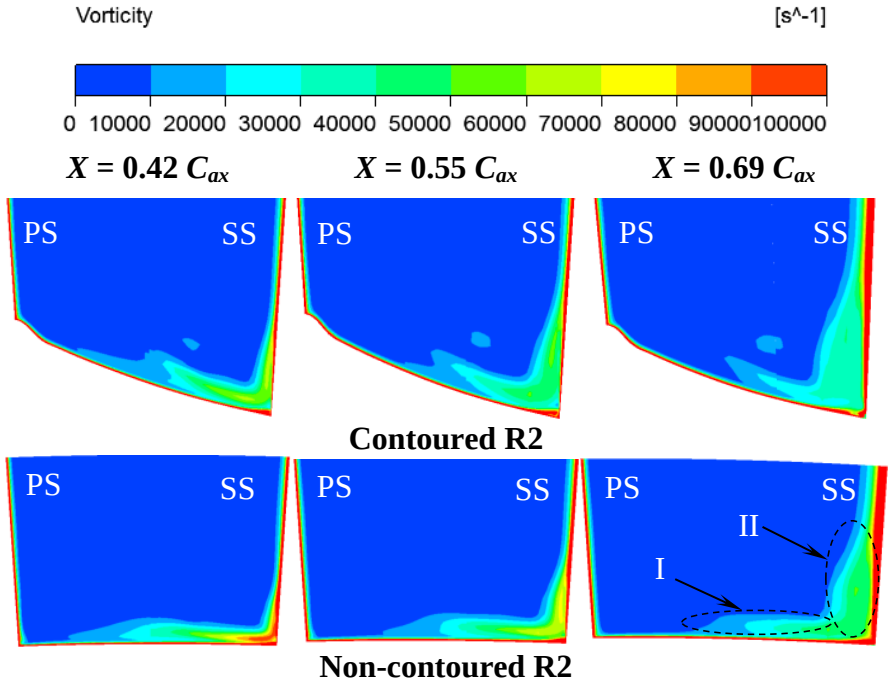

Figure 46: Vorticity distributions at X=0.42, 0.55 and 0.69 C_{ax} of second rotor for 2400 rpm. Region I is a result of the movement of crossflow and region II is mainly attributed to the developing passage vortex system.

The comparisons of the C_{SKE} at 0.55 and 0.69 C_{ax} of second rotor for both contoured and non-contoured cases for 2400 rpm are shown in Figure 47. The distribution of the secondary kinetic energy (SKE) has high similarity with the vorticity contours in Figure 46. For all cases, high-level SKE is obtained in the corresponding regions I and II respectively. As extensively discussed above, the high SKE in region I is generated due to the strong crossflow. The growing horseshoe vortex system contributes to the large SKE in region II. At both cross-sections, the SKE shows smaller magnitude for the

contoured case compared to the non-contoured one. The intensity of the secondary flow near endwall is weakened with the presence of the endwall contouring. Consistent results were obtained for other rotational conditions. Due to the concave shape of the contoured endwall in the pitchwise direction, the local radial velocity W_{rad} tends to be larger than the non-contoured case at the regions close to the endwall, which is accounted for in the SKE calculation. In such circumstance, the resulted larger W_{rad} can be controlled or even eliminated using fully 3D blade design and thus further reduce the production of SKE.

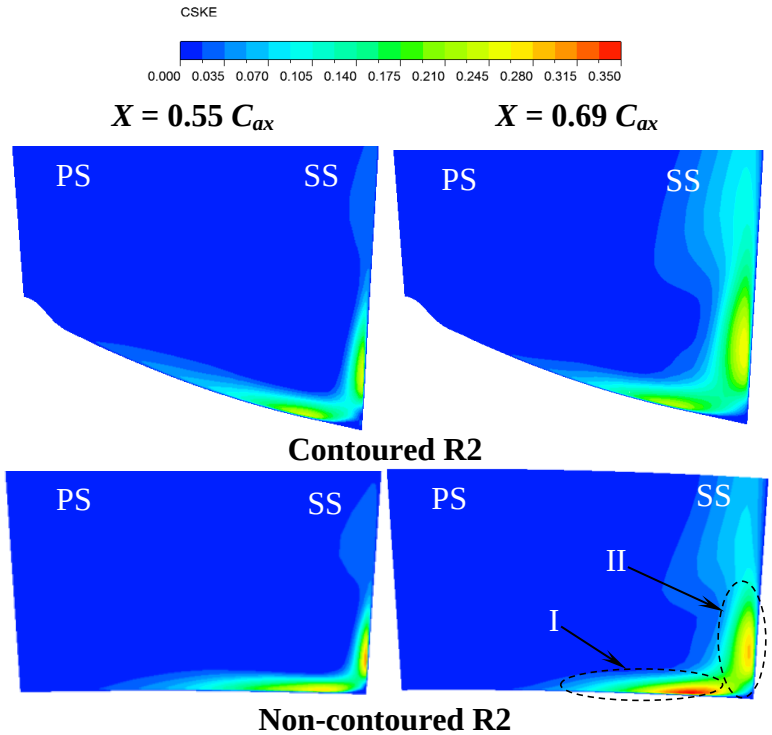

Figure 47: The distributions of C_{SKE} at X=0.55 and 0.69 C_{ax} of contoured and non-contoured second rotor at 2400 rpm. Region I is a result of the movement of crossflow and region II is mainly attributed to the developing passage vortex system.

Figure 48 shows the distributions of the relative total pressure coefficient at the exit of the contoured and non-contoured second rotor for four different operation conditions. This pressure coefficient is a dimensionless variable that reflects the distribution of relative total pressure taking the averaged P_{tr} at the rotor inlet as a reference. As shown, there are three regions with low C_{Ptr} in each contour plot. The lowest region A that is close to the rotor hub is associated to the platform passage vortex system. Region B is also initiated from the development of the passage vortices near the blade tip portion. Region C where the lowest C_{Ptr} occurs reflects the impact of the tip vortices due to the tip leakage flow. As seen, with the increasing rotational speed, the size of region A, B and C gradually shrinks and the local pressure coefficient slightly enhances too. This indicates that higher pressure loss is generated at the off-design operating conditions and the loss is progressively reduced as the rotational speed is approaching to the design point. Apparently the deviation of the incidence angle from the design condition leads to the increased pressure loss. Additionally, it is noteworthy that at each rotational speed, the region A's size for contoured R2 is smaller than the non-contoured case, which is benefited from the reduction of secondary losses due to the endwall contouring. On the contrary, the C_{Ptr} distributions above the mid-span do not show any evident difference between the contoured and non-contoured cases.

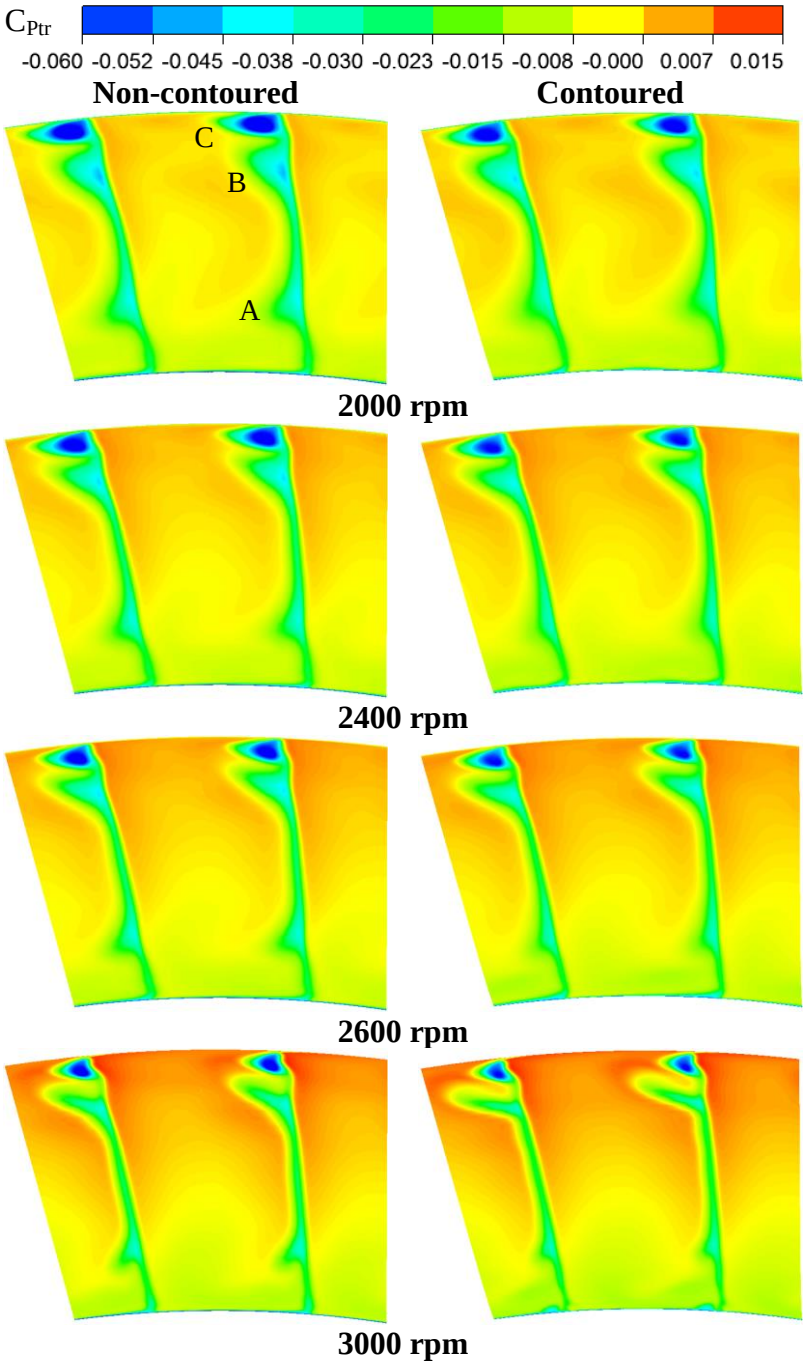

Figure 48: The distributions of relative total pressure coefficient at the exit of non-contoured (left) and contoured (right) second rotor for four different rotational speeds.

Figure 49 shows the pitchwise-averaged loss coefficient for the second rotor at X = 1.07 C_{ax} with varied rotational speeds. The definition of the loss coefficient is based on the relative total pressure that excludes the circumferential component created by rotation. To obtain a better resolution of the total pressure loss near the endwall, the averaged loss coefficient is plotted from the hub (0% span) up to the mid-span (50% span). As seen, for both contoured and non-contoured cases, there are two primary peaks of the total pressure loss in blade spanwise. The first one (i) covers the area from 2% to about 15% of the blade span. It is known that the loss peak i is caused due to the presence of the corner vortex and the movement of low-momentum boundary layer particles. The corner vortex is generated at the corner of the suction surface and the endwall. It travels along the corner creating secondary flow loss in the region very close to the rotor hub. Meanwhile, the endwall boundary layer contributes to the loss balance by shifting up the peak of the loss. Another peak (ii) is able to impact the area from 15% to 40% blade span. The loss peak ii is the largest one and also the primary portion of the endwall secondary losses. Its formation mechanism needs to trace back to the generation of the horseshoe vortex at the blade leading edge. After the generation, the horseshoe vortex is divided into pressure-side and suction-side legs. Due to the pressure gradient in pitchwise, the pressure-side leg travels towards the suction surface whereas the suction-leg stays near the suction surface. Subsequently the pressure-side leg hits the suction surface and mixes with the suction-side leg. They roll up due to the wall effect and entrain the fluid particles from the crossflow and meanstream. The vortex system keeps

traveling downstream and growing. Eventually the passage vortex is formed, which creates substantial secondary flow losses.

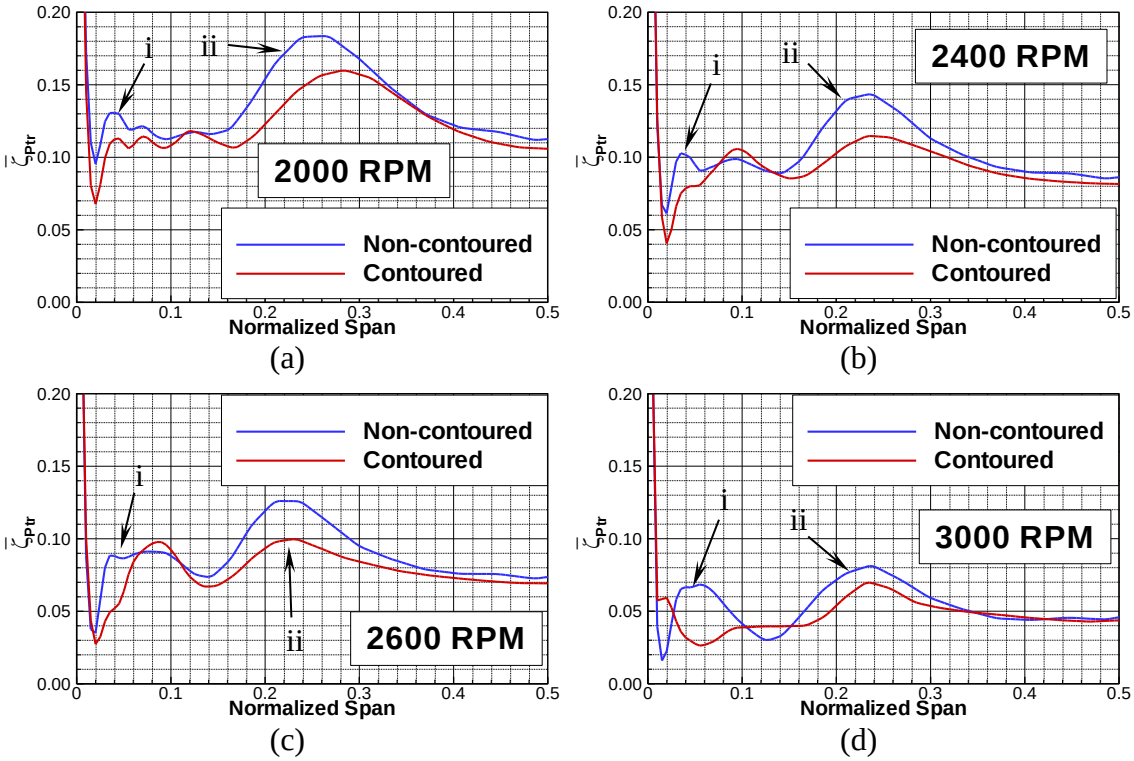

Figure 49: The predicted distributions of relative total pressure loss coefficient of contoured and non-contoured second rotor at different rotational speeds: (a) 2000 rpm, (b) 2400 rpm, (c) 2600 rpm and (d) 3000 rpm.

It is seen that the overall loss grows with the increase of the rotational speed. The lowest total pressure loss level is obtained when the turbine is running at the design point 3000 rpm. The off-design conditions create larger secondary losses mainly due to the change of the incidence angle. For all running conditions, the endwall secondary loss is significantly reduced if the endwall contouring is applied. For the off-design conditions, the reduction of the loss in region i is not as large as the design point. However, dramatic

decline of secondary losses in region ii is gained for all the operating conditions. The substantial drop of the endwall secondary losses reveals the excellent capability of the endwall contouring to control and suppress the strength of the endwall secondary flows. Particularly the off-design conditions get more improvement from the application of endwall contouring.

Figure 50 shows the vorticity distributions at three axial locations of X=0.50, 0.55 and 0.60 C_{ax} of first rotor for 2400 rpm. Likewise, two high-vorticity cores are seen close to the suction surface within the flow passage. The core I is much larger than core II in size. It indicates that the pressure-side leg of horseshoe vortex is stronger to affect more area. As seen, at all three axial locations the core I obtains lower vorticity for the contoured R1 which reflects the reduction in strength of pressure-side leg of horseshoe vortex. Moreover, the pressure-side leg seems to almost lift off from the hub with the presence of endwall contouring. However it still attaches to the flat endwall and interacts with the low-momentum boundary layer, which would generate more secondary losses. The core II is a bit stronger for the contoured R1 than the non-contoured one. It might involve the influence that comes from the slight separation mentioned earlier. Overall, the contouring for R1 is also able to partially reduce the strength of the flow vorticity.

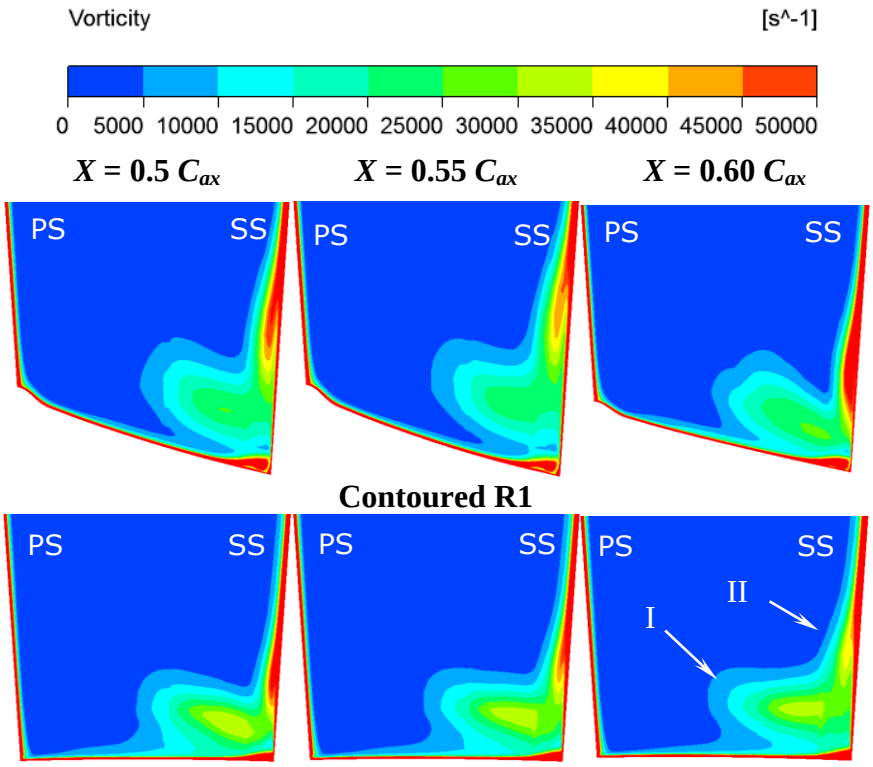

Figure 50: Vorticity distributions at X=0.50, 0.55 and 0.60 C_{ax} of first rotor for 2400 rpm.

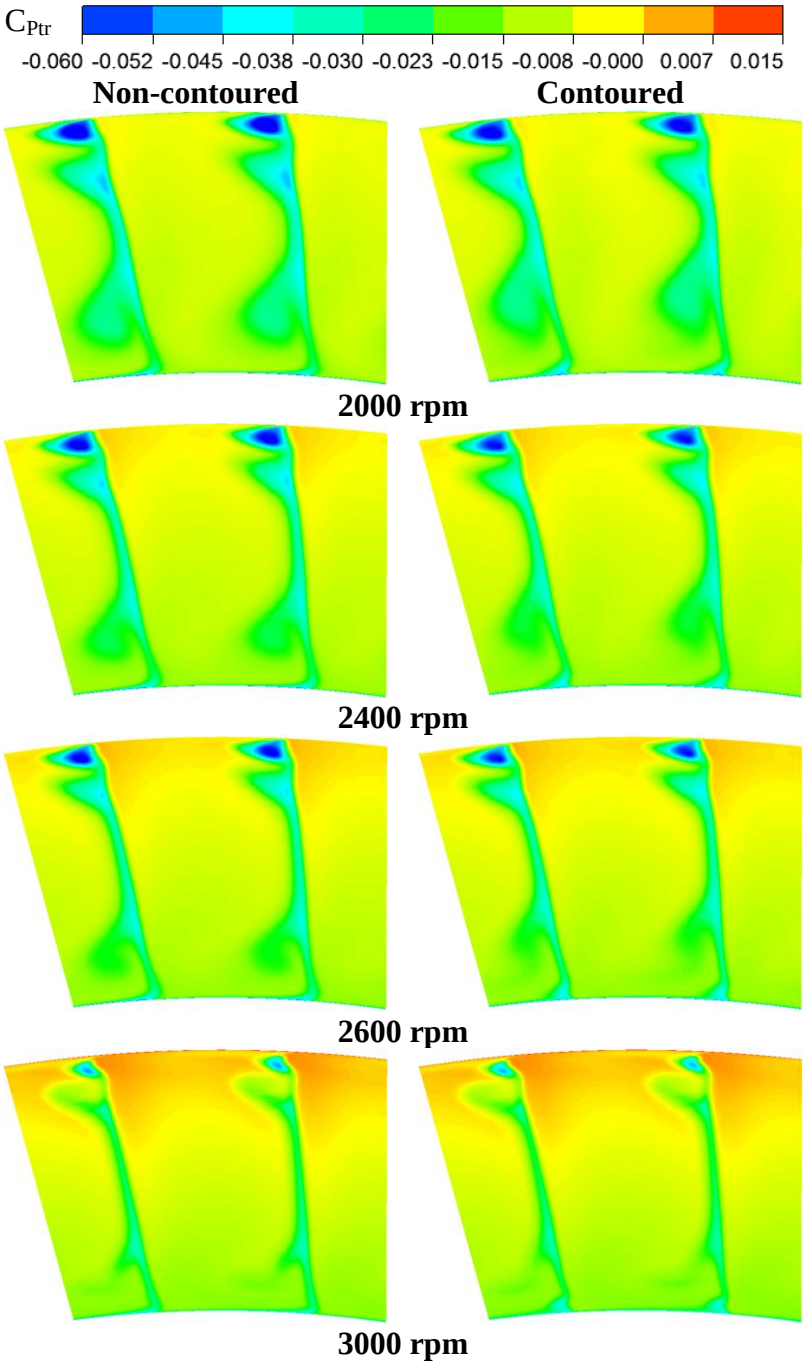

Figure 51: The distributions of relative total pressure coefficient at the exit of non-contoured (left) and contoured (right) first rotor for four different rotational speeds.

Figure 51 depicts the C_{Ptr} contours at the exit of the non-contoured and contoured R1 for four operating conditions. Likewise the reduction in relative total pressure decreases when the rotational speed gradually approaches to the design speed. However, the contoured R1 does not exhibit visible improvement on the pressure drop due to the passage vortices close to hub. This should be attributed to the shortening of the endwall contouring in the streamwise. The distributions of relative total pressure loss coefficient along the R1 spanwise for four different rotational speeds are plotted in Figure 52. As seen, the contoured R1 gains a weaker loss core ii with lower pressure loss coefficient compared to the non-contoured cases with all rotational speeds. Such decline in the primary loss refers to the reduction in the strength of passage vortex system. Similarly, more improvement is observed for the off-design conditions. However, minor loss augmentation for core i is seen for the contoured R1 which might be attributed to the development of corner vortex. Overall, the first rotor with endwall contouring also gains certain reduction in the endwall secondary losses, but not as much as that in R2 due to the limited space for contouring design.

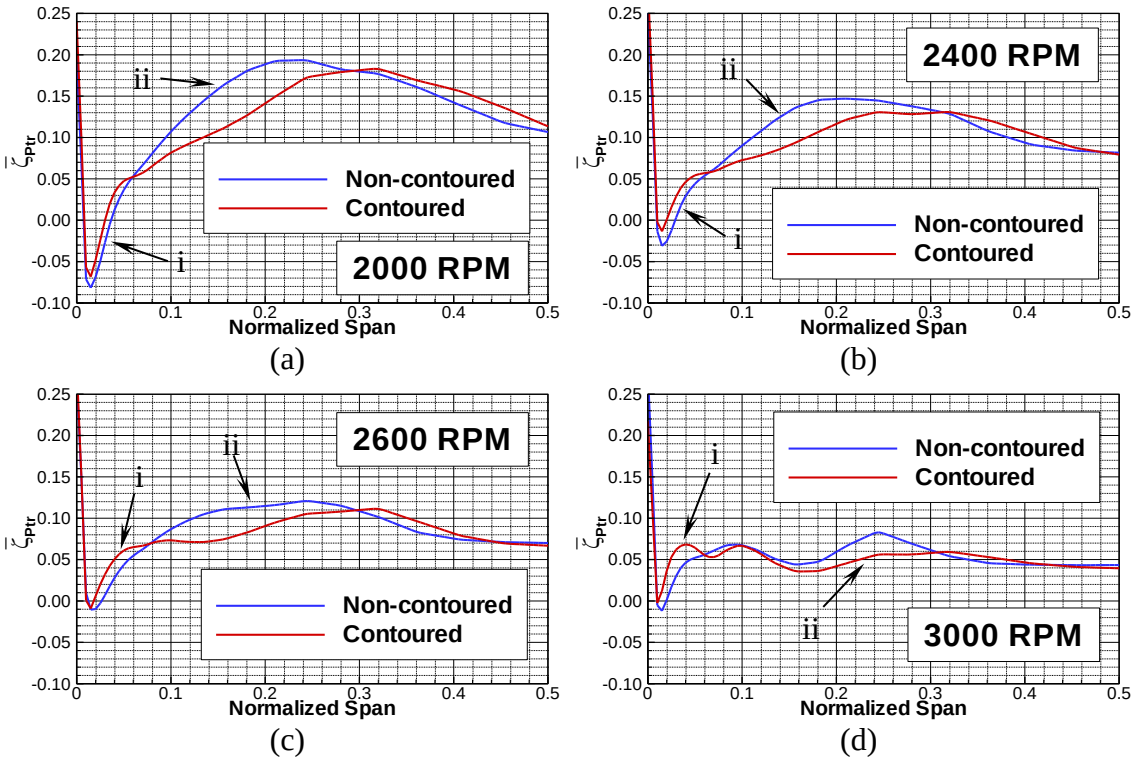

Figure 52: The predicted distributions of relative total pressure loss coefficient of first rotor for different rotational speeds: (a) 2000 rpm, (b) 2400 rpm, (c) 2600 rpm and (d) 3000 rpm.

6.3 Turbine Performance

Figure 53 compares the experimental measurements and the numerical predictions for the performance of the HP turbine with and without endwall contouring. The measured performance curve (red) for contoured turbine is higher than the non-contoured one (black) all the way. More than 1% total-to-static turbine efficiency enhancement is achieved everywhere with the presence of the endwall contouring. In particular, at the point where $u/c_o \approx 0.8$, the highest efficiency for contoured turbine reaches to 89.9%, whereas the non-contoured one obtains 88.86% in total-to-static efficiency. The corresponding turbine efficiency improvement achieves as large as

1.04%, which shows the high effectiveness of the endwall contouring and its great potential in industrial applications. The CFD predictions have the same trend as the experiments that the turbine efficiency grows with the increase in u/c_o where $u/c_o < 0.8$ and starts to drop beyond this point for both contoured and non-contoured turbines. Nevertheless, the CFD over predicts the magnitude of the efficiency for all cases. The correlated deviation varies approximately from 0.2% to 2%. In addition, up to 1% efficiency enhancement for the contoured turbine is obtained by simulations, which is lower than the measured data.

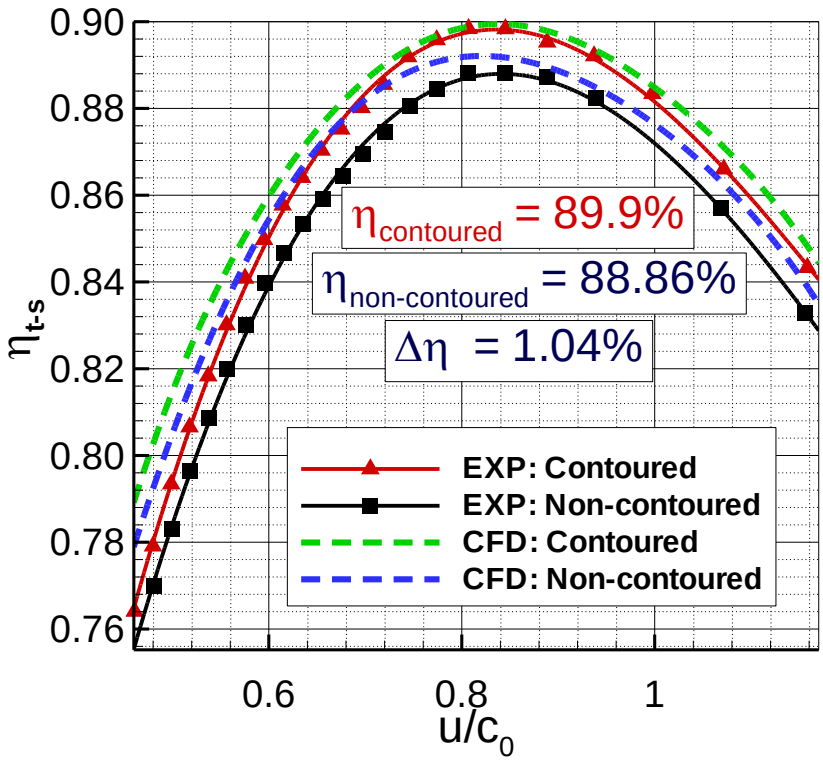

Figure 53: Comparison of performance between contoured and non-contoured turbines.

Since the full inter-stage measurements are not available yet, the detailed comparison of flow parameters is not shown. However, according to the prior TPFL studies [98], the over-prediction of the turbine efficiency can be attributed to shortages of the numerical model. First of all, the mixing planes, will in effect, wash out any upstream wake via circumferential averaging and re-impose this averaged or "mixed out" profile on the subsequent blade row as inlet boundary condition. By doing such pitchwise averaging, the impact of the upstream wakes, secondary flows, turbulence intensity, etc. will be completely eliminated, which to some extent affects the prediction of turbine losses. Secondly, some features such as the stator labyrinth are not included in the computational domain and thus the losses created by the sealing leakage flow are not considered in the efficiency calculations. Speaking of the under-prediction of the efficiency improvement by endwall contouring, it is found in [98] that the discrepancy could be attributed to model deficiencies in predicted secondary flows and secondary flow mixing effects. CFD codes were found to mix out any secondary effects rather rapidly when compared to experimentally observed secondary flow tendencies. This may explain why the predicted efficiency for the non-contoured turbine has larger difference with the experimental data due to the strong secondary flow effect. However, CFD still obtained higher efficiency for the contoured turbine when compared to the non-contoured case and provided useful information in flow behaviors and reduction mechanisms of secondary losses.

7. THE IMPACT OF ENDWALL CONTOURING ON PLATFORM FILM COOLING

Besides the detailed analysis of the impact of endwall contouring on the turbine performance, the TPFL also investigated its influence on the film cooling effectiveness and heat transfer at the first-rotor platform via both measurements and simulations. The film cooling effectiveness on the R1 hub was experimentally obtained by PSP technique which is based on mass transfer analogue, whereas the CFD evaluation was followed the conventional definition taking into account the aerodynamic heating [104].

Figure 54 shows the detailed turbine first-rotor cavity flow by CFD visualization. At the stator-rotor gap, the distributions of pressure, temperature and relative velocity exhibit strong aperiodic features, as seen in Figure 54 (a). At the cross section A-A the maximum pressure point is located upstream at the stagnation line. Similarly, the local pressure near the pressure side is higher than the suction side, which generates certain pressure gradient in the gap along the pitchwise direction. Because of the presence of pressure gradient, the purge flow tends to eject out of the stator-rotor gap asymmetrically rather than uniformly. As a matter of fact, the majority of the coolant particles exits the cavity at higher relative velocity, where it encounters the lower pressure field close to the suction surface. This high velocity field is associated with lower temperature as shown in Figure 54 (a).

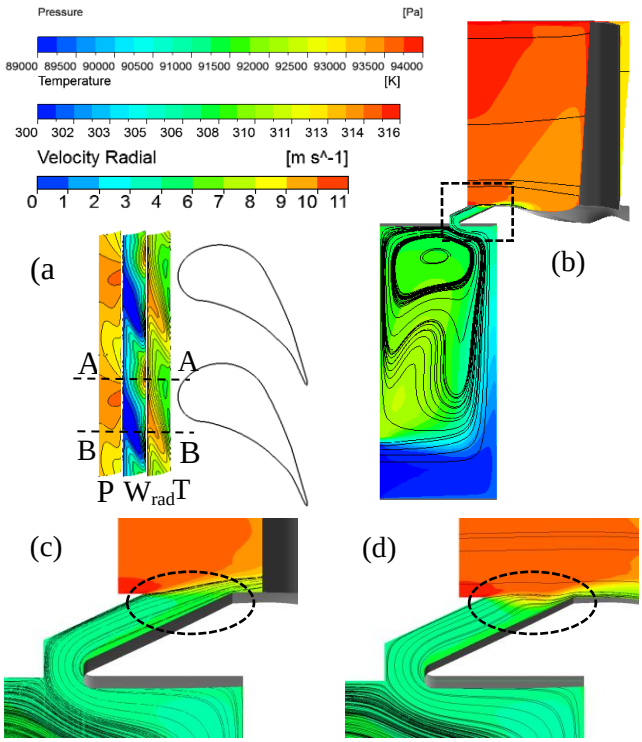

Figure 54: CFD visualized first-rotor cavity flow: (a) Distributions of pressure, radial velocity and temperature at first stator-rotor gap; (b) Streamlines and temperature contours for the cavity flow; (c) Streamlines and temperature contours at A-A cross-section; (d) Streamlines and temperature contours at B-B cross-section.

For better understanding the local flow behavior within the gap, two pitchwise cross-sections are created according to the distributions of radial velocity and temperature, as seen in Figure 54 (c) and (d). Figure 54 (c) depicts the corresponding location where the majority of coolant is ejected out. The surface streamlines reveals the flow activities at this location. As seen, the coolant flow travels along the inclined purge slot and eventually ejects through the stator-rotor gap. The ejected coolant particles penetrate into the mainstream with certain positive radial velocity and the mixing between the mainstream and purge flow takes place primarily out of the gap. However, the purge

flow behaves differently at the cross-section B-B in Figure 54 (d). Due to the resistance created by the local high pressure, the coolant flow can hardly eject trough the slot. A small portion of the mainstream flow from the upstream boundary layer is entrained into the stator-rotor gap, which afterwards mixes with the coolant in the narrow slot. It is seen from the local streamlines, temperature distribution as well as the negative radial velocity (Figure 54 (a)). It is noted that at some particular locations the hot mainstream particles will be swallowed in the slot and directly impinge on the slot surface which is going to form local hot spots and thus lead to risky burnout. In addition, some amount of the mainstream flow particles travel further into the stator-rotor cavity as shown in Figure 54 (b). They participate in the large flow circulation within the cavity due to the relative motion between the high-speed rotating rotor disk and stationary wall. Those hot mainstream particles slightly rise up the cavity flow temperature via the mixing process from the circulation, which to some extent declines the cooling capability of the purged coolant. It should be pointed out that the above discussion is based on the steady RANS calculations. In the real engine condition, the phenomena mentioned above can repeat periodically in both the time and space due to the strong stator-rotor interactions which is highly three-dimensional and unsteady. In such a circumstance, URANS must be run in order to fully capture the unsteadiness.

7.1 Pressure Distributions on the Hub of First Rotor

7.1.1 The impact of MFR

Figure 55 and Figure 56 shows the predicted pressure distribution on the first-rotor hub rotating at 3000 rpm with three different MFRs respectively. It is seen from Figure

55, the endwall contouring is able to effectively reduce the pressure difference between the pressure and suction sides within the range of 0.25 C_{ax} and 0.75 C_{ax} for all MFRs. Accordingly much less contour lines are obtained at the contoured endwall as shown in Figure 56. Except the difference caused by the contoured endwall surface, the variation in purge MFR does not generate any noticeable impact on the pressure field at the R1 hub. However, due to the presence of purge flow, the stagnation point moves from the pressure side to the leading edge shown in Figure 56. As a results, the pressure difference between the leading edge and around 0.1 C_{ax} drops to almost zero (Figure 55) due to the symmetric pressure distribution from the leading edge (Figure 56). This could be attributed to the alteration of the incidence angle close to the hub due to the interactions between the purge flow and the upstream boundary layer.

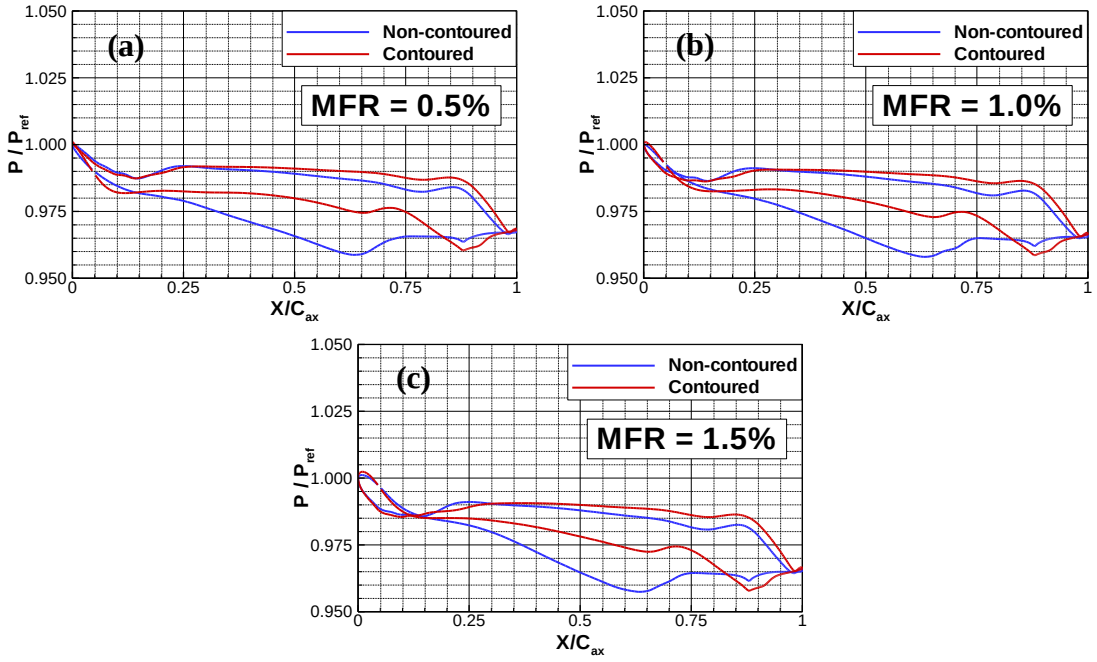

Figure 55: Predicted pressure distributions directly at the hub of first rotor at 3000 rpm with different MFRs: (a) MFR = 0.5%, (b) MFR = 1.0% and (c) MFR = 1.5%.

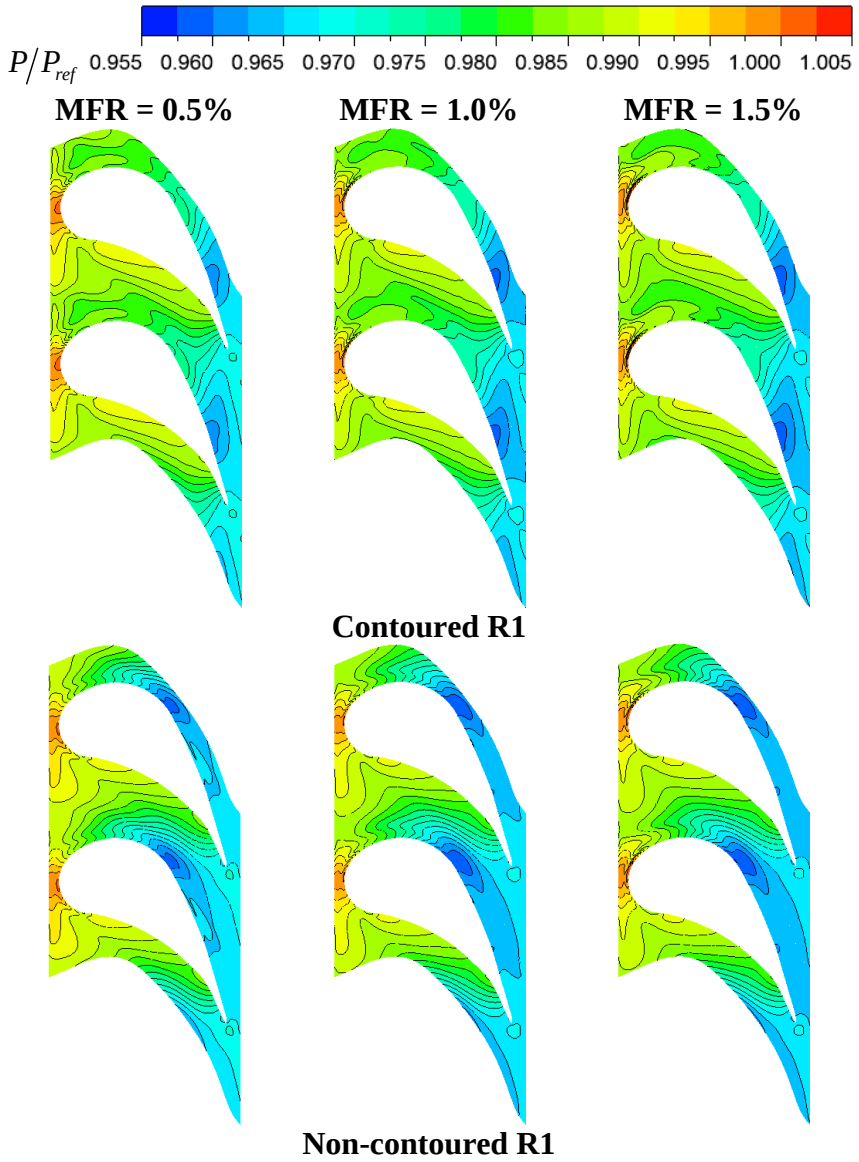

Figure 56: Predicted pressure contours on the hub of first rotor at 3000 rpm with different MFRs.

7.1.2 The impact of rotational speed

The impact of rotational speed on the pressure distribution at the R1 hub with 1% of purge flow is shown in Figure 57 and Figure 58. As seen in Figure 57, substantial ΔP reduction is observed within the area between 0.25 C_{ax} and 0.75 C_{ax} for contoured R1 at

both design and off-design conditions. In other words, the endwall contouring exposed to the purge flow is still working properly although the rotational speed alters. It is noticed that the ΔP appears again around the leading edge at the off-design conditions for both contoured and non-contoured R1. Lower rotational speed corresponds to greater ΔP which is associated with the shift of the stagnation point. This reflects the pure rotation effect on the pressure distribution. However, the ΔP is not as huge as that in the figure on page 88 due to the presence of the purged coolant. Therefore, the alteration of the rotational speed is capable to affect the location of stagnation point and its surrounding pressure field but has little impact on the function of the endwall contouring.

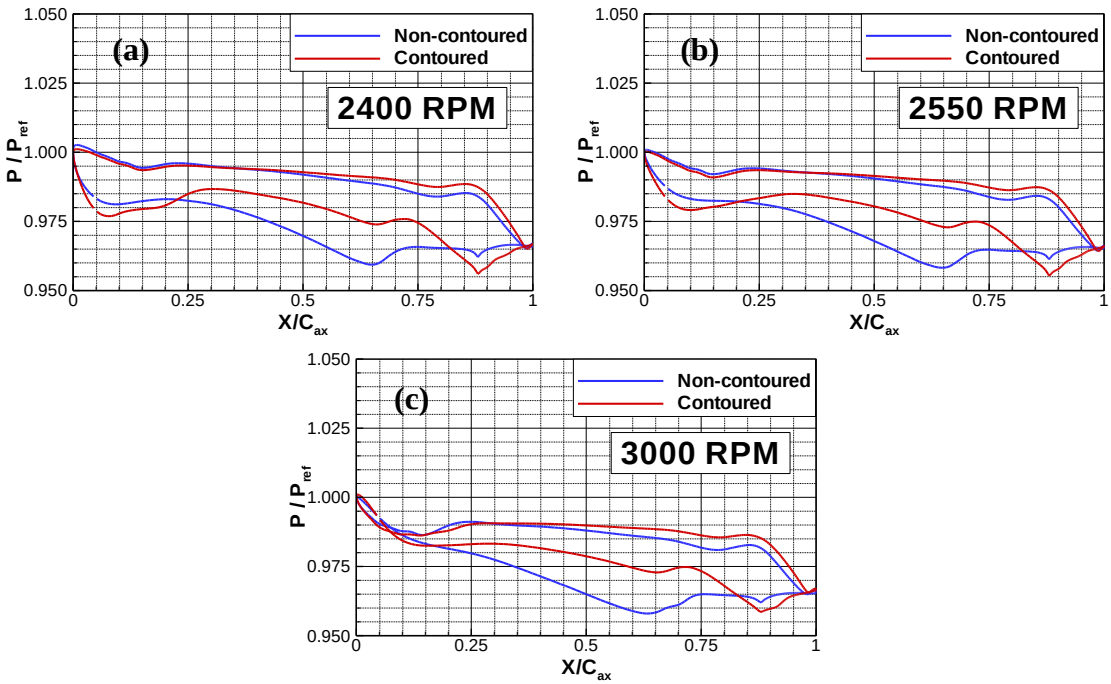

Figure 57: Predicted pressure distributions directly at the hub of first rotor with MFR = 1.0% for three different rotational speeds: (a) 2400 rpm, (b) 2550 rpm and (c) 3000 rpm.

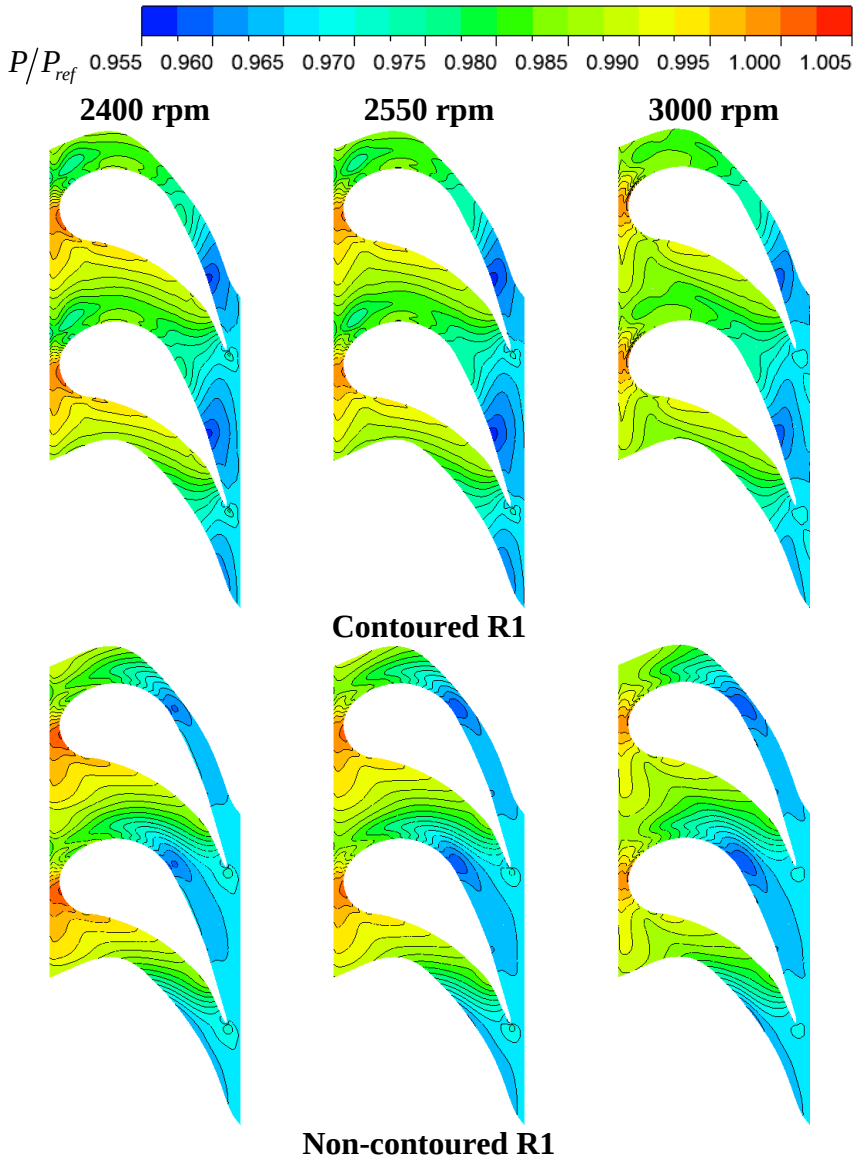

Figure 58: Predicted pressure contours on the hub of first rotor at MFR = 1.0% with different rotational speeds.

7.2 Adiabatic Film Cooling Effectiveness on the Hub of First Rotor

7.2.1 The impact of MFR

Figure 59 shows the impact of the MFR or blowing ratio on the adiabatic film cooling effectiveness on both the contoured and non-contoured rotating first rotor hub

with fixed rotational speed of 3000 rpm. Also the CFD predictions are compared with the experimental results. The comparisons for three different MFRs of 0.5%, 1.0% and 1.5%, which are corresponding to blowing ratios M = 0.12, 0.24 and 0.36, are shown. For both contoured and non-contoured cases, larger MFRs give more cooling mass as well as higher coolant momentum. As a result, more coolant particles are capable to penetrate into the highly vortical secondary flow region near the endwall and thus travel further downstream, which usually provides higher film cooling effectiveness. However, if the blowing ratio is too high, the coolant tends to shoot into the mainstream rather than stay close to the endwall, which does not necessarily provide good protection for the hub surface. In this study, the blowing ratio is less than unity and therefore both the measurements and predictions show an enhancement in film cooling effectiveness on the platform with increasing MFR or M.

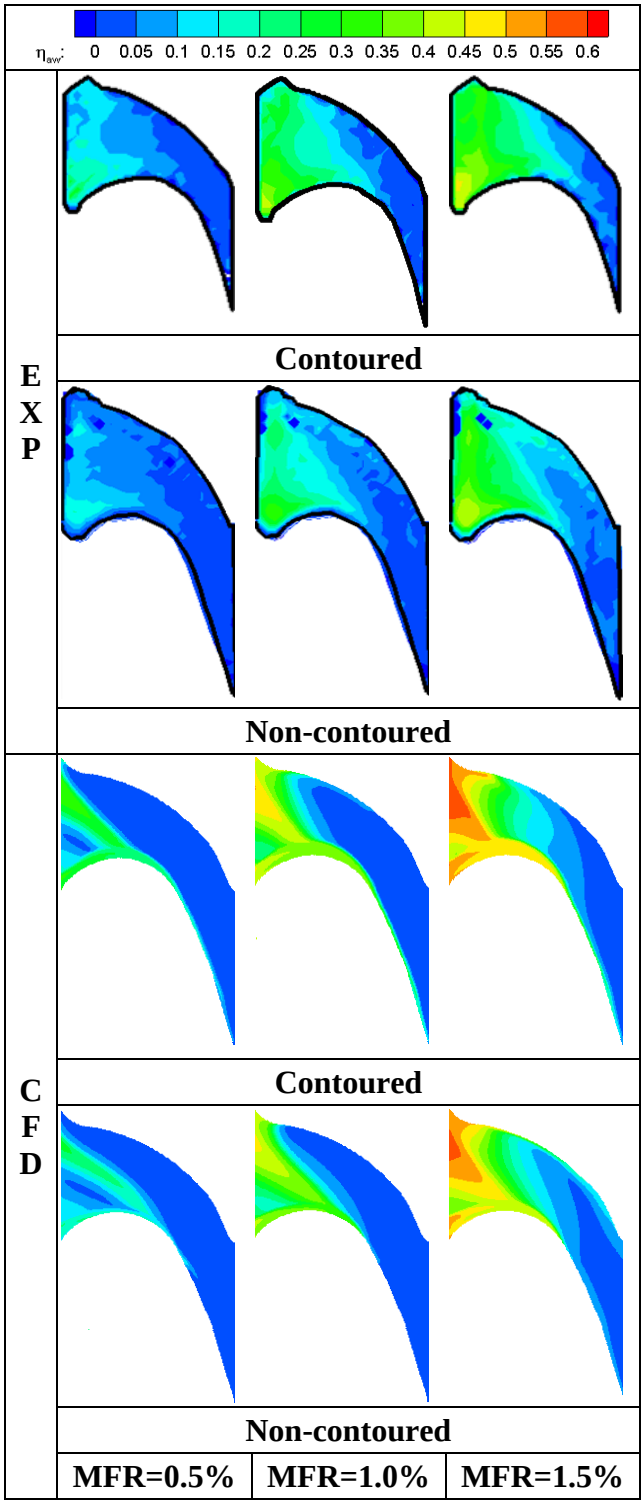

Figure 59: Comparison of measured (EXP) and predicted (CFD) film cooling effectiveness distributions on the contoured and non-contoured rotating first-rotor platforms with different MFRs at 3000 rpm.

Looking at the contour plots of the film cooling effectiveness obtained by the experiments, the endwall contouring delivers better film cooling protection than the non-contoured platform for all MFRs. As seen in Figure 59, for non-contoured cases, relatively high cooling effectiveness is obtained near the leading edge on suction side since more coolant is ejected out in this region due to the pressure distribution within the stator-rotor gap (as discussed earlier). The coolant particles can travel along the suction side from approximately 0.25 C_{ax} up to 0.5 C_{ax} with varying MFRs. However, the coverage of the cooling film decreases fast from the suction side to the pressure side. The surface near the pressure side can hardly be cooled for MFR = 0.5% and 1.0%. It becomes better when the MFR increases to 1.5% since more coolant is ejected. Still the film cooling effectiveness fades rapidly long the pressure side which resulting a triangular area covered by the cooling film. This triangular-shape area is formed due to the strong secondary flow system. The large pressure gradient between the pressure- and suction-side pushes the pressure-side leg horseshoe vortex and the crossflow from the pressure side to the suction surface. These secondary flows entrain the coolant film and take the coolant particles to travel laterally. Therefore the pressure side is much less cooled.

In contrast, more coolant particles travel along the pressure side and much larger traveling distance is obtained when the endwall contouring is used. As a result the cooling film covers more platform surface than the non-contoured case. Particularly the region covered by the coolant for MFR = 1.0% and 1.5% transforms from the triangular shape to trapezoidal shape. Additionally the effectiveness distribution is more uniform in

the pitchwise direction as well. Apparently the improvement of the film cooling is benefited from the presence of the endwall contouring. Since the contouring is able to largely decrease the pressure difference between the pressure- and suction-side and to some extent suppress the horseshoe vortex, the strength of the secondary flow is significantly weakened. Therefore the coolant can travel along the streamwise with much less interference by the secondary flow and thus spread more uniformly on the hub surface.

The CFD predictions also show that the coolant particles can travel to further downstream along the pressure side if the endwall contouring is utilized, especially for MFR = 1.0% and 1.5%. Meanwhile the coolant coverage along the streamwise tends to be more uniform with the presence of the endwall contouring. Both indicate that the film cooling has improved. However when compared to the experiments, both the effectiveness distribution and the magnitude show considerable difference. Unlike the contour plots for experiment, it seems that the majority of the coolant exits from the gap portion near the pressure side rather than the suction side.

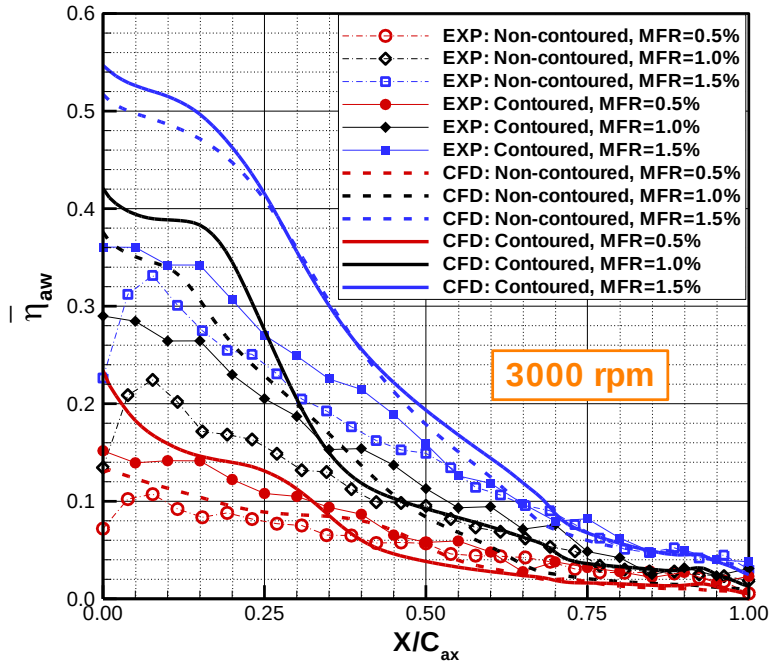

Figure 60: Pitchwise-averaged film cooling effectiveness distributions (experiment and CFD) on both contoured and non-contoured rotating first-rotor platforms with different MFRs at 3000 rpm.

The pitchwise-averaged film cooling effectiveness of both contoured and non-contoured platform for first rotor with different MFRs is plotted in Figure 60. Apparently increasing the MFR leads to the growth of cooling effectiveness magnitude for all cases. However, the averaged plots show a rapid decrease in effectiveness magnitude for the region beyond 0.6 C_{ax} remaining mostly uncovered with average effectiveness magnitudes below 0.1. Noticeably, the endwall contouring exhibits superiority in improving film cooling on platform for all studied MFRs. The observed improvement extend up to 0.6 C_{ax} for measured data whereas approximately 0.4 C_{ax} for predicted values. Hence, CFD has under-predicted coolant film coverage as discussed

earlier. However, effectiveness is over-predicted compared to the measurements. Up to 50% higher effectiveness can be seen from the leading edge to 0.25 C_{ax}.

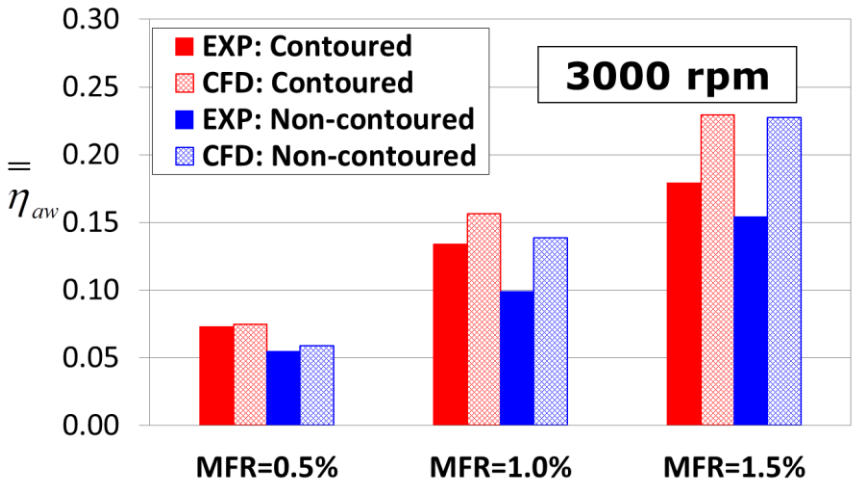

Figure 61: Area-averaged film cooling effectiveness distributions (experiment and CFD) on both contoured and non-contoured rotating first-rotor platforms with different MFRs at 3000 rpm.

The impact of MFR on area-averaged cooling effectiveness can be found in Figure 61. As seen, the measured overall effectiveness monotonically declines with decreasing MFR. At all MFRs, the endwall contouring delivers higher overall cooling effectiveness than non-contoured platform for both experimental tests and CFD predictions. The endwall contouring achieves its highest cooling performance with 1.5% coolant ejected at a rotational speed of 3000 rpm. Looking at the averaged values, it is noted that CFD is capable of providing consistent tendency with measurements. However, CFD tends to over-predict the magnitude for all different MFRs but the accuracy is still in the acceptable range.

7.2.2 The impact of rotational speed

The effect of rotation on the first-rotor platform film cooling is shown in Figure 62. This study deals with three different rotational speeds of 2400 rpm, 2550 rpm and 3000 rpm with the fixed MFR = 1.0%. Generally, when the turbine is running under off-design conditions with lower rotational speeds compared to design speed, the flow deflection becomes larger. As a result, the stagnation point moves towards the blade pressure side forming a higher pressure zone along the pressure side. The direct consequence is an increase in pressure gradient between the pressure- and suction-side on the endwall. Accordingly the strength of the secondary flow system grows due to the stronger driving force. The high pressure gradient further pushes the incoming cooling film away from the pressure side to the suction side once it exits from the stator-rotor gap. Hence, at the lower rotational speeds, the film coverage and thus, the film cooling effectiveness will be partially reduced. This is evidently seen from the experimental results in Figure 62 that the coolant covered area gradually shrinks and the effectiveness magnitude slightly declines as the rotational speed drops from 3000 rpm to 2400 rpm.

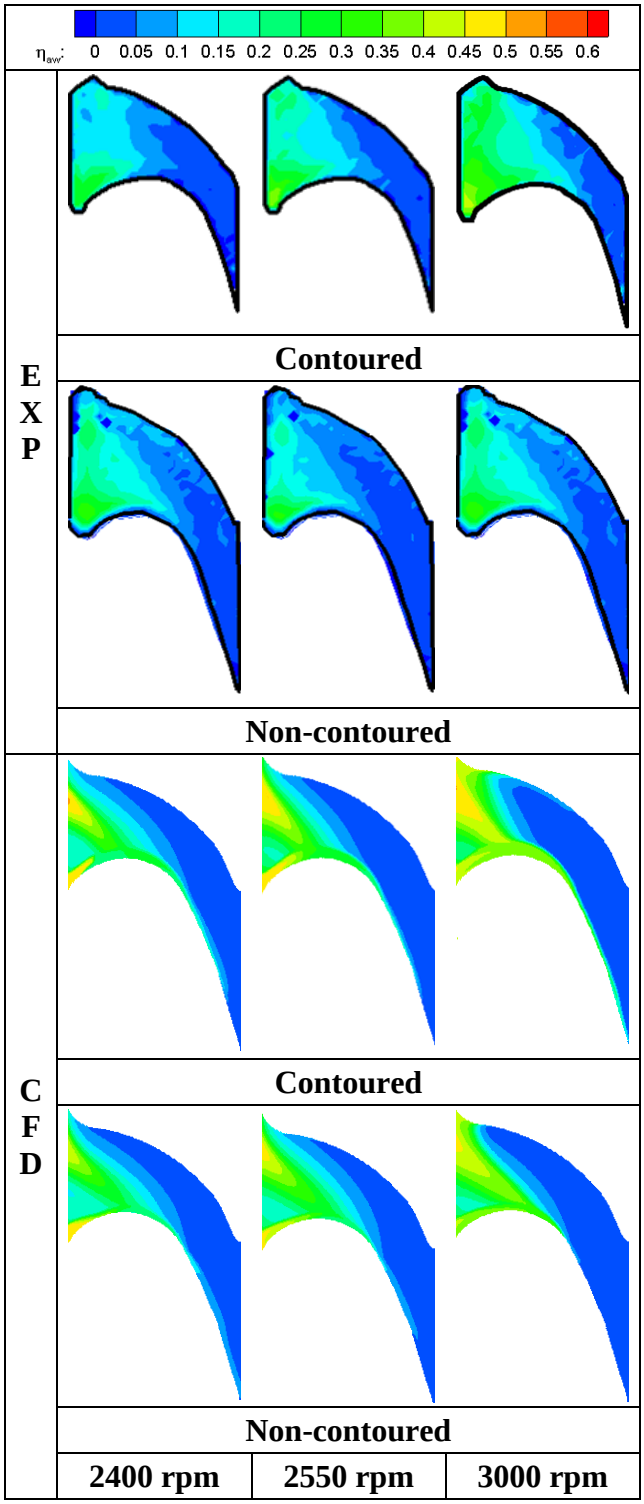

Figure 62: Comparison of measured (EXP) and predicted (CFD) film cooling effectiveness distributions on the contoured and non-contoured rotating first-rotor platform at different rotational speeds with MFR = 1.0%.

Nevertheless, even though the effectiveness of the film cooling tends to reduce by lowering down the turbine rotational speed, the contoured platform obtains better film cooling than non-contoured hub for all tested off-design conditions. In other words, the presence of the endwall contouring is able to partly compensate the reduced cooling effectiveness due to the off-design deviations and therefore reduce the potential risk of platform burnout. It also implies that the cooling mass can be to some extent reduced, which enhances the turbine aerodynamic performance associated with lower cooling mass flow.

The CFD simulations also show the tendency that the distribution of the cooling effectiveness shifts from the pressure side to the suction side for both contoured and non-contoured rotor platforms as lowering the rotational speed. However, it seems that the predicted effectiveness is less sensitive to the rotational speed of 2400 rpm and 2550 rpm. Only slight shrink in the covered area is observed when the rotating speed switches from 2550 rpm to 2400 rpm. In addition, the predicted film coverage on the contoured platform merely shows marginable improvement compared to the non-contoured case under lower rotation speeds.

Figure 63 depicts the impact of the rotational speeds on the pitchwise-averaged film cooling effectiveness on the first rotor platform. The plots compare both the experiments and CFD for contoured and non-contoured hub with 1.0% of the coolant ejected at different rotational speeds. The averaged effectiveness grows with the increasing turbine rotational speed for both experiments and CFD. However, in the tested speed range, the cooling effectiveness is not as sensitive to the rotating speed as to the MFR or blowing

ratio. As expected, the presence of endwall contouring significantly boosts the measured film cooling effectiveness up to a percentage of 100% for the first half axial chord. Similarly, the predicted cooling effectiveness on contoured hub decays more rapidly so that the benefit vanishes at about 0.35 C_{ax}. Moreover, over-prediction in the effectiveness magnitude appears for all studied rotational speeds.

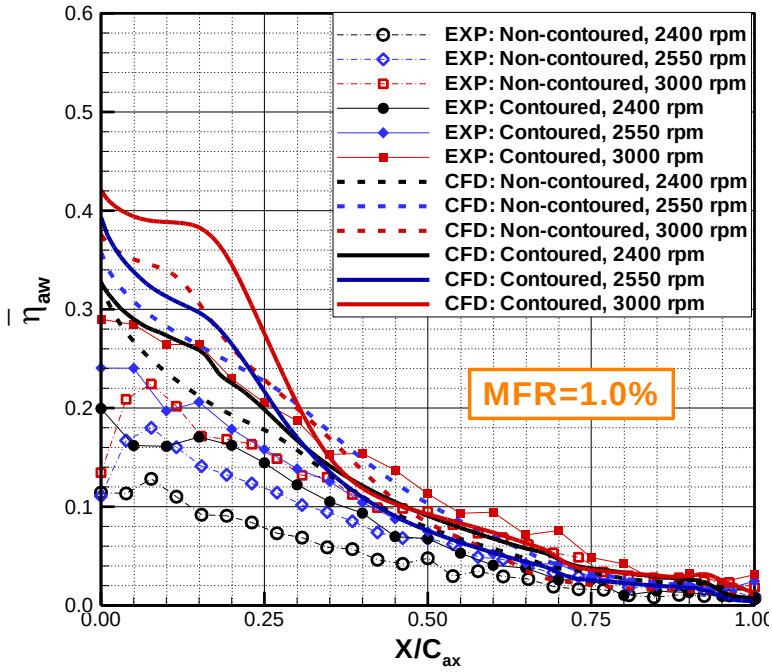

Figure 63: Pitchwise-averaged film cooling effectiveness distributions (experiment and CFD) of both contoured and non-contoured rotating first-rotor platform at different rotational speeds with MFR = 1.0%.

The impact of rotational speed on area-averaged cooling effectiveness is shown in Figure 64. As seen, the measured overall effectiveness monotonically grows with increasing rotational speed. The experimental data show that endwall contouring delivers higher overall cooling effectiveness than non-contoured platform for all rotating

conditions. The endwall contouring achieves its highest cooling performance with 1.0% coolant ejected at a rotational speed of 3000 rpm. The CFD is able to deliver similar trend with the experiments when studying the rotation effect on contoured endwall, nevertheless fails for non-contoured case.

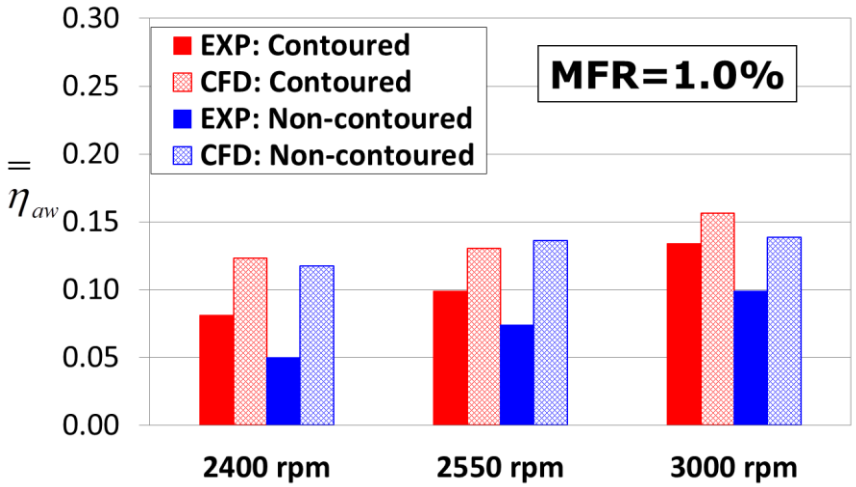

Figure 64: Area-averaged film cooling effectiveness distributions (experiment and CFD) of both contoured and non-contoured rotating first-rotor platform at different rotational speeds with MFR = 1.0%.

7.3 Heat Transfer on the Hub of First Rotor

7.3.1 The impact of MFR

Figure 65 shows the distribution of computed Nusselt number on the contoured and non-contoured R1 platforms with varied MFRs at 3000 rpm. As seen, for both the contoured and non-contoured R1, the highest Nu is obtained at the leading edge since the local boundary layer is very thin and accordingly strong heat transfer occurs here. A delta-like area with high Nu can be seen starting from the stator-rotor gap edge and

extending downstream. This area in fact is not covered by the purge flow and thus directly exposed to the mainstream. The attachment of mainstream flow raises the local Nusselt number. However, the magnitude of Nu gradually decreases along downstream because the boundary layer thickness grows as the boundary layer develops. In its downstream there are two streaks with low Nu. One starts from the leading edge and extends downstream along the suction side whereas the other one points from the pressure side to the suction surface. These two streaks should be associated with the separation lines caused by the pressure- and suction-side legs of horseshoe vortex respectively. As the MFR increases, the momentum of purge flow to some extent grows too and therefore more or less weakens the impact of horseshoe vortex on the formation of separation lines. As a result, the local Nu slightly enhances with increasing MFR. Right in the further downstream passage, a streak with high Nu is seen extending from pressure side to the suction side of the non-contoured platform. The high Nu is due to the passing of the pressure-side leg of horseshoe vortex. However, such streak disappears on the contoured R1 hub. Firstly, the substantial reduction of pressure gradient between the pressure side and suction side is able to weaken the strength of secondary flow. Secondly, the contoured surface has concave curvature that keeps diffusing when approaching downstream passage and consequently the pressure-side leg of horseshoe vortex detaches the platform while travelling downstream. Accordingly, no obvious high Nu due to the horseshoe vortex occurs at the contoured platform. Relatively high Nu occupies the rear portion of the passage since the flow keeps accelerating downstream.

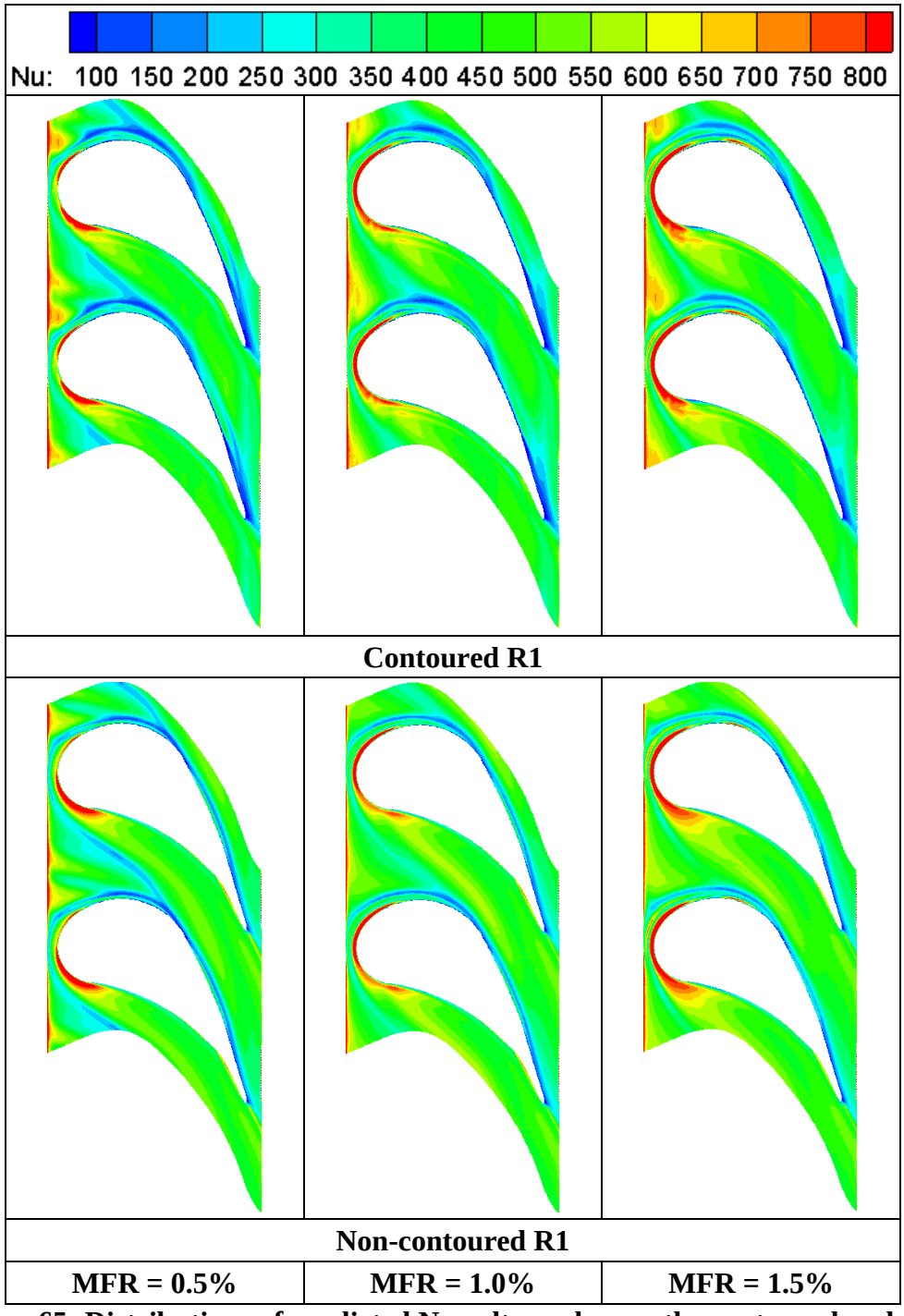

Figure 65: Distributions of predicted Nusselt number on the contoured and non-contoured first-rotor platforms with different MFRs at 3000 rpm.

The impact of MFR on the predicted pitchwise-averaged Nusselt number for both the contoured and non-contoured R1 is illustrated in Figure 66. As seen, the averaged Nu between the leading edge and 0.7 C_{ax} increases as the MFR grows. It is easy to understand that higher MFR refers to larger purge flow momentum and thus greater local Nusselt number. Therefore the impact of MFR on Nu retains till 0.7 C_{ax}. For the non-contoured endwall with MFR = 0.5%, the Nu keeps dropping from the leading edge until 0.5 C_{ax} and then increases till the point 0.75 C_{ax}. It gradually decreases again until the trailing edge. At MFR = 1.0%, the magnitude of averaged Nu maintains almost a constant between 0.2 C_{ax} and 0.75 C_{ax}. However the Nu keeps going down when MFR increases to 1.5%. The difference should be attributed to the augmentation in the purge flow momentum. The Nu distribution exhibits distinct features for the contoured endwall. From the leading edge to about 0.18 C_{ax}, the averaged Nu drops very fast due to the high deceleration rate. Between 0.18 C_{ax} and 0.7 C_{ax}, the averaged Nu is always lower than the non-contoured R1 due to the continuous deceleration. Then the Nu is enhanced between 0.7 C_{ax} and 0.9 C_{ax} because of the contraction of the flow passage. Slight separation at the suction side close to the trailing edge lowers down the Nu from 0.9 C_{ax} to trailing edge. Overall, smaller Nu is obtained at most portion of the contoured endwall with a fixed amount of purge flow. Figure 67 summarizes the impact of MFR on the area-averaged Nusselt number on both the contoured and non-contoured first-rotor platform at 3000 rpm. As seen the overall Nu monotonically increases as the MFR grows for both the contoured and non-contoured endwall. At all MFRs, the overall Nu at the contoured R1 hub is approximately 4.5 ~ 5.5% lower than that for the non-contoured

platform. Hence, the endwall contouring is able to partially reduce the Nu at the first-rotor hub for up to 1.5% purge flow.

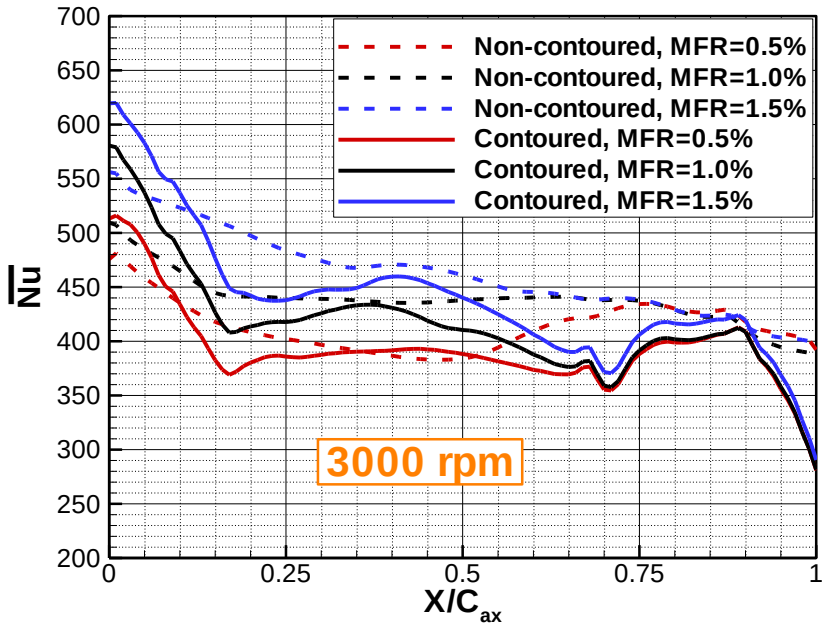

Figure 66: Predicted pitchwise-averaged Nusselt number on both contoured and non-contoured first-rotor platforms with different MFRs at 3000 rpm.

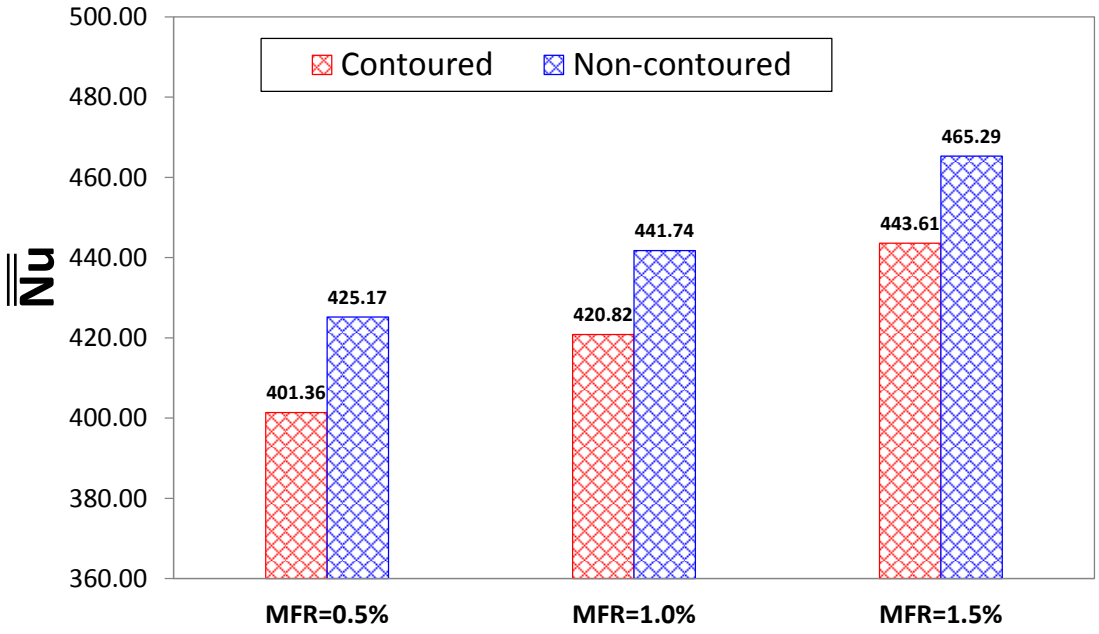

Figure 67: Predicted area-averaged Nusselt number on both contoured and non-contoured first-rotor platforms with different MFRs at 3000 rpm.

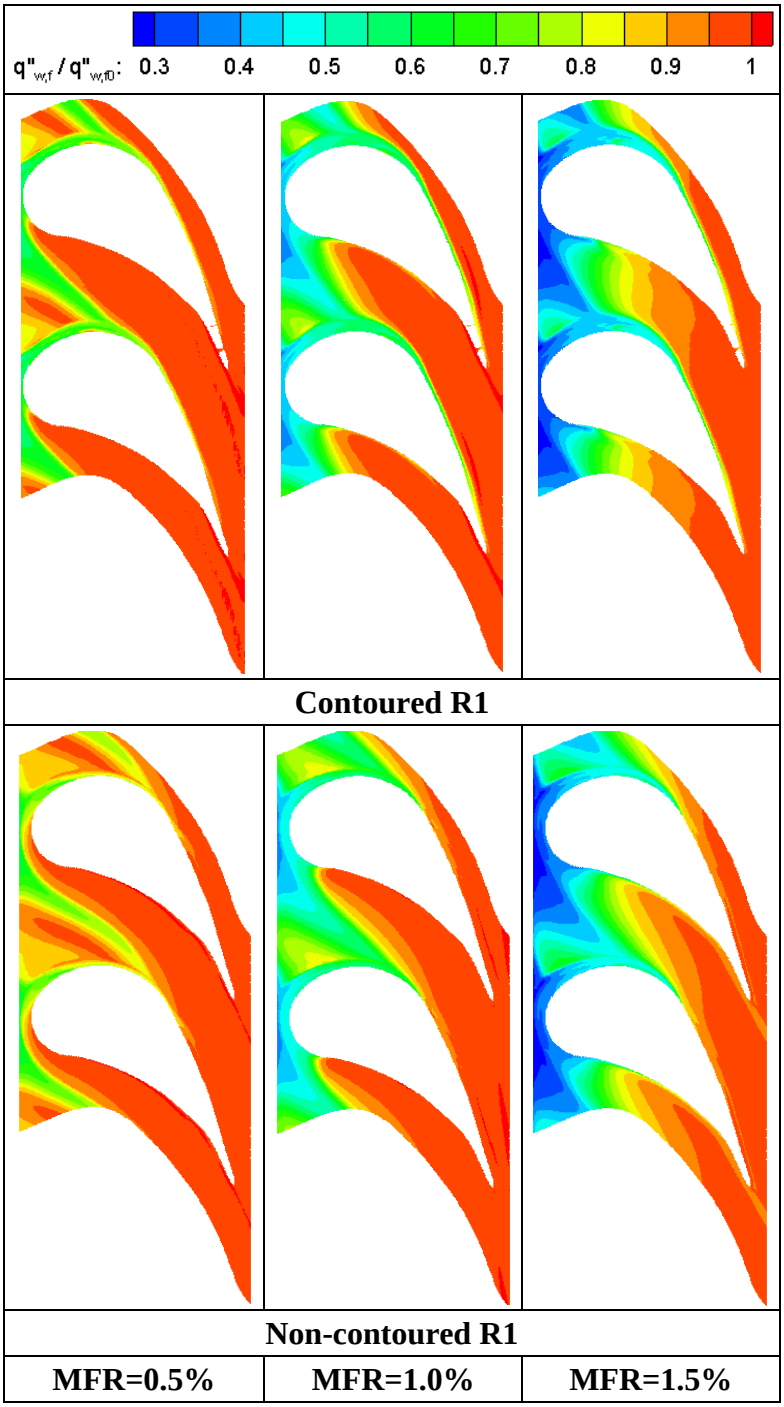

Figure 68: Distributions of predicted heat flux ratio on the contoured and non-contoured first-rotor platforms with different MFRs at 3000 rpm.

Figure 68 shows the contour plots of the predicted heat flux ratio on both the contoured and non-contoured R1 hub with varied MFRs at 3000 rpm. The heat flux ratio reflects the realistic heat load on the endwall surface. It is determined by the film cooling effectiveness and heat transfer coefficient. To be specific, the surface that is well cooled and experiences low heat transfer will encounter smaller heat load which lowers down the risk of thermal failure. As seen, the distribution of heat flux ratio has high similarity with the film cooling effectiveness shown in the figure on page 112. As the MFR enhances, the area with high heat load shrinks. Basically the upstream endwall portion where is well covered by the cooling film experiences lower heat load than the downstream passage. Once again, it is seen on contoured platform that less heat load is added to the endwall surface close to pressure side due to the reduction of secondary flow that is associated with the decreased ΔP brought by endwall contouring, especially for high MFRs. The downstream passage encounters high heat load due to the lack of coverage by film cooling. Therefore, the application of endwall contouring is able to better protect the R1 platform from excessive heat load.

The impact of MFR on the predicted pitchwise-averaged heat flux ratio on both contoured and non-contoured R1 platform at 3000 rpm is illustrated in Figure 69. As seen for both contoured and non-contoured endwall, the lowest averaged heat flux ratio occurs at the leading edge and then the magnitude gradually increases along the axial chord till almost unity at the trailing edge. This reflects the mixing process between the cooling film and mainstream. Moreover, the averaged heat load at one same location enhances with the increasing MFR but the difference keeps dropping while travelling

downstream. It is mainly due to the fade in the film cooling effectiveness. Within the section between the leading edge and 0.25 C_{ax}, the averaged heat load at the contoured endwall is always lower than the non-contoured platform. This is the result of the combination of higher film cooling effectiveness and lower local heat transfer at the contoured R1 hub. However marginal difference can be noticed beyond 0.25 C_{ax} between contoured and non-contoured cases. Figure 70 compares the area-averaged heat flux ratio for both the contoured and non-contoured cases rotating at 3000 rpm. As expected the area-averaged heat flux ratio at the endwall declines monotonically with the growing MFR for both contoured and non-contoured R1. At MFR = 0.5% and 1%, the averaged heat flux ratio on the contoured platform is 1.7% and 3.5% lower than that for non-contoured case respectively. However, the endwall contouring does not show visible advantage in heat load reduction at MFR=1.5%.

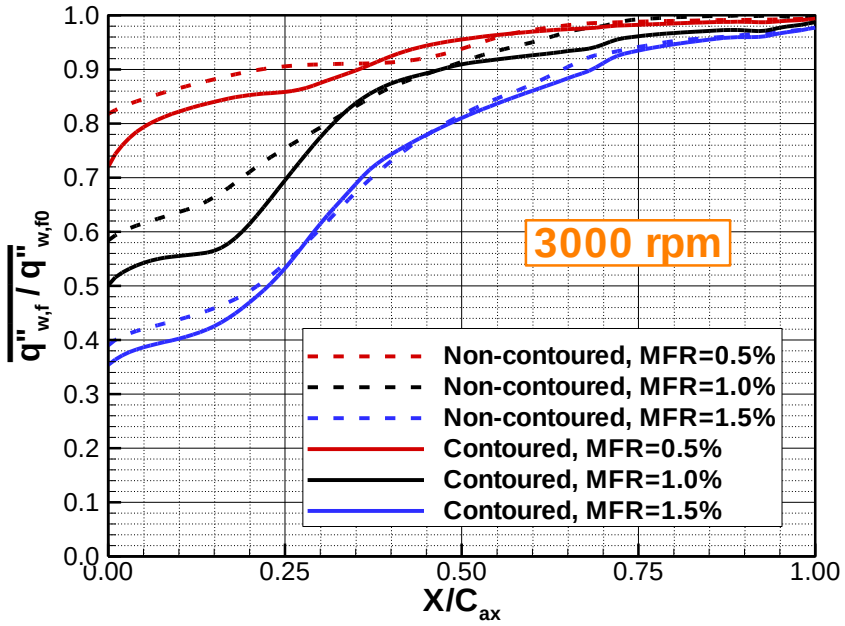

Figure 69: Predicted pitchwise-averaged heat flux ratio on both contoured and non-contoured first-rotor platforms with different MFRs at 3000 rpm.

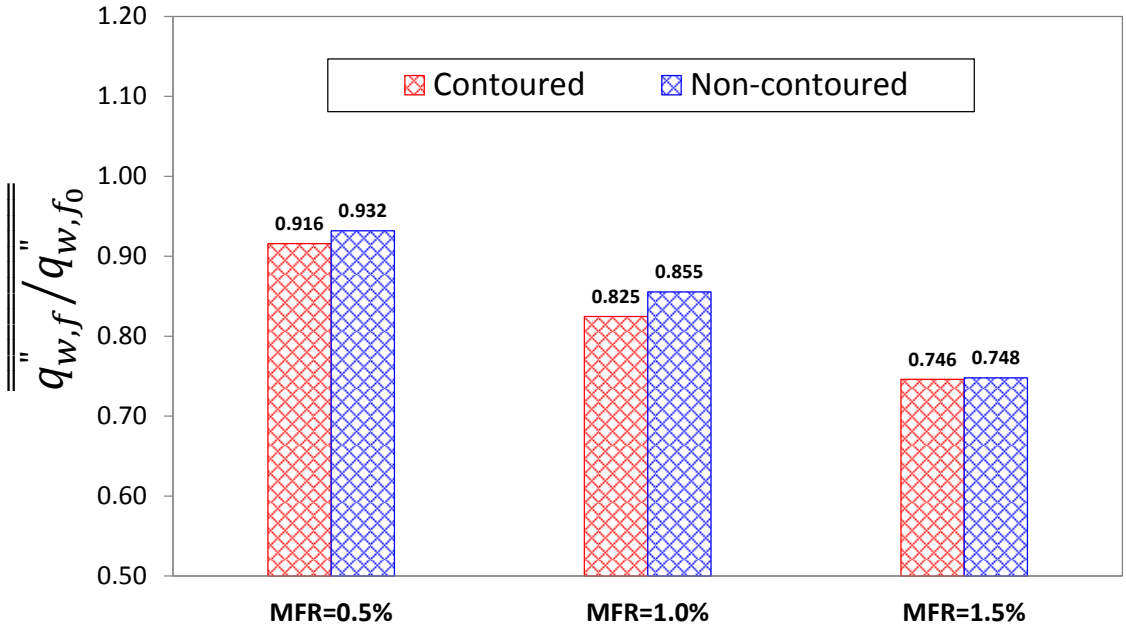

Figure 70: Predicted area-averaged heat flux ratio on both contoured and non-contoured first-rotor platforms with different MFRs at 3000 rpm.

7.3.2 The impact of rotational speed

Figure 71 shows the impact of rotational speed on the distribution of Nusselt number on the contoured and non-contoured first-rotor platforms for MFR = 1.0%. Due to the variation in incidence angle, the stagnation point moves from the suction side towards the pressure side as the rotational speed is decreased. Such change directly affects the Nu at the blade leading edge. As seen, in the vicinity of leading edge, higher Nusselt number is obtained at the pressure side rather than the suction side for lower rotational speeds, whereas slightly higher Nu is seen at the suction side for the reference condition. Further, since the cooling film spreads less uniformly at the lower rotational speeds, the direct attachment of upstream mainstream causes higher Nu right at rear edge of stator-rotor gap. It should be also noted that the high-Nu streak due to the horseshoe vortex diminishes at lower rotational speed, which is probably the result of incidence change.

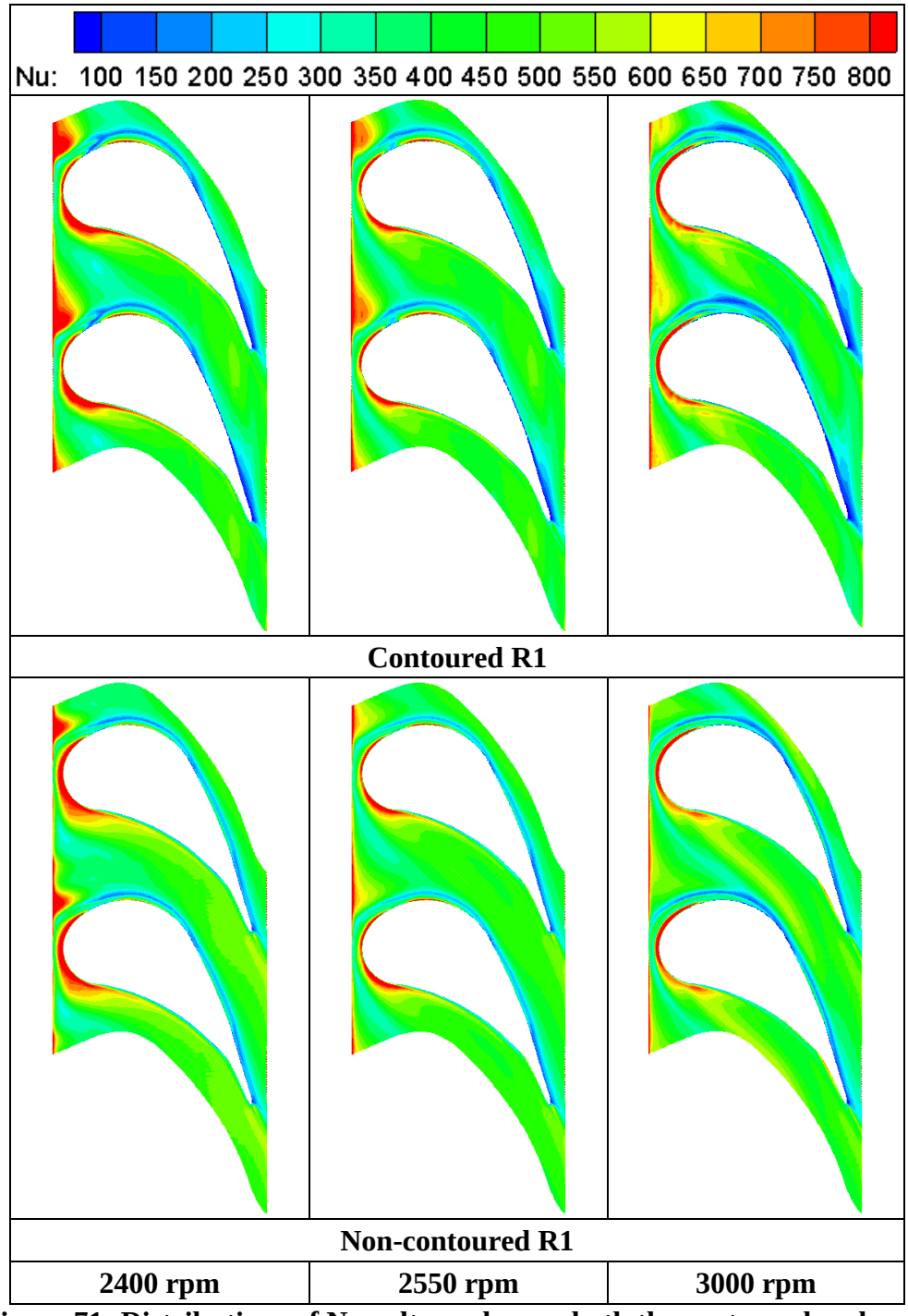

Figure 71: Distributions of Nusselt number on both the contoured and non-contoured rotating first-rotor platforms at three different rotational speeds with MFR = 1.0%.

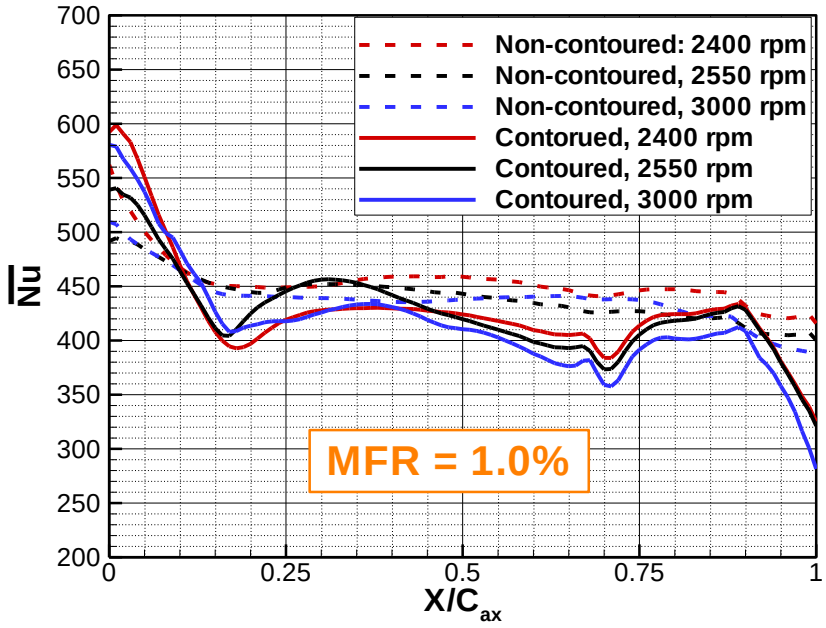

Figure 72: Pitchwise-averaged Nusselt number along the axial chord on both contoured and non-contoured first-rotor platforms at three different rotational speeds with MFR=1.0%.

The pitchwise-averaged Nusselt number along the axial chord on both contoured and non-contoured first-rotor platform at three different rotational speeds with MFR = 1.0% is shown in Figure 72. Overall the rotational speed does not generate significant impact on the pitchwise-averaged Nusselt number. As seen, due to the concave surface profile of endwall contouring, the averaged Nu at contoured R1 hub is lower at most area of the passage between 0.1 C_{ax} and the trailing edge. For the non-contoured endwall, the highest averaged Nu appears almost everywhere at 2400 rpm. This could be attributed to the relatively higher local velocity since the least energy is extracted from the gas at the lowest rotational speed as shown in Figure 73. The averaged Nu at non-contoured endwall declines with the increasing rotational speed within the area between 0.25 C_{ax}

and 0.55 C_{ax}. Then the averaged Nu at 3000 rpm becomes higher than that at 2550 rpm which is possibly the contribution of the Nu enhancement by the horseshoe vortex. For the contoured endwall, the highest averaged Nu is seen at 2550 rpm between 0.2 C_{ax} and 0.45 C_{ax}, which might be due to its weaker suction-side leg of horseshoe vortex as shown in the figure on page 132. However, the averaged Nu declines while the rotational speed is increasing at the downstream half of the contoured passage, which is also associated with the distribution of local velocity magnitude as shown in Figure 73. Nevertheless, such difference is very small, indicating the unimportant impact of rotational speed. Figure 74 compares the area-averaged Nusselt number on both contoured and non-contoured first-rotor platforms at three rotational speeds with MFR = 1.0%. As shown, the area-averaged Nuesselt number slowly goes down as the rotational speed is growing for both the contoured and non-contoured cases. The tiny difference in the area-averaged Nu among three rotational speeds indicates that the rotational effect on the endwall overall Nu is rather insignificant. At each rotating condition, lower overall Nu is obtained at the contoured endwall than the non-contoured platform. Among the three rotational conditions, the most overall Nu reduction that is up to 4.7% is achieved at the reference rotational speed of 3000 rpm.

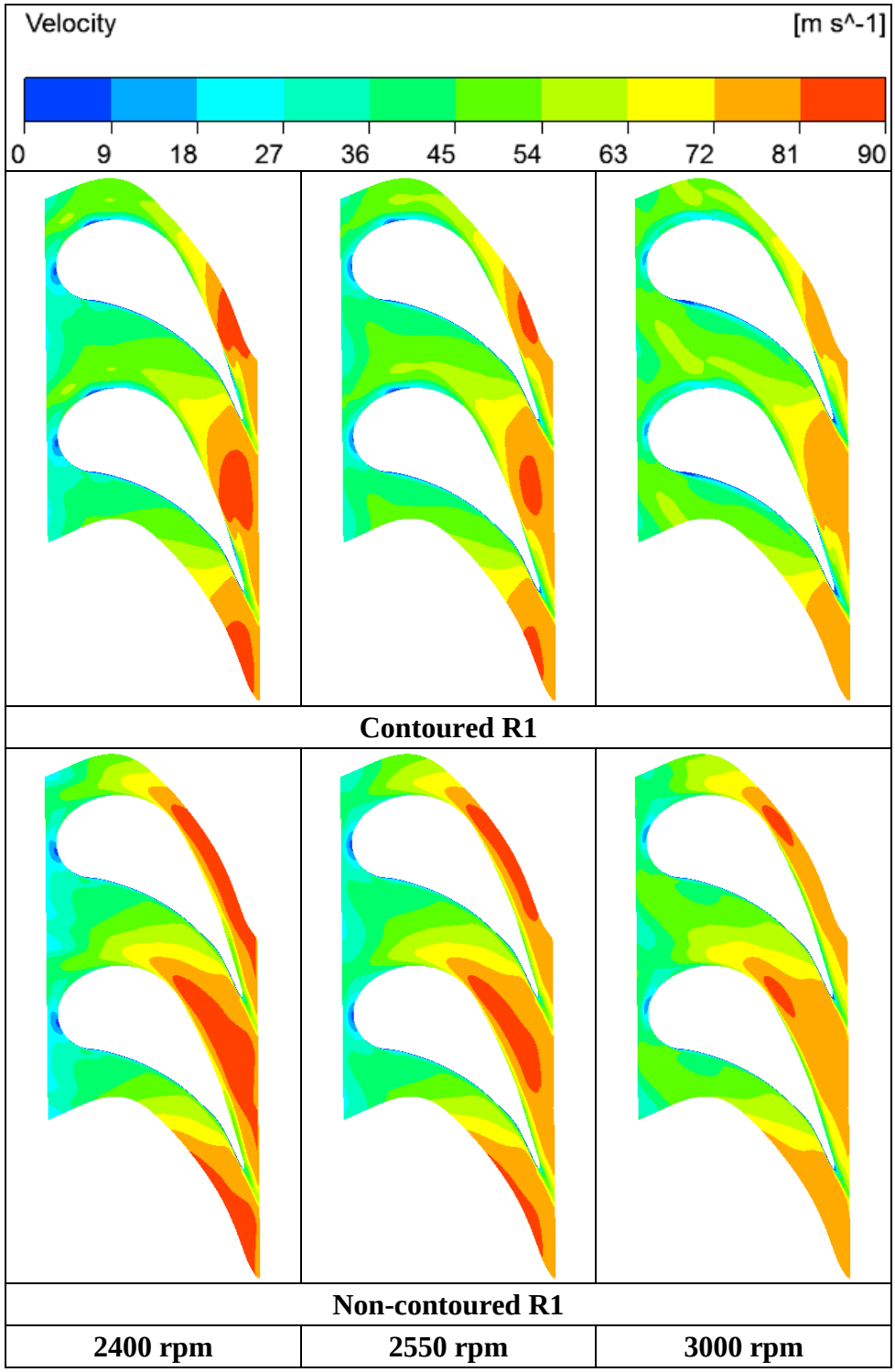

Figure 73: Magnitude of relative velocity at 1% span height of both the contoured and non-contoured first rotors at three different rotational speeds with MFR = 1.0%.

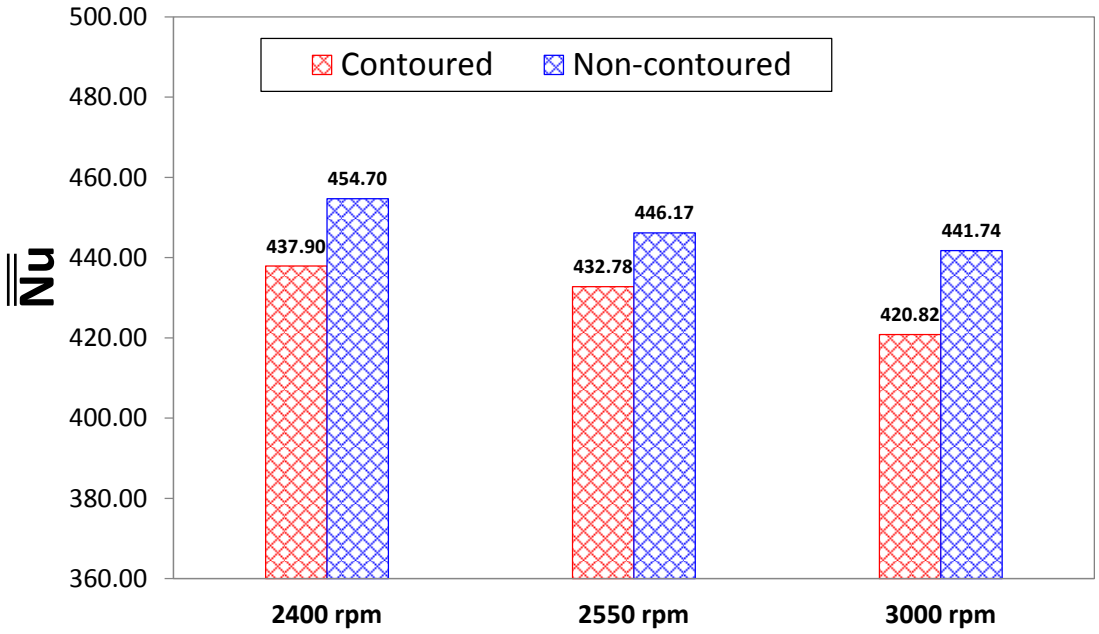

Figure 74: Area-averaged Nusselt number on both the contoured and non-contoured first-rotor platforms at three rotational speeds with MFR = 1.0%.

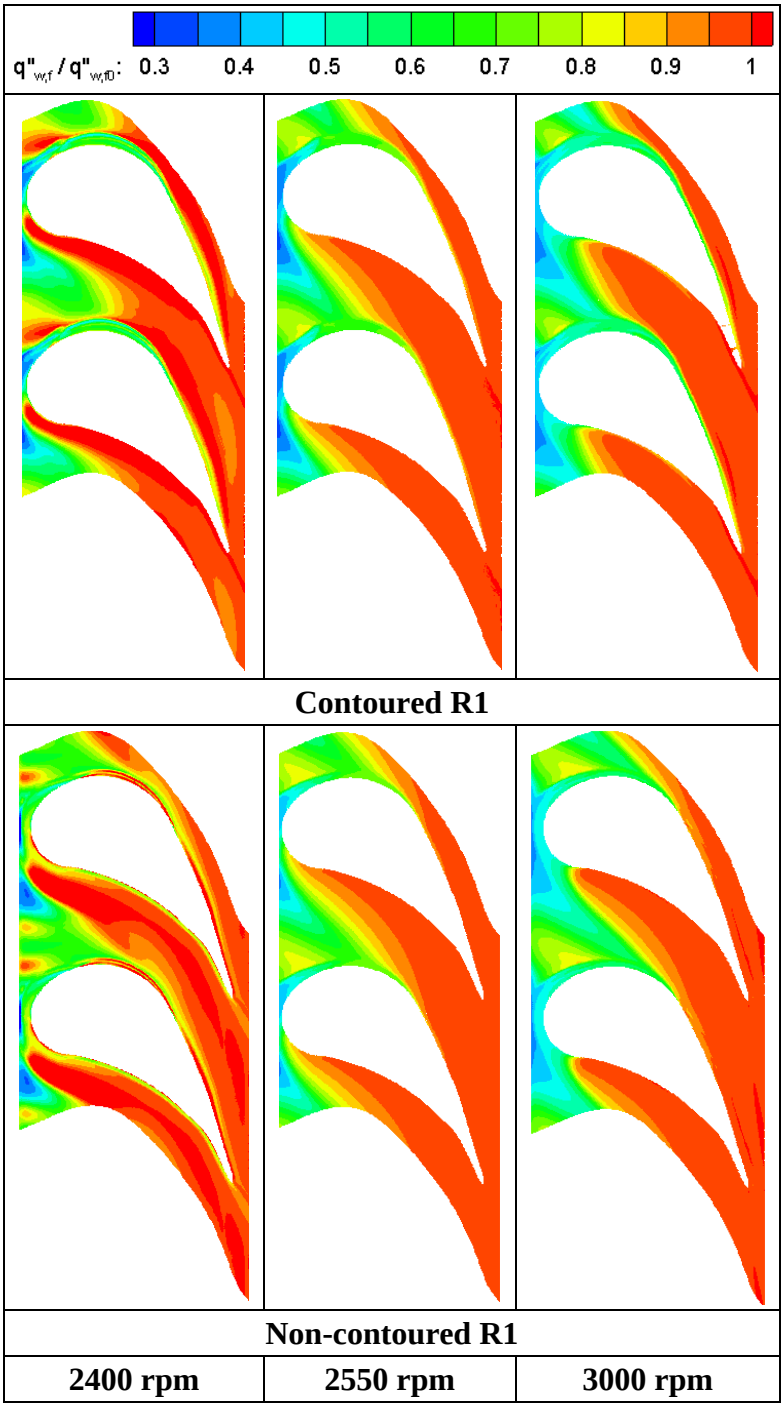

Figure 75: Distributions of heat flux ratio on both the contoured and non-contoured rotating first-rotor platforms at three different rotational speeds with MFR = 1.0%.

The distribution of heat flux ratio on both the contoured and non-contoured rotating first-rotor platforms at three different rotational speeds for MFR = 1.0% is shown in Figure 75. Since the difference in heat transfer due to the rotational effect is inconsiderable, the distribution of heat flux at the R1 hub exhibits highly consistent features as the film cooling effectiveness. In other words, the endwall surface where is well covered by the cooling film tends to experience lower heat load. As seen, since the cooling film disperses more uniformly in the endwall pitchwise direction at higher rotational speeds, more area with low heat flux ratio is obtained in the right downstream region of stator-rotor gap. At the further downstream passage, the local heat flux ratio progressively grows as the cooling effectiveness is decaying. There is almost no reduction in heat flux ratio at the rear half of the endwall surface. Such trend is seen at both the contoured and non-contoured R1 platforms. However, more reduction in heat flux ratio can be seen close to the pressure side at the contoured endwall since the cooling film is able to go further along the pressure side rather than turn to the suction surface. The presence of endwall contouring to some extent reduces the risk of excessive heat load on the pressure surface.

Figure 76 depicts the pitchwise-averaged heat flux ratio along the axial chord on both contoured and non-contoured first-rotor platforms at three different rotational speeds with MFR=1.0%. As mentioned earlier, the averaged heat flux ratio enhances with the decreasing rotational speeds at the upstream half of the endwall where is better protected by the cooling film than the downstream half. The heat flux ratio grows higher than 0.9 at 0.5 C_{ax} and almost achieves unity at the trailing edge due to the lack of

coolant protection. Between the leading edge and mid-chord, the non-contoured endwall experiences higher averaged heat load than the contoured platform at the same rotational speed, which is essentially benefited from the more uniform spread out of cooling film due to the reduced pressure gradient between the pressure side and suction side. The impact of rotational speed on area-averaged heat flux ratio at both contoured and non-contoured first-rotor platforms with MFR = 1.0% is summarized in Figure 77. As shown, the overall heat flux ratio declines as the rotational speed increases for both the contoured and non-contoured cases. Less than 20% reduction in the overall heat load is obtained at the endwall since most of the hub surface lacks the protection offered by the cooling film. At 2400 rpm and 3000 rpm, lower overall heat flux ratio at the contoured endwall is achieved than the non-contoured platform, whereas no improvement occurs at 2550 rpm.

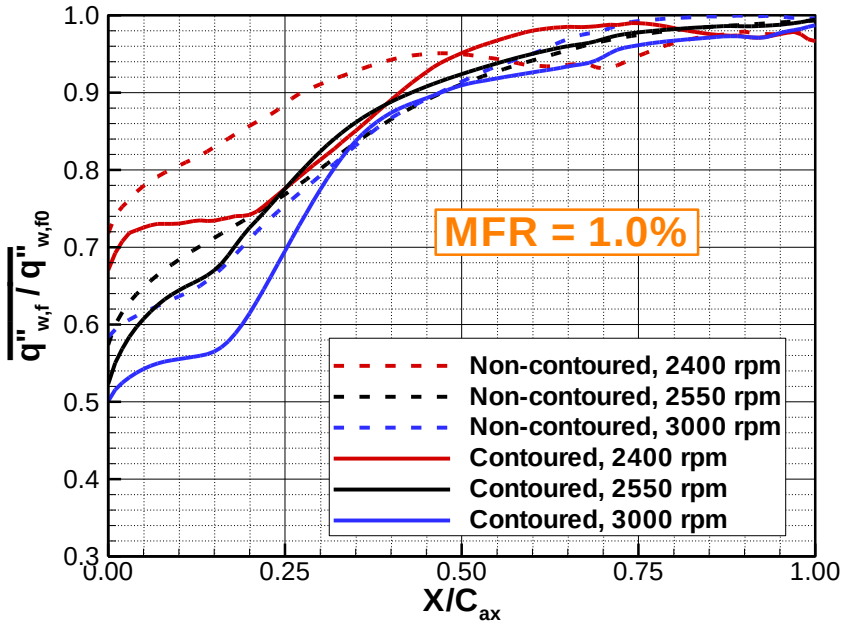

Figure 76: Pitchwise-averaged heat flux ratio along the axial chord on both the contoured and non-contoured first-rotor platforms at three different rotational speeds with MFR = 1.0%.

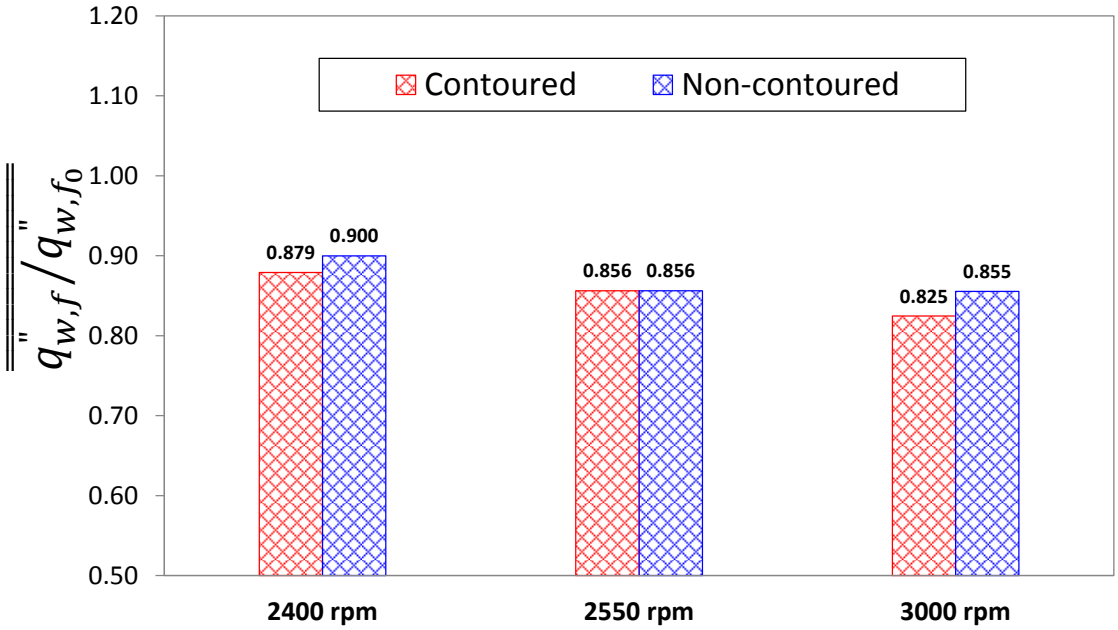

Figure 77: Area-averaged heat flux ratio on both the contoured and non-contoured first-rotor platforms at three rotational speeds with MFR = 1.0%.

8. ROTOR BLADE TIP EJECTION*

This section will numerically investigate the blade tip ejection with four film cooling configurations under rotating conditions. The pressure distribution, flow field, film cooling effectiveness, heat transfer and heat flux ratio for each blade cooling configuration will be extensively discussed and analyzed. The impact of two important factors on the film cooling will be demonstrated in detail. The magnitude of blowing ratio reflects the momentum level of the cooling jets over the mainstream flow and the variation of rotational speed helps us to understand the rotation effect. The study of the influence of both parameters on blade tip ejection has practical sense in the turbomachinery design and application community.

8.1 The Impact of Global Blowing Ratio

As a matter of fact, the blowing ratio of the film cooling is the momentum ratio of the cooling film over the mainstream. Its level strongly affects the performance of the film cooling that is supposed to protect the blade surface from overheating. A small blowing ratio may be not able to provide full protection since the cooling film can hardly overcome the momentum of mainstream flow. However, a too high blowing ratio may potentially lift off from the surface and consequently lose the protection to the metal. In addition, it could also worsen the turbine efficiency due to the excessive disturbance to

* Part of the materials are reprinted with permission from "A Combined Experimental and Numerical Study of the Turbine Blade Tip Film Cooling Effectiveness under Rotation Condition" by Mohsen Rezasoltani, Kun Lu, Meinhard T. Schobeiri and Je-Chin Han, 2015. Journal of Turbomachiney, Volume 137, pp. 051009-1-12, Copyright © 2015 by ASME.

the mainstream. Therefore, the parameter study of the blowing ratio is necessary and able to help determine the optimum blowing ratio of the ejected coolant.

8.1.1 Pressure distributions and flow characteristics

8.1.1.1 Plane and squealer tips with tip hole cooling

Generally the knowledge of the pressure field and flow behaviors is able to assist researchers to understand the relevant convective heat transfer problems. In fact, they have direct and significant influence on the film cooling in this study. Figure 78 depicts the static pressure distribution at the blade tip region for both the plane tip and the squealer tip for blowing ratios of M = 0.5, 1.0 and 1.5. For the plane tip without film cooling holes, the typical pressure distribution is obtained. The pressure side (PS) has the highest pressure and the pressure is gradually decreased towards the suction side (SS). The resulted pressure gradient pointing from PS to SS is the primary driving force of the tip-gap leakage flow. Note that the contours of pressure are smooth everywhere implying a gradual transition of the potential field. Relatively low pressure is observed at the trailing edge mainly due to the expansion process through the blade channel. Figure 78 (d) depicts the corresponding streamline patterns at the blade tip region. Since the object of the current study is a rotor blade rotating at 3000 rpm with the tip speed of 215.34 m/s, the streamlines are plotted based on the relative velocity in the rotating coordinates. Due to the blunt and round leading edge of the blade, the pressure gradient at the leading edge is not as big as that between the pressure side and suction side. Consequently, the mainstream particles entering the tip gap are not deflected immediately. Nevertheless, they keep traveling a distance along the initial direction until the pressure gradient

becomes high enough to push them to the suction side at about 0.3 C_{ax}. As a result, a small amount of flow leaks from the pressure side of the leading edge, whereas the majority moves towards the suction side forming a system of tip vortices. After 0.3 C_{ax}, the pressure gradient is dominant.

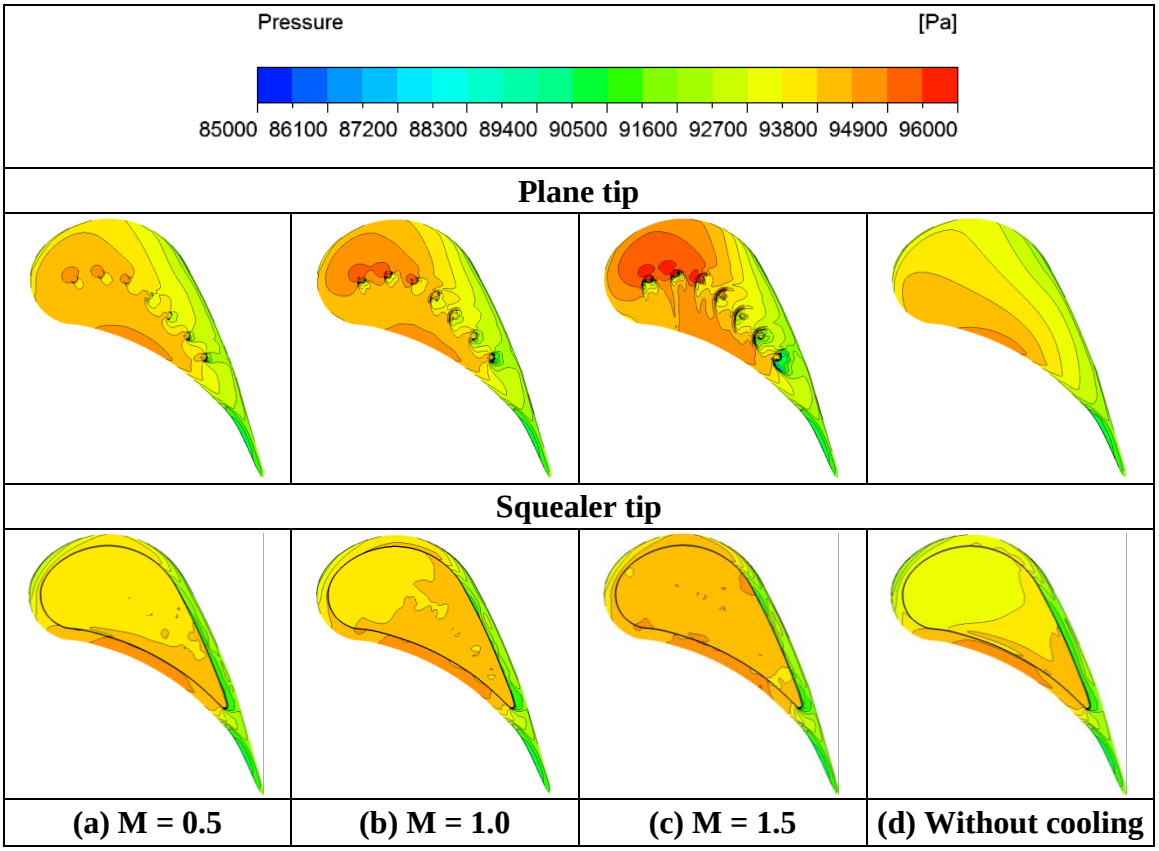

Figure 78: Impact of global blowing ratio on the distributions of the static pressure for blade tips with tip hole cooling at 3000 rpm: Blade tip for the plane tip (above); Cavity floor and rim for the squealer tip (below).

Comparing Figure 78 (a, b, c), that pertains to the film cooling injection to the figure without injection (d), shows that the presence of film cooling significantly changes the pressure field, especially in the vicinity of the cooling jets. This change of the pressure

field is directly related to the blowing ratio, which reflects the ratio of the cooling jet momentum and the momentum of the mainstream. For M = 0.5, the cooling jet does not have the momentum to overcome the main mass flow momentum. As a result, it dissipates and contributes to higher tip clearance total pressure losses. The situation changes when M is increased. At M = 1.0, the injected jet has enough momentum to significantly impact the pressure field. The radially ejecting jets at this ratio impinge on the turbine casing and generate locally a quasi-stagnation zone with higher pressure. This is illustrated for the first three holes. At M = 1.5, the front portion of the blade tip is occupied by a pressure field that is about 3.6% (3,300 Pa) above the zero injection case (d). With the increasing blowing ratio, the pressure near the leading edge tends to increase. In addition, the high-pressure area at the pressure side preserves the same shape for the non-cooling cases and cases under blowing ratios of M = 0.5 and 1.0. When it comes to the blowing ratio of M = 1.5, the area is significantly extended towards the suction side.

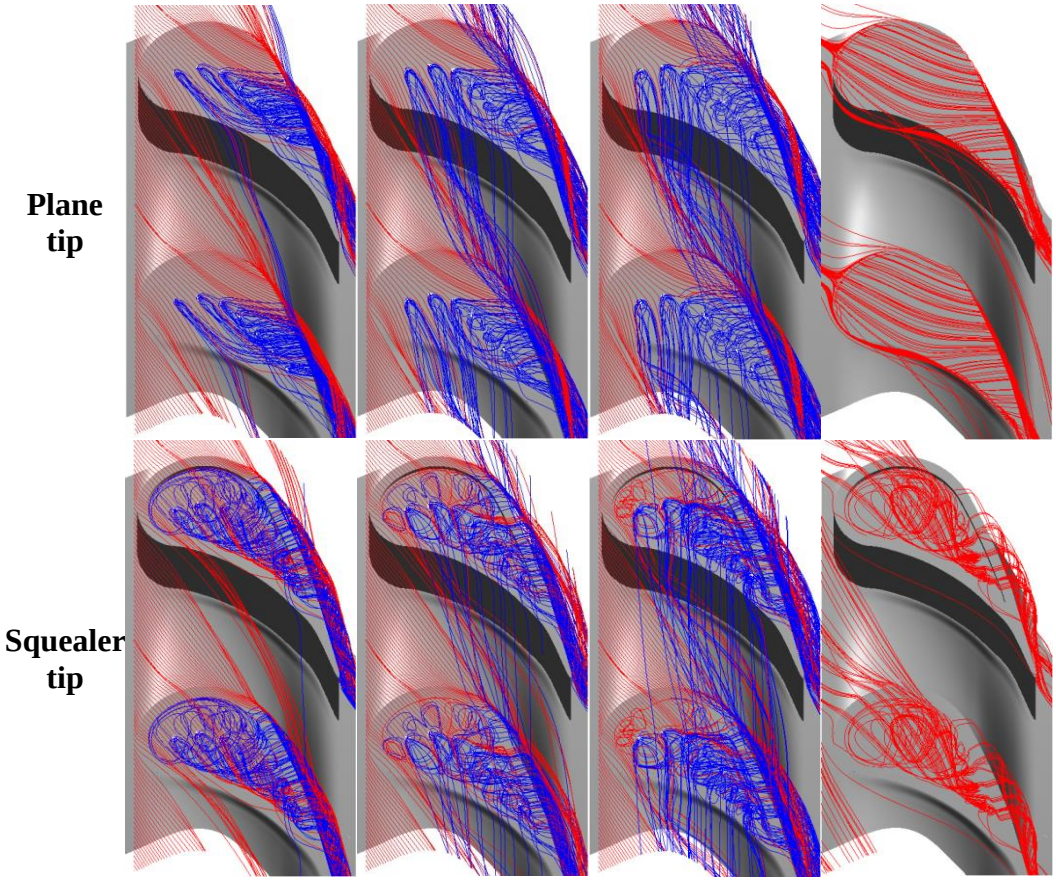

(a) M = 0.5 (b) M = 1.0 (c) M = 1.5 (d) Without cooling

Figure 79: Impact of global blowing ratio on the streamlines based on the relative velocity around the blade tips with tip hole cooling at 3000 rpm (blue indicates cooling air, red is mainstream air).

The presence of the cooling injections significantly alters the flow field as well (Figure 79 (a, b, c)). It can be clearly seen that the mainstream (red) and the cooling jets (blue) have strong interactions. Such interactions are dramatically affected by the global blowing ratio. For M = 0.5, almost all of the cooling jets are deflected towards the suction side, except that a small amount of coolant ejecting from the first cooling hole moves to the pressure side and then leaves the tip gap together with the leakage flow on the pressure side. However, most of the coolant mixes with the mainstream particles and

directly exits the tip gap from the suction side generating a system of tip secondary vortices. Under blowing ratio M=1.0, all the coolant particles exiting from the first and second cooling holes travels across the pressure side and form a passage flow by mixing with the mainstream. Small amount of coolant from other holes is observed to behave similarly. Meanwhile, the rest of the majority appears to accumulate in the vicinity of cooling-hole exits. The coolant spreads more widely and covers more of the tip, which is virtually the result of the impact of both the pressure gradient and the relative motion between the tip and shroud. Such flow behavior tends to be more salient when the blowing ratio is increased to M = 1.5. In addition, the directions of the coolant jets vary slightly with increasing blowing ratio.

It is seen that the coolant particles tend to travel in the opposite direction of rotation, especially for the cooling jets exiting from the first three cooling holes. This phenomenon is due to the rotation and does not exist in a stationary cascade. While in this particular hole configuration, the jets tend to exit radially, and the circumferential motion of the rotor causes the blade tip to move away from the jets. As a result the particle moving along a relative streamline with a relative velocity tangent to the streamline is presented in Figure 79. Therefore, the pattern of the film cooling effectiveness that will be shown later does not have any similarity with the ones measured in stationary cascades.

Note that all the blades are 2D cylindrical blades with no compound lean design, which does not take into account the variations of the flow angle along the blade span due to the increase of the rotational speed from hub to tip. As a result, the flow angle at

rotor inlet tends to decrease when approaching the tip, as shown in Figure 80 (left). Additionally, due to the non-slip assumption on the wall, the boundary layer close to the casing has very high velocity gradient and thus the magnitude of the absolute velocity decreases fast. After superposition with the large circumferential component near the shroud, the relative flow angle tends to be small. The correlated loadings at the blade tip and mid-span has distinct differences too, as shown in Figure 80 (right).

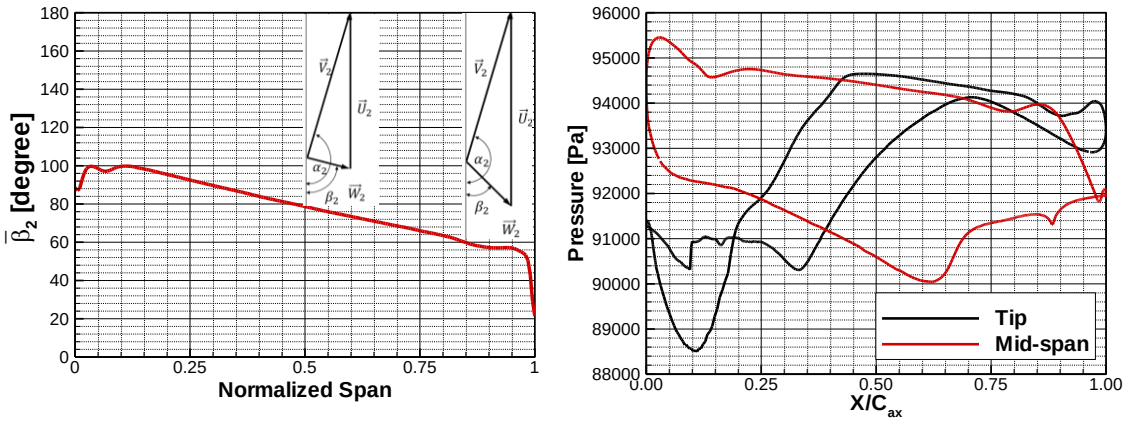

Figure 80: Pitchwise-averaged flow angle at the rotor inlet (left); Blade loading at tip and mid-span (right).

The pressure on the squealer tip shows dramatically different distributions compared with that on the plane tip. As shown in the figure on page 144, the most noticeable characteristic is that the pressure distribution on the cavity floor tends to be uniform and thus the pressure gradient on the cavity floor is significantly decreased. This is resulted from the presence of the large cavity on the tip. As seen in the figure on page 146, after crossing over the narrow gap between the casing and the squealer rim, the freestream flow is squeezed in the squealer cavity. Sudden expansion induces flow circulations

within the cavity which entraps the freestream particles. Meanwhile, strong interactions between the leakage flow and the cooling jets intensify the mixing which forms three-dimensional complex vortex systems. The majority of the mixture of the leakage flow and the coolant continues to roll and travels downstream along the cavity. Eventually, the flow particles accumulate at the trailing end of the cavity and afterward escape from the cavity by crossing over the suction side rim, which generates the suction-side tip vortex. Unlike the case for plane tips, some coolant particles (marked with blue streamlines) are transported to the leading edge portion by complicated vortices circulating at the surrounding area. Such transportation is able to partially relieve the heat loads and thus provide certain cooling protection to the cavity walls near the leading edge. However, the leading edge of the plane tip is directly exposed to the hot freestream and at risk of overheating. This is an advantage of the squealer tip. Thus, quasi homogeneous pressure distribution on the cavity floor is obtained due to the strong mixing effect. Note that the locations of the cooling holes are not detectable by seeing the pressure field, unlike the locally quasi stagnation spots on the plane tip. This is because the cavity protects the freestream from rushing against the coolant jets at the exit. The pressure field on the rim differs a lot from that on the cavity floor. As expected, high pressure is obtained on the pressure-side rim. On the contrary, low pressure is observed on the suction-side rim.

Although all the flow structures show significant similarities, the magnitude of blowing ratios definitely affects the flow field. At M = 0.5, almost all the coolant leaks from the suction side starting from nearly 0.5 C_{ax}. However, parts of the coolant particles

travel across the pressure-side rim and mixes with the cross flow in the passage when the blowing ratio is increased to M = 1.0. Even more coolant leaks to the pressure side for the case of M = 1.5. In fact, the flow patterns at three axial locations shown in Figure 81 reveal the correlated mechanism. Note that the blowing ratio is associated with the flow momentum. At the low blowing ratio of M = 0.5, the coolant jets do not penetrate all the way to the shroud since the relative low momentum can hardly overcome the cavity flow. Instead, they are deflected and diffused with the vortices before they mix with the leakage flow. Those circulations constrain the coolant flow particles in the cavity and afterwards carry them to leak from the suction side. Nevertheless, the situation changes when it comes to M = 1.0. The coolant jets penetrate all the way to the shroud and split the cavity vortex. As a result, some coolant particles mix with the leakage flow and are carried to the pressure side. Increasing the blowing ratio to M = 1.5 enhances this mass transportation. In addition, in the case without film cooling (Figure 81 (d)), sudden expansion of the leakage flow forms one large circulation at the center of the cavity, which acts as typical cavity flow with one moving boundary. With the presence of cooling ejections, two vortices rolling in the same direction are formed and divided by the cooling jet for the case of M = 0.5 and 1.0 (Figure 81 (a, b)). However, three circulations are observed when the blowing ratio reaches 1.5 (Figure 81 (c)). The two outer circulations rotate in one direction while the middle one rotates in the opposite direction.

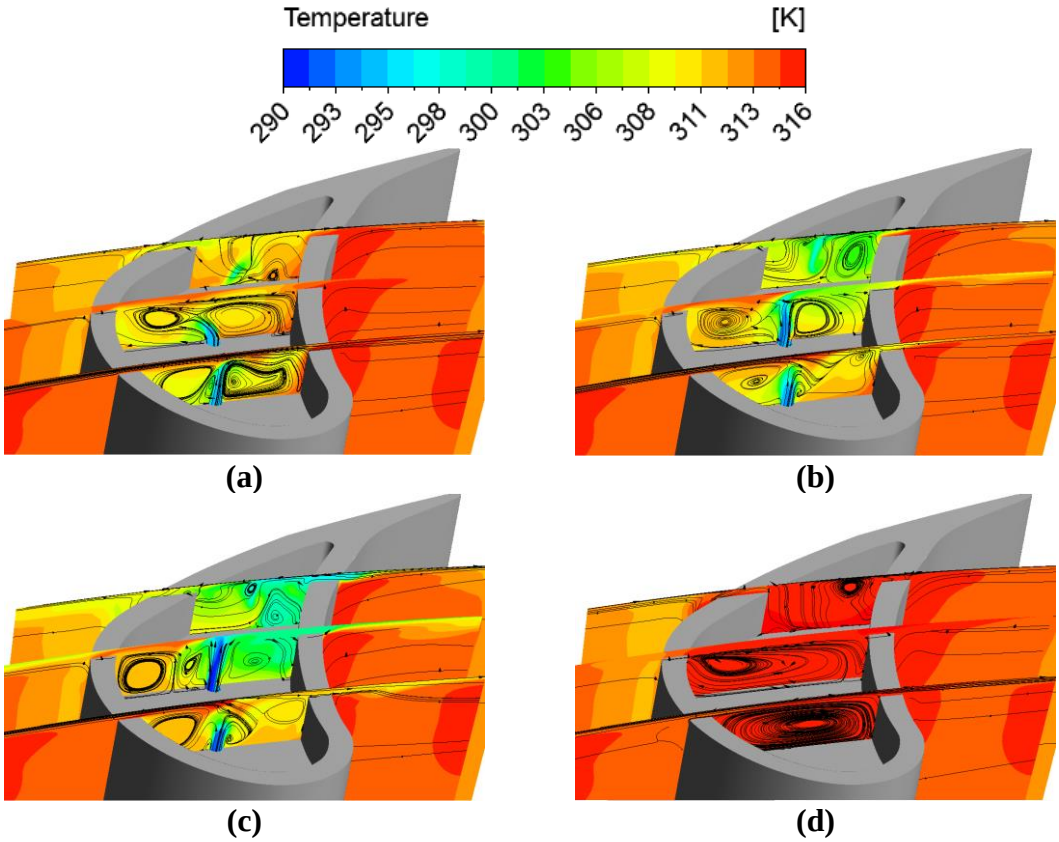

Figure 81: Temperature contours and streamlines at three axial locations of the squealer tip with tip hole cooling at 3000 rpm: (a) M = 0.5, (b) M = 1.0, (c) M = 1.5, (d) Without film cooling.

8.1.1.2 Plane and squealer tips with pressure-side hole cooling

The flow behaviors and pressure field exhibit dramatically different characteristics for the pressure-side-edge compound hole cooling than the tip hole cooling due to the distinct geometric structures. Figure 82 depicts the static pressure distribution near the blade tip region of the plane tip for blowing ratios of M = 0.5, 1.0 and 1.5 while rotating at 3000 rpm. For the plane tip with pressure-side-edge compound hole cooling, a typical pressure distribution is obtained on the tip surface for all blowing ratios. The pressure

side (PS) has the highest pressure and the pressure is gradually decreased towards the suction side (SS), which is as same as the case without film cooling. The similarity indicates that the film coolant from the pressure-side holes does not have considerable impact on the pressure distribution at the blade plane tip. However, the pressure field in the vicinity of the cooling holes is strongly perturbed by the ejected cooling jets, which takes place to the plane tip with tip hole cooling as well. In addition, flame-like areas with low pressure appear at the trailing edge of the five downstream cooling hole exits. Similar low-pressure streaks can be seen around the exit of the cooling hole near the leading edge, however these streaks attach to both sides of the hole exit rather than the trailing end. Essentially, such pressure loss is due to the intense mixing and interactions between the mainstream and cooling jets. Therefore these areas grow in size and the local pressure drops when the blowing ratio is increased. It is believed that the pressure loss occurs in the vicinity of all cooling jets however only those cooling jets that stay close to the pressure surface can leave the corresponding traces on the wall. Thus, the ejected coolant jets are able to significantly affect the pressure distribution in the surrounding area.

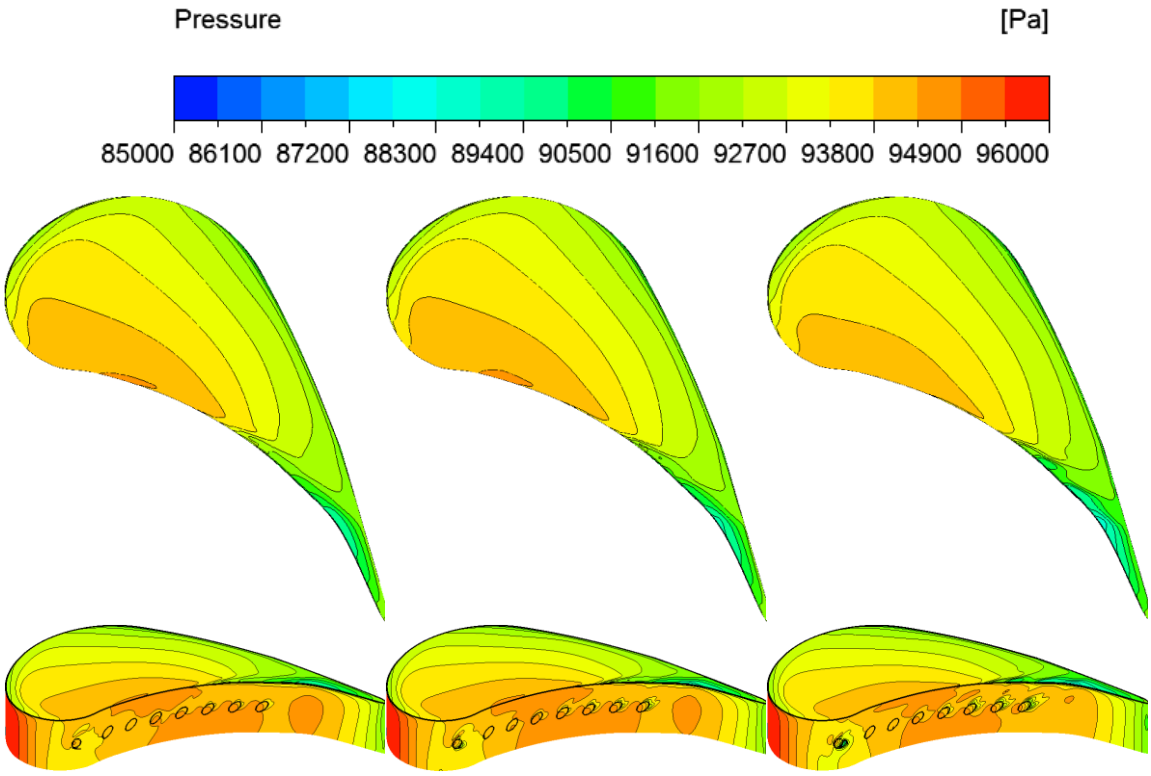

(a) M = 0.5 **(b) M = 1.0** **(c) M = 1.5**

Figure 82: Impact of global blowing ratio on distributions of the static pressure near the blade tip region for plane tip with pressure-side hole cooling at 3000 rpm.

Nevertheless, the presence of the cooling jets considerably alters the flow structures of the blade tip leakage flow, as shown in Figure 83. Since the rotor blade is rotating at 3000 rpm with the tip speed of 215.34 m/s, the flow angle near the tip is much smaller than that at mid-span (as shown in the figure on page 148). Meanwhile, due to the geometric factor of the inclined and compound angles of the cooling holes, the majority of the ejected coolant travels along the pressure side towards the blade trailing edge and ultimately exits the rotor row. During the process of approaching downstream, the coolant jets interfere with each other and mainstream forming a complex vortex system. Its size increases with the blowing ratio since more coolant is ejected into the

mainstream at higher blowing ratios. Also the cooling jets are able to penetrate further into the mainstream due to the higher momentum at larger blowing ratios. It is seen that a portion of the coolant particles climb up to the tip and cross the pressure-side edge then travel towards the suction side. Eventually those particles leak from the suction side and afterwards are entrained by the tip vortex system. The primary driving force is the pressure gradient between the PS and SS. However, the leaking of the coolant takes place beyond approximately 0.5 C_{ax} due to the particular flow field near the blade tip. In addition, the traces of the cooling jets can be identified for M = 0.5, because the jets are altered immediately after they are ejected from the cooling holes due to the relatively low momentum. However for the cases of M = 1.0 and 1.5, it turns out that almost all the coolant particles lift off from the pressure-side wall whereas a small amount of coolant is pushed towards the suction side while mixing with the leakage flow. Therefore a cooling film is seen at the aft of blade tip rather than visible independent streaks. The mixing between the coolant and leakage flow becomes stronger when the blowing ratio is larger than one.

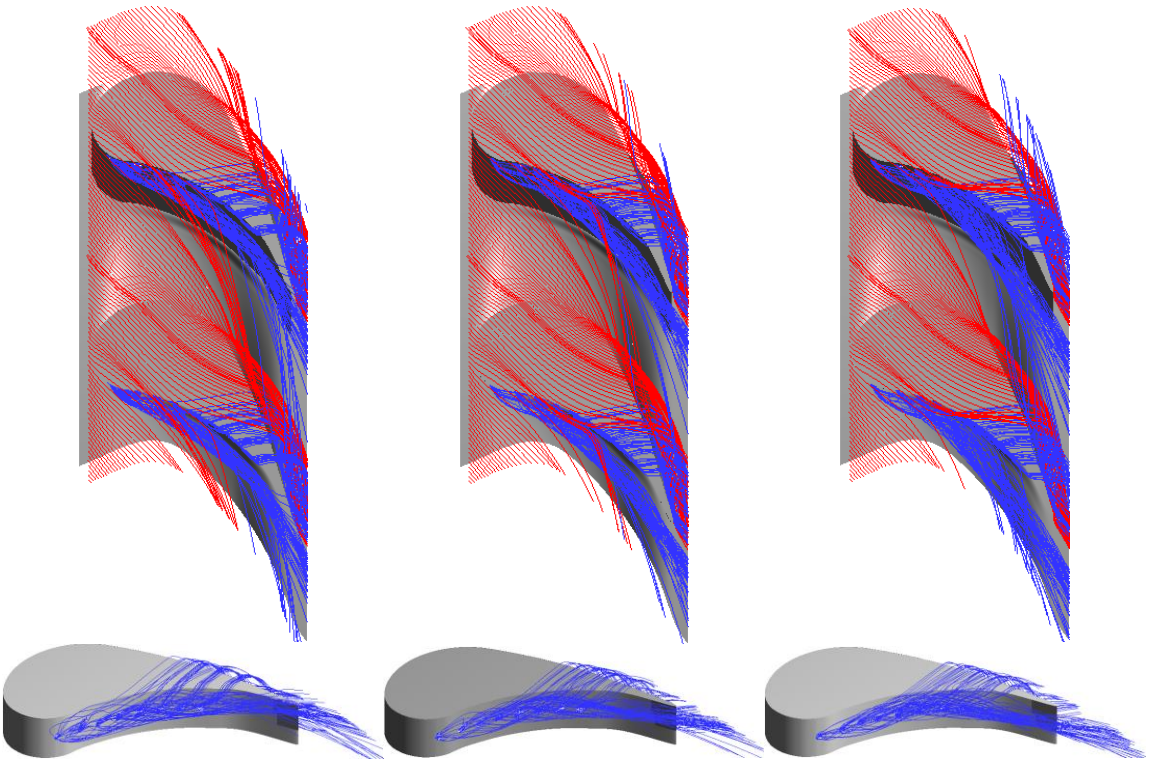

(a) M = 0.5 **(b) M = 1.0** **(c) M = 1.5**

Figure 83: Impact of global blowing ratio on streamlines based on the relative velocity near the blade tip region for plane tip with pressure-side hole cooling at 3000 rpm (blue indicates cooling air, red is mainstream air).

The distribution of the temperature near the blade tip region also reflects the similar behaviors, as shown in Figure 84. It is clearly shown that there are several streaks with low temperature on the blade tip surface reflecting the reattachments of the altered coolant jets. However, the streaks expand and diffuse with the increasing blowing ratio. Those streaks disappear for M = 1.5, instead large areas with low temperature are obtained on the tip surface. The difference can be attributed to the enhancement of mixing between the coolant and leakage due to the increased blowing ratio. The blowing ratio also impacts the cooling performance on the pressure surface. It is seen that the

coverage of the cooling film on pressure surface decreases with the increase in blowing ratio. For M = 0.5, the cooling film almost covers the surface above the cooling holes, especially in the vicinity of the five upstream holes. Three coolant streaks with low temperature are observed at the trailing edge of the three downstream holes. When the blowing ratio increases to 1.0 (Figure 84 (b)), a smaller pressure-side surface is covered by the coolant film from the five upstream holes. The streaks become more diffusive than those for M = 0.5. For M = 1.5, the coolant from the five upstream holes can hardly cool the pressure surface, as shown in Figure 84 (c). In addition, the coolant from the three downstream holes turns to be even more diffusive. At low blowing ratios, the coolant jets possess lower momentum than the mainstream, which does not allow the jets to overcome the mainstream and pressure gradient. Instead, after the coolant jets are ejected from holes, they are immediately altered by the pressure gradient and attach to the pressure surface, resulting larger coverage on the surface. However, at higher blowing ratios, the coolant jets are able to overwhelm the momentum of the mainstream and pressure gradient, and therefore tend to lift off from the surface which leads to less coverage on the pressure surface.

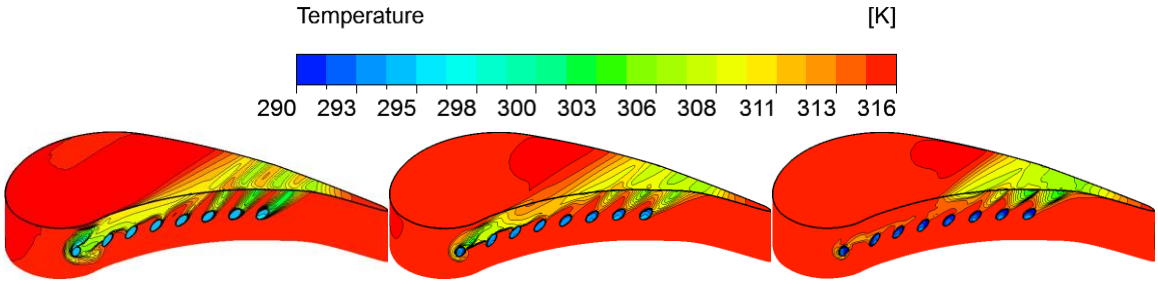

(a) M = 0.5 **(b) M = 1.0** **(c) M = 1.5**

Figure 84: Impact of global blowing ratio on distributions of the temperature near the blade tip region for plane tip with pressure-side hole cooling at 3000 rpm.

Unlike the plane tip in the figure on page 153, the pressure distribution near the tip region for squealer tip shows different contours as shown in Figure 85. Due to the presence of the squealer cavity, the pressure distribution tends to be more uniform on the cavity floor. Especially there is a large area occupied by relatively lower pressure near leading edge, which is attributed to the circulation generated by entrained mainstream flow. However, similar to the plane tip, the high pressure is obtained at the pressure-side rim whereas the low pressure for suction side. In fact after compared to the pressure field for the squealer tip with no cooling in the figure (d) right on page 144, one may conclude that the variation of blowing ratio does not deliver noticeable impact on the pressure distribution for the squealer tip region. However, the presence of cooling holes on the pressure side dramatically alters the local pressure field. The corresponding influence exhibits the same manner with that for the plane tip which has been discussed earlier.

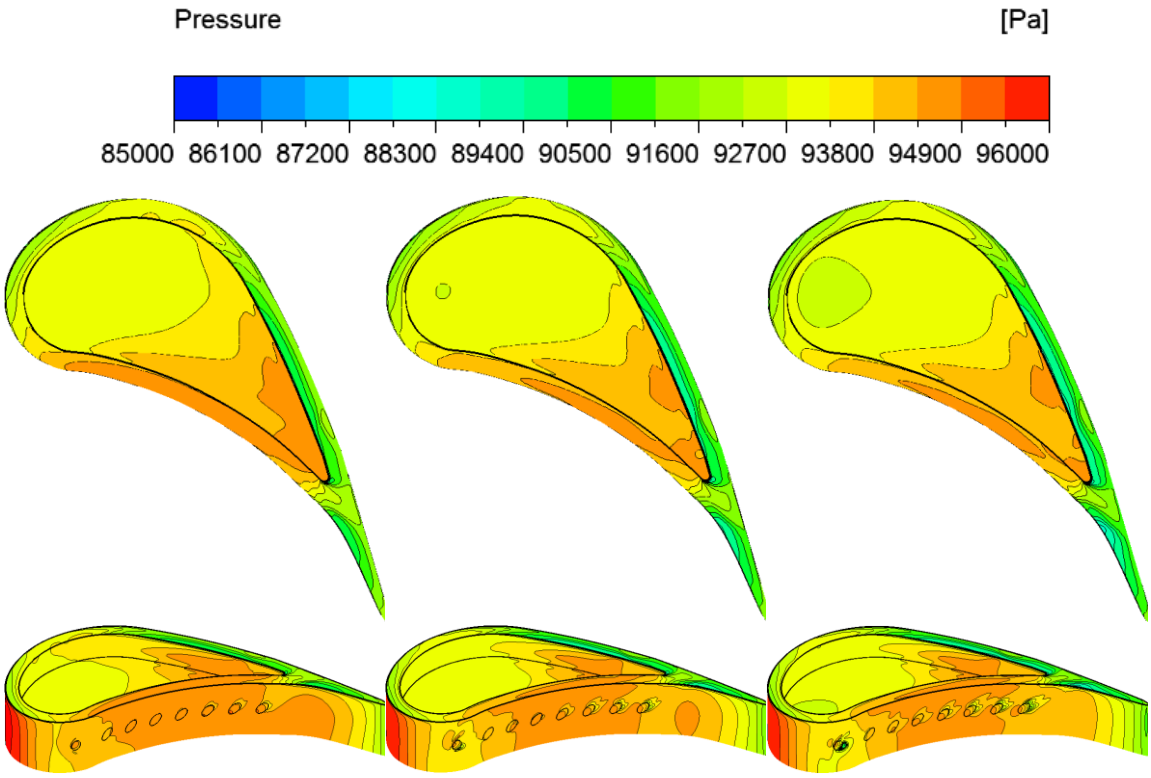

Figure 85: Impact of global blowing ratio on distributions of the static pressure near the blade tip region for squealer tip with pressure-side hole cooling at 3000 rpm.

Figure 86 depicts the streamlines near the blade tip region for squealer tip with pressure-side hole cooling at 3000 rpm, which reveals the local flow behaviors for three blowing ratios. It is shown that the presence of the squealer cavity significantly affects the local flow field near the tip region. Some mainstream particles are entrained in the squealer cavity, forming a few circulations in it. As a result most of the cavity space is occupied by the mainstream particles. These particles continue to travel towards the cavity trailing end and ultimately leak from the suction side, generating the tip vortices. It is noticed that a small amount of the coolant is able to cross the pressure-side rim and

enter the tip clearance since this part of coolant is altered by the pressure gradient and the momentum of leakage flow. Consequently, part of the pressure-side rim is cooled by the cooling film. However, since the coolant leaks from the rear portion of the blade tip, the cooling particles are unlikely to spread in the squealer cavity. Instead, they travel over the rim near the trailing edge. As a consequence, the cavity floor and inner wall is rarely cooled by the cooling film. In addition, the coolant jets tend to lift off the pressure surface when the blowing ratio is increasing and therefore smaller percentage of the coolant can go through the tip clearance and cool the blade tip.

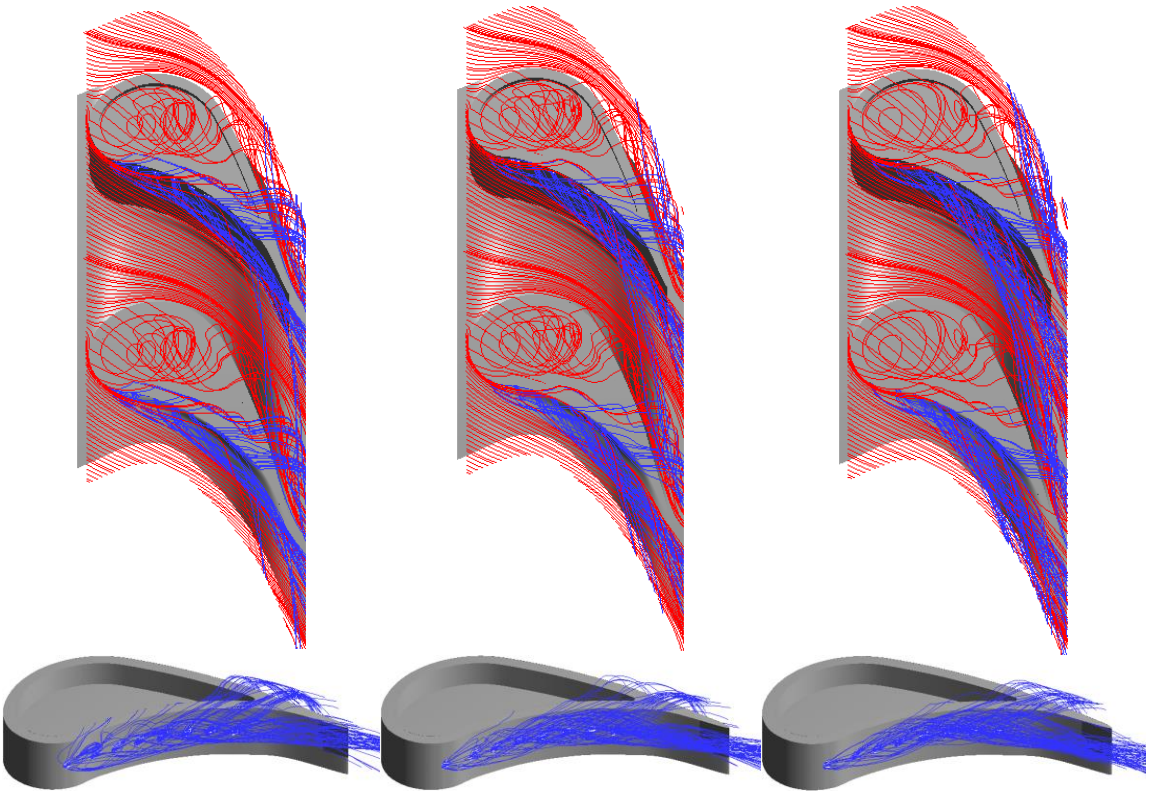

(a) M = 0.5 **(b) M = 1.0** **(c) M = 1.5**

Figure 86: Impact of global blowing ratio on streamlines based on the relative velocity near the blade tip region for squealer tip with pressure-side hole cooling at 3000 rpm (blue indicates cooling air, red is mainstream air).

The impact of the blowing ratio on the temperature distribution is shown in Figure 87. For M = 0.5, more part of the pressure-side rim is cooled by the cooling film since more coolant particles are pushed towards the suction side when the blowing ratio is lower. The cooled area of the pressure-side rim becomes smaller as the blowing ratio increases. However, the area of the aft of blade tip covered by the cooling film becomes larger if the blowing ratio grows, but lower temperature or cooling performance is seen at higher blowing ratios. Similar to the situation for plane tip, smaller blowing ratio can provide better cooling coverage on the pressure surface due to the easier reattachments of the coolant jets with lower momentum. Nevertheless for all three blowing ratios, no coolant particles are able to access the leading-edge and suction-side rims as well as the squealer cavity floor.

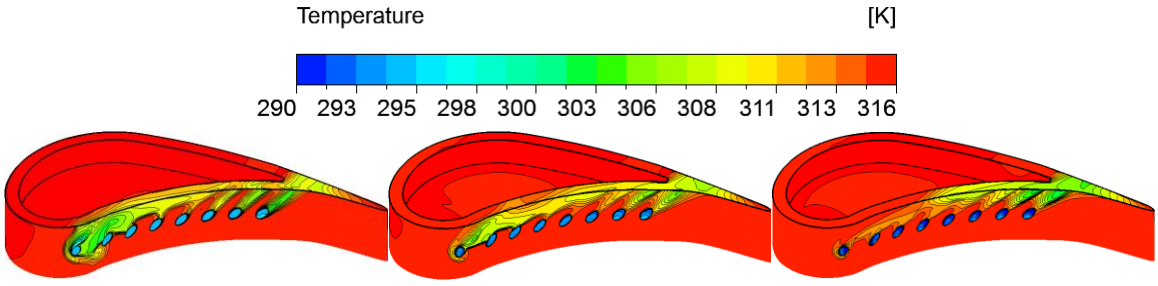

(a) M = 0.5 **(b) M = 1.0** **(c) M = 1.5**

Figure 87: Impact of global blowing ratio on distributions of the temperature near the blade tip region for squealer tip with pressure-side hole cooling at 3000 rpm.

8.1.2 Adiabatic film cooling effectiveness

8.1.2.1 Plane and squealer tips with tip hole cooling

Essentially the film cooling effectiveness is dimensionless temperature. Looking at the shape of the high effectiveness area, the shape has high coincidence with the trajectories of cooling jets. Hence the adiabatic film cooling effectiveness largely reflects the consequence of the flow behaviors. Many factors can affect the film cooling effectiveness. One of the critical parameters is the blowing ratio. Another one is the blade tip geometry. The plane tip is discussed first. At M = 0.5 (Figure 88 (a)), the trajectory of each hole appears as a narrow streak and can be clearly differentiated from each other due to the relatively small blowing ratio. The cooling effectiveness is around 0.3 within the coolant trajectories. The highest value of nearly 0.6 is obtained right at the downstream of the cooling-hole exits. The downstream cooling effectiveness is gradually decreased due to the diffusion of cooling jets and the mixing between the coolants and the leakage flow. As the blowing ratio increases to M = 1.0 (Figure 88 (b)), each coolant trajectory tends to diffuse more and thus covers more area. The trajectories of the cooling jets exiting from the first, the second and the seventh holes are easily identified, whereas a large area with high effectiveness appears in the vicinity of the rest of the cooling holes due to the coolant accumulation. It is noticeable that the highest film cooling effectiveness (above 0.7) is observed in the vicinity of the last four cooling holes. Around 50% area of the blade tip is covered by film cooling. In the case of M = 1.5 (Figure 88 (c)), the trajectory tends to be thicker and thus the film cooling performance is even better as expected. Higher film cooling effectiveness is achieved

especially when it comes to the last four cooling holes due to the coolant accumulation. More than 50% of the blade tip surface is well covered by the film coolant.

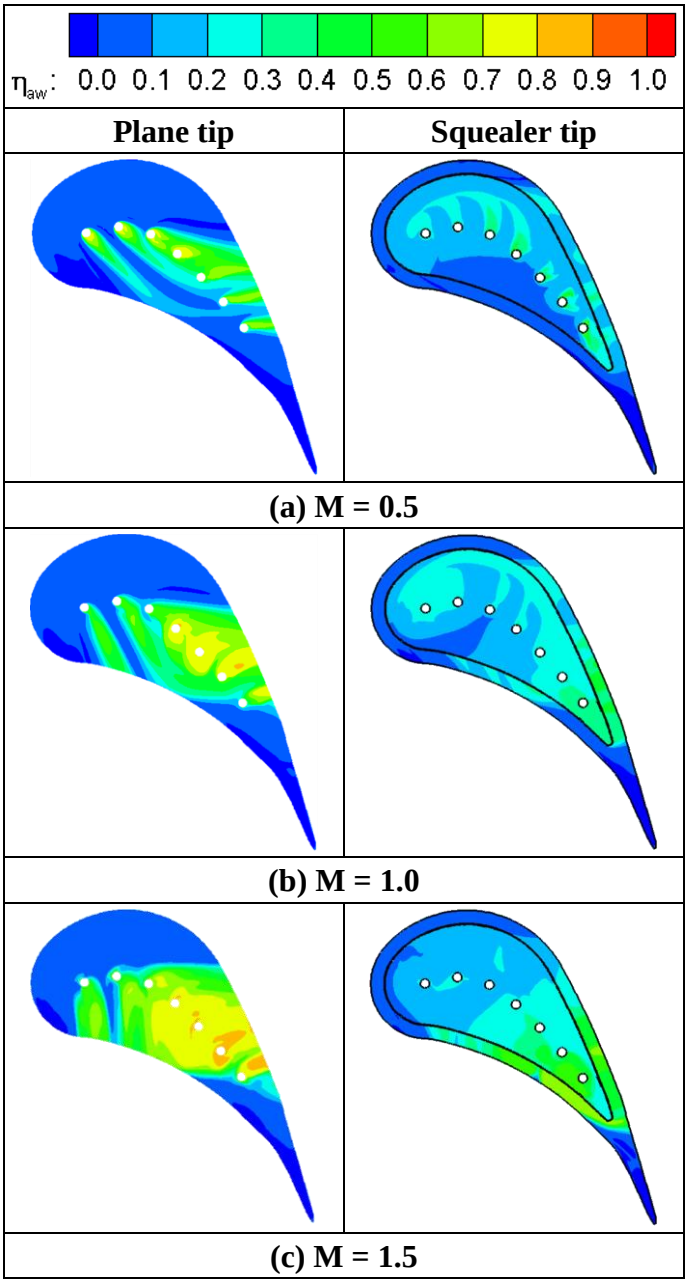

Figure 88: Impact of global blowing ratio on distributions of the adiabatic film cooling effectiveness for blade tips with tip hole cooling at 3000 rpm: Blade tip for the plane tip (left); Cavity floor and rim for the squealer tip (right).

The difference of the cooling capability among seven cooling holes can be explained by the local blowing ratio shown in the second figure on page 165. Because the coolant is discharged from the plenum, the pressure difference between the inlet and the exit of each cooling hole is hardly identical. This leads to different mass flow for each single hole and thus different local blowing ratio. Because of the relatively lower pressure at exit, the last four cooling holes eject more coolant and therefore create higher local blowing ratios. Accordingly, larger local blowing ratios provide locally higher film cooling effectiveness.

Different effectiveness contours were obtained when it comes to the squealer tip. At M = 0.5 (Figure 88 (a)), nearly the entire cavity floor is to some extent protected by the cooling film. Apparently the area of the cavity close to the pressure side is not cooled, whereas cooling effectiveness on the rest of the cavity floor is above 0.1. Effectiveness as high as 0.2 is observed within the flame-shaped streaks pointing from the cooling-hole exit to the suction side. The mechanism is illustrated in the figure (a) on page 151. The coolant particles participating in the suction-side circulation roll down and meet the cavity floor causing little mixing with the hot leakage flow. Therefore higher cooling effectiveness is obtained on the side of hole exit near suction side. The pressure-side circulation rolls up the rest of the coolant particles. Then the coolant is strongly mixed with the leakage flow. The mixture becomes hot before it reaches the cavity floor. Hence the cavity floor near the pressure side is less cooled than the area near the suction side. Relatively high effectiveness is obtained at the suction-side rim between 0.5 C_{ax} and 0.9 C_{ax} due to the leakage originating from the cavity. However, the rest of the rim has not

been protected by the film coolant. For M = 1.0 (Figure 88 (b)), those flame-shaped streaks disappear. Instead, a large area with relatively high effectiveness on the cavity floor is observed near the suction side and the trailing end of cavity. The reason is that the cooling jets penetrate higher towards the shroud due to higher momentum, which leads to better mixing and therefore more uniform cooling effectiveness. The resulted cooling effectiveness on the cavity floor close to the pressure side is slightly increased up to 0.1. Maximum effectiveness is found in the vicinity of the cavity trailing end due to the accumulation of coolant coming from the upstream. More coolant leaking from the suction side causes higher cooling effectiveness. It is noticed that part of the pressure-side rim has effectiveness as high as 0.2 since some coolant leaks across this area. Better film cooling is provided when the blowing ratio is raised to M = 1.5 (Figure 88 (c)), especially from 0.5 C_{ax} to 0.9 C_{ax}. Even higher cooling effectiveness at the suction-side rim and especially the pressure-side rim is obtained due to larger amount of coolant ejected. Furthermore, Figure 89 depicts the film cooling effectiveness on the cavity inner wall of the squealer tip. Spots with relatively high cooling effectiveness are observed near the cavity trailing end since the majority of the coolant travels downstream and the accumulation takes place. However, the effectiveness is not as high as that on the plane tip where the accumulation occurs. Apparently, the intense interactions between the coolant and the leakage flow considerably diminish the cooling effectiveness. In this study, more area of the squealer tip is protected by the film cooling when compared with the plane tip. However, the local cooling effectiveness on the squealer tip tends to be lower.

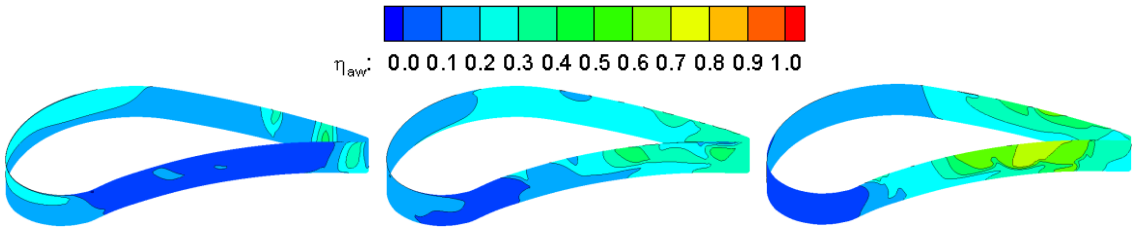

(a) M = 0.5 **(b) M = 1.0** **(c) M = 1.5**

Figure 89: Impact of global blowing ratio on distributions of the adiabatic film cooling effectiveness for the cavity inner wall of the squealer tip with tip hole cooling at 3000 rpm.

The impact of the local blowing ratio on the cooling effectiveness might be less important for the squealer tip. For high blowing ratios of M = 1.0 and 1.5, the local blowing ratio is almost identical for each cooling hole, as shown in Figure 90 (b). But the local blowing ratio monotonically goes down from the first hole to the seventh hole for M = 0.5. The possible reason is that the small amount of cooling flow is prone to be sensitive to the slight pressure difference.

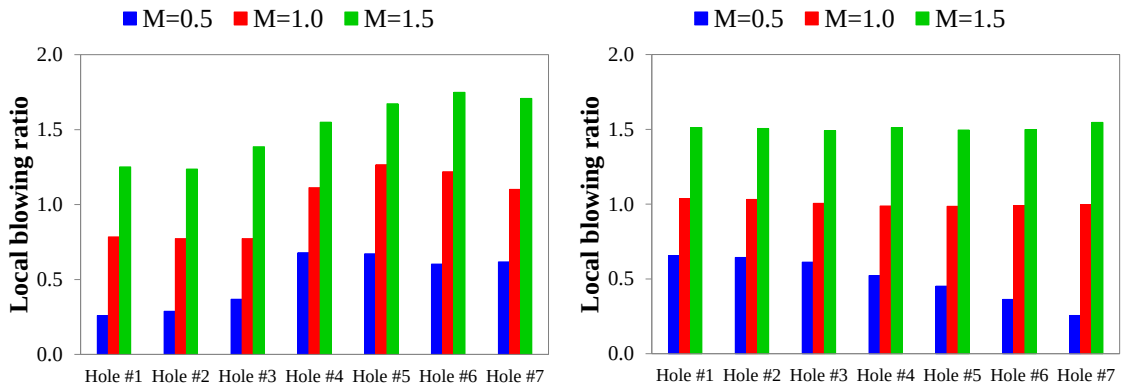

(a) **(b)**

Figure 90: Local blowing ratio for each cooling hole at 3000 rpm: (a) Plane tip with tip hole cooling, (b) Squealer tip with tip hole cooling.

The film cooling effectiveness at the blade tip region is pitchwise averaged and shown in Figure 91. The discussion is made for the plane tip first. It is seen that the coverage of the film cooling starts from nearly 0.15 C_{ax} and ends at 0.9 C_{ax}. For M = 0.5, the averaged value seems to gradually increase along the axial chord within the covered area. Seven peaks are observed and each of them represents the location of every film cooling hole. At M = 1.0, the averaged film cooling effectiveness is slightly lower than 0.2 from 0.2 C_{ax} to 0.4 C_{ax}. This area corresponds to the first three cooling holes which is consistent with the contour plots. However, the averaged value dramatically increases when it reaches 0.5 C_{ax}. Between 0.5 C_{ax} and 0.8 C_{ax}, the averaged film cooling effectiveness is as high as 0.4. This is due to the relatively large local blowing ratios of the rear four cooling jets. Even higher film cooling effectiveness is obtained when the blowing ratio reaches M = 1.5.

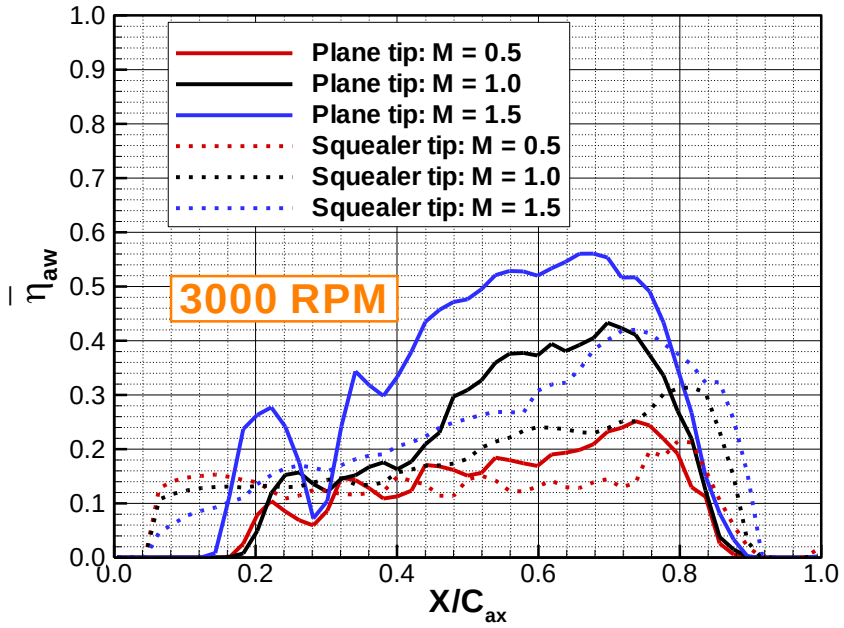

Figure 91: Impact of global blowing ratio on the pitchwise-averaged adiabatic film cooling effectiveness along axial chord for blade tips with tip hole cooling at 3000 rpm.

The squealer tip shows quite different trends in Figure 91. Note that the squealer tip is comprised of the squealer cavity floor, the squealer cavity inner wall, and the rim. The film cooling is effective from about 0.05 C_{ax} to 0.9 C_{ax} for all the blowing ratios. For M = 0.5, the pitchwise-averaged film cooling effectiveness is stabilized around 0.14 until it bumps up a bit at 0.8 C_{ax}. However, the averaged cooling effectiveness gradually grows from 0.1 to 0.3 when the blowing ratio becomes 1.0. A similar trend is obtained for the blowing ratio M = 1.5, but the average slope is slightly larger compared with M = 1.0. The highest value of 0.42 appears at about 0.7 C_{ax} where it is believed to be close to the cavity trailing end. In fact, the peak value is found in the same area for all three blowing ratios. Moreover, it is seen that the leading edge rim is not cooled at all, as well as the

trailing edge portion. Further, within 0.4 C_{ax} and 0.8 C_{ax}, the plane tip offers higher averaged cooling effectiveness than the squealer tip does.

The area-averaged film cooling effectiveness versus the blowing ratio at the blade tip region is shown in Figure 92. It is seen that the overall film cooling effectiveness for every part increases monotonically as the blowing ratio is increased. This is consistent with the contour plots in the figure on page 162 and the first figure on page 165. Note that the overall effectiveness on the plane tip is slightly lower than that on the squealer tip for M = 0.5. With increasing blowing ratios, the situation is altered. Higher overall effectiveness is obtained on the plane tip for both M = 1.0 and 1.5. The value reaches 0.32 for the plane tip at M = 1.5 whereas this number for the squealer tip is as high as 0.23. For the plane tip, the coolant accumulating in the vicinity of the rear four cooling holes partially blocks the leakage flow passing through and weakens the mixing process. Such accumulation significantly increases the local cooling effectiveness. This is essentially the result of the high blowing ratio and the tip-shroud relative motion. However, in case of the squealer tip, the mechanism is altered. On the one hand, higher blowing ratio delivers more coolant and thus higher effectiveness. On the other hand, it also causes stronger mixing of the coolant and the leakage flow, which to some extent weakens the cooling capability of the coolant. This is confirmed by looking at the averaged cooling effectiveness on both the cavity floor and the side wall at M = 1.5. As a result, the squealer tip with tip hole cooling does not provide as much protection as the plane tip under high blowing ratios. Additionally, among the three parts of the squealer tip, the cavity inner wall has the largest contribution on overall effectiveness. It is

observed that the rim of the squealer tip is the part least cooled for blowing ratios of M = 0.5 and 1.0 but gets improved at M = 1.5. Generally, higher blowing ratios corresponds to better film cooling performance on the blade tips. From the point of view of the overall film cooling effectiveness, the plane tip with M = 1.5 provides the best protection to the blade tip.

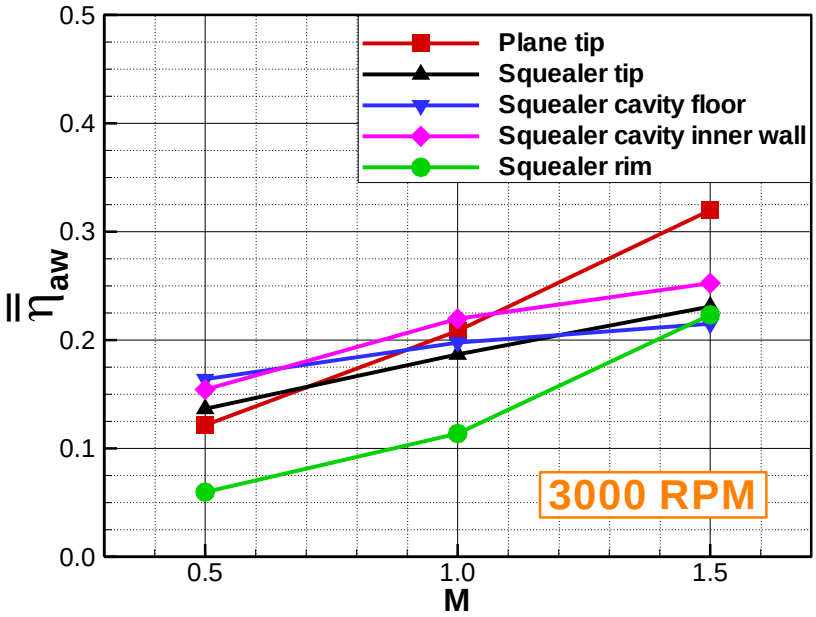

Figure 92: Impact of global blowing ratio on the area-averaged adiabatic film cooling effectiveness for blade tips with tip hole cooling at 3000 rpm.

8.1.2.2 Plane and squealer tips with pressure-side hole cooling

Figure 93 depicts the distributions of the adiabatic film cooling effectiveness for both the plane and squealer tips with pressure-side hole cooling with varying blowing ratios at 3000 rpm. For the plane tip (Figure 93 left), due to the impact of the flow incidence, the blade tip surface is cooled beyond approximately 0.5 C_{ax} and the corresponding coolant-

covered area is much less than 50% of the blade tip. At M = 0.5, a few streaks with high effectiveness can be seen from around 0.65 ~ 0.9 C_{ax}. These streaks are associated with the low-temperature areas in the figure on page 157. Similarly, these streaks become larger and more diffusive when the blowing ratio increases to 1.0. A patchy area with high effectiveness is obtained for M = 1.5. In these area with high effectiveness, the effectiveness magnitude is between 0.3 ~ 0.4, whereas approximately $\eta_{aw} \approx 0.1 \sim 0.2$ is obtained in other covered areas. The leading edge portion is not cooled at all no matter what blowing ratio is applied. In addition, the area covered by cooling film decreases with the increasing blowing ratio, since the cooling jets are easier to be altered at lower blowing ratio that is associated with smaller momentum. The distribution of the cooling effectiveness is consistent with the temperature distribution in the figure on page 157.

The distribution of film cooling effectiveness on the blade tip for the squealer tip (Figure 93 right) exhibits different characteristics from the plane tip. It is seen that the more portion of the pressure side rim is cooled at M = 0.5. The covered area shrinks as the blowing ratio increases. As explained above, the cooling jets with lower blowing ratio are more likely to be deflected due to their smaller momentum. However, higher local effectiveness is obtained when it comes to M = 1.5. The effectiveness magnitude is as high as 0.3 for M = 1.5 whereas it declines to about 0.15 for M = 0.5. The aft of the blade tip is almost covered for all three blowing ratios. However the effectiveness grows with the increasing blowing ratio. Additionally, the cavity floor and suction-side rim is not cooled at all no matter what blowing ratio is used. Therefore, the squealer tip with

pressure-side hole cooling provides worse protection of the tip surface when compared to the plane tip.

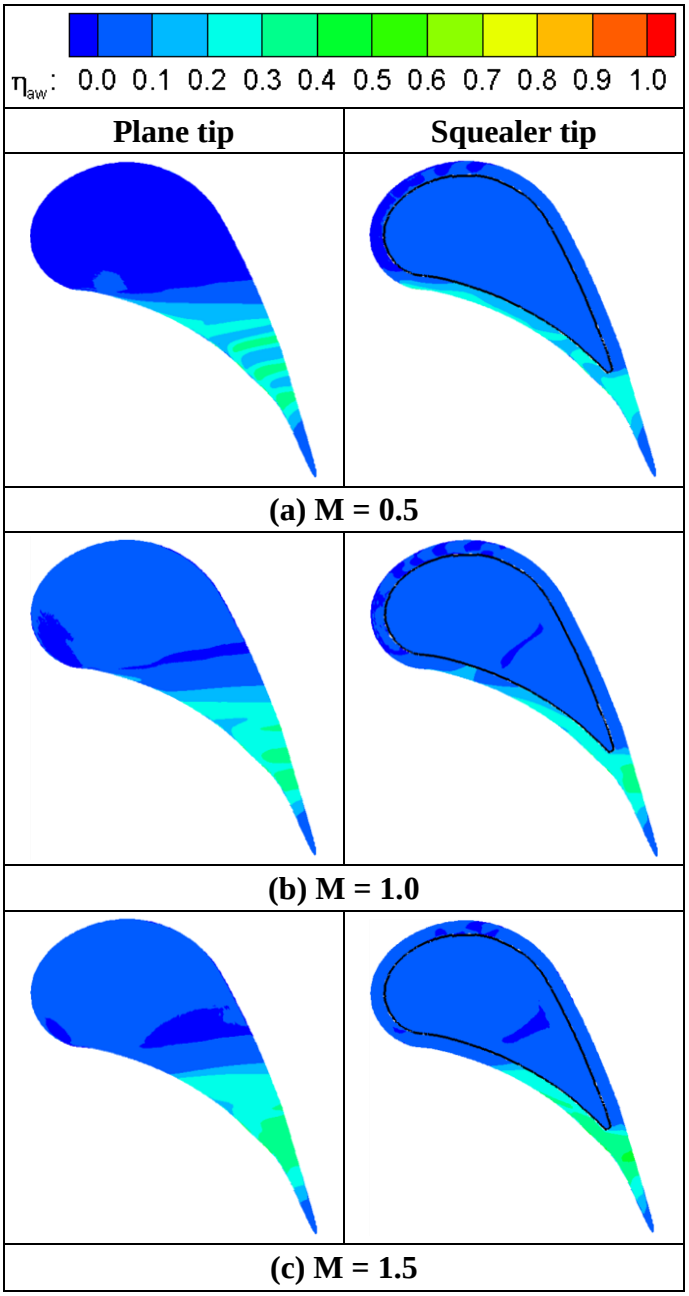

Figure 93: Impact of global blowing ratio on distributions of the adiabatic film cooling effectiveness for blade tips with pressure-side hole cooling at 3000 rpm: Blade tip for the plane tip (left); Cavity floor and rim for the squealer tip (right).

Figure 94 depicts the pitchwise-averaged film cooling effectiveness along the axial chord at both the plane and squealer tips with pressure-side hole cooling on the emphasis of the impact of blowing ratio. Unlike the tip hole cooling, the direct impact of the cooling holes on the cooling effectiveness is absent at the blade tip for the pressure-side hole cooling. Therefore the curves for the averaged effectiveness look quite smooth. For the plane tip, it is seen that the averaged effectiveness is approximately zero between the leading edge and 0.5 C_{ax}. Beyond the mid-chord, the averaged effectiveness starts to increase along the axial chord and achieves its maximum at around 0.9 C_{ax}. Then the effectiveness quickly drops to nearly zero at the trailing edge. Such single-wave-shape distribution of the averaged effectiveness can be seen for all the blowing ratios. However, the peak value tends to be larger as the blowing ratio enhances. By seeing the averaged effectiveness distribution, the cooling film ejecting from the pressure side can cover the tip surface between 0.5 C_{ax} and 0.95 C_{ax} for the plane tip. Therefore only the aft of the blade tip which is only a small portion is cooled. The averaged effectiveness distribution also looks similar to a single wave for the squealer tip. However the primary portion of the "wave" extends from around 0.8 C_{ax} to 0.95 C_{ax} which is as wide as half of that for the plane tip. Apparently the presence of the squealer cavity dramatically reduces the coolant coverage. Likewise, the maximum effectiveness decreases with the increasing blowing ratio.

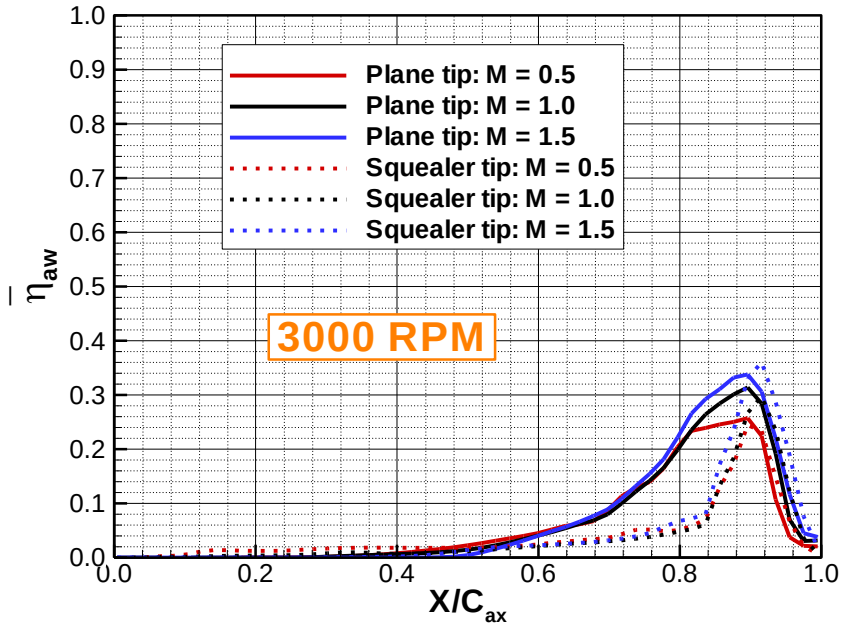

Figure 94: Impact of global blowing ratio on the pitchwise-averaged adiabatic film cooling effectiveness along axial chord for blade tips with pressure-side hole cooling at 3000 rpm.

The area-averaged cooling effectiveness versus blowing ratio for both the plane and squealer tips with pressure-side hole cooling is shown in Figure 95. As seen, increasing the blowing ratio can result in slow growth in the overall cooling effectiveness for both the plane and squealer tips. The magnitude for the plane tip is approximately 0.05 whereas for the squealer tip is more than 50% lower. As shown, the coolant is unable to protect the squealer cavity floor and inner wall since the overall effectiveness is too small that can be neglected. However on average, the highest effectiveness is obtained on the squealer rim since certain area of the rim is more or less covered by the cooling film. Overall, the pressure-side hole cooling is not able to provide effective protection for either the plane or squealer tips no matter what blowing ratio is applied.

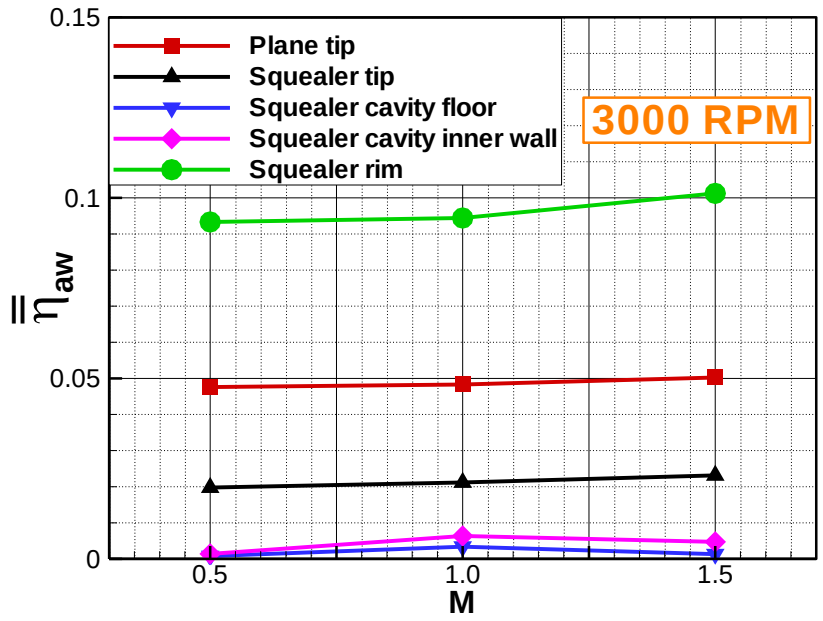

Figure 95: Impact of global blowing ratio on the area-averaged adiabatic film cooling effectiveness for blade tips with pressure-side hole cooling at 3000 rpm.

8.1.3 Heat transfer

8.1.3.1 Plane and squealer tips with tip hole cooling

Figure 96 depicts the distributions of Nusselt number for both the plane and squealer tips with tip hole cooling at 3000 rpm. In this section, to study the impact of the blowing ratio on the Nusselt number, three different global blowing ratios with relatively low, medium and high levels are investigated while the rotational speed is fixed at 3000 rpm. Apparently due to the difference in the geometric configurations and thus the distinct flow behaviors, very different distributions of the Nusselt number are obtained for the plane tip and squealer tip relatively. For the plane tip, a crescent-like area with high Nu occupies a part of the leading edge for all three blowing ratios. As shown in the figure on page 146, the ejected coolant particles are not able to access to this portion of leading

edge. Therefore the locally high Nusselt number is due to the formation of tip leakage flow when the mainstream flow is squeezed through the tiny tip gap.

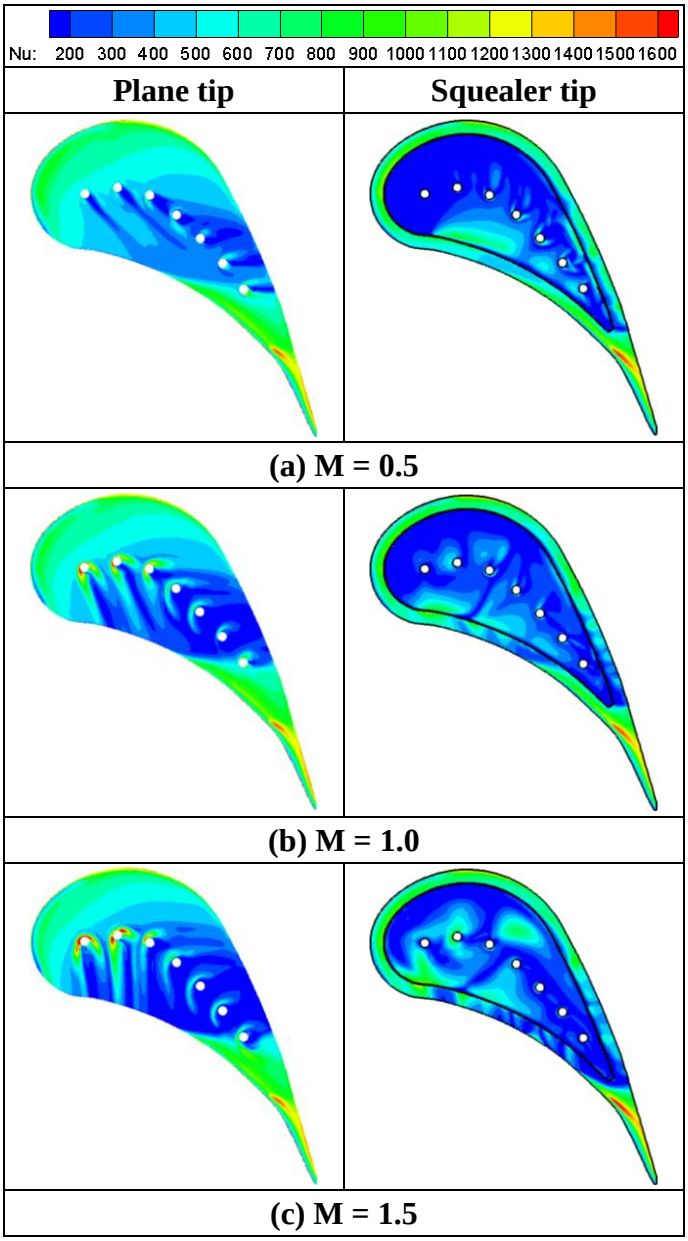

Figure 96: Impact of global blowing ratio on distributions of the Nusselt number for blade tips with tip hole cooling at 3000 rpm: Blade tip for the plane tip (left); Cavity floor and rim for the squealer tip (right).

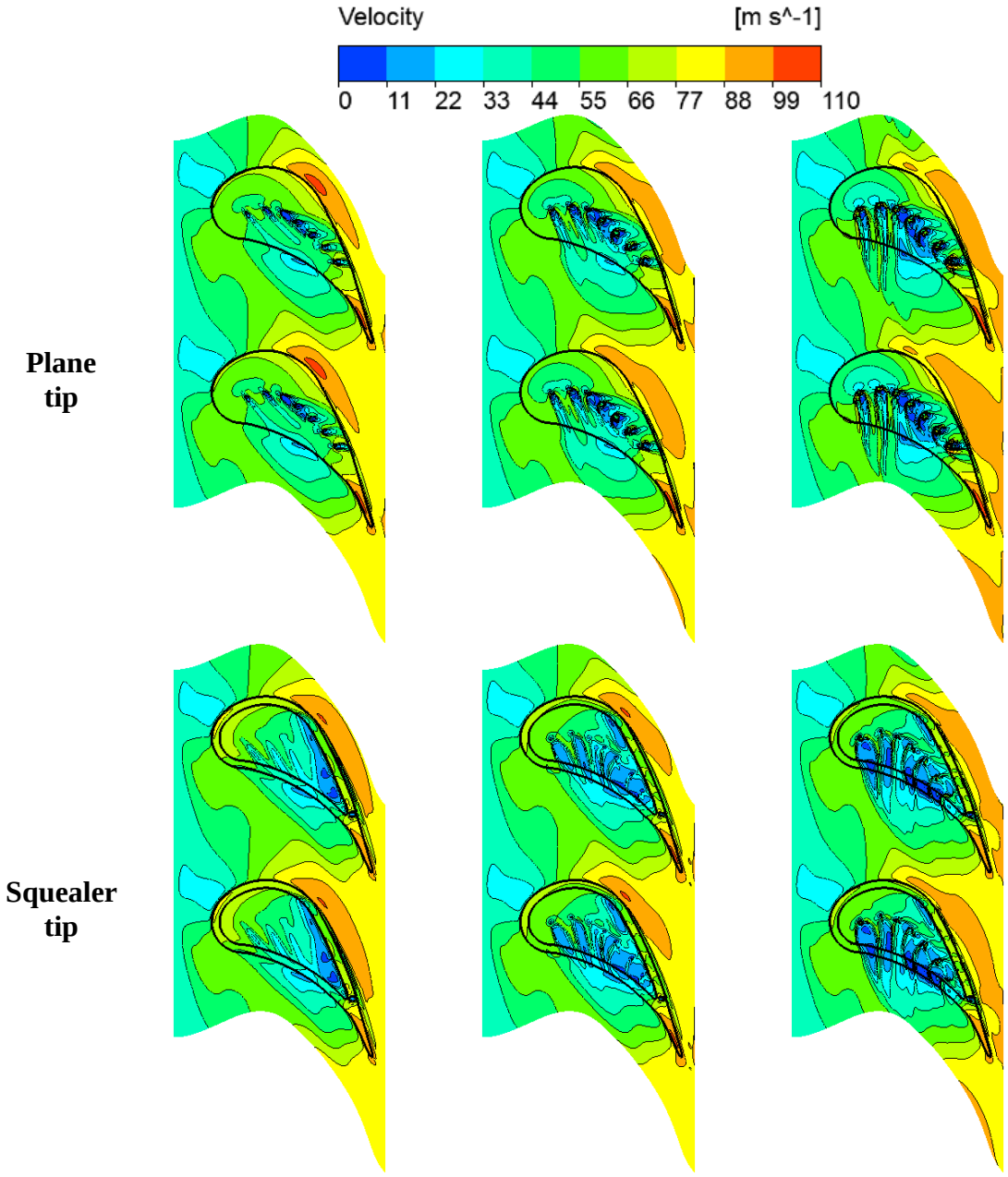

Figure 97: Impact of global blowing ratio on distributions of relative velocity at mid-tip-gap (colored with velocity magnitude) for tip hole cooling at 3000 rpm.

During this process, the mainstream flow particles are accelerated due to the high pressure at the stagnation point as shown in Figure 97, which is also necessarily

associated with the high Nusslet number. In addition, the particularly thin boundary layer attached to the tip surface can help to enhance the convective heat transfer as well. Regarding the portion with high Nu at the suction side, it is largely associated with the flow particles being accelerated even more (Figure 97) due to the local big pressure gradient as shown in the figure on page 144. However, the magnitude of Nu gradually declines as the leakage flow is approaching to the upstream three cooling holes. Since the cooling holes are perpendicular to the blade tip surface, the coolant jets are ejected radially and therefore orthogonal to the leakage flow direction. As a result, the radial coolant jets to some extent block the tip clearance through which the leakage flow is passing. Consequently, high pressure and corresponding low velocity (Figure 97) are obtained locally. Hence the Nu progressively decreases along with the flow deceleration. In the middle portion of the blade tip ranging from about 0.2 to 0.8 C_{ax}, the lowest Nu is seen in this region. By comparing it with the figure on page 162, one can find out that the low Nu region coincides with the high cooling effectiveness area that is well covered by the cooling film. Essentially, this is due to the locally low flow speed as shown in Figure 97. Most importantly, the coolant jets exit from the cooling holes in the radial direction that is perpendicular to the leakage flow. As a consequence, the momentum of both the cooling jets and leakage flow considerably drops due to the intense mixing and associated dissipation. Therefore, the relatively slow flow and thus low Nu occurs in the area that is well covered by the cooling film. However, high Nu can be seen in the vicinity of the cooling hole exits. For both M = 1.0 and 1.5, there are streaks with high Nusselt number appearing by both sides of the cooling holes, whose directions are

parallel to the local flow directions. These streaks are formed by the vortices that are induced when the incoming leakage flow encounters the cooling jets. Larger blowing ratio corresponds to streaks with higher Nu due to more effective blockage provided by the cooling jets with greater momentum. Thus such streaks can hardly be seen for M = 0.5 since the coolant with weak momentum is immediately blown away once exiting the cooling holes. Moreover, high Nu can be observed at the aft of the blade tip for each blowing ratio. Both the area shape and Nu magnitude are independent to the blowing ratio because it is not covered by the cooling film at all. The high Nu that occurs at this place is caused by the significant flow acceleration due to the expansion process.

As mentioned earlier, the distribution of Nu for the squealer tip differs a lot from that for the plane tip due to the geometries and therefore the flow characteristics, as show in the figure on page 175. For all three blowing ratios, high Nu can be observed at the leading-edge rim. This should be attributed to the behaviors of leakage flow. The mainstream flow particles are entrained into the squealer cavity while travelling downstream, which forms relatively high local flow speed over the squealer rim as shown in the figure on page 176. As a result, the local Nu is enhanced by the flow acceleration. The location is quite similar to the plane tip however the Nu level is higher. This is due to the higher local velocity for the squealer tip, since the leakage flow is not directly blocked by the radially ejecting coolant jets. The Nusselt number on the cavity floor has the lowest level and quite uniform distribution for all three blowing ratios. Such pattern is determined by the flow behaviors within the squealer cavity. Due to the strong mixing and flow circulations in the cavity as explained in section 8.1.1, the flow

speed in the cavity is much lower than leakage flow as shown in Figure 98 (b). As seen unlike the plane tip (Figure 98 (a)), the leakage flow squeezes through the tiny tip gap and suddenly expands into the squealer cavity. The immediate expansion dramatically reduces the flow velocity and thus momentum. Accordingly, the slow cavity flow is able to keep the Nusselt number on the cavity floor at a low level. However a few spots with higher Nu can be seen on the cavity floor close to the pressure-side rim. It can be attributed to the vortex system formed by the mixing of leakage flow and coolant that travels along the pressure-side rim. More high Nu spots appear at the cavity floor for M = 1.5. The possible reason is that the coolant jets with high momentum split the leakage flow into two separated vortices at both sides of the mean camberline where the cooling holes locate. Moreover, the Nu at the pressure-side rim drops as the blowing ratio increases. Since the cooling jets are more likely to penetrate the cavity flow at high blowing ratios, the flow momentum and therefore the velocity is largely reduced during the mixing and interactions with the leakage flow. Eventually a small amount of flow leaks from the pressure-side tip gap at quite low speed as shown in the figure on page 176. It also shows that higher blowing ratio can cause more flow leaking from the pressure side and thus lower Nu on pressure-side rim. High Nu is obtained at the suction-side rim regardless the magnitude of the blowing ratio, because most of the leakage flow exits the tip gap from the suction side where the flow particles are accelerated by the pressure gradient. In addition, the aft of blade tip also experiences high Nu due to the flow expansion in the rotor which is similar to the plane tip.

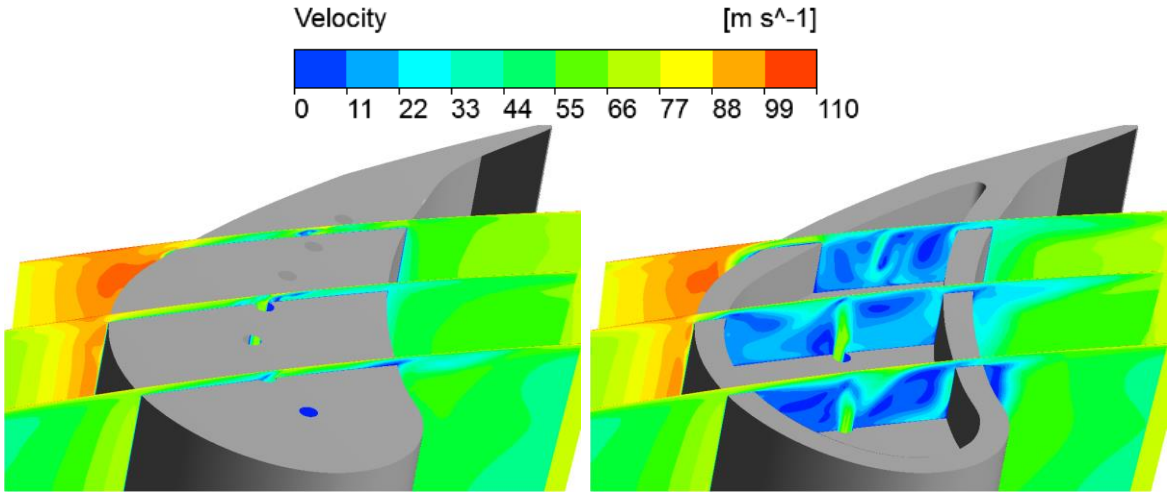

(a) **(b)**

Figure 98: Relative velocity contours (colored with velocity magnitude) at three axial locations for tip hole cooling with (a) plane tip and (b) squealer tip at M = 1.0, 3000 rpm.

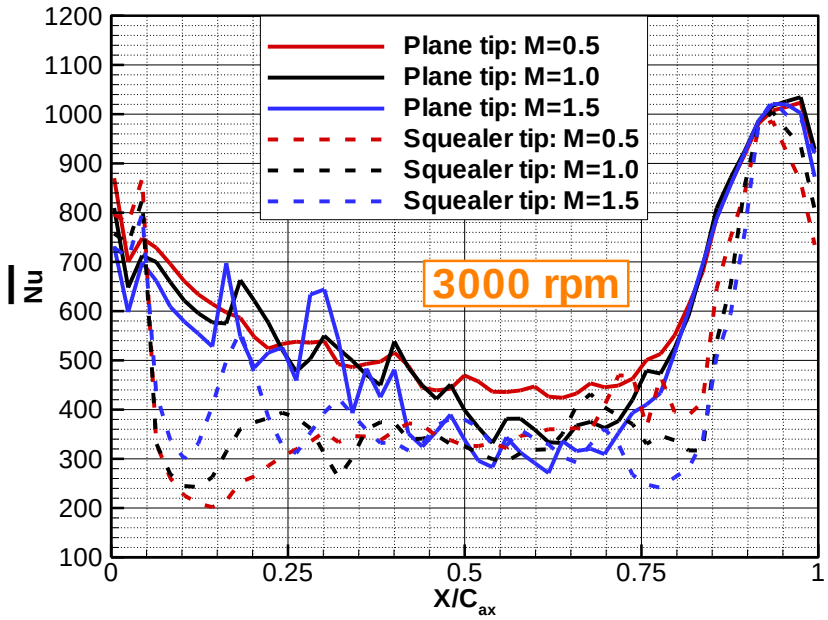

Figure 99: Impact of global blowing ratio on the pitchwise-averaged Nusselt number along the axial chord for blade tips with tip hole cooling at 3000 rpm.

Figure 99 depicts the pitchwise-averaged Nusselt number along the axial chord for both the plane and squealer tips with tip hole cooling at 3000 rpm. As seen, for the plane tip the averaged Nu gradually drops along the axial chord from the leading edge to approximately 0.15 C_{ax} for all three blowing ratios. Moreover, the magnitude of the averaged Nusslet number goes down as the blowing ratio increases. As explained earlier, the decline in Nu is due to the blockage effect of the cooling jets. Higher blowing ratio provides greater blocking capability therefore the Nu is reduced as the blowing ratio grows. However, such trend is interrupted by a few pulses appearing from 0.15 C_{ax} to about 0.4 C_{ax}. These pulses are associated with the vortices formed by the interaction and mixing of leakage flow and cooling jets in the vicinity of the hole exits. The blowing ratio is higher, the vortices are stronger and thus the local $\overline{\mathrm{Nu}}$ is more intense. Nevertheless, the overall trend keeps going down in the averaged Nu along the axial chord. The averaged Nu continues to drop down but in a slower speed for all the blowing ratios between 0.4 C_{ax} to about 0.65 C_{ax}. This is due to the further deceleration of leakage flow in the region. The small pulses reflect the locations of the cooling holes. Since the velocity of leakage flow is further reduced and the downstream cooling holes stay in the wake of upstream cooling jets, the averaged Nu fluctuates but in a moderate level. Again, higher blowing ratio is corresponding to smaller averaged Nu. Beyond 0.65 C_{ax}, the averaged Nu grows very fast because the flow keeps expanding and the impact of the film cooling fades quickly in this area. The peak value is achieved at approximately 0.95 C_{ax}. The reduction near the trailing edge might be due to some locally slight separation.

The distribution of pitchwise-averaged Nusslet number shows significant differences when it comes to the squealer tip. From leading edge to about 0.05 C_{ax}, the averaged Nu is a bit higher than that for the plane tip and decreases with the blowing ratio. It is associated with the leading edge rim where the leakage flow crosses over in a high speed. Then the magnitude of Nusselt number suddenly drops below 300, which indicates the starting point of the squealer cavity. However, the averaged Nu starts to grow till 0.2 C_{ax}. This should be attributed to the large Nu at both pressure-side and suction-side rims. In addition, larger blowing ratio may lead to stronger mixing in the cavity and thus higher averaged Nu. As shown, the Nusslet number remains around 300 for the most of cavity floor ranging from 0.3 C_{ax} to about 0.7 C_{ax}. The averaged magnitude is smaller almost everywhere than that for the plane tip. As discussed, the low level of averaged Nu is benefited from the slow cavity flow due to the sudden expansion and momentum dissipation. Further, it is noticed that the impact of the blowing ratio on averaged Nu is negligible within the squealer cavity. Similarly, the averaged Nu climbs up fast from cavity downstream and exhibits the same trend as the plane tip.

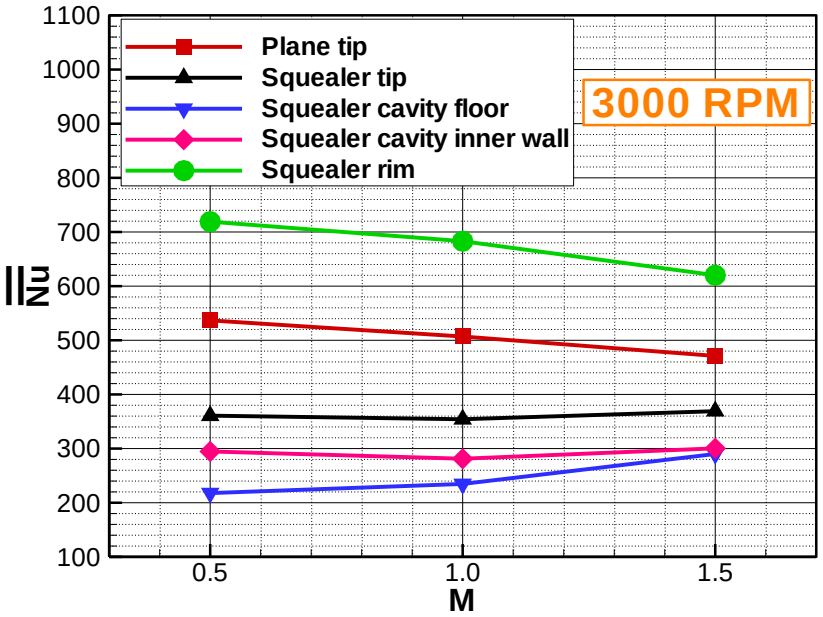

Figure 100: Impact of global blowing ratio on the area-averaged Nusselt number for blade tips with tip hole cooling at 3000 rpm.

The impact of the global blowing ratio on the area-averaged Nusslet number for both the plane and squealer tips with tip hole cooling is shown in Figure 100. As seen, the overall Nusslet number monotonically decreases with the increasing blowing ratio for the plane tip. In contrast, the area-averaged Nu for the squealer tip nearly remains as constant, which could almost be considered as independent to the blowing ratio. Therefore, increasing the blowing ratio will be helpful to reduce the overall Nu for the plane tip however it has little influence on the squealer tip. Additionally based on the blowing ratios studied, the squealer tip is capable to reduce the overall Nu approximately 22% ~ 33% when compared to the plane tip. However, the squealer rim suffers from the highest overall Nusince the leakage flow is dramatically accelerated when crossing over the thin rim. As expected, the lowest overall Nu on the cavity floor is obtained for all the

blowing ratios although larger blowing ratio can enhance the Nu at the floor. The relevant mechanisms have been pointed out earlier.

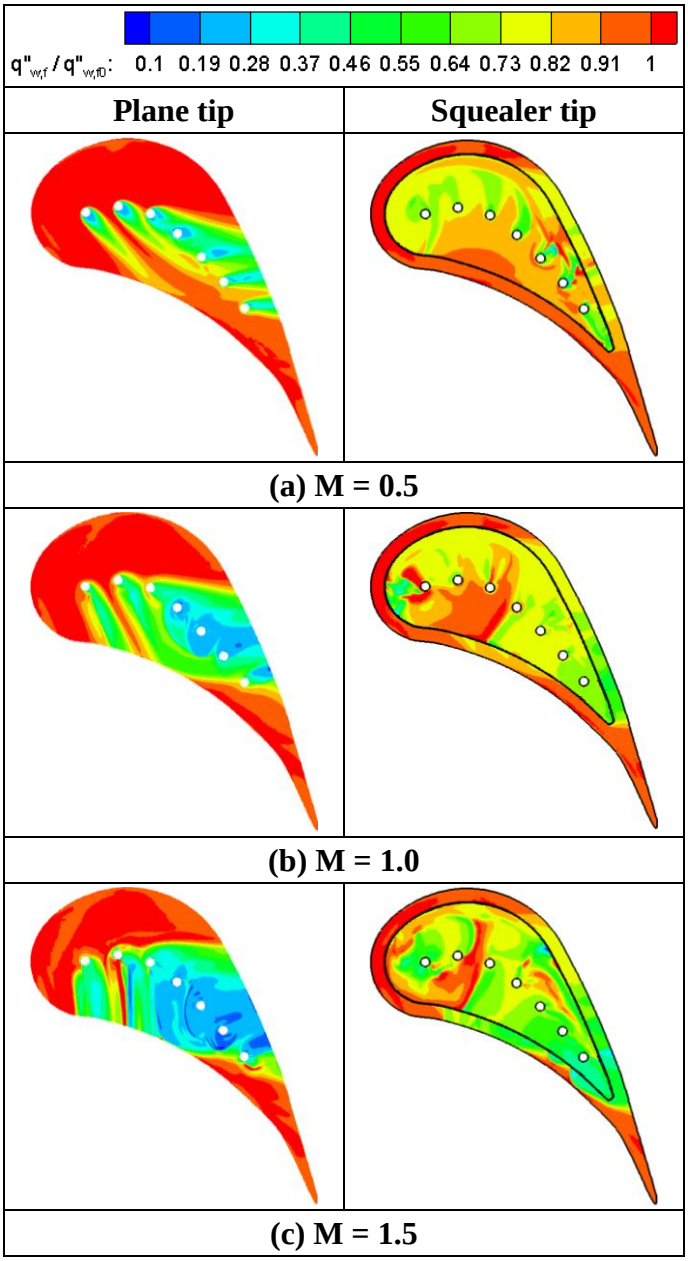

Figure 101: Impact of global blowing ratio on distributions of the heat flux ratio for blade tips with tip hole cooling at 3000 rpm: Blade tip for the plane tip (left); Cavity floor and rim for the squealer tip (right).

Figure 101 depicts the impact of blowing ratio on the heat flux ratio for both the plane and squealer tips with tip hole cooling rotating at 3000 rpm. Apparently the distribution of heat flux ratio on the plane tip exhibits dramatically different characteristics when compared to that for the squealer tip. However, one may find out the connections among the distributions of heat flux ratio, cooling effectiveness and Nusselt number after comparing the figures on pages 162, 175 and Figure 101. Apparently the low heat flux ratio is corresponding to the high cooling effectiveness and low Nu. For the plane tip, the area with relatively low heat flux ratio is almost as same as the high-effectiveness region. It is very straightforward that better cooling effectiveness will result in less heat load. Further, the cooling film also reduces the Nu on the plane tip which leads to the decline in the heat load. In contrast the portions that are not covered by the cooling film is experiencing high heat load, such as the leading edge and trailing edge. It is evident that the heat load on the plane tip decreases as the blowing ratio grows. The situation becomes a bit complicated with the squealer tip. Again the part of squealer rim with low heat flux ratio is consistent with the high-effectiveness area. As seen, the suction-side rim suffers less heat load for all the blowing ratios. And more amount of coolant leaks from the pressure side with the increasing blowing ratio and therefore the heat load on the pressure-side rim drops as more coolant is ejected. Relatively low heat flux ratio is seen at the squealer cavity floor too. Due to the strong mixing and interactions within the squealer cavity, more or less reduction in heat load is obtained for almost all the floor surface area. Particularly, the lowest heat load appears at the trailing end of the squealer cavity since the majority of leakage flow along with the

coolant accumulates here before exiting the tip clearance from the suction side. Meanwhile, the leading-edge rim and trailing edge suffer from high thermal load due to the lack of cooling. It is expected to reduce the heat load for squealer tip by increasing the blowing ratio too.

The pitchwise-averaged heat flux ratio along the axial chord at the plane and squealer tips are plotted for three blowing ratios in Figure 102. As seen for the plane tip, the heat flux ratio starts to drop from about 0.15 C_{ax} and keeps going down till around 0.75 C_{ax} where is well covered by the cooling film. Beyond 0.75 C_{ax} the heat load quickly climbs up again and goes back to 1 at approximately 0.9 C_{ax}. The rear 0.1 C_{ax} is not cooled at all. Overall less heat load is added to the plane tip as more coolant is ejected as shown in Figure 102. The sudden pulse at nearly 0.3 C_{ax} for M = 1.5 is due to the gap between the first two upstream cooling jets. In addition it is noted that more than 50% of heat load is reduced between 0.5 C_{ax} and 0.75 C_{ax} when blowing ratio reaches 1.5. Similar trend is seen for the squealer tip. However, the heat load reduction occurs between 0.05 C_{ax} and 0.9 C_{ax} which is wider than the plane tip due to the presence of the squealer cavity. Nevertheless, the reduction rate is not as high as the plane tip at the middle portion of the blade tip where is well cooled by the same amount of coolant. Also the heat load reduction enhances as the blowing ratio increases for the squealer tip.

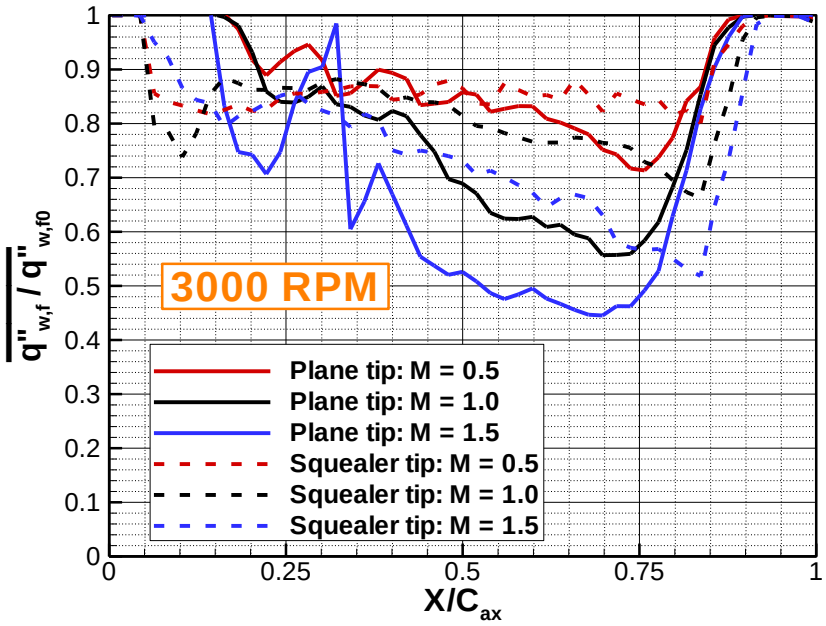

Figure 102: Impact of global blowing ratio on the pitchwise-averaged heat flux ratio along the axial chord for blade tips with tip hole cooling at 3000 rpm.

Figure 103 summarizes the impact of blowing ratio on the area-averaged heat flux ratio at the plane and squealer tips with tip hole cooling. As shown, the averaged heat flux ratio declines with the increasing blowing ratio for both the plane and squealer tips. At M = 0.5, the squealer tip has lower heat load than the plane tip. This should be attributed to the low Nu and somewhat cooling effectiveness at the cavity floor. However, as the blowing ratio increases, the averaged heat flux ratio at the plane tip drops faster than the squealer tip. The primary reason could be that the stronger mixing and interactions between the leakage flow and cooling jets in the cavity to some extent suppress the augmentation in the film cooling capability. In addition, higher-momentum cooling jets associated with the larger blowing ratio are able to push more coolant directly leaking from the tip gap rather than participating to the circulations within the

squealer cavity. It is seen that over 30% of the reduction in heat load for the plane tip at M = 1.5 whereas less than 25% is for the squealer tip. The other portions of the squealer tip also obtain the same trend as the blowing ratio increases. The squealer rim encounters highest heat load where there is least cooled and the local Nu is high. In sum, the variation in the blowing ratio can cause more substantial influence on the averaged heat load at the plane tip than the squealer tip. In other words, the reduction in the averaged heat load responds more quickly to the increasing blowing ratio for the plane tip.

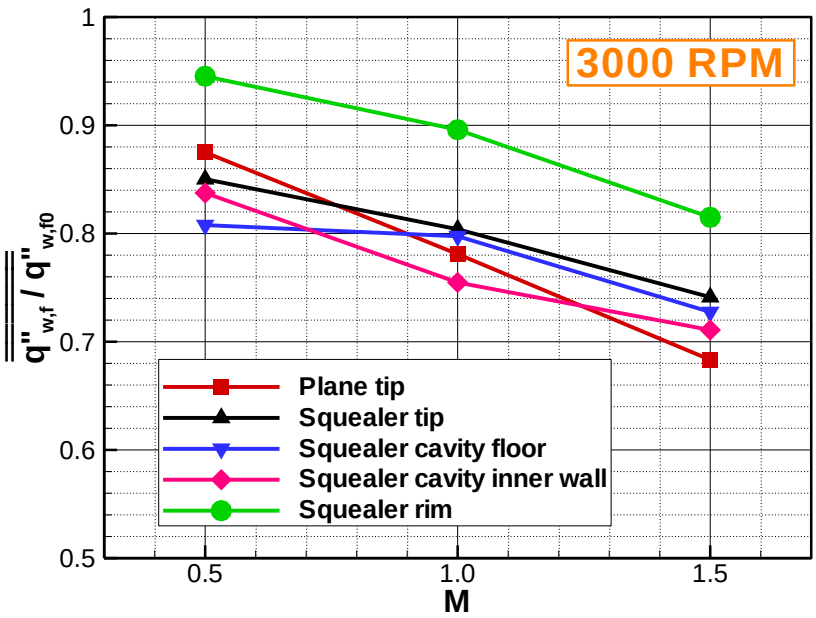

Figure 103: Impact of global blowing ratio on the area-averaged heat flux ratio for the blade tips with tip hole cooling at 3000 rpm.

8.1.3.2 Plane and squealer tips with pressure-side hole cooling

The impact of blowing ratio on the distributions of the Nusselt number at both the plane and squealer tips with pressure-side hole cooling rotating at 3000 rpm is shown in

Figure 104. As expected, the distinct characteristics are illustrated at the plane tip and squealer tip respectively. For the plane tip, a crescent-shaped area with high Nu is seen close to the leading edge at all three blowing ratios. This is associated with the acceleration of mainstream when entering the tip gap. Moreover, the "sweet spot" that corresponds to low Nu appears nearly at the middle part of the blade tip for all three blowing ratios. The earlier discussion indicates that only the rear portion of the blade tip is affected by the cooling jets. Therefore the Nu distribution at the front half of blade tip is independent to the blowing ratio. The rear half portion of blade tip experiences high Nu due to the passing through of the cooling film. Particularly a few spots with high Nusselt number can be seen close to the pressure side, which is essentially due to the re-attachment of the cooling jets. As seen, the larger blowing ratio causes higher Nu at the rear portion of blade tip.

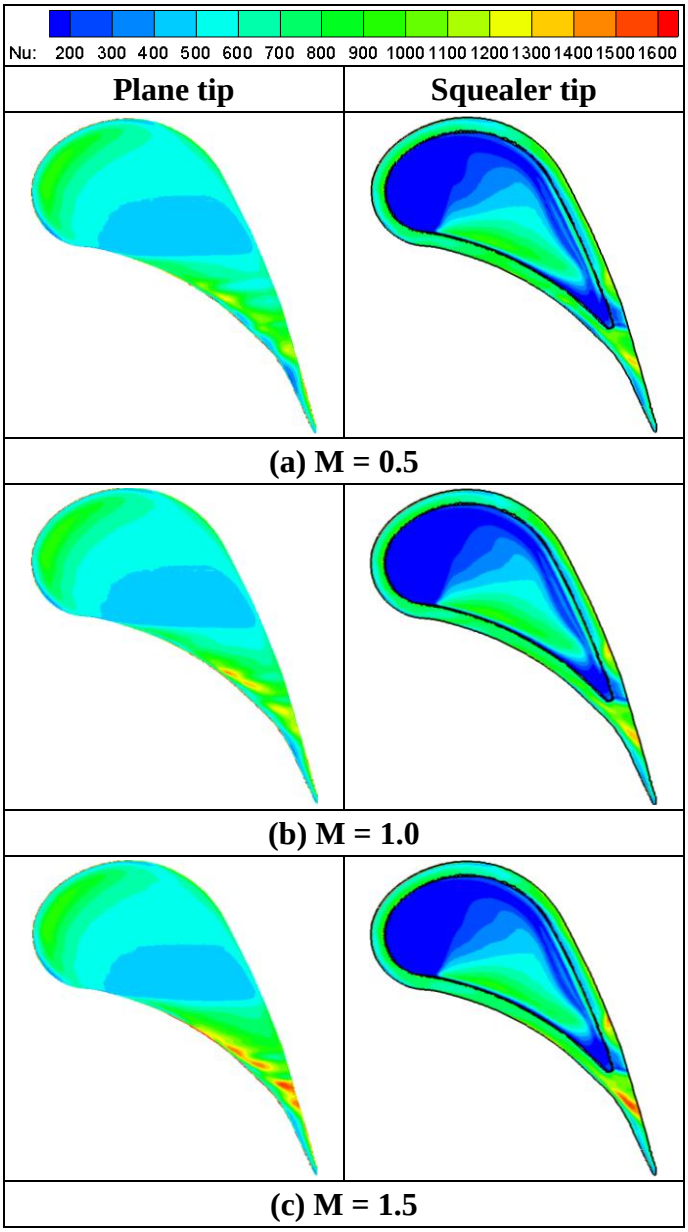

Figure 104: Impact of global blowing ratio on distributions of the Nusselt number for blade tips with pressure-side hole cooling at 3000 rpm: Blade tip for the plane tip (left); Cavity floor and rim for the squealer tip (right).

Figure 105, which depicts the velocity magnitude at the mid-tip-gap for both the plane and squealer tips with three blowing ratios, is able to help explain the relevant mechanism. At M = 0.5, there is an elliptical area with low velocity close to the pressure-side surface of the rear blade portion. This is due to the mixing and interaction between the mainstream and cooling jets which have lower momentum. As a result, the momentum of leakage flow is to some extent reduced and accordingly the velocity within the tip gap declines as well. Therefore the local Nu is relatively low, however grows with the increasing blowing ratio since the velocity of leakage flow rises. Similar trend takes place at the aft of blade with the squealer tip as shown in both Figure 104 and Figure 105. However, due to the presence of squealer cavity, smaller area of the rear portion of blade tip is influenced by the blowing ratio. As expected, the entire rim surface undergoes high Nu. The flow acceleration over the leading-edge and suction-side rim causes high Nu whereas the re-attachment of cooling film leads to high Nu on the pressure-side rim. It is noticed that delta-shape area at the cavity floor close to the pressure-side rim suffers much higher Nu than the rest portion of cavity floor. This is due to the reattachment of leakage flow on the cavity floor as seen in the figure on page 159. The low-speed cavity flow is able to keep Nu in the rest area of cavity floor at the lowest level.

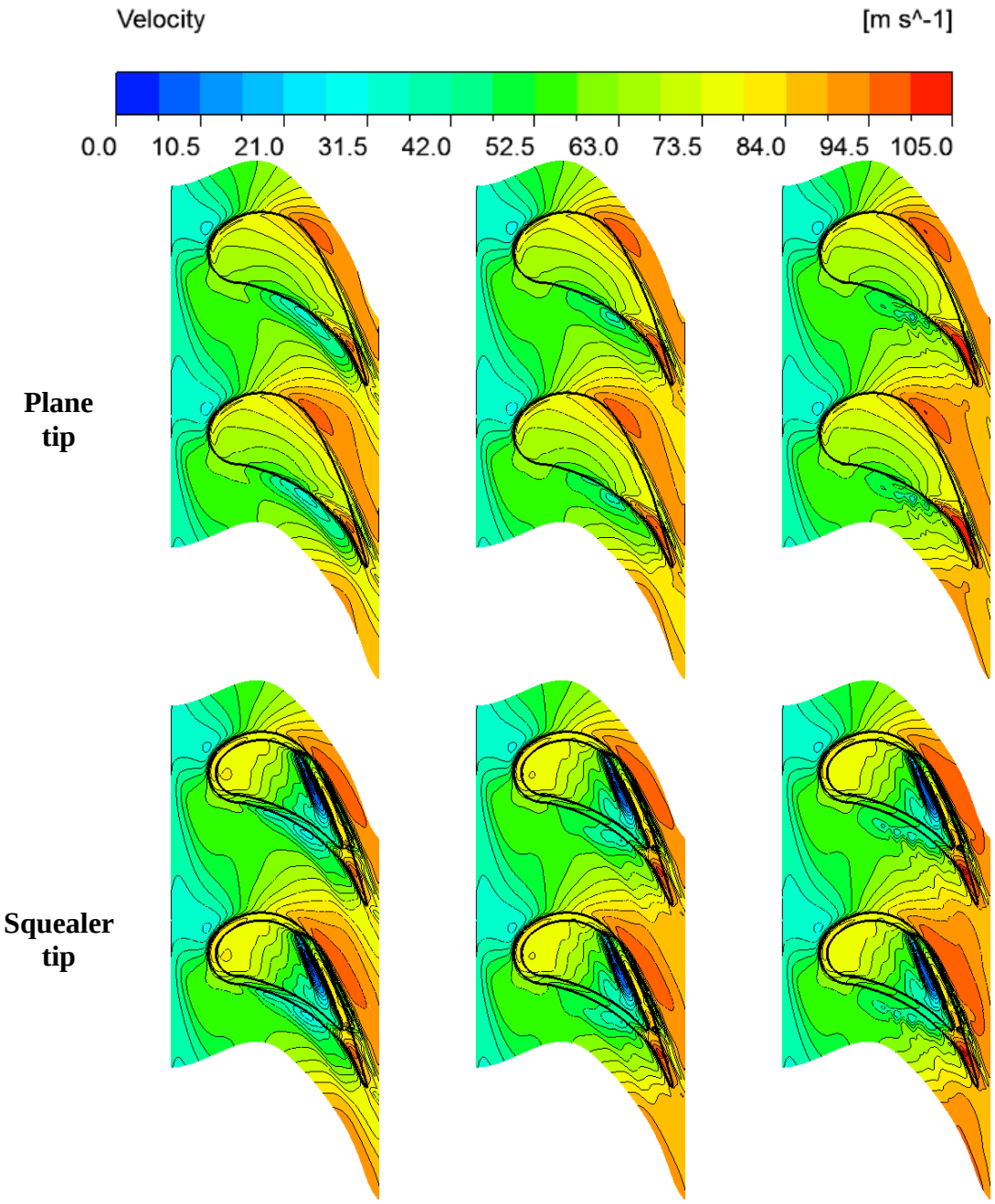

(a) M = 0.5 **(b) M = 1.0** **(c) M = 1.5**

Figure 105: Impact of global blowing ratio on distributions of relative velocity at mid-tip-gap (colored with velocity magnitude) for pressure-side hole cooling at 3000 rpm.

Figure 106 shows the pitchwise-averaged Nusselt number along the axial chord for both the plane and squealer tips with pressure-side hole cooling at 3000 rpm with three blowing ratios. The high averaged Nu is seen at the leading edge for the plane tip at all blowing ratios. Then it gradually goes down until reaching nearly 0.43 C_{ax}. From 0.43 C_{ax} to about 0.9 C_{ax}, the magnitude of averaged Nu climbs up again due to the influence of the cooling jets. It grows very fast especially between 0.75 C_{ax} to 0.9 C_{ax} but quickly drops in downstream 0.1 C_{ax}. As seen, the coolant ejection does not impact the upstream half of the blade tip therefore the averaged Nu remains the same for three blowing ratios between the leading edge and 0.5 C_{ax}. In the downstream area between 0.5 C_{ax} and 0.95 C_{ax}, the averaged Nu enhances as the blowing ratio increases, since the larger blowing ratio leads to higher local velocity and thus greater Nu. In contrast, the averaged Nu exhibits distinct distributions when it comes to the squealer tip. High Nu is obtained at the leading-edge rim but the magnitude suddenly drops to approximately 200 due to the presence of the squealer cavity. Since the leakage flow re-attaches to the surface of cavity floor, the heat transfer keeps growing between 0.15 C_{ax} and 0.8 C_{ax}. The sudden jump of averaged Nu at 0.8 C_{ax} is primarily due to the high-speed leakage flow that crosses over the rear portion of squealer rim. The peak appears at about 0.9 C_{ax} that is same as the plane tip. Similarly, the averaged Nu enhances with the increasing blowing ratio between 0.6 C_{ax} and 0.95 C_{ax} where is affected by the cooling jets. Admittedly the presence of the cavity significantly reduces the averaged Nu at the squealer tip. The area-averaged Nu versus blowing ratio for both the plane and squealer tips with pressure-side hole cooling at 3000 rpm is shown in Figure 107. As seen the averaged Nu

monotonically increases with the growing blowing ratio for both the plane and squealer tips. The averaged Nu at the squealer tip is more than 20% lower than that at the plane tip for all three blowing ratios. Moreover, the growing rate of averaged Nu for the squealer tip is smaller than the plane tip since less squealer rim is impacted by the cooling jets. Similar trend is viewed for the squealer cavity inner wall and rim whereas the Nu remains almost a constant at the squealer cavity floor. It is also noticed that the highest Nu occurs at the squealer rim for all blowing ratios.

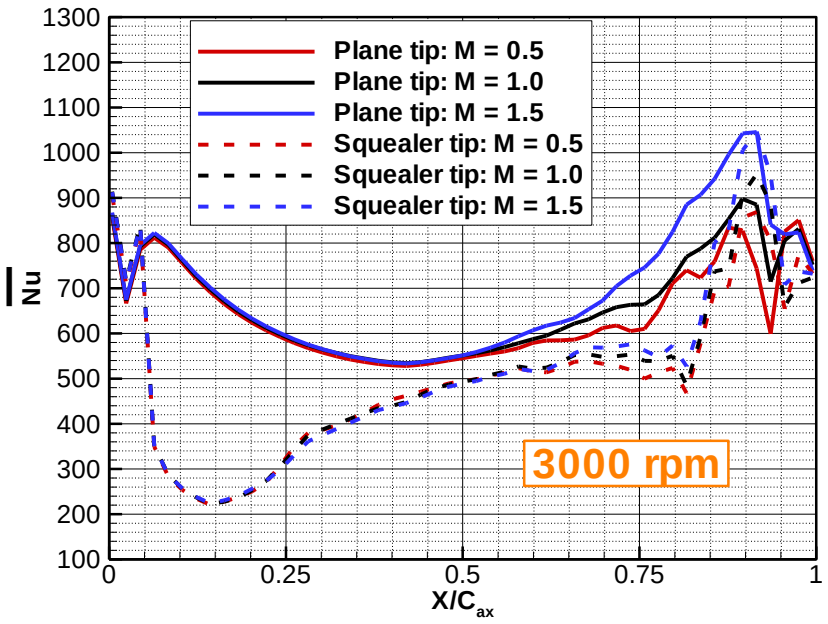

Figure 106: Impact of global blowing ratio on the pitchwise-averaged Nusselt number along the axial chord for blade tips with pressure-side hole cooling at 3000 rpm.

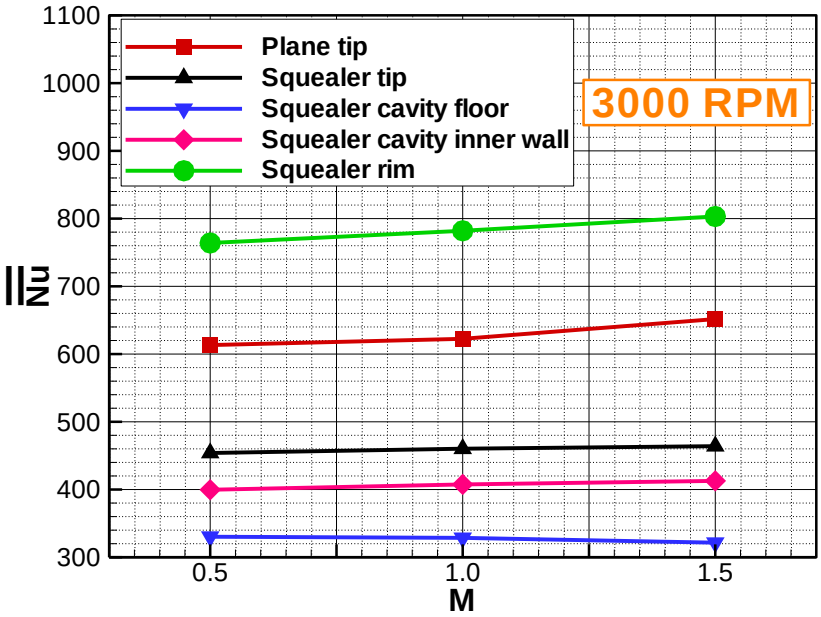

Figure 107: Impact of global blowing ratio on the area-averaged Nusselt number for blade tips with pressure-side hole cooling at 3000 rpm.

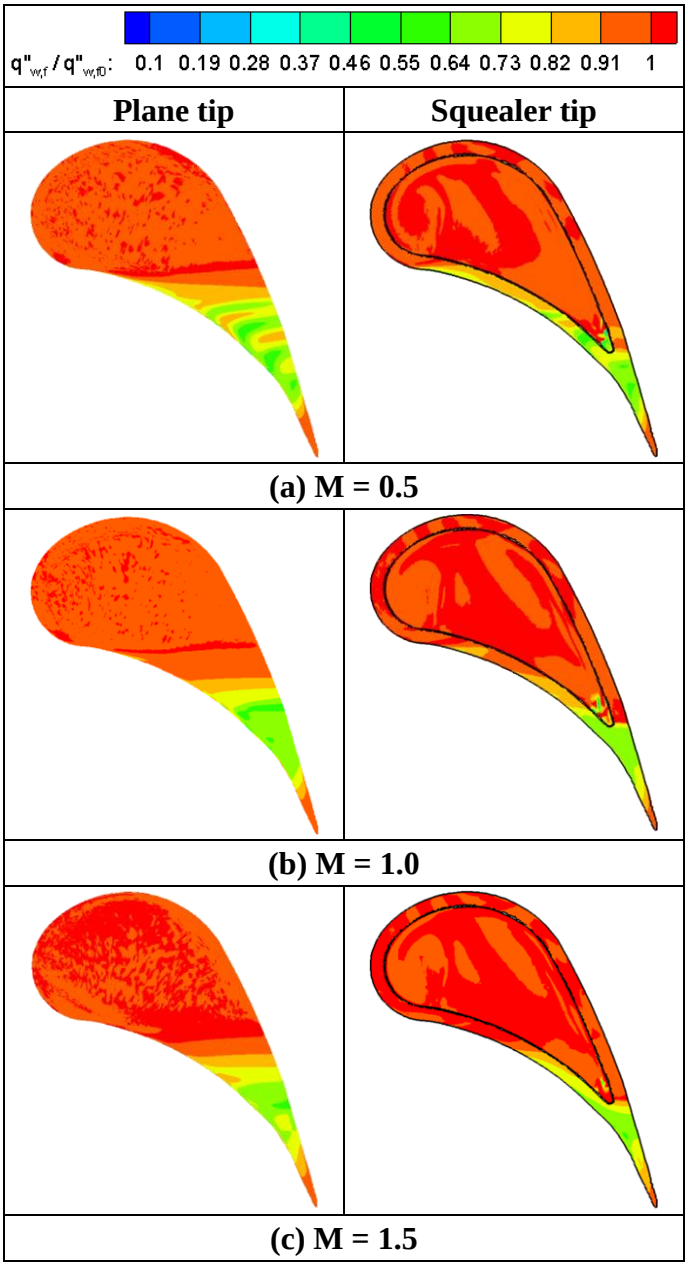

Figure 108: Impact of global blowing ratio on distributions of the heat flux ratio for blade tips with pressure-side hole cooling at 3000 rpm: Blade tip for the plane tip (left); Cavity floor and rim for the squealer tip (right).

Figure 108 depicts the impact of blowing ratio on the heat flux ratio at both the plane and squealer tips with pressure-side hole cooling at 3000 rpm. For the plane tip, low heat

flux ratio is obtained for the rear portion of blade tip whereas the most of blade tip surface from the leading edge to 0.5 C_{ax} experiences very high heat load. Overall, the area with low heat flux ratio corresponds to the region where is well covered by the cooling film and has low heat transfer coefficient. Therefore, it is seen that more blade tip surface gets low heat load at M = 0.5. Besides the cooling film covered a larger area, it also generates lower local heat transfer coefficient. Therefore both the film cooling effectiveness and Nu should be considered when looking into the heat flux ratio. The distribution of heat flux ratio becomes dramatically different when it comes to the squealer tip. As seen, the relatively low heat flux ratio is obtained at part of pressure-side rim and the aft of blade tip, where the cooling film is passing over. In contrast, the squealer cavity floor, the leading-edge rim and suction-side rim suffer from high heat load due to lack of film cooling. Similarly, largest tip area with low heat flux ratio is achieved at the squealer tip when the blowing ratio is lowest.

The pitchwise-averaged heat flux ratio along the blade axial chord for both the plane and squealer tips with pressure-side hole cooling at 3000 rpm with three blowing ratios is plotted in Figure 109. A trough-shape distribution is seen at both the plane and squealer tips. For the plane tip, the averaged heat flux ratio remains almost unity between the leading edge and 0.5 C_{ax}. Then it quickly drops to approximately 0.7 at 0.88 C_{ax} where the "trough" is located. Eventually it rapidly returns to almost one at the trailing edge. It is noted that the "trough" is corresponding to the area that is affected by the cooling film. As the blowing ratio increases, the heat load between 0.5 C_{ax} and 0.88 C_{ax} becomes heavier as well. Apparently the squealer tip obtains a narrower "trough"

and it also shifts a bit downstream due to the existence of the squealer cavity. Also the averaged heat flux ratio is slightly smaller at lower blowing ratios. The impact of blowing ratio on the area-averaged heat flux ratio for both the plane and squealer tips at 3000 rpm is summarized in Figure 110. As seen, the area-averaged heat flux ratio monotonically grows as the blowing ratio is increased for both the plane and squealer tips. However, the growth rate is very small since only the rear portion of blade tip is affected by the cooling film. As expected the higher heat load is added to the squealer tip at all three blowing ratios. In addition, the averaged heat flux ratio at the squealer cavity floor and inner wall equals almost one, whereas the squealer rim experiences lowest heat load in average which is benefited from the protection by the cooling film.

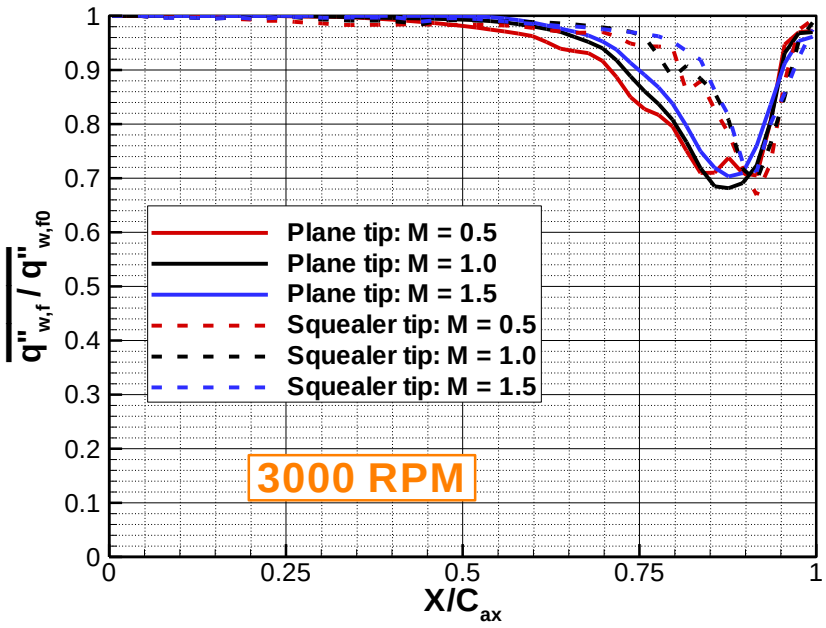

Figure 109: Impact of global blowing ratio on the pitchwise-averaged heat flux ratio along the axial chord for blade tips with pressure-side hole cooling at 3000 rpm.

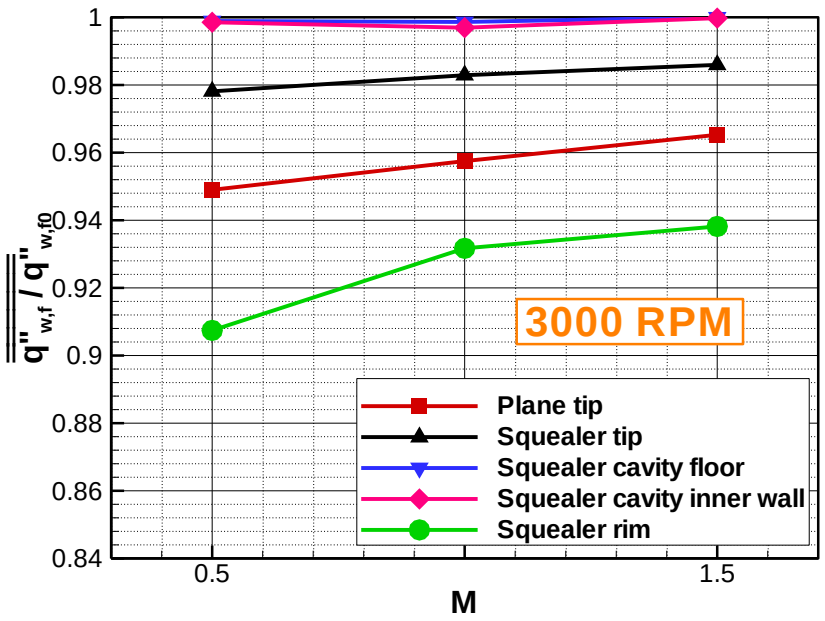

Figure 110: Impact of global blowing ratio on the area-averaged heat flux ratio for blade tips with pressure-side hole cooling at 3000 rpm.

8.2 The Impact of Rotational Speed

After discussing the impact of blowing ratio on the cooling effectiveness in last section, this section is focusing on the effect of the rotational speed on the cooling effectiveness for both the plane and squealer tips with tip hole and pressure-side hole cooling. Accordingly, the blowing ratio is fixed at medium level while three different rotational speeds (2000 rpm, 2550 rpm and 3000 rpm) at both design and off-design conditions are studied.

8.2.1 Pressure distributions and flow characteristics

8.2.1.1 Plane and squealer tips with tip hole cooling

Figure 111 depicts the impact of rotational speed on the pressure distribution at the blade tip region for both the plane and squealer tips with tip hole cooling for M = 1.0.

For the plane tip, the pressure distribution on the tip surface is not smooth due to the presence of the cooling jets. The pressure contour lines are broken in the vicinity of cooling hole exits. It is shown that the variation of rotation speed significantly affect the pressure distribution on the tip surface. At 2000 rpm, the leading edge portion is occupied by high pressure. This high-pressure region extends from leading edge to approximately 0.25 C_{ax}, which is due to the resistance of the cooling jets. As the rotation speed increases, this area shrinks and deforms due to the shift of the stagnation point. When the rotation speed reaches 3000 rpm, this area is much smaller than 2000 rpm and another high-pressure area is obtained at pressure side. In addition, right at downstream regions of the cooling hole exits, certain pressure loss occurs which is associated with the mixing and interaction between the leakage flow and cooling jets. However, their shapes and positions vary due to the alteration in the rotational speed.

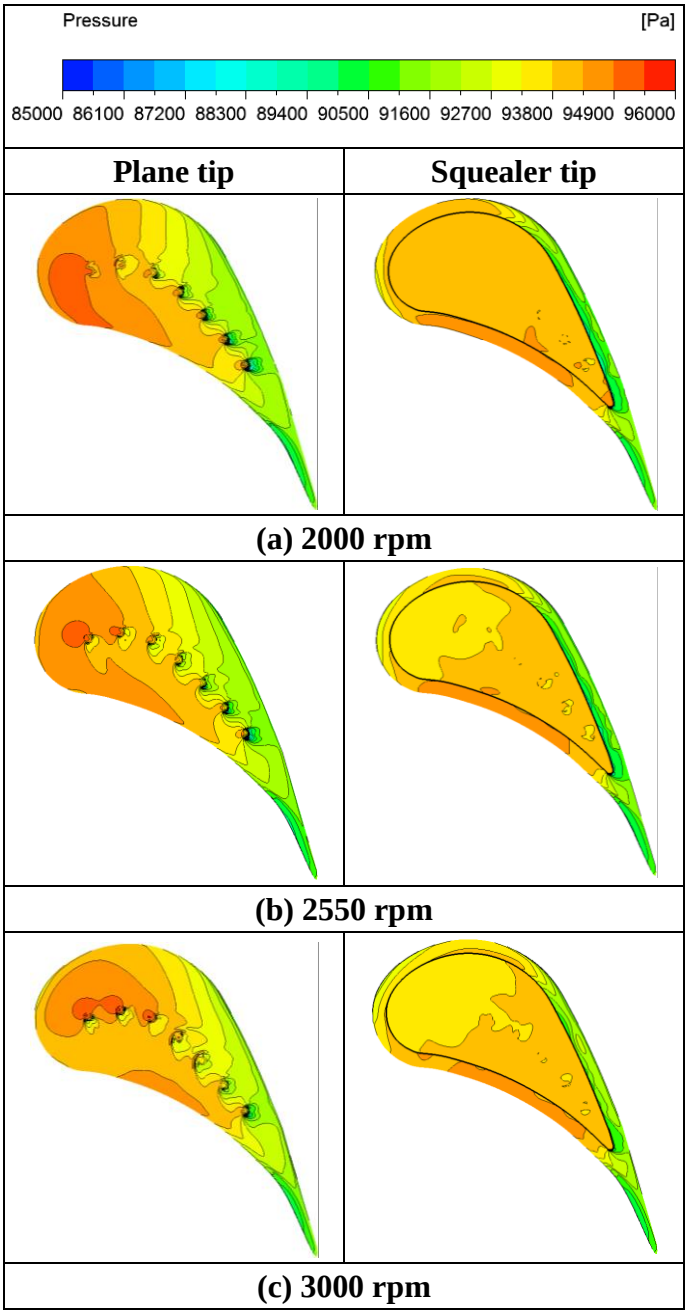

Figure 111: Impact of rotational speed on distributions of the static pressure for blade tips with tip hole cooling at M = 1.0: Blade tip for the plane tip (left); Cavity floor and rim for the squealer tip (right).

However, the circumstance becomes different when it comes to the squealer tip. Although high pressure is obtained at the pressure-side rim and low pressure for the suction-side rim, the pressure field on the squealer cavity floor shows quite uniform distribution. Unlike the plane tip, the locations of cooling holes cannot be identified only from the pressure distribution for the squealer tip. At 2000 rpm, the pressure on the cavity floor is almost constant. However, an area with slightly low pressure can be seen at the leading edge portion for 2550 rpm and 3000 rpm, which might be attributed to the circulation of leakage flow in the cavity. In sum, the change of rotation speed can dramatically impact the pressure distribution at the plane tip, since the cooling jets directly encounters the mainstream with different incidence. However, only negligible effect of the rotation speed can be observed for squealer tip due to the presence of the squealer cavity.

Basically the variation of rotation speed will change the relative flow angle at rotor inlet and therefore alter the downstream flow behaviors. Figure 112 illustrates the streamlines near the blade tip for both the plane and squealer tips for tip hole cooling at fixed M = 1.0 whereas the rotational speed alters. It is seen that the mainstream inlet flow incidence has significant impact on the behaviors of cooling jets for plane tip. At 2000 rpm, all the coolant jets are pointing to the suction side and most of the coolant leaks from the suction side. When the rotation speed increases to 2550 rpm, the direction of the cooling jet at the farthest upstream is turned to the pressure side. In addition, a small amount of the coolant from the three upstream holes leaks from the pressure side due to the incidence change. The majority exits the tip clearance from the suction side.

For 3000 rpm, the directions of two cooling jets at the farthest upstream are completely altered. As a result, all the coolant from first two holes leaks from the pressure side. Also it is noticed that part of the coolant from the third upstream hole travels to the pressure side. Some coolant accumulates in the vicinity of the last four cooling hole exits, which might be attributed to pressure gradient and rotation effect. Overall, the first three upstream cooling jets are influenced primarily by the incidence angle, since they directly face to the incoming mainstream. However the last four jets are dominated by pressure gradient from pressure side to suction side. Although incoming flow incidence change can be seen clearly for the squealer tip, the flow structure within the squealer cavity does not show noticeable relevance to the variation of rotation speed. It is seen that the mainstream is entrained into the squealer cavity, mixing with the ejected coolant while traveling along the pressure-side inner wall and eventually leaking from the suction side. Similar process takes place for all rotation speeds. Therefore, the rotation speed has negligible impact on the flow behaviors near the blade tip region for squealer tip.

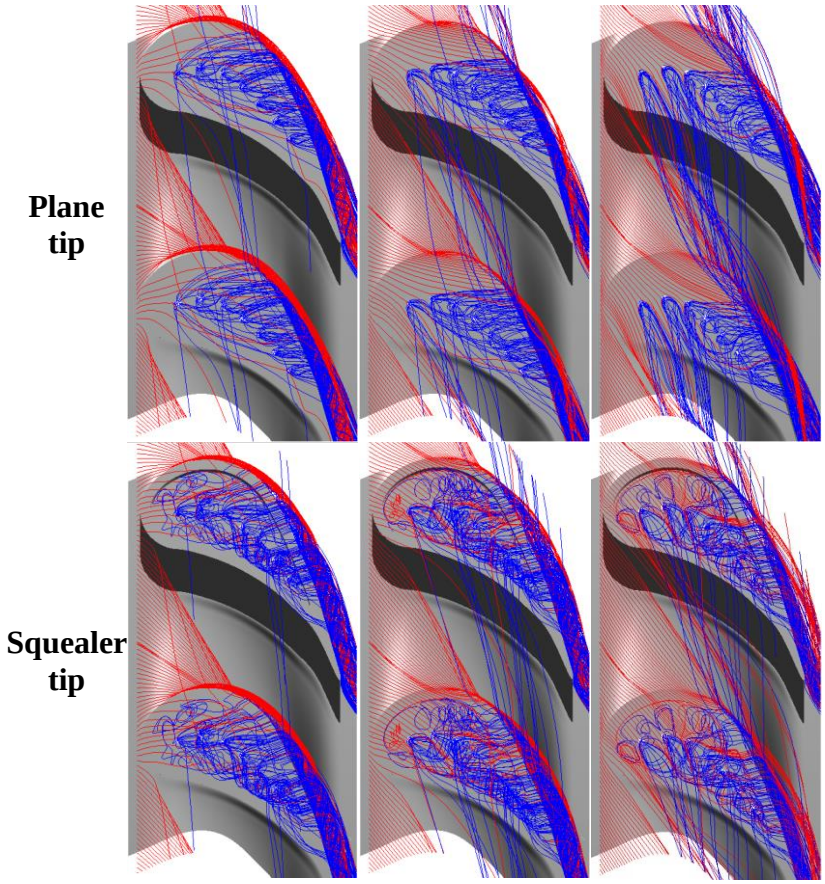

Figure 112: Impact of rotational speed on streamlines based on the relative velocity at the blade tip region for tip hole cooling at M = 1.0 (blue indicates cooling air, red is mainstream air).

8.2.1.2 Plane and squealer tips with pressure-side hole cooling

This section is focusing on the impact of the rotation speed on the film cooling for both the plane and squealer tips with pressure-side hole cooling. Figure 113 shows the influence of the rotation speed on the pressure distribution near the blade tip region for the plane tip. In order to eliminate the impact of blowing ratio (even though little influence can be observed in the figure on page 153), the blowing ratio is fixed as 1.0 whereas three rotation speeds (2000 rpm, 2550 rpm and 3000 rpm) are compared. It is

seen that the change in rotation speed can significantly affect the pressure distribution. Due to the variation of rotating speed, the circumferential velocity will vary and accordingly the flow incidence will be altered. As shown in Figure 113, the stagnation point moves towards the pressure side as the rotation speed decreases. As a result, the high-pressure area on the blade tip surface moves from the pressure side to the leading edge and consequently the direction of the pressure gradient is altered. The shape of the correlated area is transforming as well. Nevertheless, it is noticed that the pressure on the pressure-side surface enhances due to the movement of the stagnation point. In addition, the low-pressure streaks on the pressure-side wall due to the pressure loss can be seen at the trailing edge of all the cooling holes for low rotational speeds of 2000 rpm and 2550 rpm. However those at 3000 rpm are seen for the first upstream hole and the five downstream holes. Such difference reflects the alterations in the relative flow angle.

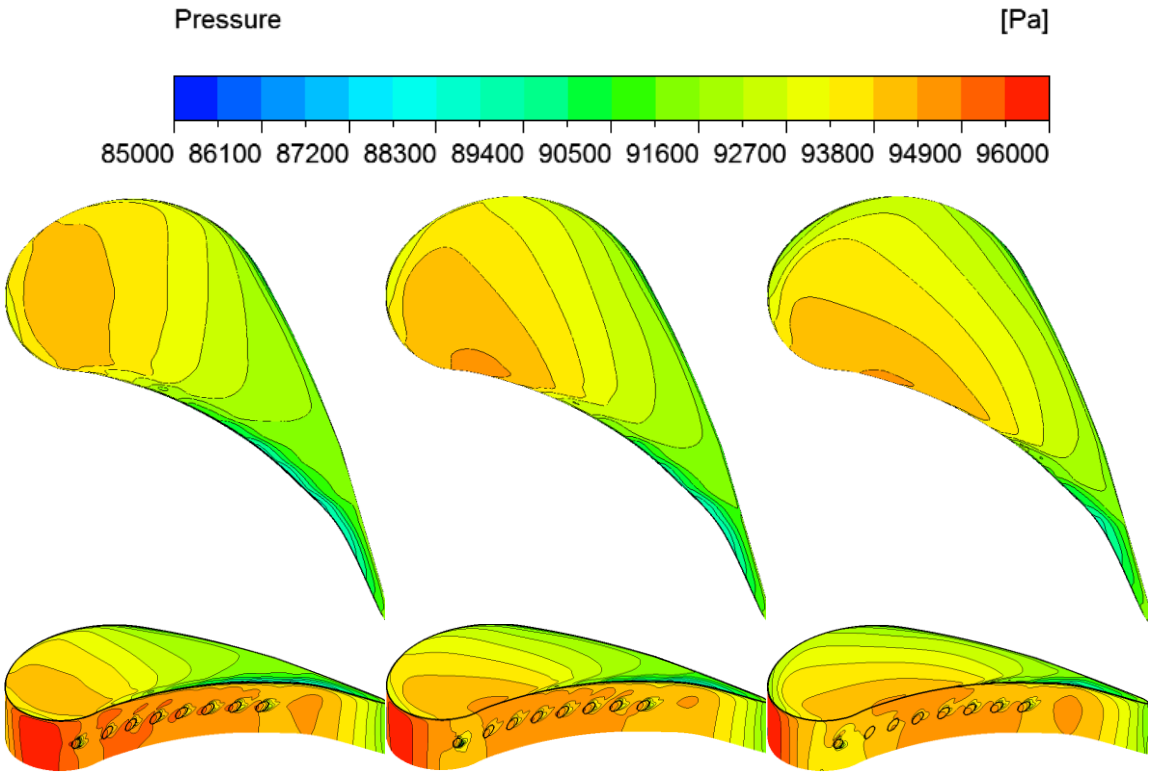

(a) 2000 rpm **(b) 2550 rpm** **(c) 3000 rpm**

Figure 113: Impact of rotational speed on distributions of the static pressure near the blade tip region for plane tip with pressure-side hole cooling at M=1.0.

The change of the pressure field near the tip region is associated with the variation of the local flow behaviors. Figure 114 shows the streamlines based on the relative velocity near the blade tip region with different rotation speeds. The alteration of the direction of red streamlines (mainstream) indicates the change in flow incidence angle. The relative flow angle reduces with the increasing rotational speed. As a result, the coolant jets are significantly affected. As shown in Figure 114 (a), the coolant jets from all cooling holes are pushed towards the suction surface immediately after the coolant particles are ejected out of the holes. Almost all of the coolant crosses the pressure-side edge and then travels towards the suction side. In the end these coolant particles leak from the suction-side

edge contributing to the formation of tip vortex system. This is due to the large incidence angle and relatively high local pressure. As the rotation speed increases to 2550 rpm (Figure 114 (b)), the directions of most coolant jets are also altered and accordingly majority of the coolant particles leak from the suction side. However, for the rotation speed of 3000 rpm (Figure 114 (c)), only a small amount of the coolant particles are pushed to the suction side, whereas the rest of the coolant lifts off the pressure surface and mixes with the mainstream while traveling downstream. It is easily noticed that more blade tip surface is covered by the cooling film when the rotation speed is lower.

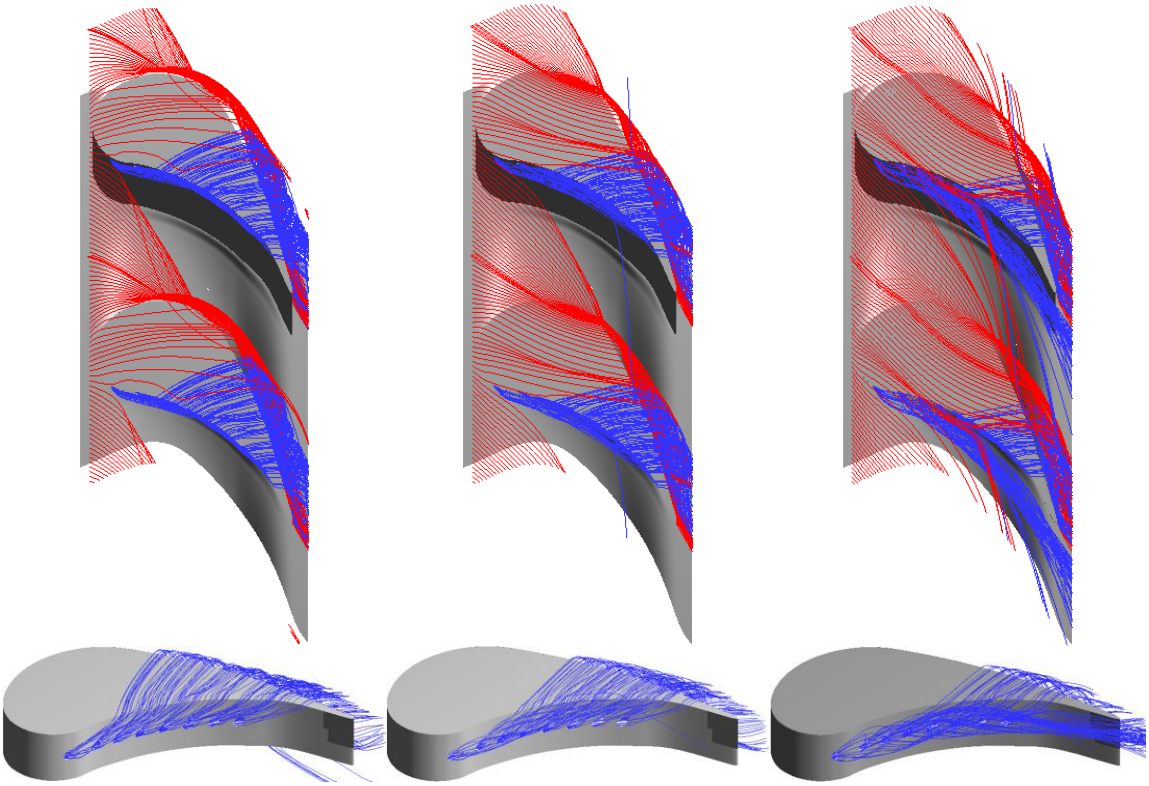

(a) 2000 rpm **(b) 2550 rpm** **(c) 3000 rpm**

Figure 114: Impact of rotational speed on streamlines based on the relative velocity near the blade tip region for plane tip with pressure-side hole cooling at M = 1.0 (blue indicates cooling air, red is mainstream air).

Figure 115 depicts the distribution of the temperature near the blade tip region for the plane tip at M = 1.0. As mentioned above, almost all the coolant jets re-attach to the pressure surface at 2000 rpm, forming distinct streaks with low temperature right at downstream of the cooling hole exits. No obvious interaction is observed among the cooling jets. However, when the rotation speed increases to 2550 rpm, the coolant jets from the first two upstream holes start to interfere with each other. For the rotation speed of 3000 rpm, only the cooling jets from the three downstream holes show reattachment to the pressure surface, whereas most of the rest coolant lifts off the surface and travels downstream along with mainstream particles. Noticeably, since more coolant travels through the tip clearance at lower rotation speed, more tip surface is covered by the cooling film. Meanwhile the temperature is lower as well in the covered regions. Based on current geometries and running conditions, the plane tip with pressure-side hole cooling has better performance at off-design conditions.

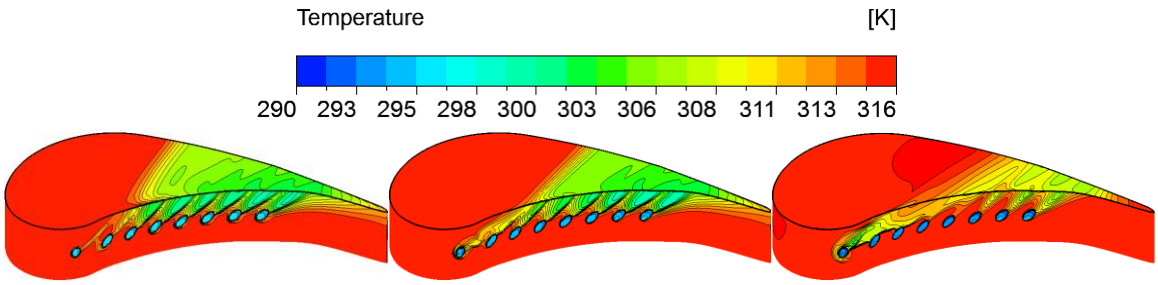

(a) 2000 rpm **(b) 2550 rpm** **(c) 3000 rpm**

Figure 115: Impact of rotational speed on distributions of the temperature near the blade tip region for plane tip with pressure-side hole cooling at M = 1.0.

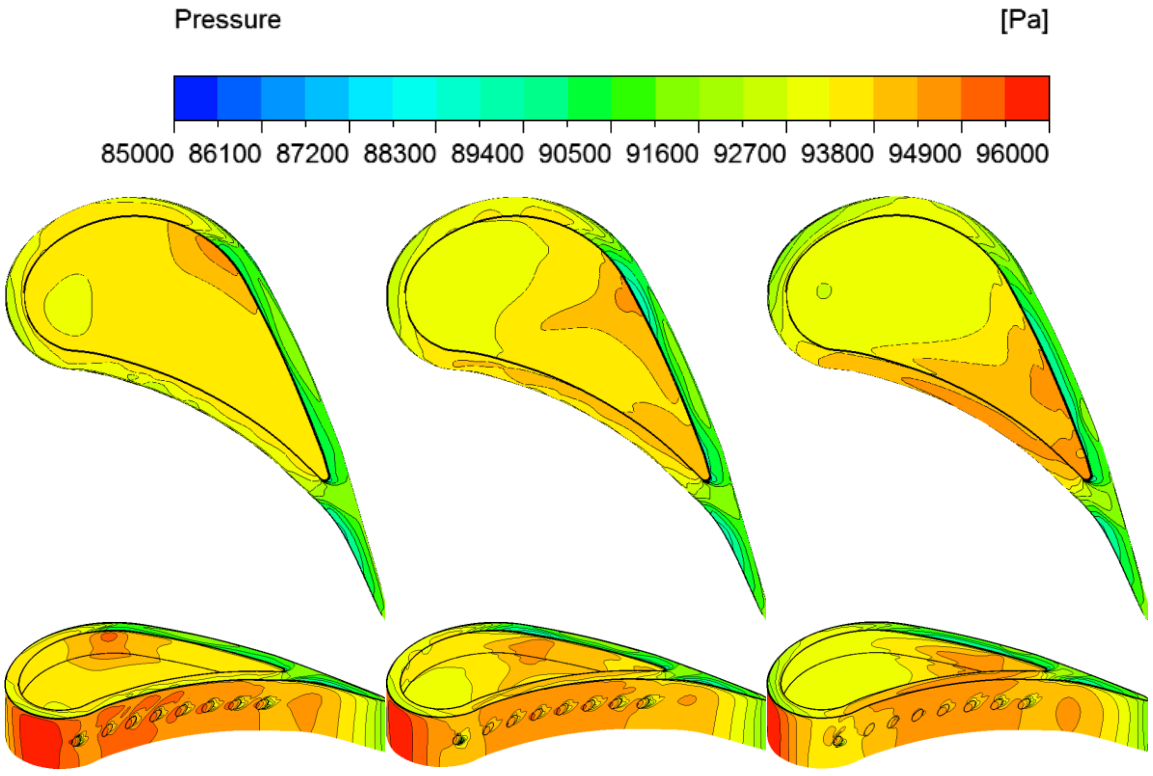

(a) 2000 rpm **(b) 2550 rpm** **(c) 3000 rpm**

Figure 116: Impact of rotational speed on distribution of the static pressure near the blade tip region for squealer tip with pressure-side hole cooling at M = 1.0.

Figure 116 depicts the impact of the rotation speed on the pressure distribution near the blade tip region for squealer tip with pressure-side hole cooling at M = 1.0. It is seen that the variation of rotation speed can significantly influence the pressure distribution on the blade tip. Similarly, due to the decrease in rotating speed, the stagnation point moves towards the pressure side and the incidence angle increases as well. As a result, the high-pressure area on the squealer cavity floor moves along the suction-side inner wall from the cavity trailing end to upstream. The correlated area is deforming as well. However, the pressure on the cavity floor appears more uniform than that on the plane

tip surface as shown in the figure on page 206. In addition, the pressure in the vicinity of the cooling holes enhances too due to the movement of the stagnation point.

Figure 117 shows the streamlines near the blade tip region for squealer tip with three different rotation speeds. The turning of red streamlines (mainstream) indicates the impact of the rotation speed on flow incidence angle. Unlike the plane tip, the presence of the squealer cavity significantly alters the behaviors of the leakage flow and thus affects the cooling film. It is seen that most of the coolant passes through the tip clearance however very few coolant particles are entrained in the squealer cavity at 2000 rpm. Consequently, the cavity floor and inner wall can be hardly cooled. Similar to the plane tip, the coolant jets are significantly affected by the rotation speed. In Figure 117 (a), the coolant jets from all cooling holes are pushed towards the suction surface immediately after the coolant particles exit the holes. Almost all of the coolant crosses the pressure-side rim and then travels towards the suction side. Eventually these coolant particles leak from the suction side edge contributing to formation of tip vortex system. As the rotation speed grows to 2550 rpm (Figure 117 (b)), most of the coolant jets are also altered and accordingly majority of the coolant particles exit from the suction side. However, for the rotation speed of 3000 rpm (Figure 117 (c)), only a small amount of the coolant particles travel to the suction side, whereas the rest of the coolant lifts off from the pressure surface and flows downstream while mixing with the mainstream and also the downstream ejecting cooling jets. It is easily concluded that more rim surface is covered by the cooling film when the rotation speed is lower. However based on the streamline visualization, the cavity floor and inner wall are rarely cooled.

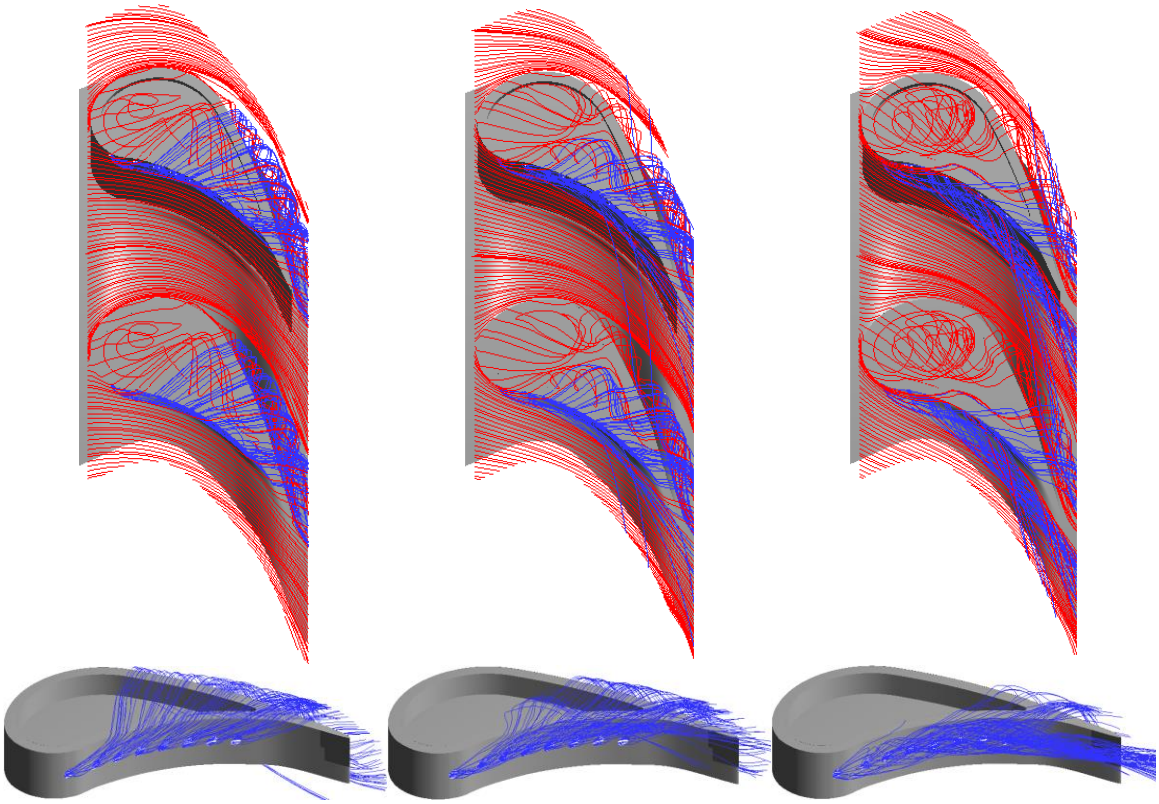

(a) 2000 rpm **(b) 2550 rpm** **(c) 3000 rpm**

Figure 117: Impact of rotational speed on streamlines based on the relative velocity near the blade tip region for squealer tip with pressure-side hole cooling at M = 1.0 (blue indicates cooling air, red is mainstream air).

Figure 118 depicts the influence of the rotational speed on the temperature distribution at the blade tip region for the squealer tip with pressure-side hole cooling at M = 1.0. Similar to the plane tip, almost all the coolant jets re-attach to the pressure surface at 2000 rpm. As a result, distinct streaks with low temperature right at the cooling-hole exits are generated. No noticeable interaction takes place among the cooling jets. When the rotation speed increases to 2550 rpm, the coolant jets from the first two upstream holes interfere with each other. For the rotation speed of 3000 rpm, only the last three downstream cooling jets reattach to the pressure surface, whereas

most of the rest coolant lifts off the surface and penetrates into the mainstream. It has been seen in Figure 117 that larger area of the rim is cooled if the rotation speed is lower. For 2000 rpm and 2550 rpm, the pressure-side rim is well cooled and the surface temperature is lower than the case of 3000 rpm. In addition, part of the suction-side rim and cavity inner wall is somewhat cooled for 2000 rpm and 2550 rpm, which is due to the entrainment of coolant particles into the cavity. Because the rotation speed varies, the location of the cooled area changes too. However, the suction-side rim is not cooled at all when the blade rotates at 3000 rpm, since the leaking location of the coolant is at downstream of the cavity trailing end. Although the pressure-side hole cooling can also cover more blade tip area at off-design conditions for the squealer tip, it delivers even worse cooling performance when compared to the plane tip.

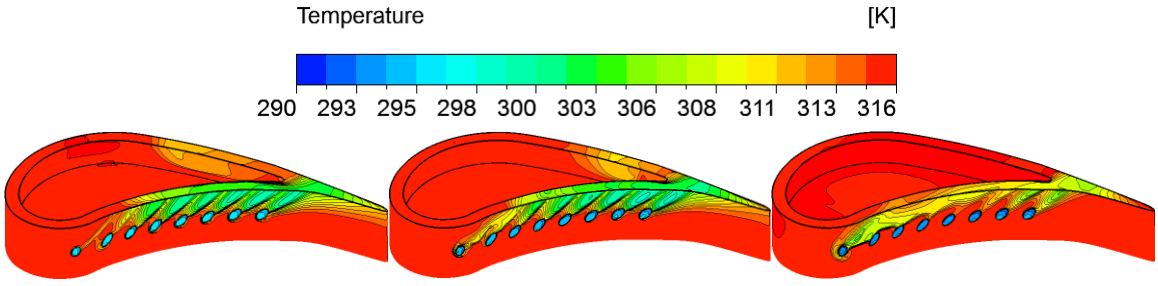

(a) 2000 rpm **(b) 2550 rpm** **(c) 3000 rpm**

Figure 118: Impact of rotational speed on distributions of the temperature near the blade tip region for squealer tip with pressure-side hole cooling at M = 1.0.

8.2.2 Adiabatic film cooling effectiveness

8.2.2.1 Plane and squealer tips with tip hole cooling

The flow structure directly determines the film cooling effectiveness. Figure 119 depicts the distribution of adiabatic film cooling effectiveness at the blade tip region for both the plane and squealer tip. Evidently, the distribution of cooling effectiveness shows substantial difference for plane tip with varied rotational speed. For the rotation speed of 2000 rpm, since all the coolant jets are altered to the suction side (figure on page 204), the cooling film covers the blade tip surface close to the suction side. Streaks with relatively high effectiveness are found right downstream of the cooling hole exits. Almost all the trace of cooling jets can be identified from these streaks. Within the covered area, the cooling effectiveness is approximately as high as 0.4. At 2550 rpm, because the first cooling jet is turned by the mainstream, it cools part of the tip surface near the pressure side. However, the rest of the coolant leaks from the suction side and therefore cools the tip surface at its downstream near suction side. Similar streaks are observed for the last four holes. The effectiveness distribution shows completely different pattern when it comes to 3000 rpm. The first two upstream cooling jets and part of the third upstream jet are pushed to the pressure side. Consequently, more area near the pressure side is protected than that at 2550 rpm. Additionally, the accumulation of coolant contributes to high effectiveness in the vicinity of the last four cooling hole exits. However, the leading edge is not protected by the cooling film for all rotation speeds. Hence, the rotation speed has considerable impact on the film coverage and cooling effectiveness for plane tip.

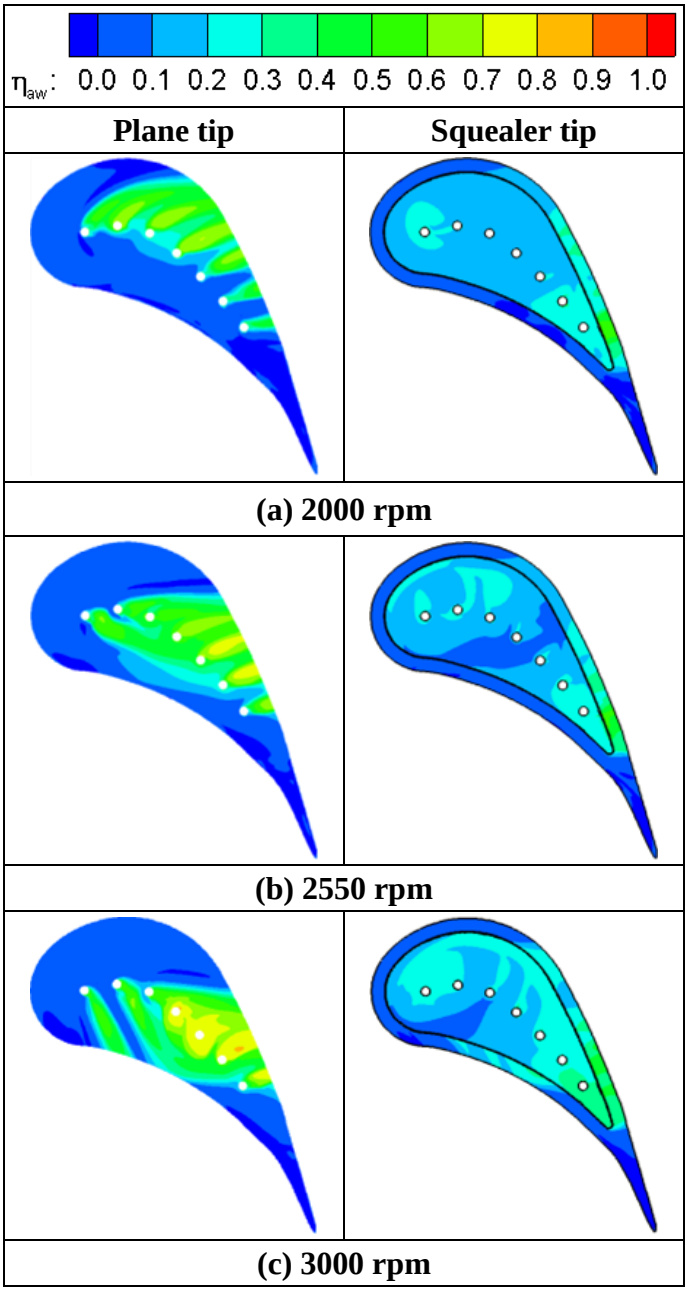

Figure 119: Impact of rotational speed on distributions of the adiabatic film cooling effectiveness for blade tips with tip hole cooling at M = 1.0: Blade tip for the plane tip (left); Cavity floor and rim for the squealer tip (right).

In contrast, few effect of the rotation speed can be observed when it comes to squealer tip. The distribution of cooling effectiveness exhibits similar profiles for all

rotation speed. Almost uniform distribution of low effectiveness is seen on the cavity floor. Relatively high effectiveness appears at the region of cavity trailing edge since most of the coolant exits from this location. In addition, nearly half of the suction-side rim is cooled for all rotation speeds but the pressure-side rim is partially protected at 3000 rpm. However, it does not change the fact that the rotation speed barely impacts the cooling effectiveness for squealer tip.

Figure 120 and Figure 121 show the pitchwise- and area-averaged for both plane and squealer tip respectively. As seen in Figure 120, the cooling film covers from 0.2 C_{ax} to 0.85 C_{ax} for the plane tip with all rotating speeds. Within the range of 0.2~0.5 C_{ax}, the averaged cooling effectiveness increases from 0.1 to approximately 0.25 for all rotation speeds. However, the averaged effectiveness increases monotonically with the rotation speed. This is attributed to the change in directions of the cooling jets, which leads to more coolant leaking from this location when the rotation speed is higher. The peak value is about 0.44 at 0.7 C_{ax}. However, the distribution lines are different for the squealer tip. The presence of squealer cavity extends the coverage to 0.05 ~ 0.9 C_{ax}, However, within the range of 0.05 ~ 0.5 C_{ax}, the averaged effectiveness is around 0.15 for all rotation speeds. From 0.5 C_{ax}, the effectiveness gradually increases and the peak value is reached at 0.85 C_{ax}. Basically the rotation speed does not have substantial effect on the averaged effectiveness for squealer tip. Slightly higher effectiveness at 3000 rpm is due to the coolant leakage from the pressure side. The peak value is about 0.3 for the squealer tip which is lower than plane tip. For overall effectiveness in Figure 121, different trends are obtained for the plane tip and squealer tip respectively. The overall

effectiveness increases monotonically with the rotation speed for the plane tip. However, the overall effectiveness of squealer tip is almost identical for 2000 rpm and 2550 rpm, but slightly increases at 3000 rpm. Separate parts of the squealer tip show similar trends. Additionally as expected, the squealer rim is the least cooled portion.

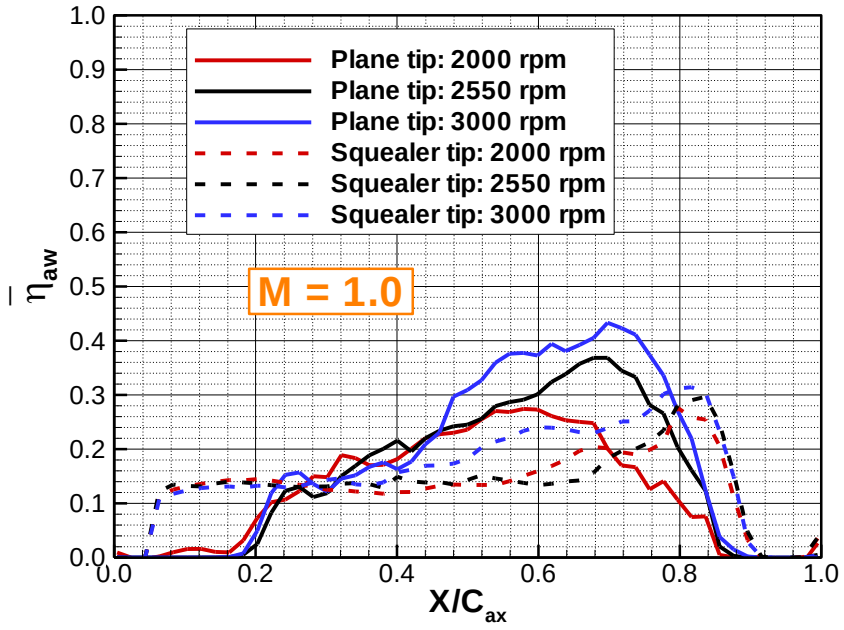

Figure 120: Impact of rotational speed on the pitchwise-averaged adiabatic film cooling effectiveness along axial chord for blade tips with tip hole cooling at M = 1.0.

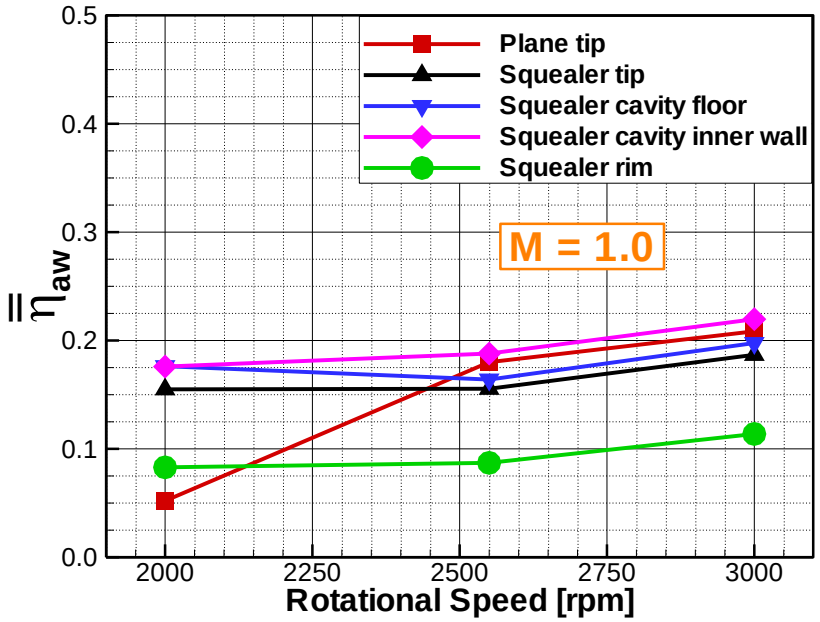

Figure 121: Impact of rotational speed on the area-averaged film cooling effectiveness for blade tips with tip hole cooling at M = 1.0.

8.2.2.2 Plane and squealer tips with pressure-side hole cooling

Figure 122 shows the impact of the rotation speed on the film cooling effectiveness at the blade tip surface for both the plane and squealer tips with pressure-side hole cooling. The blowing ratio is fixed at a moderate level of M = 1.0. It is seen that at lower rotation speed, the cooling film is able to cover more blade tip surface than the case at higher rotation speed. Meanwhile the magnitude of effectiveness is higher as well. The reason is that the incidence angle and pressure at the pressure surface tend to be larger at lower rotational speeds, which can drive more coolant particles passing through the tip clearance. Therefore the cooling effectiveness highly depends on the amount of cooling particles that travel across the blade tip surface. However, the leading edge is not cooled at all, which might be improved by putting cooling holes at the leading edge. The

corresponding mechanism has been explained earlier. Compared to the influence of the blowing ratio in the figure on page 171, the impact of the rotation speed is more significant for the plane tip with pressure-side hole cooling.

Figure 122 also shows the impact of the rotation speed on the film cooling effectiveness at the blade tip region for squealer tip at M = 1.0. It is seen that at lower rotation speeds of 2000 rpm and 2550 rpm, the cooling effectiveness on the pressure-side rim is as high as 0.4. The corresponding coverage extends from 0.3 ~ 0.8 C_{ax}. However, the effectiveness on the pressure-side rim does not exceed 0.25 for 3000 rpm, since less coolant travels through the tip clearance than lower rotating conditions. As mentioned earlier, part of the suction-side rim is cooled at lower rotation speeds. More cooled area of the suction-side rim is obtained at 2000 rpm than 2550 rpm. However, no effective cooling is observed on the suction-side rim for 3000 rpm. Additionally, the cooling film does not provide any protection for the leading-edge rim and cavity floor for all rotation speeds due to the absence of coolant. Although the impact of the rotation speed is more significant than blowing ratio on the pressure-side hole cooling, the benefit is marginal for squealer tip.

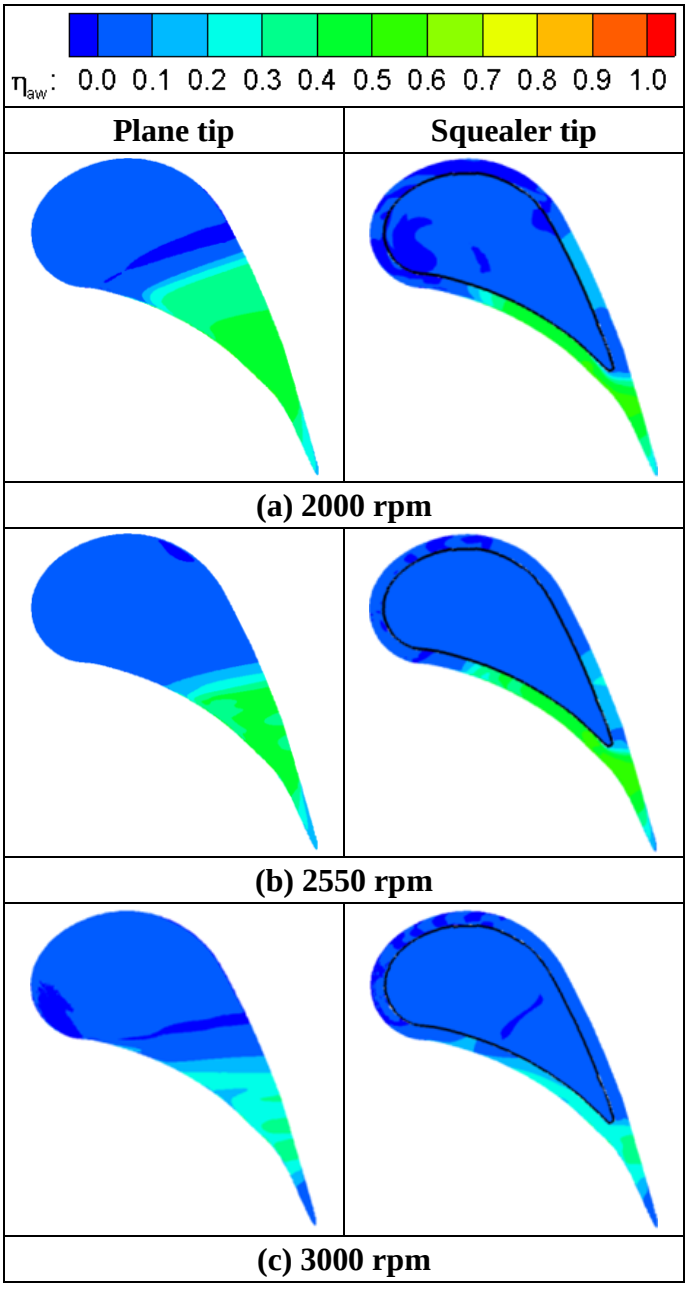

Figure 122: Impact of rotational speed on distributions of the adiabatic film cooling effectiveness for blade tips with pressure-side hole cooling at M = 1.0: Blade tip for the plane tip (left); Cavity floor and rim for the squealer tip (right)..

Figure 123 depicts the influence of the rotational speed on the pitchwise-averaged cooling effectiveness along the axial chord for both the plane and squealer tips with

pressure-side hole cooling at M = 1.0. For the plane tip, there is almost no effectiveness between the leading edge and 0.4 C_{ax}. The cooling effectiveness begins to rise beyond C_{ax}. However, the averaged effectiveness grows faster at lower rotational speeds. Again the peak location is found at 0.9 C_{ax}. It is noted that no difference in averaged effectiveness is seen between the 2000 rpm and 2550 rpm from about 0.75 C_{ax} to the trailing edge however the magnitude at 3000 rpm is much lower. Once again, the "wave" of averaged effectiveness is much narrower for the squealer tip although the peak magnitude is slightly larger than the plane tip. In addition, it turns out that the CFD software is not sensitive to the rotational speed when it grows from 2000 rpm to 2550 rpm, since the distributions of averaged effectiveness are almost identical for both cases. Nevertheless, the effectiveness dramatically drops when the rotational speed reaches 3000 rpm.

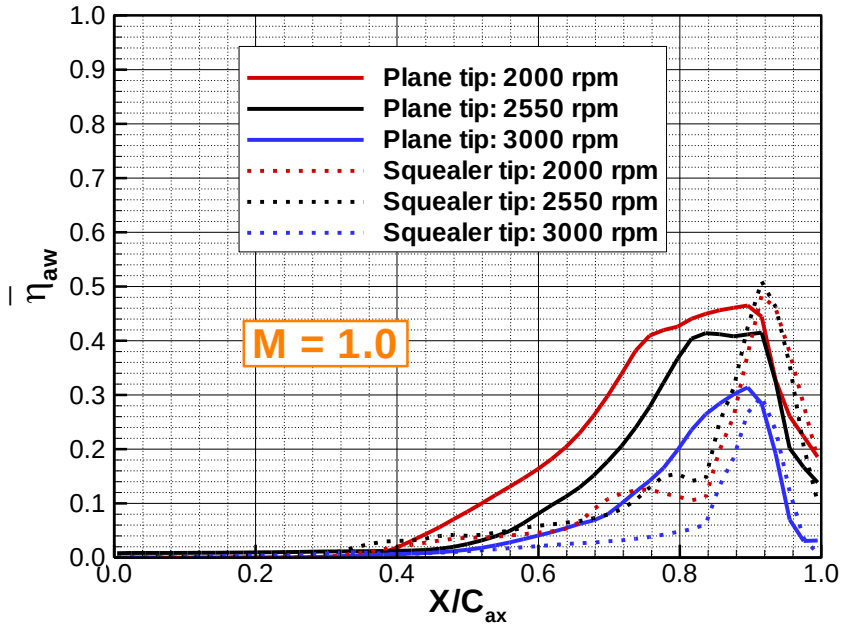

Figure 123: Impact of rotational speed on the pitchwise-averaged adiabatic film cooling effectiveness along axial chord for blade tips with pressure-side hole cooling at M = 1.0.

The area-averaged cooling effectiveness versus the rotational speed for both the plane and squealer tips with pressure-side hole cooling is plotted in Figure 124. As seen, the overall cooling effectiveness is inversely proportional to the rotational speed for the plane tip. Moreover, the rotational speed has more significant effect than the blowing ratio for the plane tip. For the squealer tip, the overall effectiveness is less than 50% of that for the plane tip since the squealer tip possesses larger surface area however less area is cooled. Different from the trend for the plane tip, the effectiveness at 2550 rpm is slightly higher than that of 2000 rpm however profoundly drops for 3000 rpm. Similar trend is predicted for the squealer cavity inner wall and rim. In addition, the squealer cavity floor is not protected from the hot gas at all for all rotational conditions.

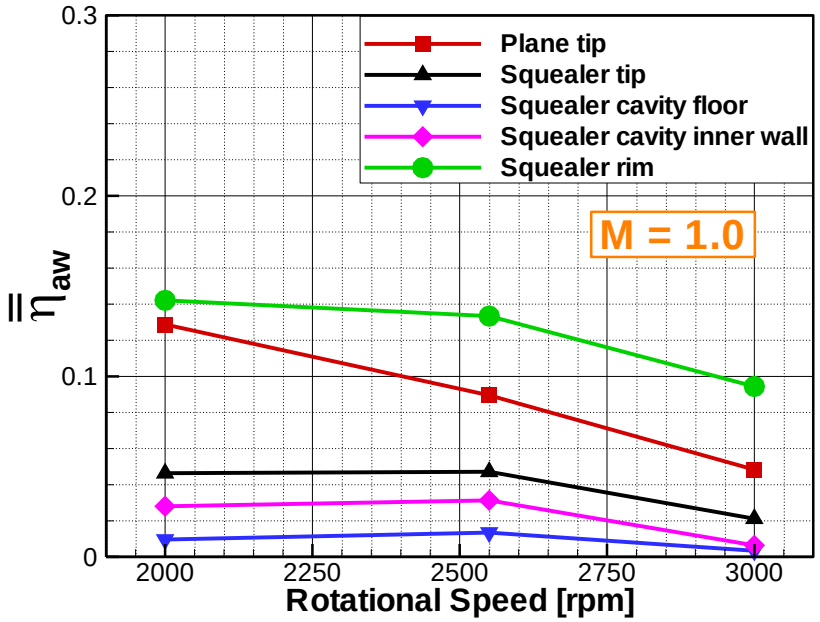

Figure 124: Impact of rotational speed on the area-averaged adiabatic film cooling effectiveness for blade tips with pressure-side hole cooling at M=1.0.

8.2.3 Heat transfer

As discussed in the early sections, the variations in the turbine rotational speed alter the circumferential velocity which leads to the changes in the flow angle, shift of the stagnation point and therefore the entire flow field. The off-design conditions have been confirmed to be able to affect the pressure field, temperature distribution and cooling effectiveness for the tip hole cooling. This section aims to reveal the impact of the rotational speed on the heat transfer at the blade tips with the presence of tip hole cooling.

8.2.3.1 Plane and squealer tips with tip hole cooling

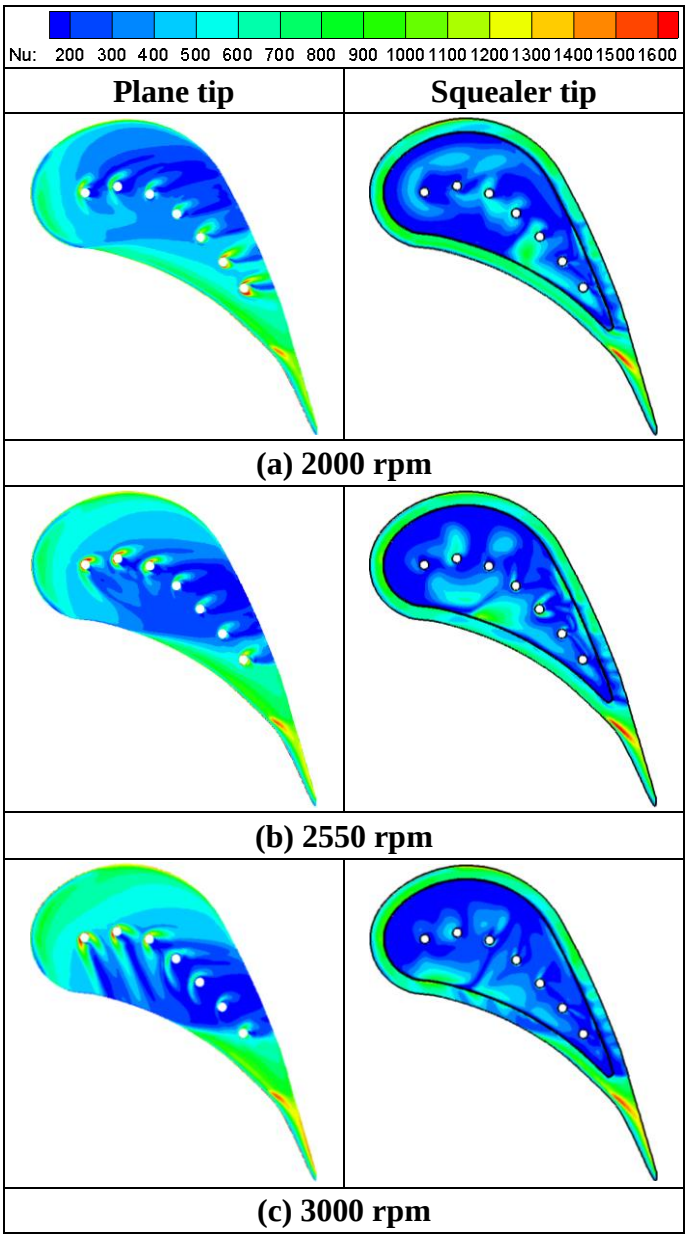

Figure 125: Impact of rotational speed on distributions of the Nusselt number for blade tips with tip hole cooling at M = 1.0: Blade tip for the plane tip (left); Cavity floor and rim for the squealer tip (right).

Figure 125 illustrates the distribution of Nusslet number on both the plane and squealer tips with tip hole cooling at three different rotational speeds while the blowing ratio is fixed at unity. Once again, the Nu contour plots exhibits distinct characteristics between the plane and squealer tips with tip hole cooling. For the plane tip rotating at 2000 rpm, the stagnation point moves to the starting point of the mean camberline. As a result, the leakage flow enters the narrow tip gap along the camberline where the cooling holes are positioned. In such circumstance, the resistance from the three upstream cooling jets becomes stronger when compared to that at 3000 rpm.

This can be recognized from the local high pressure in the figure on page 201 and corresponding low velocity (Figure 126) at the leading edge region. The consequence is that only a small tip portion close to the leading edge is experiencing high Nu and its intensity quickly decays along the blade chord. It is worth mentioning that high Nu is obtained along the pressure side for 2000 rpm. This is associated with the flow direction of the cooling jets. As seen, all the coolant particles are pushed towards the suction surface due to the change of the leakage flow angle and variations in pressure distribution. In the meantime the leakage flow is entrained in the tip gap from the pressure side at a high speed as shown in Figure 126. Thus the local Nu is strengthened which differs from the situation at 3000 rpm. However, there is one similarity that the Nu tends to be low in the area where the cooling film covers. In addition, longer and wider streaks with high Nu are observed in the vicinity of the downstream two cooling holes for 2000 rpm. Unlike the case at 3000 rpm, these two cooling jets do not stay in the wake of upstream cooling film. Therefore the leakage flow is largely accelerated

near the suction side which generates stronger vortices at both sides of the hole exits. It is easy to notice that the Nu on the plane tip for 2550 rpm exhibits the distribution that stays between the 2000 rpm and 3000 rpm. In addition, for all rotational speeds, the aft of the blade tip is occupied with high Nu. In contrast, the variations in the rotational speed do not cause substantial influence on the distributions of Nu on squealer tip surfaces. The most noticeable difference is that high Nu is seen on the pressure-side rim at lower rotational speeds. Apparently certain amount of leakage flow is entrained from the pressure side at low rotating speed rather than the case that the coolant leaks from the pressure side at 3000 rpm. As expected, the Nu on the cavity floor retains low and uniform no matter what rotational speed is. Those spots with high Nu at the cavity floor are formed due to the complex interactions between the coolant jets and leakage flow within the squealer cavity.

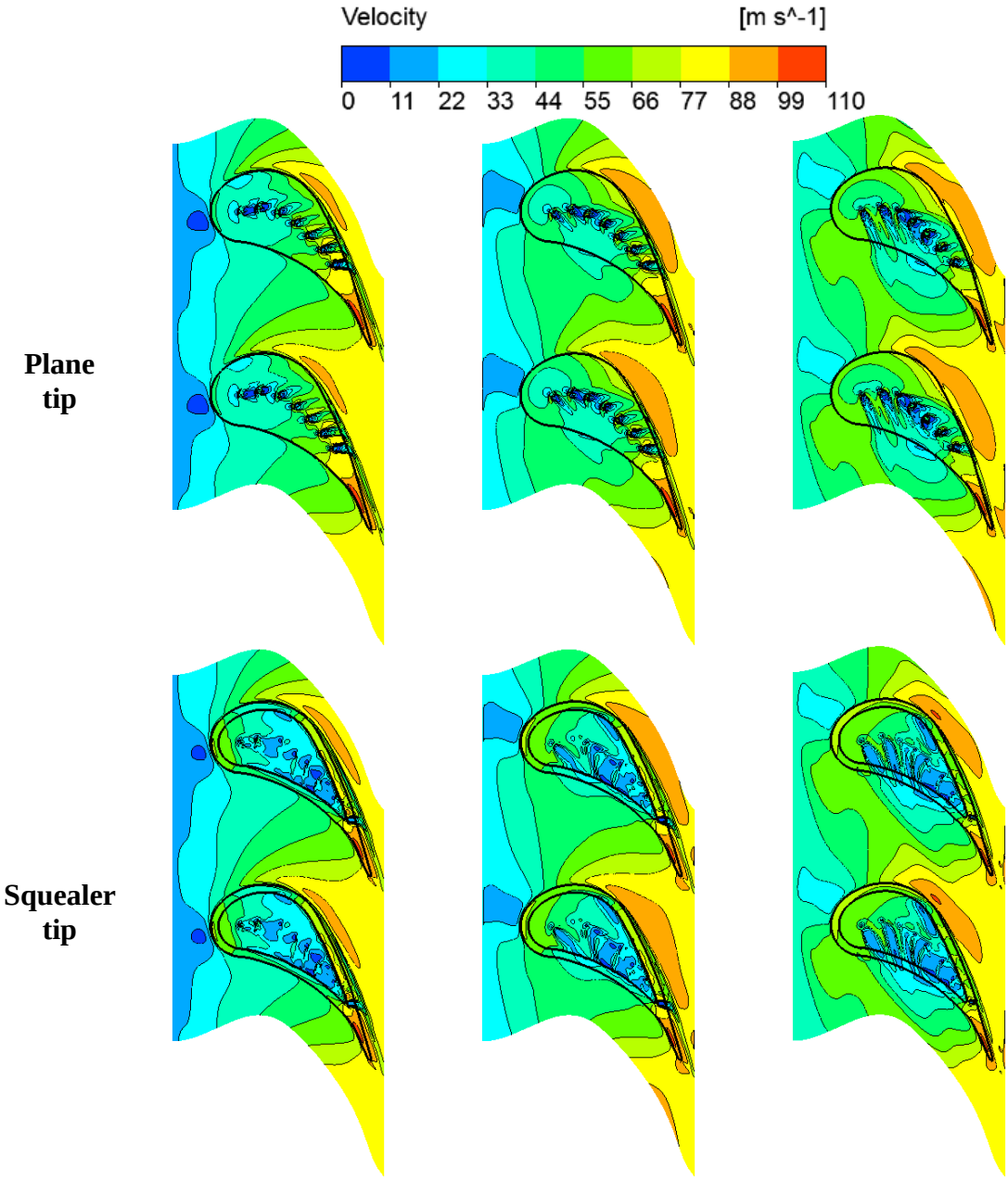

Figure 126: Impact of rotational speed on distributions of relative velocity at mid-tip-gap (colored with velocity magnitude) for tip hole cooling with plane and squealer tips at M = 1.0.

The impact of the rotational speed on the pitchwise-averaged Nusselt number at both the plane and squealer tips with tip hole cooling is shown in Figure 127. As seen, for the plane tip, the averaged Nusselt number keeps dropping from the leading edge till around 0.6 C_{ax} where the lowest Nu is achieved. This is due to the continuous flow deceleration caused by the resistance of coolant jets. Moreover, since lowering the rotational speed can reduce the relative velocity of the leakage flow (Figure 126), within the area the averaged Nu declines as the rotational speed decreases. However, the trend reverses and thus the Nu rebounds back quickly when traveling downstream. Also it is seen that the lower rotational speed is corresponding to higher Nu between 0.6 C_{ax} to 0.8 C_{ax}. It should be attributed to the presence of streaks with high Nu at the vicinity of downstream cooling holes. Stronger streaks are obtained at lower rotational speed therefore contribute higher local Nu as shown in the figure on page 223. The peak value appears at approximately 0.9 C_{ax} for all three rotational speeds. Larger numbers correspond to higher rotational speeds which could be the result of greater relative velocity of leakage flow. On the contrary, the impact of the rotational speed on the averaged Nu at squealer tip seems much less significant than that for the plane tip. Again, the leading-edge rim experiences higher Nu than the plane tip but tends to be insensitive to the rotational speed. As expected, the averaged Nusselt number retains low magnitude at the squealer cavity floor ranging from 0.05 C_{ax} to roughly 0.8 C_{ax}. Apparently, the squealer cavity is able to better protect the majority of blade tip surface from high Nu than the plane tip. The fluctuation in the Nu at the cavity floor is associated with the complex flow behaviors in the squealer cavity however no evident

effect of the rotational speed on the Nu can be viewed. Similarly, the aft of the blade tip encounters high Nu due to the flow expansion and lack of protection of the cooling film.

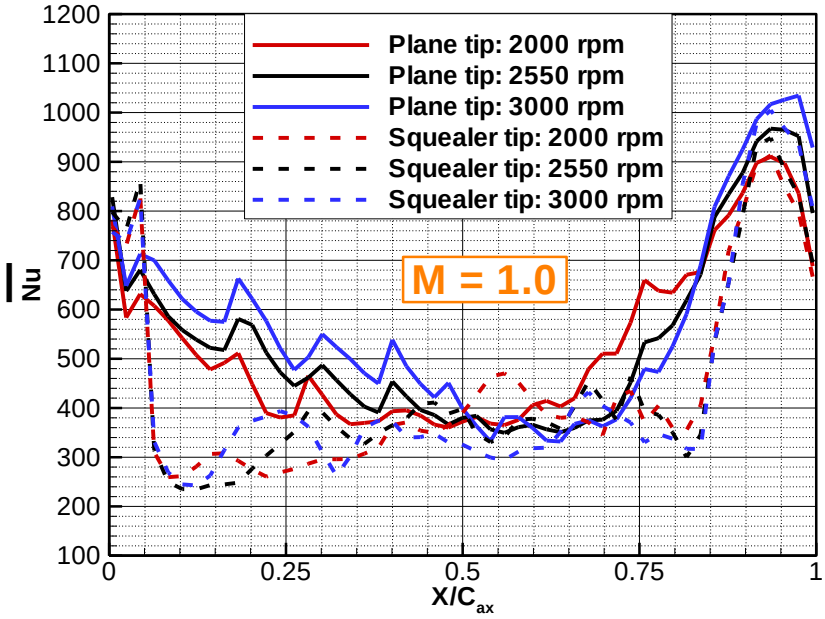

Figure 127: Impact of rotational speed on the pitchwise-averaged Nusselt number along the axial chord for blade tips with tip hole cooling at M = 1.0.

Figure 128 depicts the area-averaged Nusselt number versus the rotational speed for both the plane and squealer tips with tip hole cooling at M = 1.0. Overall, the rotational speed has very small impact on the Nu averaged at blade tip area. It is seen that the plane tip obtains higher Nu than the squealer tip for all three rotational speeds. The magnitude is slightly larger at 3000 rpm than that at lower rotational speed for the plane tip whereas it is a bit smaller for the squealer tip. Otherwise, the area-averaged Nu at both the squealer cavity inner wall and rim surface shows independency to the rotational speed. In addition, the Nu at the cavity floor slightly drops when the rotational speed reaches

3000 rpm. Based on the current study results, one may conclude that the overall Nu is independent to the rotational speed for both the plane and squealer tips with tip hole cooling.

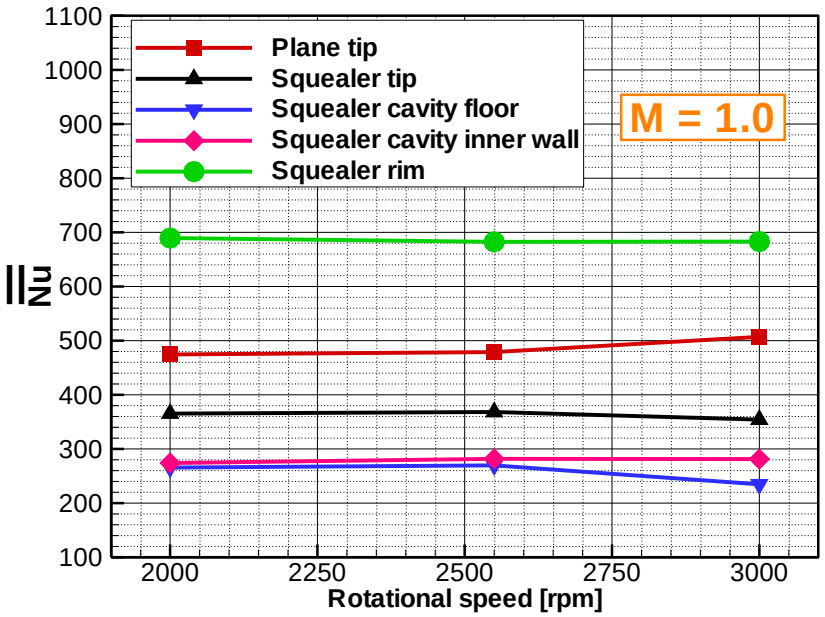

Figure 128: Impact of rotational speed on the area-averaged Nusselt number for blade tips with tip hole cooling at M = 1.0.

The impact of rotational speed on the distribution of heat flux ratio at both the plane and squealer tips is exhibited in Figure 129. From the contour plots, apparently different effect of the rotational speed is shown for the plane tip and squealer tip respectively. As seen, since the cooling jets for the plane tip are directly exposed to the mainstream, the directions of cooling jets are altered at different rotational speeds due to the variation in the incidence angle. This can be recognized from the deformation of the area with low heat flux ratio. Basically these patches or streaks that maintain low heat load are

associated with the coverage of film cooling where high cooling effectiveness and low heat transfer occur. Therefore their shape and size varies that directly affect the heat load at the plane tip. Accordingly, the leading edge and trailing edge undergo high heat load. However, the rotational effect on the squealer tip is not as explicit as the plane tip. It is seen that the heat load at pressure-side rim drops with the increasing rotational speed since more coolant leaks from the pressure side at higher rotational speed. Most of the suction-side rim experiences relatively low heat load at all three rotational speeds. Additionally the heat load at the squealer cavity floor declines as the rotational speed enhances. It could be associated with the complicated mixing and interaction process within the cavity. Essentially the reduced mainstream velocity may weaken the mixing between the leakage flow and coolant at lower rotational speed. In the meantime, the increased flow angle might also alter the flow interactions within the cavity, for instance the location, size and strength of circulations. In addition, the leading-edge rim and the trailing edge are easily burned due to the local high heat load.

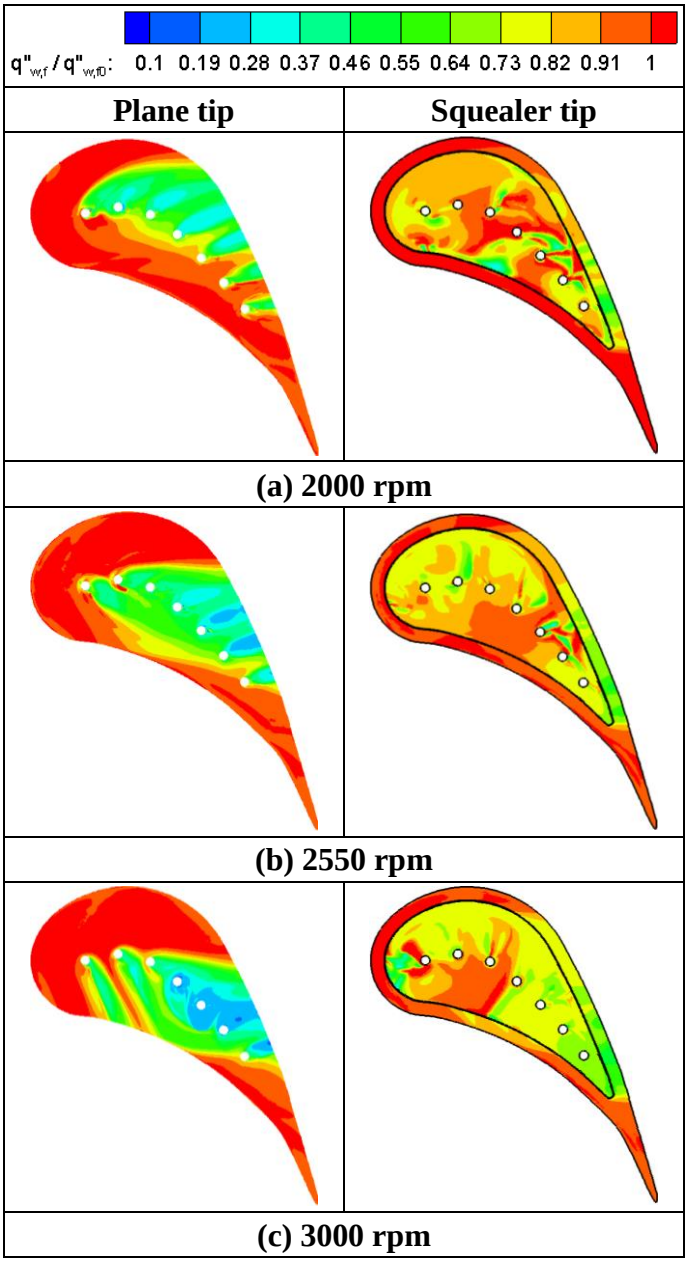

Figure 129: Impact of rotational speed on distributions of the heat flux ratio for blade tips with tip hole cooling at M = 1.0: Blade tip for the plane tip (left); Cavity floor and rim for the squealer tip (right).

Figure 130 shows the influence of the rotational speed on the pitchwise-averaged heat flux ratio along the axial chord for the plane and squealer tips with tip hole cooling

at M = 1.0. Based on the averaged distribution, it is seen that the heat load reduction occurs between the 0.2 C_{ax} and 0.9 C_{ax} for the plane rotating at all speeds. The rotation effect can be explicitly seen from approximately 0.5 C_{ax} to 0.8 C_{ax} where the heat flux ratio declines as the rotational speed rises. This is benefited from the coolant accumulation in the vicinity of the four downstream cooling holes at high rotational speed. The presence of squealer cavity extends the range of heat load reduction from 0.05 C_{ax} and 0.9 C_{ax} for all the rotational speeds. It is noticed that the averaged heat flux ratio right downstream of the leading-edge rim drops down as the blade rotates faster. As mentioned earlier, it should be related to the change of circulations close to the leading edge due to the alteration in the incidence angle. Overall higher heat load is observed at lower rotational speeds at further downstream. The area-averaged heat flux ratio versus rotational speed for tip hole cooling is summarized in Figure 131. As shown, the averaged heat flux ratio monotonically declines with the increasing rotational speed for both the plane and squealer tips. At all rotational speeds, more overall heat load is obtained at the squealer tip than the plane tip. Moreover, the overall values indicate that the area-averaged heat load at squealer tip is more sensitive to the rotational speed since it drops faster when the rotational speed increases. In addition, all the parts of the squealer tip encounter smaller overall heat load at higher rotational speeds. By comparing with Figure 103, one can conclude that the overall heat load at the plane tip is more sensitive to the blowing ratio whereas it is more likely to be affected by the rotational speed for the squealer tip.

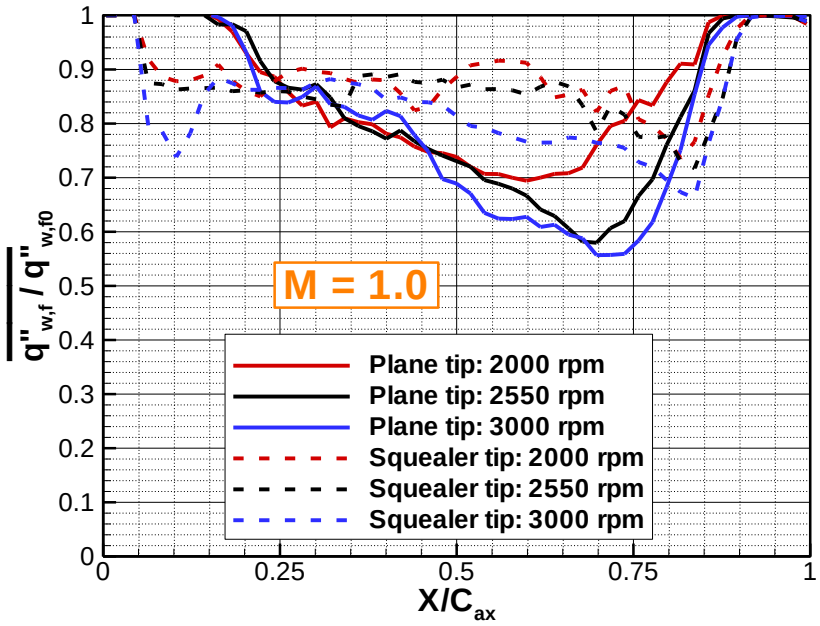

Figure 130: Impact of rotational speed on the pitchwise-averaged heat flux ratio along the axial chord for blade tips with tip hole cooling at M = 1.0.

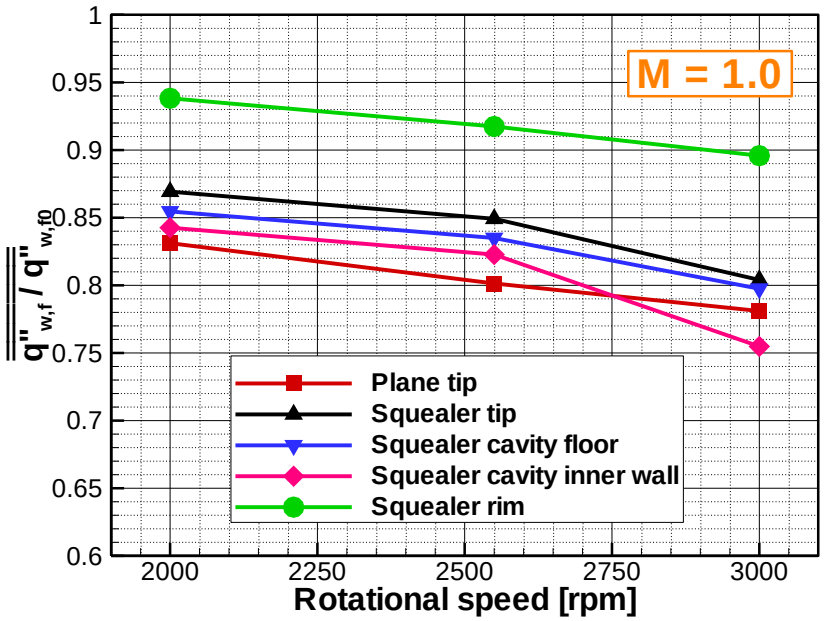

Figure 131: Impact of rotational speed on the area-averaged heat flux ratio for blade tips with tip hole cooling at M = 1.0.

8.2.3.2 Plane and squealer tips with pressure-side hole cooling

The distribution of Nusselt number on both the plane and squealer tips with pressure-side hole cooling at three rotational speeds for M = 1.0 is shown in Figure 132. As seen, the variation of rotational speed causes the alterations in the Nu distribution for both the plane and squealer tips. Due to the changes of the incidence angle, not only the location but also the shape of "sweet spot" on the plane tip has been shifted. The size of the "sweet spot" is smallest when rotating at 3000 rpm. Meanwhile, the crescent-shape area with high Nu close to the leading edge moves towards the pressure side as the rotational speed reduces. Since the attack angle increases, more coolant particles are pushed into the tip gap and thus pass over the plane tip surface. As a result, the re-attachment of the cooling jets generates more spots with high Nu at 2000 rpm and 2550 rpm. Relatively high Nu is obtained in the vicinity as well. One may notice that slightly higher Nu occurs at these re-attachment spots at 2550 rpm and 3000 rpm. The primary reason is that the a few upstream cooling jets at 2550 rpm are not altered immediately like those at 2000 rpm. Instead, they flow downstream and re-attach to the tip surface with other jets and form accumulation effect as shown in figures on pages 207 and 208, which thus to some extent enhances the local Nu. Such phenomenon is even more obvious for 3000 rpm. For the squealer tip, high Nu is obtained at the squealer rim for all three rotational speeds. The most significant impact of the rotational speed appears at the squealer cavity floor. As seen, due to the variation of the flow angle, the re-attachment point of the leakage flow, where the high Nu occurs, moves from the pressure-side rim to the suction-side

rim as the rotational speed declines. Otherwise, the rest of the cavity floor remains lowest Nu level.

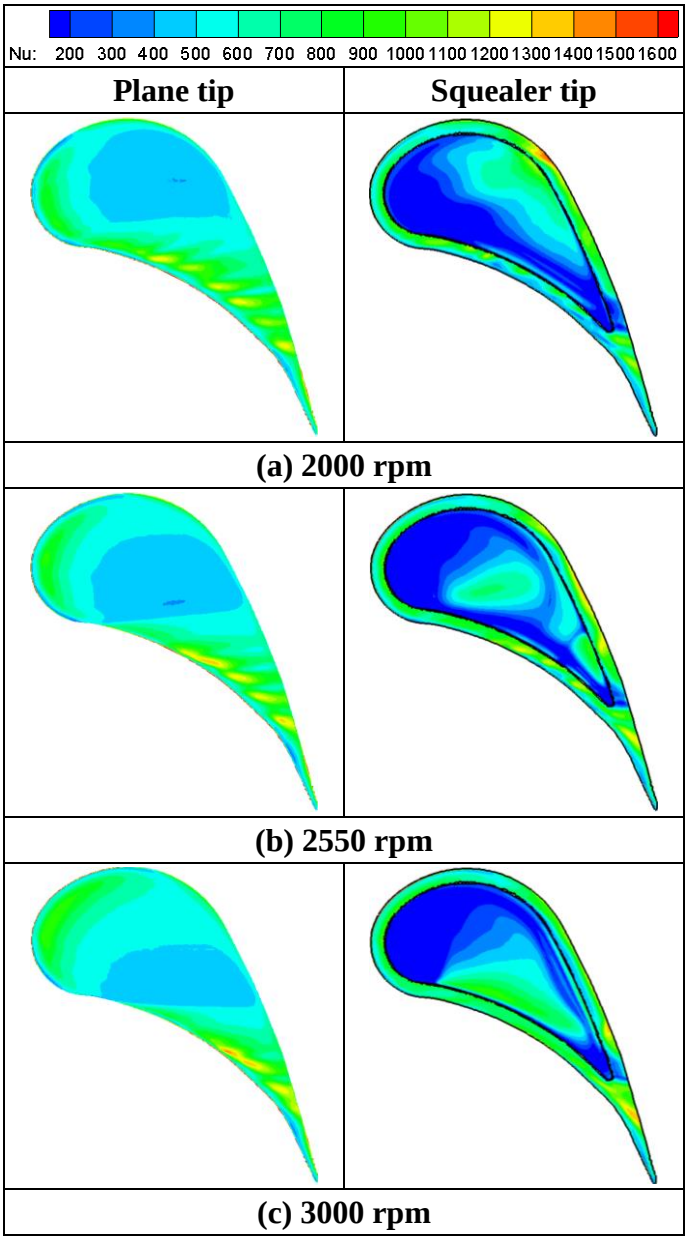

Figure 132: Impact of rotational speed on distributions of the Nusselt number for blade tips with pressure-side hole cooling at M = 1.0: Blade tip for the plane tip (left); Cavity floor and rim for the squealer tip (right).

Figure 133 depicts the pitchwise-averaged Nusselt number along the axial chord of both the plane and squealer tips with pressure-side hole cooling at M = 1.0 for three rotational speeds. Between the leading edge and 0.2 C_{ax} of the plane tip, the greatest Nu is corresponding to the highest rotational speed due to its largest local flow speed. Beyond this point, the Nu at 2000 rpm becomes larger than that at 2550 rpm, which is due to the re-attachment of coolant originating from the upstream cooling holes. After the transitional section from 0.2 C_{ax} to 0.5 C_{ax}, the trend reverses so that the averaged Nu decreases with the growing rotational speed between 0.5 C_{ax} and 0.85 C_{ax}. As mentioned earlier, the re-attachment of more cooling particles at lower rotational speeds enhances the local Nu. In contrast, the averaged Nu is much lower in most area of the squealer tip than the plane tip due to the presence of squealer cavity. The sudden jump of the averaged Nu at 2000 rpm and 2550 rpm is primarily due to the re-attachment of the leakage flow on the cavity floor. The area-averaged Nusselt number along the axial chord on the plane and squealer tips with pressure-side hole cooling at M = 1.0 with three rotational speeds is shown in Figure 134. As seen, the impact of rotational speed on the overall Nu is very tiny so that it should be fair to state that the area-averaged Nu at both the plane and squealer tips is independent to the rotational speed. Even though the difference among the three rotational speeds is very small, the smallest averaged Nu is found at 2550 rpm. It might be the balance of the rotational effect and coolant re-attachment. As expected, the presence of squealer cavity helps reduce about 25% Nu in average than the plane tip. Again, the highest Nu occurs at the squealer rim whereas the lowest on the cavity floor for all rotational speeds.

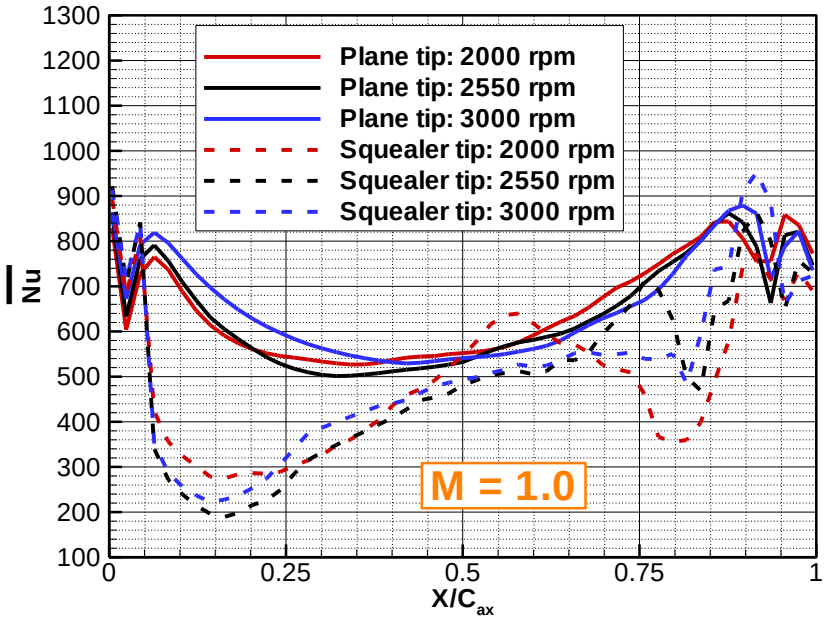

Figure 133: Impact of rotational speed on the pitchwise-averaged Nusselt number along the axial chord for blade tips with pressure-side hole cooling at M = 1.0.

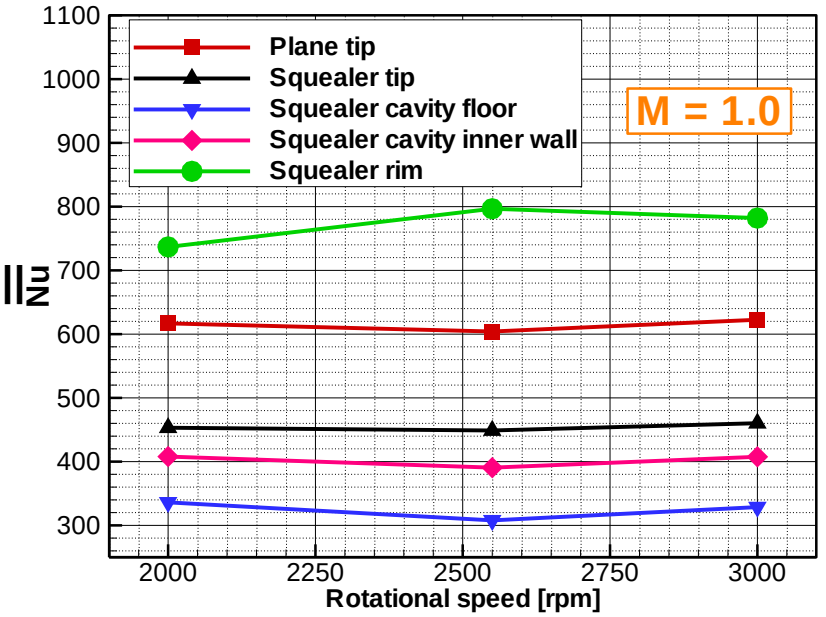

Figure 134: Impact of rotational speed on the area-averaged Nusselt number for blade tips with tip hole cooling at M = 1.0.

Figure 135 depicts the impact of rotational speed on the distribution of heat flux ratio on both the plane and squealer tip with pressure-side hole cooling at 3000 rpm with M = 1.0. Since it turns out that the rotational effect on the heat transfer is insignificant, the heat flux ratio is highly relevant to the film cooling effectiveness. This can be seen by comparing the figure on page 219 and Figure 135. As seen, lower heat flux ratio is obtained where is well covered by the cooling film for both the plane and squealer tips. For the plane tip, the cooling film is only able to cover the rear portion. At lower rotational speed due to the increase in the incidence angle, more coolant particles are pushed towards the suction side and thus cross over the plane tip surface. As a result, both the coverage area and film cooling effectiveness are enhanced and accordingly lower heat flux ratio is obtained in a wider region. Similar situation can be viewed at the squealer rim since it is the only part over which the cooling film passes. As seen, lower heat flux ratio is obtained on the pressure-side rim and trailing edge at the off-design rotational speeds. Due to the increase of incidence angle, more coolant is able to travel through the tip gap therefore more area of the suction-side rim gains lower heat flux ratio at the smaller rotational speeds. When the rotating speed reaches 3000 rpm, no heat load reduction is observed at the suction-side rim. In addition, a patchy area with low heat flux ratio is seen at the trailing end of squealer cavity, which is primarily due to the entrainment of a few coolant particles at lower rotational speed. Almost no heat reduction occurs at most of the cavity floor and the leading-edge rim.

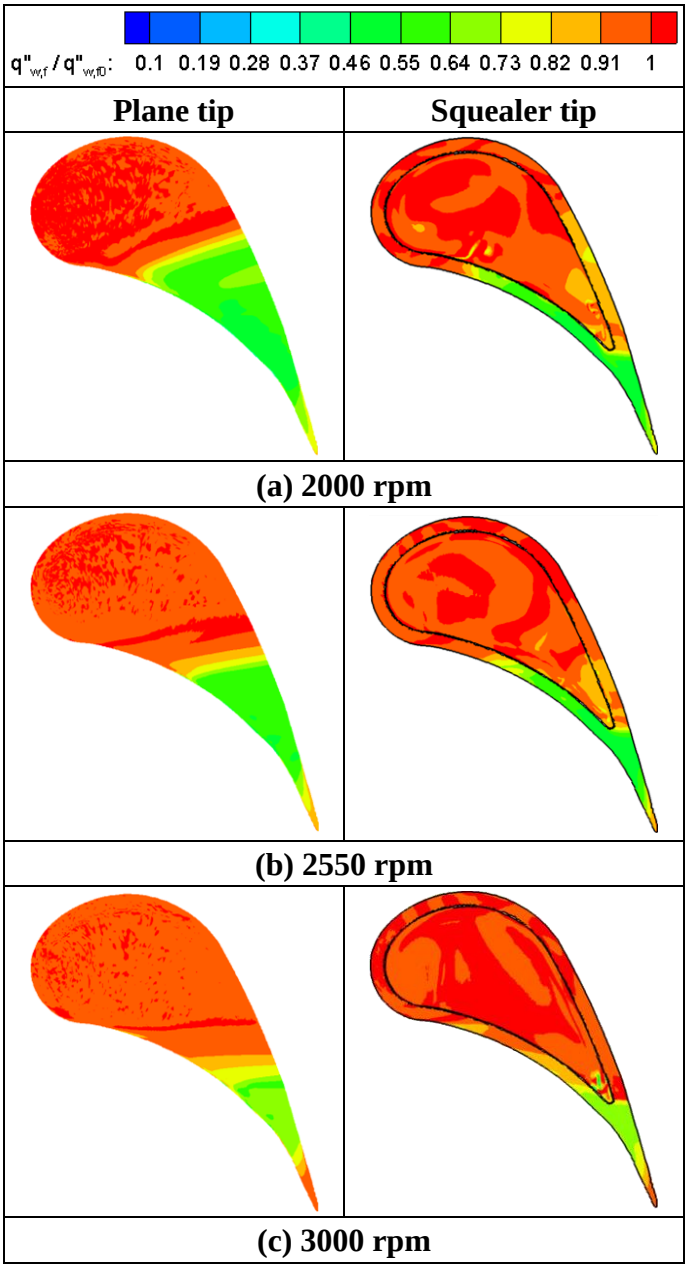

Figure 135: Impact of rotational speed on distributions of the heat flux ratio for blade tips with pressure-side hole cooling at M = 1.0: Blade tip for the plane tip (left); Cavity floor and rim for the squealer tip (right).

The pitchwise-averaged heat flux ratio along the blade axial chord on both the plane and squealer tips with pressure-side hole cooling at M = 1.0 with three rotational speeds

is plotted in Figure 136. The overall trend is that the averaged heat flux ratio at the plane and squealer tips decreases as the rotational speed is reduced. For the plane tip, the averaged heat flux ratio is almost unity at the leading edge and such level maintains till at least 1/3 C_{ax}. The averaged heat load starts to drop at 0.35 C_{ax} for 2000 rpm whereas approximately 0.5 C_{ax} for 2550 rpm and 3000 rpm. As seen, it drops faster at the lower rotational speeds due to the higher film cooling effectiveness. The averaged heat flux ratio at the plane tip keeps dropping and reaches its lowest magnitude at around 0.88 C_{ax} for all three rotational speeds. The minimum averaged heat load goes down with the decreasing rotational speed. At 2000 rpm, almost 46% reduction in averaged heat flux ratio is obtained at the minimum point whereas about 32% at 3000 rpm. Beyond 0.88 C_{ax}, the averaged heat flux ratio grows again. In contrast, smaller reduction in the averaged heat flux ratio is obtained between the leading edge and 0.75 C_{ax} for the squealer tip than the plane tip, since only the squealer rim is well cooled in this range. Then the averaged heat load rapidly drops to the minimum point at about 0.9 C_{ax}. At this point, almost 50% reduction in averaged heat flux ratio is seen at 2000 rpm whereas around 30% for 3000 rpm. The "trough" width is smaller for the squealer tip due to the presence of the squealer cavity. Figure 137 summarizes the area-averaged heat flux ratio versus rotational speed for the plane and squealer tips with pressure-side hole cooling at M = 1.0. As expected, the area-averaged heat flux ratio at the plane and squealer tips monotonically grows with the increasing rotational speed. Moreover, the averaged heat load at the plane tip is always lower than that at the squealer tip for all three rotational conditions, simply because more plane tip surface is cooled. In addition, apparently the

squealer cavity floor has the highest heat load in average whereas the largest averaged heat load reduction occurs at the squealer rim.

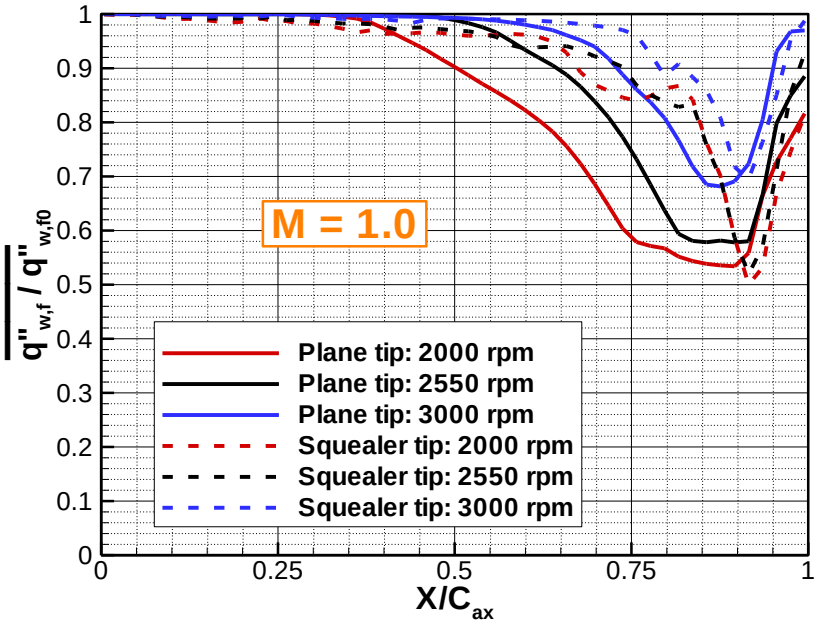

Figure 136: Impact of rotational speed on the pitchwise-averaged heat flux ratio along the axial chord for blade tips with pressure-side hole cooling at M = 1.0.

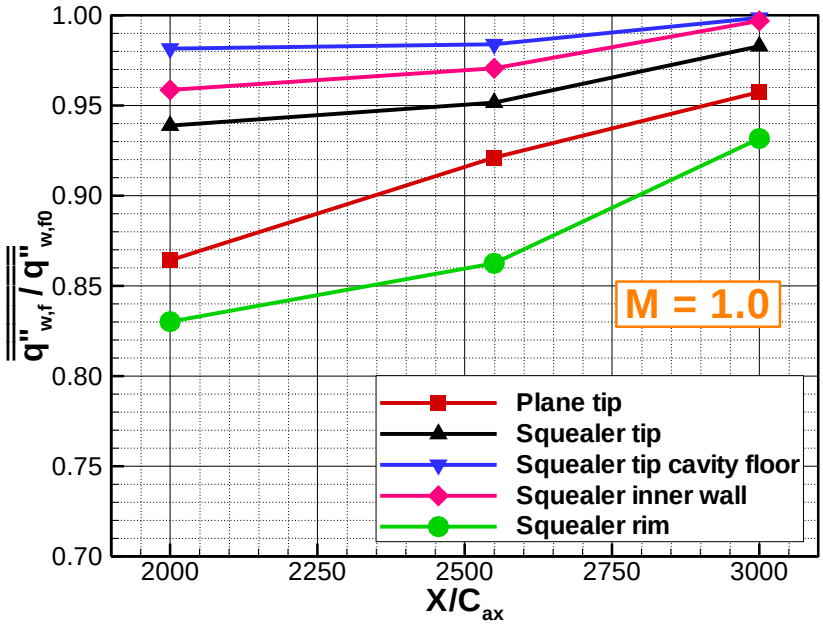

Figure 137: Impact of rotational speed on the area-averaged heat flux ratio for the blade tips with pressure-side hole cooling at M = 1.0.

9. CONCLUSIONS

An effort is made to numerically study the impact of rotating turbine conditions on flow and film cooling with the application of the endwall contouring and blade tip ejection. The main conclusions from this study are summarized below.

9.1 Endwall Contouring

9.1.1 Aerodynamic performance

(1) The predicted pressure difference between the pressure- and suction-side gradually increases as the turbine rotational speed decreases from the reference point (3000 rpm) to off-design states with lower rotational speeds. For all rotational conditions, the presence of the endwall contouring for second rotor effectively reduces the pressure difference by 30~40%.

(2) For the contoured endwall, the numerical results show significant reduction in passage vorticity, secondary kinetic energy and rotor total pressure loss in second rotor for both design and off-design conditions. Remarkable shrink in the loss core due to the passage vortex system reflects the significant drop in strength of secondary flows. More loss reduction is obtained at lower rotational speeds which are associated with stronger secondary flows.

(3) Both experiments and simulations show an increase in the turbine total-to-static efficiency when comparing the contoured turbine with non-contoured reference turbine. Particularly, the measured largest efficiency improvement achieves 1.04% whereas CFD predicts overall 0.5%~0.77% of increase.

9.1.2 Film cooling effectiveness and heat transfer

(1) MFR effects: The purged cooling film effectively covers about 30 to 40% of axial chord length on the first-rotor endwall. PSP measurements show larger covered platform surface and higher film cooling effectiveness with more coolant (higher MFR) purged out. The coolant film covers more pressure-side area and spreads out more uniformly in pitchwise direction on the contoured endwall. However, in case of non-contoured endwall its cooling effectiveness diminishes due to strong secondary flows. CFD captures the trend however over-predicts the magnitude. The Nusselt number on the front portion of the rotor hub grows with the increasing MFR for both the contoured and non-contoured cases. However, the Nu on the contoured endwall is lower than that on the non-contoured platform primarily due to the expanding contouring profile in streamwise. In addition, the heat flux ratio on the endwall declines as the MFR grows since the cooling protection improves. Higher film cooling effectiveness and lower heat transfer coefficient or Nusselt number on the contoured hub result in smaller heat flux ratio when compared to the non-contoured endwall.

(2) Rotation effects: For a fixed coolant mass flow, the measured cooling film tends to decay in both coverage and effectiveness as the rotational speed decreases. Up to 50% notable improvement in film cooling is obtained for contoured endwall regardless of varied rotational speed conditions. Nonetheless, CFD shows a small sensitivity to the rotation effect. Similarly, although Nusselt number drops with an increase in the rotational speed for both the contoured and non-contoured cases, the influence of rotational speed on the endwall Nusselt number is rather insignificant. Again, due to the

diverging shape of endwall contouring, the Nu on contoured endwall is smaller than the reference case. Since the film cooling effectiveness tends to enhance while the heat transfer coefficient declines as the rotational speed increases, the heat flux ratio on the rotor endwall drops for all cases. The heat load on the contoured endwall is slightly smaller than the reference case.

(3) Quantitative and qualitative discrepancies between experimental and numerical results were observed in this study. Many factors can affect the accuracy of numerical simulations, which include numerical models, turbulence models, transitional models, etc. RANS is generally capable of obtaining the trend accurately and thus can be utilized as a useful tool for parameter studies. A convincing example is that the contouring in this study was finalized according to RANS predictions however excellent performance is confirmed by experiments. URANS might be more appropriate and sometimes necessary to simulate flows with highly unsteady phenomena such as stator-rotor interactions.

9.2 Blade Tip Ejection

(1) Blowing ratio effects: The film cooling effectiveness on the blade tips monotonically increases with increasing blowing ratio for all the four tip cooling configurations. For the tip hole cooling, although the local and overall film cooling effectiveness on the plane tip has higher magnitude, more uniform distributions and thus larger coverage are obtained on the squealer tip. In contrast, much worse cooling protection is seen for the pressure-side hole cooling than the tip hole cooling because only the aft of the blade tip is cooled by the coolant jets ejected from the pressure side.

For the pressure-side hole cooling, better film cooling performance is obtained on the plane tip due to the larger coverage. The Nusselt number on the plane tip with tip hole cooling decreases with an increases in the blowing ratio, whereas the impact of blowing ratio on the squealer tip with tip hole cooling is rather inconsiderable. The re-attachment of cooling jets reverses the trend when it comes to the plane tip with pressure-side hole cooling however the blowing ratio effects on the squealer tip are barely notable. As a result the heat flux ratio for the tip hole cooling mitigates with the increasing blowing ratio, whereas it slowly rises for the pressure-side hole cooling.

(2) Rotation effects: The changes in the rotational speed primarily lead to the alterations of the mainstream incidence angle and consequently impact the film cooling and heat transfer with tip ejections. For the tip hole cooling, the film cooling effectiveness tends to increase when the rotational speed grows, whereas the reverse trend is obtained for the pressure-side hole cooling. The Nusselt number on the blade tips is much less sensitive to the rotational speed for all the cooling ejection configurations although the local distributions exhibit variations due to the shift of the incidence angle. The heat flux ratio obtained on the tip reduces with the increasing rotational speed for the tip hole cooling whereas enhances as the rotational speed rises when it comes to the pressure-side hole cooling. Nevertheless the squealer tip encounters higher overall heat load on the tip surface than the plane tip for both two film cooling systems.

REFERENCES

[1] Dennis, R.A., and Harp, R., 2007, "Overview of the U.S. Department of Energy's Office of Fossil Energy Advanced Turbine Program for Coal Based Power Systems with Carbon Capture," Proceedings of ASME Turbo Expo 2007, GT2007-28338.

[2] Ewen, J.S., Huber, F.W. and Michell, J.P., 1973, "Investigation of the Aerodynamic Performance of Small Axial Turbines," J. Eng. Gas Turbines Power 95(4), 326-332.

[3] Malzacher, F.J., Gier, J. and Lippl, F., 2003, "Aerodesign and Testing of an Aero-Mechanically Highly Loaded LP Turbine," Proceedings of ASME Turbo Expo 2003, GT2003-38338.

[4] Schobeiri, M.T., Suryanarayanan, A., Jermann, C. and Neuenschwander, T., 2004, "A Comparative Aerodynamic and Performance Study of a Three-Stage High Pressure Turbine with 3-D Bowed Blades and Cylindrical Blades," Proceedings of ASME Turbo Expo 2004, GT2004-53650.

[5] Atkins, N.R., Miller, R.J. and Ainsworth, R.W., "The Development of Aerodynamic Performance Measurements in a Transient Test Facility," Proceedings of ASME Turbo Expo 2004, GT2004-53813.

[6] Atkins, N.R. and Ainsworth, R.W., "The Measurement of Shaft Power in a Fully Scaled Transient Turbine Test Facility," Proceedings of ASME Turbo Expo 2005, GT2005-68998.

[7] Rao, N.M. and Camci, C., 2005, "Visualization of Rotor Endwall, Tip Gap, and Outer Casing Surface Flows in a Rotating Axial Turbine Rig," Proceedings of ASME Turbo Expo 2005, GT2005-68264.

[8] Behr, T., Kalfas, A.I. and Abhari R.S., "Unsteady Flow Physics and Performance of an One-and-1/2-Stage Unshrouded High Work Turbine," Proceedings of ASME Turbo Expo 2006, GT2006-90959.

[9] Abdelfattah, S.A. and Schobeiri, M.T., 2010, "Experimental and Numerical Investigations of Aerodynamic Behavior of a Three-Stage HP-Turbine at Different Operating Conditions," Proceedings of ASME Turbo Expo 2010, GT2010-23564.

[10] Abdelfattah, S.A., Chibli, H.A. and Schobeiri, M.T., 2011, "Aerodynamic Investigation of the Performance of a Two Stage Axial Turbine at Design and Off-Design Conditions," ASME Turbo Expo 2011, GT2011-45909.

[11] Schobeiri, M. "Turbomachinery Flow Physics and Dynamic Performance," 2nd edition. Berlin; London: Springer, 2012. Print.

[12] Denton, J.D., 1993, "Loss Mechanisms in Turbomachines," J. TURBOMACH, Vol. 115, pp. 621-656.

[13] Eymann, S., Reinmöller, U., Niehuis, R., Förster, W., Beversdorff, M. and Gier, J., 2002, "Improving 3D Flow Characteristics in a Multistage LP Turbine by Means of Endwall Contouring and Airfoil Design Modification-Part 1: Design and Experimental Investigation," Proceedings of ASME Turbo Expo 2002, GT2002-30352.

[14] Vogt, H.F. and Zippel, M., 1996, "Sekundärströmungen in Turbinengittern mit geraden und gekrümmten Schaufeln; Visualisierung im ebenen Wasserkanal," Forschung im Ingenieurwesen-Engineering Research, vol. 62, no. 9, pp 247-253.

[15] Moustapha, S.H., Paron, G.J. and Wade, J.H.T., 1985, "Secondary Flows in Cascades of Highly Loaded Turbine Blades," Journal of Engineering for Gas Turbines and Power, Vol. 107, pp. 1031-1038.

[16] Hodson, H.P. and Dominy, R.G., 1987, "Three-Dimensional Flow in a Low-Pressure Turbine Cascade at Its Design Condition," J. TURBOMACH, Vol. 109, pp. 177-185.

[17] Harrison, S., 1990, "Secondary Loss Generation in a Linear Cascade of High-Turning Turbine Blade," J. TURBOMACH, Vol. 112, pp. 618-624.

[18] Wang, H.P., Olson, S.J., Goldstein, R.J. and Eckert, E.R.G., 1997, "Flow Visualization in a Linear Turbine Cascade of High Performance Turbine Blades," J. TURBOMACH, Vol. 119, pp. 1-8.

[19] Schobeiri, M.T. and Lu, K., 2011, Endwall Contouring Using Continuous Diffusion, a Breakthrough Method and its Application to a Three-stage High Pressure Turbine, ASME Paper, GT2011-45931.

[20] Hazelbach, F., Schiffer, H.P., Horsman, M., Dressen, S., Harvey, N. and Read, S., 2001, "The Application of Ultra-High Lift Blading in the BR715 LP Turbine," Proceeding s of ASME Turbo Expo 2001, 2001-GT-0436.

[21] Praisner, T. J., Allen-Bradley, E., Grover, E.A., Knezevici, D.C. and Sjolander, S.A., 2007, "Application of Non-Axisymmetric Endwall Contouring to

Conventional and High-Lift Turbine Airfoils," Proceedings of ASME Turbo Expo 2007, GT2007-27579.

[22] Zess, G.A. and Thole, K.A., 2001, "Computational Design and Experimental Evaluation of Using A Leading Edge Fillet On A Gas Turbine Vane," Proceedings of ASME Turbo Expo 2001, 2001-GT-0404.

[23] Shih, T.I-P. and Lin, Y.-L., 2002, "Controlling Secondary-Flow Structure by Leading-Edge Airfoil Fillet and Inlet Swirl to Reduce Aerodynamic Loss and Surface Heat Transfer," Proceedings of ASME Turbo Expo 2002, GT-2002-30529.

[24] Becz, S., Majewski, M.S. and Langston, L.S., 2003, "Leading Edge Modification Effects on Turbine Cascade Endwall Loss," Proceedings of ASME Trubo Expo 2003, GT2003-38898.

[25] Becz, S., Majewski, M.S. and Langston, L.S., 2004, "An Experimental Investigation of Contoured Leading Edges for Secondary Flow Loss Reduction," Proceedings of ASME Turbo Expo 2004, GT2004-53964.

[26] Saha, A.K., Mahmood, G.I. and Acharya, S., 2006, "The Role of Leading-Edge Contouring on End-Wall Flow and Heat Transfer: Computations and Experiments," Proceedings of ASME Turbo Expo 2006, GT2006-91318.

[27] Nagel, M.G. and Baier, Ralf-D., 2003, "Experimentally Verified Numerical Optimisation of a 3D-Parametrised Turbine Vane with Non-Axisymmetric End Walls," Proceedings of ASME Turbo Expo 2003, GT2003-38624.

[28] Torre, D., Vázquez, R., Blanco, E.R. and Hodson, H. P., 2006, "A New Alternative for Reduction of Secondary Flows in Low Pressure Turbines," Proceedings of ASME Turbo Expo 2006, 2006GT -91002.

[29] Saha, A.K. and Acharya, S., 2006, "Computations of Turbulent Flow and Heat Transfer through a Three-Dimensional Non-Axisymmetric Blade Passage," Proceedings of ASME Turbo Expo 2006, GT2006-90390.

[30] Gustafson, R., Mahmood G. and Acharya, S., 2007, "Aerodynamic Measurements in A Linear Turbine Blade Passage with Three-Dimensional Endwall Contouring," Proceedings of ASME Turbo Expo 2007, GT2007-28073.

[31] Knezevici, D.C., Sjolander, S.A., Praisner, T.J., Allen-Bradley, E. and Grover, E.A., 2008, "Measurements of Secondary Losses in A Turbine Cascade with the Implementation of Non-Axisymmetric Endwall Contouring," Proceedings of ASME Turbo Expo 2008, GT2008-51311.

[32] Knezevici, D.C., Sjolander, S.A., Praisner, T.J., Allen-Bradley, E. and Grover, E.A., 2009, "Measurements of Secondary Losses in A High-Lift Front-Loaded Turbine Cascade with the Implementation of Non-Axisymmetric Endwall Contouring, " Proceedings of ASME Turbo Expo 2009, GT2009-59677.

[33] Ingram, G., Gregory-Smith, D., Rose, M., Harvey, N. and Brennan G., 2002, "The Effect of End-Wall Profiling on Secondary Flow and Loss Development in A Turbine Cascade," Proceedings of ASME Turbo Expo 2002, GT-2002-30339.

[34] Ingram, G., Gregory-Smith, D. and Harvey, N., 2004, "Investigation of A Novel Secondary Flow Feature in A Turbine Cascade with End Wall Profiling," Proceedings of ASME Turbo Expo 2004, GT2004-53589.

[35] Brennan, G., Harvey, N.W., Rose, M.G., Fomison, N. and Taylor M.D., 2001, "Improving the Efficiency of the Trent 500 HP Turbine Using Non-Axisymmetric End Walls: Part 1 Turbine Design," Proceedings of ASME Turbo Expo 2001, 2001-GT-0444.

[36] Rose, M.G., Harvey, N.W., Seaman, P., Newman, D.A. and McManus, D., 2001, "Improving the Efficiency of the Trent 500 HP Turbine Using Non-Axisymmetric End Walls. Part II: Experimental Validation," Proceedings of ASME Turbo Expo 2001, 2001-GT-0505.

[37] Harvey, N.W., Brennan, G., Newman, D.A. and Rose, M.G., 2002, "Improving Turbine Efficiency Using Non-Axisymmetric End Walls: Validation in the Multi-Row Environment and with Low Aspect Ratio Blading," Proceedings of ASME Turbo Expo 2002, GT-2002-30337.

[38] Germain, T., Nagel, M., Raab, I., Schuepbach, P., Abhari, R.S. and Rose, M., 2008, "Improving Efficiency of A High Work Turbine Using Non-Axisymmetric Endwalls Part I: Endwall Design and Performance," Proceedings of ASME Turbo Expo 2008, GT2008-50469.

[39] Schuepbach, P., Abhari, R.S., Rose, M.G., Germain, T., Raab, I. and Gier, J., 2008, "Improving Efficiency of a High Work Turbine Using Non-Axisymmetric

Endwalls. Part II: Time-Resolved Flow Physics," Proceedings of ASME Turbo Expo 2008, GT2008-50470.

[40] Snedden, G., Dunn, D., Ingram, G. and Gregory-Smith, D., 2009, "The Application of Non-Axisymmetric Endwall Contouring in a Single Stage, Rotating Turbine," Proceedings of ASME Turbo Expo 2009, GT2009-59169.

[41] Snedden, G., Dunn, D., Ingram, G. and Gregory-Smith, D., 2010, "The Performance of a Generic Non-Axisymmetric End Wall in a Single Stage, Rotating Turbine at On and Off-Design Conditions," Proceedings of ASME Turbo Expo 2010, GT2010-22006.

[42] Blair, M.F., 1974, "An Experimental Study of Heat Transfer and Film Cooling on Large-Scale Turbine Endwalls," J. Heat Transfer 96(4), 524-529.

[43] Graziani, R.A., Blair, M.F., Taylor, J.R. and Mayle R.E., 1980, "An Experimental Study of Endwall and Airfoil Surface Heat Transfer in a Large Scale Turbine Blade Cascade," J. Eng. Gas Turbines Power 102(2), 257-267.

[44] Gaugler, R.E. and Russell, L.M., 1984, "Comparison of Visualized Turbine Endwall Secondary Flows and Measured Heat Transfer Patterns," J. Eng. Gas Turbines Pwer 106(1), 168-172.

[45] Harvey, N.W., Rose, M.G., Coupland, J. and Jones, T.V., 1999, "Measurement and Calculation of Nozzle Guide Vane End Wall Heat Transfer," J. TURBOMACH., 121(2), 184-190.

[46] Nicklas, M., 2001, “Film-Cooled Turbine Endwall in a Transonic Flow Field: Part II—Heat Transfer and Film-Cooling Effectiveness,” J. TURBOMACH., 123(4), 720-729.

[47] Knost, D.G. and Thole, A., 2003, “Computational Predictions of Endwall Film-Cooling for a First Stage Vane,” Proceedings of ASME Turbo Expo 2003, GT2003-38252.

[48] Lynch, S.P. and Thole, K.A., 2008, “The Effect of Combustor-Turbine Interface Gap Leakage on the Endwall Heat Transfer for a Nozzle Guide Vane,” J. TURBOMACH., 130(4), 041019.

[49] Liu, K., Yang, S.F. and Han, J.C., 2013, “Influence of Coolant Density on Turbine Platform Film-Cooling with Stator-Rotor Purge Flow and Compound-Angle Holes,” Proceedings of ASME Turbo Expo 2013, GT2013-94155.

[50] Piggush, J.D. and Simon, T.W., 2007, “Heat Transfer Measurements in a First-Stage Nozzle Cascade Having Endwall Contouring: Misalignment and Leakage Studies,” J. TURBOMACH., 129(4), 782-790.

[51] Gustafson, R., Mahmood, G.I. and Acharya, S., 2007 “Flowfield in a Film-Cooled Three-Dimensional Contoured Endwall Passage: Aerodynamic Measurements,” Proceedings of ASME Turbo Expo 2007, GT2007-28154.

[52] Mahmood, G.I. and Acharya, S., 2007, “Measured Endwall Flow and Passage Heat Transfer in a Linear Blade Passage with Endwall and Leading Edge Modifications,” Proceedings of ASME Turbo Expo 2007, GT2007-28179.

[53] Barigozzi, G., Franchini, G., Perdichizzi, A. and Quattrore, M., 2008, "Endwall Film Cooling Effects on Secondary Flows in a Contoured Endwall Nozzle Vane," Proceedings of ASME Turbo Expo 2008, GT2008-51065.

[54] Okita, Y. and Nakamata, C., 2008, "Computational Predictions of Endwall Film Cooling for a Turbine Nozzle Vane with an Asymmetric Contoured Passage," Proceedings of ASME Turbo Expo 2008, GT2008-50878.

[55] Saha, A.K. and Acharya, S., 2008, "Computations of Turbulent Flow and Heat Transfer Through a Three-Dimensional Nonaxisymmetric Blade Passage," J. TURBOMACH., 130(3), 031008.

[56] Mahmood, G.I., Gustafson, R. and Acharya, S., 2009, "Flow Dynamics and Film Cooling Effectiveness on a Non-Axisymmetric Eontour Endwall in a Two Dimensional Cascade Passage," Proceedings of ASME Turbo Expo 2009, GT2009-60236.

[57] Thrift, A.A., Thole, K.A. and Hoda, S., 2011, "Effects of an Axisymmetric Contoured Endwall on a Nozzle Guide Vane: Convective Heat Transfer Measurements," J. TURBOMACH., 133(4), 041008.

[58] Thrift, A.A., Thole, K.A. and Hoda, S., 2011, "Effects of an Axisymmetric Contoured Endwall on a Nozzle Guide Vane: Adiabatic Effectiveness Measurements," J. TURBOMACH., 133(4), 041007.

[59] Blair, M.F., 1994, "An Experimental Study Heat Transfer in a Large-Scale Turbine Rotor Passage," J. TURBOMACH., 116(1), 1-13.

[60] Paniagua, G., Dénos, R. and Almeida, S., 2004, "Effect of the Hub Endwall Cavity Flow on the Flow-Field of a Transonic High-Pressure Turbine," J. TURBOMACH., 126(4), 578-586.

[61] Ong, J.H.P., Miller, R.J. and Uchida, S., 2006, "The Effect of Coolant Injection on the Endwall Flow of a High Pressure Turbine," Proceedings of ASME Turbo Expo 2006, GT2006-91060.

[62] Yang, H., Gao, Z., Chen, H.C., Han, J.C. and Schobeiri, M.T., 2009, "Prediction of Film Cooling and Heat Transfer on a Rotating Blade Platform With Stator-Rotor Purge and Discrete Film-Hole Flows in a 1-1/2 Turbine Stage," J. TURBOMACH., 131(4), 041003.

[63] Suryanarayanan, A., Mhetras, S.P., Schobeiri, M.T. and Han, J.C., 2009, "Film-Cooling Effectiveness on a Rotating Blade Platform," J. TURBOMACH., 131(1), 011014.

[64] Suryanarayanan, A., Ozturk, B., Schobeiri, M.T. and Han, J.C., "Film-Cooling Effectiveness on a Rotating Turbine Platform Using Pressure Sensitive Paint Technique," J. TURBOMACH., 132(4), 041001.

[65] Marini, R. and Girgis, S., 2007, "The Effect of Blade Leading Edge Platform Shape on Upstream Disk Cavity to Mainstream Flow Interaction of a High-Pressure Turbine Stage," Proceedings of ASME Turbo Expo 2007, GT2007-27429.

[66] Schuepbach, P., Abhari, R.S., Rose, M.G. and Gier, J., 2009, "Influence of Rim Seal Purge Flow on Performance of an Endwall-Profiled Axial Turbine," Proceedings of ASME Turbo Expo 2009, GT2009-59653.

[67] Jenny, P., Abhari, R.S., Rose, M.G., Brettschneider, M. and Gier, J., 2011, "A Low Pressure Turbine with Profiled End Walls and Purge Flow Operating with a Pressure Side Bubble," Proceedings of ASME Turbo Expo 2011, GT2011-46309.

[68] Metzger, D.E., Bunker, R.S. and Chyu, M.K., 1989, "Cavity Heat Transfer on a Transverse Grooved Wall in a Narrow Flow Channel," J. Heat Transfer, Vol. 111, pp. 73-79.

[69] Bunker, R.S., "A Review of Turbine Blade Tip Heat Transfer," Heat Transfer in Gas Turbine Systems, Annals of the New York Academy of Sciences, 934, May 2001, pp. 64-79.

[70] Azad, G.S., Han, J.C. and Teng, S., 2000, "Heat Transfer and Pressure Distributions on a Gas Turbine Blade Tip," Proceedings of ASME Turbo Expo 2000, 2000-GT-194.

[71] Azad, G.S., Han, J.C. and Boyle, R.J., 2000, "Heat Transfer and Flow on the Squealer Tip of a Gas Turbine Blade," Proceedings of ASME Turbo Expo 2000, 2000-GT-195.

[72] Bunker, R.S., Ameri, A.A. and Bailey, J.C., 2000, "Heat Transfer and Flow on the First-Stage Blade Tip of a Power Generation Gas Turbine: Part 1-Experimental Results," J. TURBOMACH, Vol. 122, pp. 263-271.

[73] Ameri, A.A. and Bunker, R.S., 2000, "Heat Transfer and Flow on the First-Stage Blade Tip of a Power Generation Gas Turbine: Part 2-Simulation Results," J. TURBOMACH, Vol. 122, pp. 272-277.

[74] Kim, Y.W. and Metzger, D.E., 1995, “Heat Transfer and Effectiveness on Film Cooled Turbine Blade Tip Models,” J. TURBOMACH, Vol. 117, pp. 12-21.

[75] Kim, Y.W, et al, 1995, “A Summary of the Cooled Turbine Blade Tip Heat Transfer and Film Effectiveness Investigations Performed by Dr. D. E. Metzger,” J. TURBOMACH, Vol. 117, pp. 1-11.

[76] Kwak, J.S. and Han, J.C., 2002, “Heat Transfer Coefficient and Film-Cooling Effectiveness on a Gas Turbine Blade Tip,” Proceedings of ASME Turbo Expo 2002, GT2002-30194.

[77] Kwak, J.S. and Han, J.C., 2002, “Heat Transfer Coefficient and Film-Cooling Effectiveness on the Squealer Tip of a Gas Turbine Blade,” Proceedings of ASME Turbo Expo 2002, GT2002-30555.

[78] Acharya, S., Yang, H., Ekkad, S.V., Prakash, C. and Bunker, R. 2002, “Numerical Simulation of Film Cooling on the Tip of a Gas Turbine Blade,” Proceedings of ASME Turbo Expo 2002, GT2002-30553.

[79] Christophel, J.R., Thole, K.A. and Cunha, F.J., 2004, “Cooling the Tip of a Turbine Blade Using Pressure Side Holes - Part 1: Adiabatic Effectiveness Measurements,” Proceedings of ASME Turbo Expo 2004, GT2004-53251.

[80] Yang, H., Chen, H.C. and Han, J.C., 2004, “Numerical Prediction of Film Cooling and Heat Transfer with Diffenrent Film-Hole Arrangements on the Plane and Squealer Tip of a Gas Turbine Blade,” Proceedings of ASME Turbo Expo 2004, GT2004-53199.

[81] Gao, Z., Narzary, D., Mhetras, S. and Han, J.C., 2009, “Effect of Inlet Flow Angle on Gas Turbine Blade Tip Film Cooling,” J. TURBOMACH, Vol. 131, pp. 1-12.

[82] Achary, S., Kramer, G., Moreaux, L. and Nakamata, C., 2010, “Squealer Tip Heat Transfer with Film Cooling,” Proceedings of ASME Turbo Expo 2010, GT2010-23688.

[83] Naik, S., Georgakis, C., Hofer, T. and Lengani, D., 2012, “Heat Transfer and Film Cooling of Blade Tips and Endwalls,” J. TURBOMACH, Vol. 134, pp. 1-11.

[84] Metzger, D.E., Bunker, R.S. and Chyu, M.K., 1989, “Cavity Heat Transfer on a Transverse Grooved Wall in a Narrow Flow Channel,” J. Heat Transfer, Vol. 111, pp. 73-79.

[85] Metzger, D.E., Dunn, M.G., and Hah, C., 1991, "Turbine Tip and Shroud Heat Transfer,” ASME J. TURBOMACH, Vol. 113, pp. 502-507.

[86] Dunn, M.G. and Haldeman, C.W., 2000, “Time-Averaged Heat Flux for a Recessed Tip, Lip, and Platform of a Transonic Turbine Blade,” ASME J. TURBOMACH, Vol. 122, pp. 692-697.

[87] Srinivasan, V. and Goldstein, R.J., 2003, “Effect of Endwall Motion on Blade Tip Heat Transfer,” J. TURBOMACH, Vol. 125, pp. 267-273.

[88] Zhou, C., Hodson, H.P., Tibbott, I., and Stokes, M., 2011, “Effects of Endwall Motion on the Aero-Thermal Performance of a Winglet Tip in a HP Turbine,” Proceedings of ASME Turbo Expo 2011, GT2011-46373.

[89] Acharya, S., and Moreaux, L., 2012, "Numerical Study of the Flow Past a Turbine Blade Tip: Effect of Relative Motion between Blade and Shroud," Proceedings of ASME Turbo Expo 2012, GT2012-69192.

[90] Yang, D., Yu, X. and Feng, Z., 2008, "Investigation of Leakage Flow and Heat Transfer in a Gas Turbine Blade Tip with Emphasis on the Effect of Rotation," Proceedings of ASME Turbo Expo 2008, GT2008-51215.

[91] Zhang, D.H., Zeng, M. and Wang, Q.W., 2009, "The Influence of Rotating Speed on Film Cooling Characteristics on GE-E3 Blade Tip with Different Tip Configurations," Proceedings of ASME Turbo Expo 2009, GT2009-60295.

[92] Schobeiri, M.T., 1999, "Efficiency, Performance and Flow Measurement of Siemens-Westinghouse HP-Turbine Blades," Series 9600 and 5600, Final Report.

[93] Sharma, K., 2011, "Inter-Stage and Performance Tests of a Two-Stage High-Pressure Turbine," Master's thesis, Texas A&M University.

[94] Holman. J. P., 2000, Experimental Methods for Engineers, McGraw Hill, New York.

[95] Rezasoltani, M., Schobeiri, M.T. and Han, J.C., "Experimental Investigation of the Effect of Purge Flow on Film Cooling Effectiveness on a Rotating Turbine with Non-Axisymmetric Endwall Contouring," Proceedings of ASME Turbo Expo 2013, GT2013-94807.

[96] Menter, F., 1993. "Zonal Two Equation k-ω Turbulence Models for Aerodynamic Flows". AIAA Paper 93-2906.

[97] Menter, F., 1994. “Two-Equation Eddy-Viscosity Turbulence Models for Engineering Applications”. AIAA Journal, 32, pp. 1598-1605.

[98] Abdelfattah, S.A., 2013, “Numerical and Experimental Analysis of Multi-Stage Axial Turbine Performance at Design and Off-Design Conditions,” Dissertation, Texas A&M University.

[99] Schobeiri, M.T., Lu, K., Han, J.C., “Effect of Purge Flow on Aerodynamics, Performance and Film Cooling Effectiveness on a Rotating Turbine with Non-Axisymmetric Endwall Contouring,” ASME Paper GT2012-69069.

[100] Schobeiri, M.T., 2010, “Fluid Mechanics for Engineers,” A Graduate Textbook, Springer Verlag, ISBN978-3-642-11593-6.

[101] Schobeiri, M.T. 1979, “Theoretische und experimentelle Untersuchungen laminarer und Turbulenter Strömungen in Diffusoren, Dissertation, Technische Hochschule Darmstadt, D17.

[102] Schobeiri, M.T., Gilarranz, J., and Johansen, E., “Final Report on: Efficiency, Performance, and Interstage Flow Field Measurement of Siemens-Westinghouse HP-Turbine Blade Series 9600 and 5600,” September, 1999.

[103] Schobeiri, M.T., Gillaranz, J. L., and Johansen, E.S., 2000, “Aerodynamic and Performance Studies of a Three Stage High Pressure Research Turbine with 3-D Blades, Design Point and Off-Design Experimental Investigations,” Proceedings of ASME Turbo Expo 2000, 2000-GT-0484.

[104] Lu, K., Schobeiri, M.T. and Han, J.C., "Numerical Simulations of Film Cooling on Rotating Blade Tips within a High-Pressure Turbine", Proceedings of ASME Turbo Expo 2013, GT2013-94806.